Engineered nanostructures of binary and ternary metal oxides for gas and humidity sensing application

Thesis Submitted to AcSIR for the Award of the Degree of

DOCTOR OF PHILOSOPHY
In Chemical Sciences

By

Satish S. Badadhe
Registration Number: 10CC11J26103

Research Guide
Dr. Manjusha V. Shelke
Scientist

Research Co-guide
Dr. Satishchandra B. Ogale
Chief Scientist

CSIR-National Chemical Laboratory, Pune-411008, India

2015

Engineered nanostructures of binary and ternary metal oxides for gas and humidity sensing application

Thesis Submitted to AcSIR for the Award of the Degree of

DOCTOR OF PHILOSOPHY
In Chemical Sciences

By

Satish S. Badadhe

Registration Number: 10CC11J26103

Research Guide
Dr. Manjusha V. Shelke
Scientist

Research Co-guide
Dr. Satishchandra B. Ogale
Chief Scientist

CSIR-National Chemical Laboratory, Pune-411008, India

2015

Certificate

This is to certify that the work incorporated in this Ph.D. thesis entitled **"Engineered nanostructures of binary and ternary metal oxides for gas and humidity sensing application"** submitted by **Mr. Satish Shivaji Badadhe** to Academy of Scientific and Innovative Research (AcSIR) in fulfillment of the requirements for the award of the Degree of **Doctor of Philosophy in Chemical Sciences,** embodies original research work under my supervision. I further certify that this work has not been submitted to any other University or Institution in part or full for the award of any degree or diploma. Research material obtained from other sources has been duly acknowledged in the thesis. Any text, illustration, table etc., used in the thesis from other sources, have been duly cited and acknowledged.

Research Student

Mr. Satish S. Badadhe

Research Guide

Dr. Manjusha V. Shelke

Scientist

Research Co-guide

Dr. Satishchandra B. Ogale

Chief Scientist

Declaration

I hereby declare that the thesis entitled **"Engineered nanostructures of binary and ternary metal oxides for gas and humidity sensing application"** submitted for the degree of **Doctor of Philosophy** in Chemical Sciences to the Academy of Scientific & Innovative Research (AcSIR), has been carried out by me at the Physical and Materials Chemistry Division of National ChemicalLaboratory, Pune under the guidance of **Dr. Manjusha V. Shelke and Dr. Satishchandra B. Ogale**. Such material as has been obtained by other sources has been duly acknowledged in this thesis. The work is original and has not been submitted in part or full by me for any other degree or diploma to other University.

Date
National Chemical Laboratory,
Pune - 411008

Research Student
Mr. Satish S. Badadhe

Dedicated to

My Beloved Mom…

Acknowledgements

I would like to express my sincere gratitude to all thosepeople who have contributed directly or indirectly to my thesis and made this journey enjoyable. I will cherish their contribution forever.

I express my foremost and deepest gratitude to my research guide, Dr. (Mrs.) Manjusha Shelke who gave me an opportunity to work under her guidance. I have been fortunate as she gave me complete freedom to execute and explore new ideas and assisted methroughout this time when I needed help. Her keen observation, analysis and positive approach towards research has always motivated me to do better.

I am also grateful to my research co-guide Dr. Satishchandra Ogale. I am very fortunate to work under his able guidance and vibrant laboratory atmosphere. He is a source of inspiration and enthusiasm and has always motivated me with his devotion, dedication, hard work, optimistic approach and eagerness to learn new things. I will never forget his endless support, patience, encouragement throughout this study period. I learned a lot from his knowledge, experience, and philosophy of life which moulded me into a good human being. His scientific discussions, keen observation, analytical ability, critical comments nurtured my scientific skill and also inspired me to strive to be a good researcher.

I would also like to thank Dr. I. S. Mulla for giving me the opportunity to work in the National Chemical Laboratory. He has always encouraged me to do better in all aspects of life. His invaluable suggestions and discussions throughout this study helped me a lot. I wish to express my heartfelt gratitude towards him for his warm and friendly support throughout this journey.

I would also like to thank Dr. Vijay Dangat for his constant support, motivation, throughout this journey. He helped me in taking my initial footsteps into research.

I sincerely thank the Council of Scientific and Industrial Research (CSIR) for fellowship and the Department of Science and Technology (DST) for funding support. I would also like to express my gratitude to Dr. Vijaymohanan Pillai (Director NCL), Dr. S. Sivaram, and Dr. Sourav Pal (former Directors, CSIR-NCL), and Dr. Anil

Kumar (Head of the Physical and Materials Chemistry Division) for providing the infrastructure and advanced facilities for research and giving me an opportunity to work at CSIR NCL.

I sincerely like to thank my Doctoral Advisory Committee (DAC) members Dr. BLV Prasad, Dr. Suresh Bhat, and Dr. P. A. Joy (chairman), for regular evaluation, guidance and discussion which helped me to improve my research work.

I am also thankful to Student Academic Office (SAO) staff initially led by Dr. P. A. Joy and Dr. C. G. Suresh and now by Dr. M.S. Shashidhar for their constant help and co-operation. I would further like to thank Dr. C. Gadgil (AcSIR co-ordinator, NCL), Mrs. Kolhe and Ms. Deepa for their invaluable help. I also acknowledge and admire the efficiency of the Deans of AcSIR (headquarters) and their staff. I am grateful to administrative and engineering staff for their invaluable help and co-operation.

I deeply acknowledge my laboratory seniors/friends Dr. Vivek Dhas, Dr. Subas Muduli, Dr. Abhimanyu Rana, Dr. Anup Kale, Dr. Arif Shaikh, Dr. Parvez Shaikh, Dr. Vivek Antad, Dr. Harish Gholap, Dr. Ashish, Dr. Sambhaji, Dr. Prasad, Dr. Onkar, Dr. Datta, Dr. Rohan, Dr. Abhik, Dr. Mandakini, Dr. Minakshi, Dr. Sarika, Dr. Meenal Deo, Dr. Shruti, Dr. Lily, Vishal, Anil, Rounak, Satyawan, Pradeep, Aniruddha, Yogesh, Umesh, Wahid, Reshma, Dipti, Dhanya, Divya, Pooja, Shraddha, Mukta, Supriya, Ketaki, Nilima, Aparna, Rupali, Poonam, Srashti, Ishita, Shital, Swati, Golu, Ajay and Neha for creating a wonderful laboratory atmosphere. I would specially like to thank Upendra, Jefrina, Rohit, Anand, Tushar Amabade for their help during this study.

I would also like to thank my friends Dr. Girish, Dr. Mukta, Dr .Rupali, Dr. Sonali, Dr. Padmakar, Ajit, Sachin Kunjir, Manoj, Abhijit, Yohesh, Umesh Sankapal, Sachin suryawanshi, Sachin Rodhiya, and Abhishek for their help, constant support, and motivation. I sincerely express my gratitude to all my teachers from primary school till my master's degree for imbibing good values and knowledge in me. I would also like to thanks Deshmukh kaka and kaku, Mr. Jadhav for their constant support throughout this journey.

I whole heartedly thank my family, my father, sisters and all aunties and uncles for their constant support and unconditional love. I would specially like to thank Sushila

aunty for her constant support and blessing which gave me the strength to fulfil my dream. I would also like to thank my uncles Ramesh, Babaso, Shivaji, and Shankar who have always supported unconditionally and motivated me for higher studies. I would like thank my grandmother Sonabai (late) for her unconditional love and support. I miss you....

Finally, I thank almighty God for giving me a great life, strength to chase my dreams, and being with me in all my failure and success!

Satish S. Badadhe

List of Abbreviations

AFM	Atomic Force Microscopy
at%	Atomic percent
AZO	Aluminium doped Zinc Oxide
CB	Conduction Band
DOS	Density of States
DRS	Diffuse Reflectance Spectroscopy
EIS	Electrochemical Impedance Spectroscopy
E_f	Fermi level
FESEM	Field Emission Scanning Electron Microscope
FB	Flat Band
FTO	Fluorine doped Tin oxide
FWHM	Full Width at Half Maximum
FVO	FeV_3O_8
HJ	Heterojunction
HOMO	Highest Occupied Molecular Orbital
HRTEM	High Resolution Transmission Electron Microscope
I_a	Current in air
I_g	Current in gas
ITO	Indium doped Tin Oxide
IZO	Indium doped Zinc oxide
NCO	$NiCo_2O_4$
NRs	Nanorods

OPD	Optical Path Difference
R_a	Resistance in air
R_g	Resistance in gas
SAED	Selected Area Electron Diffraction
STM	Scanning Tunneling Microscope
SEM	Scanning Electron Microscope
TEM	Transmission Electron Microscope
VB	Valence Band
XPS	X-ray Photoelectron Spectroscopy
XRD	X-ray Diffraction
ZTO	Zinc stannate (Zn_2SnO_4)

Content

Section I

Chapter 3

3I: H_2S gas sensitive indium-doped ZnO thin films: Preparation and characterization

3II: Effect of aluminium doping on structural and gas sensing properties of zinc oxide thin films deposited by spray pyrolysis

Abstract

As a consequence of rapid development and related industrial growth tons of hazardous and eco-antagonist gases are being constantly released in the atmosphere. Safeguard of environment and living creatures is thus a serious problem of this century. In order to control this problem, it is essential to monitor these harmful gases. Recently, sensing of toxic gases has received tremendous attention due to excessive production and increase of exposure levels to these gases. Semiconducting oxide gas sensors based on surface reactions between analyte molecules and adsorbed oxygen species lead to the change in concentration of charge carrier of oxide. The field of gas sensors is still plagued with issues such as low sensitivity, poor selectivity, large response and recovery time, high operating temperature etc. One way to improve the gas sensor properties is to explore doped systems, composites, or hybrid systems of nanomaterials.

A brief explanation of the methodologies used is given below in each chapter.

The first chapter introduces working principles of gas and humidity sensor. Factor affecting sensing properties such as particle size, morphology, catalyst, effect of doping, heterojunction, ternary systems etc. are reviewed in context of gas response, selectivity and other important related parameters.

The second chapter deals with synthesis and characterization techniques involved in gas sensing study. The synthesis techniques namely spray pyrolysis, hydrothermal, successive ionic layer adsorption and reaction (SILAR) method used for obtaining desired nanostructures are briefly discussed. The gas sensor set-up and measurement techniques namely static and dynamic are discussed.

The presentation of the thesis is divided in two sections I and II. In section I the results on the gas sensing properties of the functional binary oxide ZnO are reported. Two cases are discussed, namely a) the effects of dopants, and b) the effect of forming a hetero-interface with a suitable partner material (in this case CdS). In section II detailed results on the gas and humidity sensing properties of three interesting ternary oxide systems which are important and interesting in their own right are presented, analyzed and discussed.

Section I: Tailoring the properties of the binary oxide ZnO for gas sensing

The third chapter deals with effect of doping on gas sensing properties of ZnO thin films. This chapter comprises two sections namely indium and aluminium doping effect on gas sensing properties of ZnO. In first section high quality indium-doped ZnO (IZO) thin films (~100 nm) have been deposited onto the glass substrates by using a conventional spray pyrolysis technique. Their response towards various gases was measured at different operating temperatures and different levels of In-dopants. The 3 at.% In-doped ZnO showed response as high as ~13,000 for 1000 ppm H_2S at 250^0C. It exhibited fast response (~2 s) and recovery time (~4 min). Second section also deals with a facile spray pyrolysis route to deposit aluminium doped ZnO (AZO) thin films on to the glass substrates. It is observed that on aluminium doping the particle size of ZnO reduces significantly; moreover, uniformity of particle also gets enhanced. The gas response studies of ~800 nm thick Al-doped ZnO films at different operating temperatures show that 5 at.% Al-doped ZnO thin film exhibits highest response towards H_2S gas at 200^0C.

In fourth chapter, we report visible light assisted room temperature NO_2 and H_2S gas sensing of ZnO nanorods (NRs)/CdS heterojunction. ZnO NR/CdS heterojunction shows improved optical absorption in the visible region. The visible light assisted gas sensing performance of ZnO NRs and ZnO NR/CdS were carried out. In presence of light ZnONR/CdS heterojunction showed enhanced NO_2 response compared to ZnO. Further, ZnO/CdS heterojunction exhibits light assisted H_2S response.

Section II: Ternary oxides for gas and humidity sensing

The fifth chapter deals with facile synthesis of vertically aligned nanosheets of FeV_3O_8 on the fluorine doped tin oxide (FTO) by simple hydrothermal technique. The schematic gas sensing study of FeV_3O_8 nanosheets were performed for NH_3, CO, H_2S and NO_2 for different operating temperature between 50^0C and 350^0C. The FeV_3O_8 nanosheets exhibit good response and selectivity towards H_2S at low operating temperature of 150^0C.

In the sixth chapter, we report facile synthesis of $NiCo_2O_4$ nanograss using simple hydrothermal method. Interestingly, nano-blades of each $NiCo_2O_4$ nanograss is constituted of ~10-15 nm sized nanoparticles with throughout mesopores along the

nanoblades. Gas sensing study of $NiCo_2O_4$ nanograss exhibits large surface area, porous nature, and high catalytic activity. $NiCo_2O_4$ nanograss exhibits good response to NH_3 and CO.

In the seventh chapter, we report hydrothermal synthesis of single phase zinc stannate. Zn_2SnO_4 (ZTO) film of ~10 μm thick films showed ~4 order changes in its response towards humidity. The complex ac impedance of ZTO films are taken between 11% and 92% relative humidity(RH) at 1V with 50 mV amplitude of ac signal between 10^{-2} and 10^6 Hz. AC impedance analysis shows when sensor is operated at 0.1 Hz with 50 mV at 1V gives better response over entire range of humidity (11% RH to 92% RH).

Chapter 8 presents conclusions of the thesis and future scope for research in gas sensor field.

Chapter 1

Introduction

The present thesis is based on engineered nanostructures of metal oxides for gas and humidity sensing applications. This chapter initially presents the overview of sensor and types of chemical sensor. The main focus of this chapter is based chemiresistive gas sensor based on semiconductor oxides. This chapter briefly discusses working principle, factor affecting gas sensing performance, performance parameters sensors, different engineered metal oxides like binary, ternary, doped, hetero-junction of semiconductor metal oxides. Lastly, working principle and literature survey of humidity sensors is presented. The outline of the chapters to follow is provided at the end of the chapters.

1. Introduction

Sensors are used in almost every sector of our life and their uses have now become almost inevitable. Recent years have seen tremendous improvements in sensor technology. The advancements in sensor manufacturing technologies are driven by the developments in miniaturization technologies, lowering of costs, enhancements of speed, lowering of power for supporting microelectronic circuits, and advances in signal conditioning processes. It is a continuous quest to develop efficient, reliable and good quality sensors for commercial competitiveness. In order to improve sensor output data, simulation technologies and design aides are now playing crucial roles in saving time and improving product quality. In this chapter, we briefly introduce sensor basics, their classification, and finally focus on various aspects and parameters involved in metal oxides based gas and humidity sensors.

1.1 Sensor: Basic introduction

Sensor is a transducer which senses/detects characteristic properties of its surrounding environment. It recognizes change in a measurable quantity and converts it into corresponding output signal processable by a data acquisition system. Nowadays sensors are used in most of the everyday operations such as touch sensitive elevators buttons and dimming/brightening lamps by touching their base. There is ample number of sensor applications that most of people are unaware of even though they are in frequent use. The uses of sensors have been expanded with recent advances in micro-machining and microcontroller platforms. Sensors have very diverse applications base which includes various industrial manufacturing processes, machineries, cars, airplanes, aerospace, robotics, mobiles, and the huge medical sector. Sensors are always a key integral part of a larger system which may include detector, signal conditioners and processors, data recorders, memory devices, actuators etc. The term ‘sensor’ started earning respectability and wide spread use during the 1970s[1]. The uprising in the field of sensors was caused by the then technological revolution and the pace of the corresponding developments continues till date. The unprecedented development in microelectronics during the past few decades has resulted in an evolving technical intelligence which has led to the production of more intelligent autonomous machines involving multiple sensing features.

The world is moving fast and sensors have increasingly crucial roles to play in every aspect of life. Most sensors are either in contact of the inspected object or exchange signals with the same, the corresponding nonelectrical information is then to be transformed into electrical signals at a rapid pace (fast response), they must operate incessantly in repeated cycles, and should be small in size to be effectively integrated into the operational systems architecture. These are some broadly approved attributes of any sensor system [1]. The most desirable characteristics of a sensor are high sensitivity, high stability, and nearly perfect repeatability. The utility of sensors is defined and limited by these three characteristics which can be specified over a certain range of measured values and operation times. In many cases highly sensitive devices are not useful as their output signal drifts during the time of operation and the data obtained is not reliable. The other important features like selectivity, linearity can be compensated for by signal conditioning circuits or using other independent sensors.

The classification of sensors needs to take into account various possible simple to complex phenomena that enable sensor functionality. The classification of sensors can be done based on stimulus, physical phenomenon employed, mechanism of signal accumulation and conversion, choice of specific material system(s), and applications. Sensors classified based on applied stimulus are thermal, acoustic, electric, optical, magnetic etc.

1.2 Chemical Sensors

A chemical sensor recognizes and is sensitive to the chemical composition of its surrounding environment. It is self-efficient analytical device which gives information about a solid, liquid or gas phase in its vicinity. The sensors signal is directly related to the type and analyte concentration i.e. the chemical element to be detected. They are also named as artificial noses or artificial tongues depending on what is being sensed or detected, and these aptly resemble the biological systems. The similarity between a biological system and technological systems in use is illustrated in Fig. 1.1. In a biological system, receptor organs recognize and transmit signals to the brain through sensory neurons. Similarly, in technological systems sensing element acts as a receptor that responds to its environment by changing its inherent property. A transducer converts this primary information into electrical signal which is then supplied to data acquisition system i.e. a computer which functions similar to the

central nervous system of the brain. Recently, amplifiers are being increasingly used to amplify the signals of devices. Hence, for the effective functioning of sensors two key steps are involved namely recognition and transduction. In chemical sensors, the recognition step deals with selective interaction of analyte molecules with receptor sites or molecules of sensing elements. Subsequent changes in characteristic physical parameters are converted by means of integrated transducers which generate the useful analytical signal.

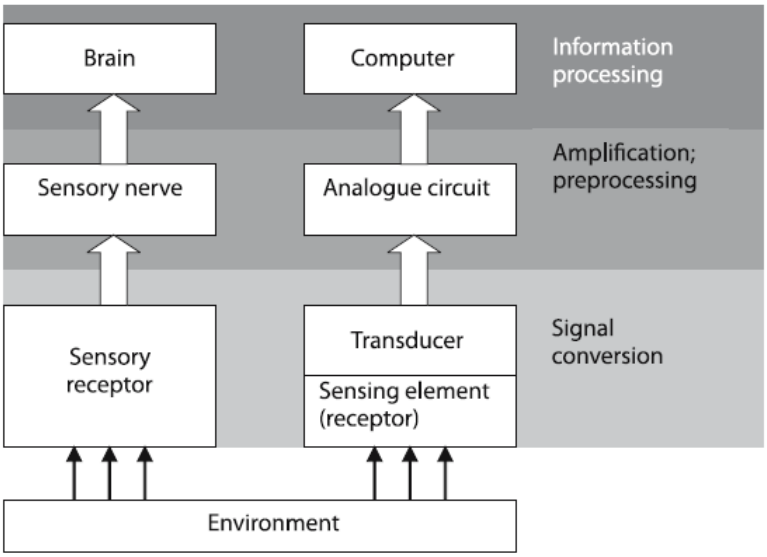

Figure 1.1: Signal processing in biological and technical systems [Printed with permission[1].

In 1991, the International Union of Pure and Applied Chemistry (IUPAC)[2] defined chemical sensor as *"A chemical sensor is a device that transforms chemical information, ranging from concentration of a specific sample component to total composition analysis, into an analytically useful signal"*. The chemical information, referred in the definition, may emanate from a chemical interaction of analyte molecules or a physical property of the system studied. Some authors have proposed different definitions of a chemical sensor. Wolfbeis [3] defined chemical sensors as *small-sized devices having a recognition element and a signal processor competent of continuously and reversibly reporting a chemical concentration*. Here, reversibility implies that the sensor should provide dynamic response with change in concentration and not 'freeze' during measurements. According to Göpel and Schierbaum [4]

chemical sensors are devices that convert a chemical state into an electric signal. Chemical sensors are thus a measuring chain link between the chemical world and the world of electronics. Stetter and Penrose have stated some typical features of chemical sensors [5] and these are as follow: A sensitive layer in chemical contact with analyte/test molecules, reaction of the analyte with the sensitive layer leading to alteration in the chemistry of the layer, transduction of the corresponding change to an electrical signal, physically small, performing in real time, inexpensive and suitable for the same chemical measurements over another equivalent instrument.

An analyzer is an essential component of a chemical sensor. It is an automated part of a system containing devices which function for operations such as sampling, sample transport, signal processing, data processing. As discussed earlier, the receptor part of the sensor interacts with analyte molecules generating physical/ chemical properties variation. The transducer measures the energy formed due to chemical interaction carrying useful chemical information into usable analytical signal. This transducer part has nothing to do with selectivity.

Receptor part of chemical sensor can be based on the following principles:

- Physical (no chemical reaction) e.g. temperature, conductivity, refractive index, absorbance, or mass change.
- Chemical (Reaction with analyte produces the analytical signal).
- Biochemical (a biochemical process generates the analytical signal) e.g. Microbial potentiometric or immuno sensors. They are also known as biosensors.

1.2.1 Classification of chemical sensors

The classification of chemical sensor can be carried out in a number of ways. The classification based on transducer's operating principle, as given by IUPAC[2], is shown in Table 1.1. Chemical sensors can also be classified based on applications (e.g. pH sensor, metal ions sensors, O_2 or other gaseous sensors), modes of applications (e.g. specific process monitoring, *in vivo* use etc.), Different classifications methods can be employed based on logical and clearly defined principles.

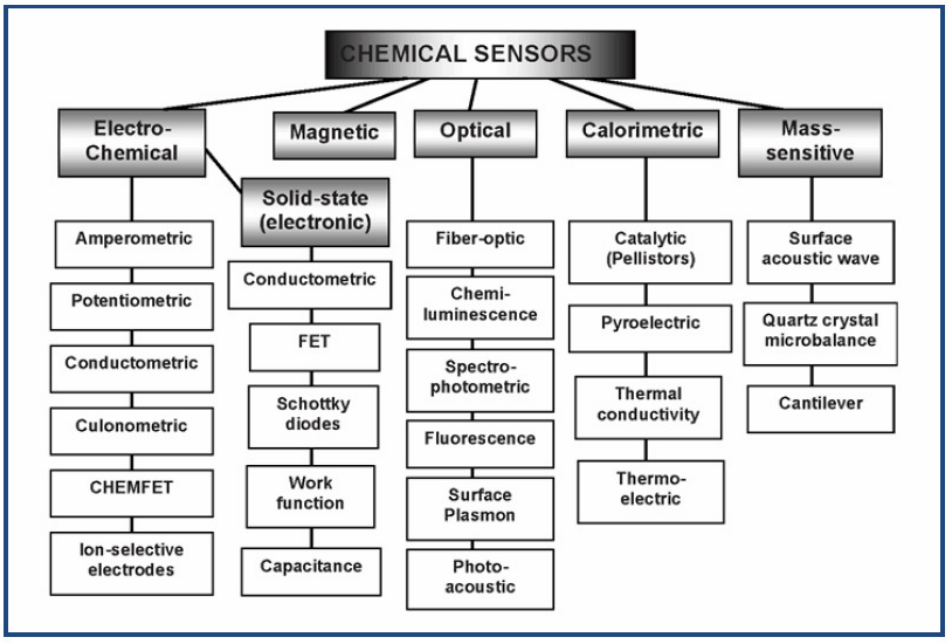

Table 1.1: Classification of chemical sensors based on operating principles of transducers [Reprinted with permission[6].

1.3 Gas Sensors

The main goal and responsibility of the present generation is to monitor air quality and address the related health problems. In the last few decades, the living standards of human beings have been improving at great pace owing to continued industrial revolution. Such unprecedented technological developments have however created severe environmental safety issues for human and living animals. Air pollution has been constantly increasing as a result of growing industrialization; vehicular exhaust being one of the leading contributors. Hence, Industrialization requires detection and monitoring of toxic pollutants and gases emanating from refining, explosives, and processing establishments for environmental protection and safety monitoring. The detection, measurement and possible elimination of a specific hazardous gas in the ambient is the key part in product development, process control, and environmental monitoring and control. Therefore, it is essential to develop sensors which detect toxic and inflammable gases operating under the ambient conditions.

Gas sensor is a subclass of chemical sensors. It has numerous applications in industrial process control, and environmental monitoring. For many gases, sensitive

sensor systems have been developed significantly in the recent years. Toxic/ stringent smelling gases like H_2S, NH_3 and other hazardous gases used in industrial processes have been continuously targeted by researchers. In food industries, detection of smell generated from food and food products, and different volatile gases is necessary to determine and monitor the quality of products. These gases are present in very minute levels and are generally mixed with other interfering gases. It is necessary to develop sensors for toxic gases such as SO_x, CO_x, NO_x, etc. which cause air pollution and can be applied to control combustion exhausts from stationary automobiles facilities.

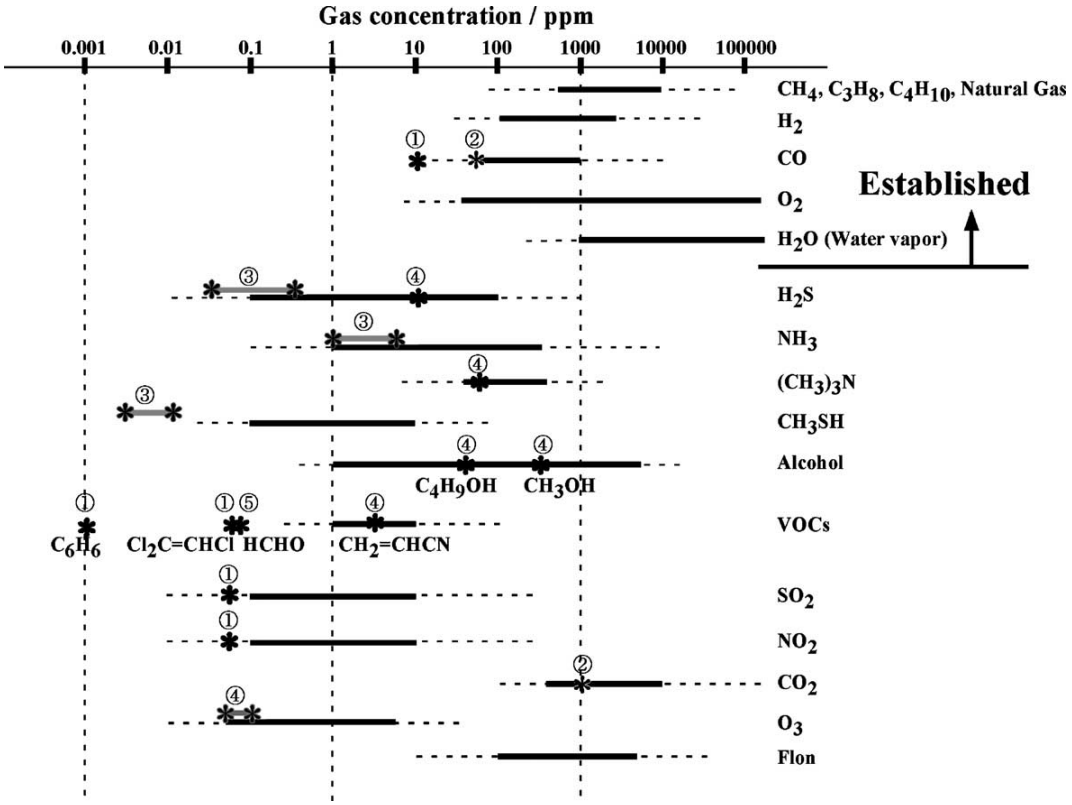

Figure 1.2: Concentration levels of typical gas components concerned. * indicate the standards of the gases legislated in Japan by (1) Environmental Standard, (2) Ordinance on Health Standards in the Office, (3) Offensive Odor Control Law, (4) Working Environment Measurement Law, and (5) Ordinance by Ministry of Health, Labour and Welfare[Reprinted with permission[7].

There is always a need to develop novel gas selective sensors for various gases. It is requisite in some cases to develop different sensors for the same analyte which

depend on sensor operation conditions. In order to monitor air pollution, gas sensors need to measure pollution level in the atmosphere, so that appropriate action can be followed. The flammable gas sensors are also essential to avoid unwanted fire/explosion. Explosive gases (like H_2) are not toxic at ppm level but above a threshold value they form an explosive mixture. Therefore, flammable/hazardous gas sensors have tremendous demand for their usefulness towards safety purposes. It is necessary that gas sensors are developed which detect the toxic gases in parts per million in the atmosphere. Figure 1.2 reveals the respective limits for typical toxic and or flammable gases present in the atmosphere[7].

It is necessary to have the concept of gas sensor design to develop various gas sensors to fulfil the demands from gas sensors. As discussed earlier, a gas sensor should have two basic functions, namely the receptor function (recognition of analyte molecules) and the transducer function (translate recognition into a sensor signal). The recognition of gas molecules occurs as a result of adsorption or chemical reactions of analyte molecules with sensing materials. Transduction function mainly depends on materials being used for analyte recognition. In the case of semiconducting materials, sensor signal is transduced into an electrical resistance alteration. In many cases capacitance, resonant frequency, electromotive force, optical absorption and emission can also be used as sensing signal for different sensing elements.

1.4 Different technologies used for gas sensors

The gas sensors are commonly divided into three groups based on the technology employed.

- Optical
- Spectroscopic
- Solid State

In an optical sensor, the target gas molecules are stimulated by light and measured via the corresponding specific absorption spectra. Optical sensor technology needs complex measurement system, in many cases a monochromatic source for excitation, and optical sensor to analyze the absorption spectra. Analysis of gas can also be done by techniques such as infrared spectroscopy, chromatography, ultraviolet fluorescence etc. These techniques are very accurate and sophisticated, but require

skilled/experienced technician to operate them to obtain good results. The optical and spectroscopic systems are very expensive for common domestic purpose, also due to their large size they cannot be used or implemented in car engines. Therefore, solid state gas sensors are very useful due to the possibility of making them in miniaturized size, feasibility of implementing them for online work, and non-requirement of a skilled operator. Hence, solid state gas sensors have attracted tremendous attention.

1.5 Solid State gas sensors

Solid state sensors have many advantages such as fast response, ease of operation, small size, portability, low-power and most importantly their low cost[8,9]. In addition, these sensors can work online without the requirement of trained operators. Solid state gas sensors are good candidates for commercial use for a broad range of applications[10-12]. Solid state gas sensors have continuously attracted scientific and industrial world due to their various advantages such as small sizes, high sensitivities (ppm or even ppb level detection) towards various gases, compatibility for on-line operation, possibility of batch production, and low cost. Conventional analytical method such as nuclear magnetic resonance (NMR), chromatography, mass spectrometer on the other hand are complex, large in size and expensive. Real-time analysis is difficult with many of these techniques as sample preparation is necessary for the analysis. Solid state gas sensors however have several problems such as accuracy, stability etc. Advances in nanotechnology have overcome these issues in many ways through manipulation of novel nanostructured systems, fabrication of novel nanomaterials with better gas sensing properties etc.

Solid state gas sensors are based on reversible chemical reactions of analyte molecules with sensor. The reaction of analyte gas with the surface of sensing elements leads to change in conductivity, capacitance, mass, work function, energy released due to reaction, optical property variation etc. Thus, sensing performance of sensing elements can be determined by measuring any of the above mentioned

properties. Solid state gas sensing materials have been used as pellets, thin or thick films. For the design of solid state gas sensors, theoretically there are no restrictions for use of any materials based on their chemical, physical, electrical or structural properties. Different materials such covalent semiconductors, solid electrolytes, semiconductor metal oxides, polymers, organic semiconductors, ionic membranes have been used in gas sensors prototypes[13-24]. There are numerous reports on gas sensing characteristics and performance based on these materials. However, all the gas sensors are not equally effective; hence the key problem is the selection of optimal gas sensor material with required operating parameters for the design and manufacture of a good and effective gas sensor[25-30].

In the market, three main types of gas sensors are produced in large scale [11]. These are based on solid state electrolyte, catalytic combustion, and modulations of resistance sensors. These are termed as electrochemical, pellistor, and conductometric or chemiresistance sensors, respectively. The present thesis is based on third type gas sensor i.e. conductometric gas sensor. Table 1.2 presents a comparison between semiconductor gas sensors with other types of solid state gas sensors. [31].

Table 1.2: Comparison of various types of gas sensors [Adopted from [31]]

Parameter	**Type of gas sensors**				
	Semi-conductor	**Catalytic combustion**	**Electro-chemical**	**Thermal conductive**	**Infrared absorption**
Sensitivity	e	g	g	b	e
Accuracy	g	g	g	g	e
Selectivity	p	b	g	b	e
Response time	e	g	p	g	p
Stability	g	g	b	g	g
Durability	g	g	p	g	e
Maintenance	e	e	g	g	p
Cost	e	e	g	g	p
Suitability to portable instruments	e	g	p	g	b
e: excellent, g:good, p: poor, b:bad					

Semiconductor gas sensors based on chemiresistive (or conductometic) properties have been extensively used to detect harmful and combustible gases due to their ease of operation and low cost. The chemiresistive gas sensor is based on the interaction

between an analyte gas molecule and a semiconductor which leads to a change in the electrical resistance of sensor[25]. Such sensors exhibit high sensitivity, rapid response time, compatibility for design of portable instruments, and low cost. These qualities compensate over their drawbacks and open opportunities to their use in alarm systems, and some portable gas sensing instruments.

1.6 Semiconductor Metal Oxides Gas Sensors:

In 1953, Bardeen and Brattain for the first time reported a gas sensor based on the formation of space charge layer on the surface of germanium[32]. Subsequently, in 1962, Seiyama et al. reported gas detection based on the same principle using a new semiconductor oxide ZnO[33]. In the same year, Taguchi first patented SnO_2 resistive gas sensor based on the same principle and commercially implemented this idea to develop semiconductor oxide based gas sensors[34]. Figaro Engineering Inc. is the leading company in gas sensor market with their popular product Taguchi gas sensor (TGS). Since then there has been a continuous quest to develop gas sensing materials and gas sensor technology to fulfil various performance parameters required for different applications. Improving the performance parameters of the available gas sensors is one of the focussed areas of investigation. Apart from this, there is an unending research quest devoted to investigations of novel gas sensing materials and mechanisms for understanding and applying the basic science behind the processes. Therefore not only further improvements in the gas sensing performance of gas sensors are possible but new science and mechanisms are also likely to appear on the sensors scene. There are many literature reports which give brief overview of and insights into further expected developments in this field of research.

The performance parameters of a gas sensor can be optimized by controlling the crystallite phase, grain size, morphology, and employing a multi-component system such as doping (by noble metal, transition elements, inert impurity etc) or composites, heterojunction etc. Such choices along with preferred microstructures affect the physico-chemical properties such as stabilization of a preferred oxidation state, improvement in the catalytic activity, chemical and thermal stability, increase in the density of free charge carriers and their rate of exchange, and the control of surface potential and inter-grain surface barriers. In chemiresistive gas sensors, the influence on the physical properties of typical metal oxides when an analyte gas molecule gets

adsorbed on the grain-boundary of the corresponding polycrystalline material is illustrated in Fig. 1.3[31].

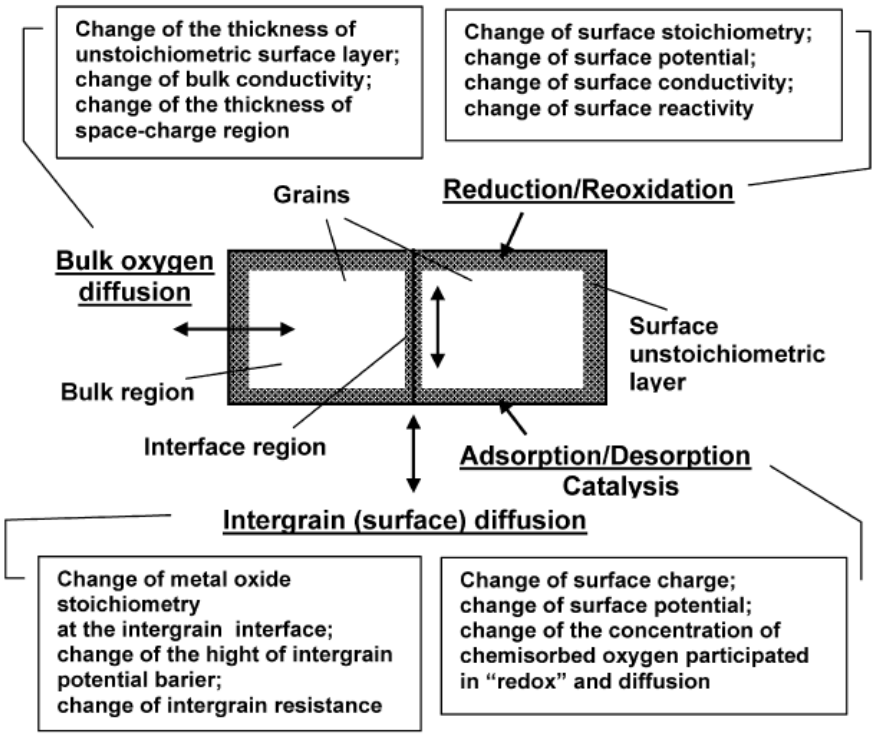

Figure 3.3: shows a diagram illustrating the different processes occurring in metal oxides during gas detection and their consequences for polycrystalline metal oxides properties [Reprinted with permission[31]].

As stated above, the semiconductor metal oxide based gas sensors are chemiresistive type of gas sensors. The construction of solid state gas sensor is simple; first a semiconducting material is deposited/constructed on an insulating substrate and then metal wire contacts are used as electrodes. The sensor signal is generated due to change in the resistance of semiconductor metal oxide upon analyte adsorption. Semiconductors metal oxide gas sensors have a tremendous market value due to their capability to detect wide range of toxic and combustible gases. These gas sensors suffer from lack of selectivity till date. Yet other sensor performance criteria such as low cost, reliability make them faster growing gas sensor devices in the market.

1.6.1 Working Principle of Semiconductor Metal Oxide gas sensor

The working principle of a metal oxide based gas sensor is described using surface reactions taking place on grains and corresponding variations in energy band is shown in Figure 1.4[35]. In the presence of air, oxygen molecules are chemisorbed on the surfaces of grains by extracting electrons and forming depletion layer around the grains. The depletion layer is also known as Debye layer or space charge layer. At the grain boundaries, back to back space charge layer is formed which forms potential barrier for the electron across the grains. This increases resistance of n-type metal oxides. The temperature dependent oxygen reaction with metal oxide is shown in following equation[36].

Oxygen reactions

$$MO + O + e^- \longrightarrow MO - O^- \quad \text{(between 150°C and 300°C)} \qquad (1.1)$$

$$MO + 2O + e^- \longrightarrow MO - O_2^- \quad \text{(between 30°C and 150°C)} \qquad (1.2)$$

The above reactions lead to extraction of electrons and as a result the resistance of sensor element increases.

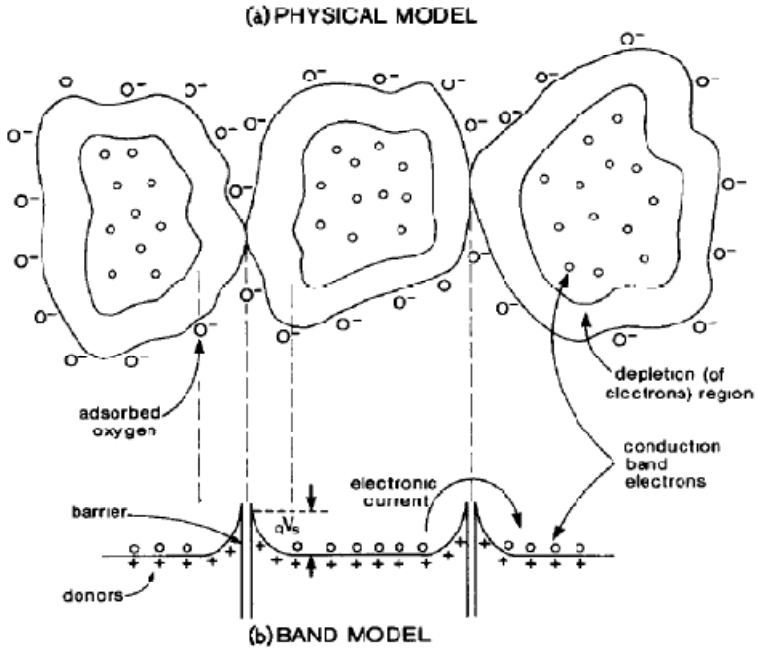

Figure 1.4: shows that ionosorbed oxygen affects inter-granular electron transport as depicted by the physical and band models. The height of the energy barrier is qV_s [Reprinted with permission [35]].

In presence of a reducing gas, oxygen molecules are removed from surface and electrons are released back to the grains. This reduces the depletion layer, thereby decreasing the resistance of the sensor element.

Reducing gas reaction

$$R + MO - O- \longrightarrow MO + RO + e- \quad (1.3)$$

However, in the presence of oxidizing gas, electrons are extracted from the metal oxide which further increases depletion layer and thus increases resistance of metal oxides.

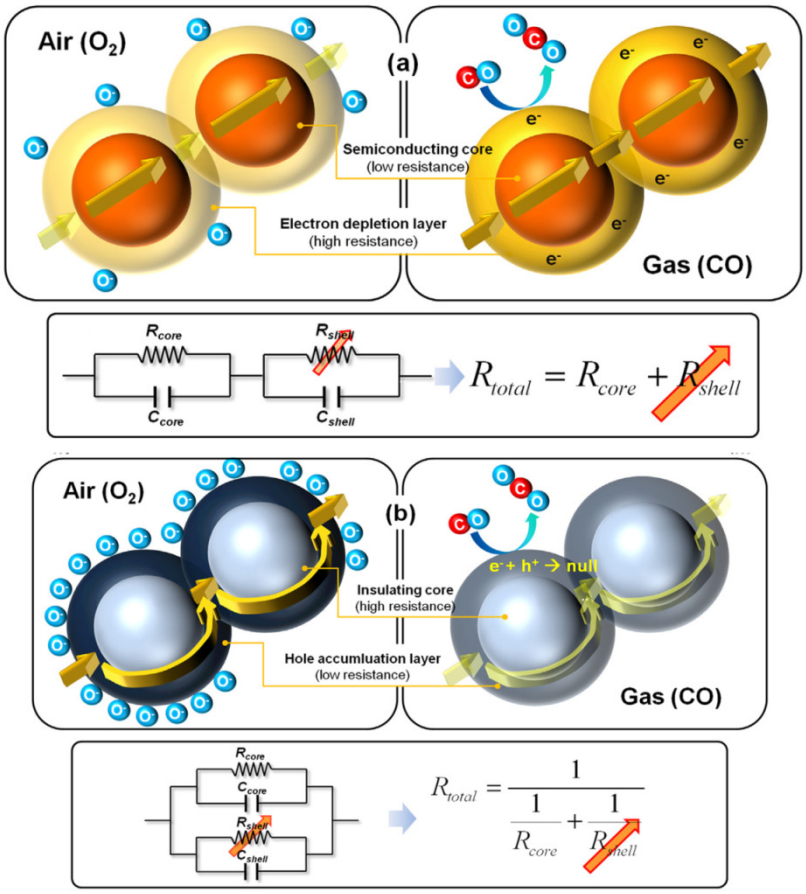

Figure 1.5: presents a pictorial representation of gas sensing mechanism and corresponding equivalent circuits involved of (a) n-type and (b) p-type semiconductor metal [Reprinted with permission [37]].

Oxidizing gas reaction

This reaction is represented by,

$$MO - O- + O + e- \longrightarrow MO - O_2^- \quad (1.4)$$

For both n- and p-types of semiconducting metal oxides, similar adsorption of oxygen onto the surface of a metal oxide is observed[37]. However, the conductivity mechanism is totally different. In n-type metal oxides, ionosorbed oxygen depletes the surface of carriers by extracting electron i.e. the surface region is more resistive (Fig. 1.5 a). However, in the p-type semiconducting metal oxide, the ionosorbed oxygen forms an accumulation layer (holes) and thus the surface becomes more conductive (Fig. 1.5 b). Thus, in n- and p-type metal oxides opposite behaviour of conductivity is observed for the same test gas [Figure 1.6].

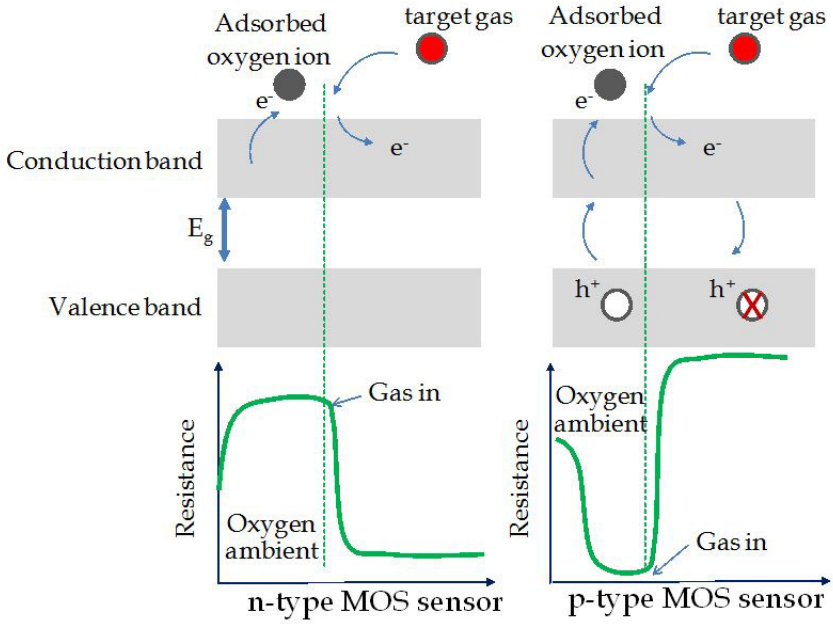

Figure 1.6: shows a schematic representing the effect of reducing gas on the resistance of n-type and p-type metal oxides [Reprinted with permission[38]].

The gas sensing mechanism of metal oxides discussed above briefly does not tell the whole story. In reality, modulation depletion layer not only affects the number of charge carriers but also their mobility[39-40]. There is still an ongoing debate whether sensing is due to oxygen ionosorption or oxygen vacancies[41-42].

1.6.2 Fundamental aspects of gas sensors

The main challenge of gas sensors is to detect toxic and inflammable gases at low concentrations and that too selectively. Therefore, currently there is a growing need for gas sensors with advantageous properties such as high sensitivity, selectivity,

stability, robustness etc. Hence to improve gas sensor performance, the fundamentals aspects of the working principles of gas sensors should be understood.

There are many factors affecting the gas sensing properties such as kinetics of reactions, diffusivity of analyte on the surface of the sensor element, the microstructure of sensor etc. Figure 1.7 represents the basic functioning of a gas sensor. The entire gas sensing process is classified into three parts namely receptor function, transducer function, and utility. Therefore, the properties of gas sensors can be altered or modified by tuning each of these aspects separately or concurrently.

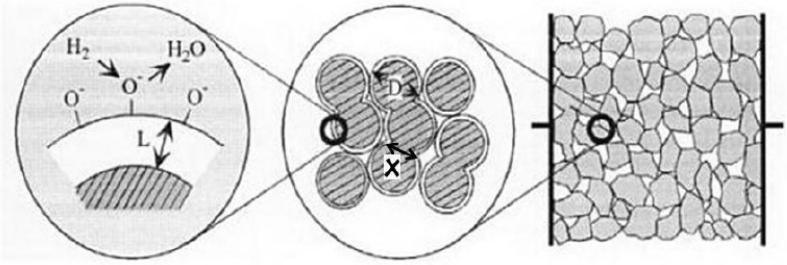

Figure 1.7: Schematic diagram of receptor and transducer functions of the semiconducting gas sensor. Where, D: particle size, X: neck size, L: thickness of space charge layer[Reprinted with permission [43]].

1.6.2.1 The Receptor Function

The interaction between gas molecules with the sensor surface is known to define the receptor function. The receptor function converts chemical information into a certain kind of energy which can be measured by transducers[2]. The chemical interaction between the surface of a sensor and the analyte molecules can be adsorption, exchange of ions, and electrochemical reactions. In the presence of air, oxygen adsorbs on the surface of sensor and forms negatively charged oxygen species. This forms a surface depletion layer around the surface of grains resulting in a band bending (increase in the work function) of the sensor[44]. The reducing gas reacts with charged oxygen species resulting in decrease in the thickness of the surface depletion layer and band bending by injecting electrons into the conduction band,

thereby decreasing the work function of the grain. In the case of oxidizing gas (NO_2), the thickness of depletion layer and band bending further increases due to extraction of electrons by the oxidizing gas from the conduction band of the sensor material. The change in the potential barrier height in the presence of gas is supposed to be the source of conductance response of sensor[45]. In case of metal oxides, the corresponding receptor function is highly influenced by the intrinsic electronic properties and deviation from chemical stoichiometry. Oxygen vacancy is an inherent defect in metal oxides. It leads to formation of space charge layer by forming ionosorbed oxygen on the surface of metal oxide. The mobility of main charge carrier is very important as it determines proportionality constant of change in the electrical conductivity when analyte molecules interact with sensor[46]. Stoichiometric metal oxides have lower conductivity. The conductivity of metal oxides can be enhanced by doping or forming defects. Therefore, the receptor function can be modified by doping or inclusion of additives with foreign receptor. For example, PdO on SnO_2 brings more change in the work function as PdO is a strong receptor. This results in enhanced sensitivity of PdO doped SnO_2 as compared to pristine SnO_2.

1.6.2.2 Transducer Function

The transduction function basically deals with effective conversion of molecular information into an accessible signal i.e. electrical resistance. It deals with the ability to transport electrons through grain boundaries. The change in the electrical resistance as a result of the change in the work function is addressed by the transducer function. For developing an understanding on this, the change in resistance of single crystal of SnO_2 (a typical sensing material) and concept of receptor function is needed to be considered in more detail. Oxygen molecules adsorbed on the crystal surface form negatively charged oxygen species by extraction of electrons from the crystal and result in breaking of periodicity of SnO_2. The new energy levels arise due to dangling bonds or unsaturated sites. The formation of negatively charged oxygen species is represented by the following equation,

$$\frac{\beta}{2}O_2(g) + \alpha e^- \leftrightarrow O_\beta^{-\alpha}(s) \quad (1.5)$$

Where α is 1 or 2 depending on oxidation state of oxygen, β =1 for single atom/ions or 2 for molecules. S is site on the SnO_2 surface. The formation of electron depletion

layer on the surface due to adsorbed charged oxygen species results in the formation of an electric field at the surface. The energy band bends upward (for negative ion upward bending occurs). In other words the process of trapping of electrons caused by formation of depletion regions results in an increase in the resistance of sensor. When such a depleted surface is exposed to reducing gases (like CO) it results in oxidation of the gas, as given by the following reaction,

$$\beta CO_{(g)} + O_{\beta}^{-\alpha} \rightarrow \beta CO_{2(g)} + \alpha e^{-} \quad (1.6)$$

The above reaction releases trapped electrons into coduction band of the sensor resulting in decrease in the resistance of the sensor. This is how a variation in chemical information is transformed into an electrical signal. Here, we discussed gas sensing behaviour of single crystal SnO_2 however, in reality, gas sensor materials are mostly polycrystalline and hence many factors affect the sensor output signal.

1.6.3. Factors affecting gas sensor performance of metal oxides

In a gas sensor, adsorbed oxygen reacts with analyte molecules and is removed from the surface of sensor. The surface is further replenished from the atmosphere and gets ready for the second event detection. Thus the reaction rate and equilibrium state depend on the rates of the actions of removal and re-adsorption of oxygen. The different sensitivity towards various gas concentrations and analytes is dependent on the partial pressure of reducing gas as the surface replenishment depends on it. These reactions depend on diffusion which in turn depend on the temperature of the sensor. The microstructure of metal oxide also plays a crucial role in improving different gas sensing performance features such as sensitivity, selectivity, stability etc. The various microstructural aspects of metal oxides which affect gas sensing performance are discussed in the following section.

1.6.3.1 Effect of grain size

In sintered or polycrystalline semiconductor metal oxides, grain size plays a crucial role in determining the sensitivity of sensor. The formation of Schottky barrier between the grain boundaries affects the transport properties of electrons and the variation in barrier height results in the change electrical resistance of the sensor. The thickness of the depletion layer is given by the following equation:

$$L_s = L_D\sqrt{\frac{eV_s^2}{kT}} \tag{1.7}$$

Where, L_D is the Debye length, V_s is the Schottky potential, k is the Boltzmann constant, T is the temperature. The Debye length (L_D) and the Schottky barrier potential (V_s) is given by

$$L_D = \frac{2\pi q^2 N_s^2}{\varepsilon N_d} \tag{1.8}$$

$$V_s = \sqrt{\frac{\varepsilon kT}{2\pi e^2 N_d}} \tag{1.9}$$

Where, ε is the dielectric constant, N_d is the concentration of the donor impurity, N_s is the concentration of surface charge states, q is surface state charge. The dependence of the depletion layer thickness L_s on crystallite size (D) has been empirically observed[47]. The values of L_s are typically in range of 0-100 nm. The dependence of sensitivity on crystallite size is shown by using sintered SnO_2 with different crystallite sizes[Fig. 1.8].

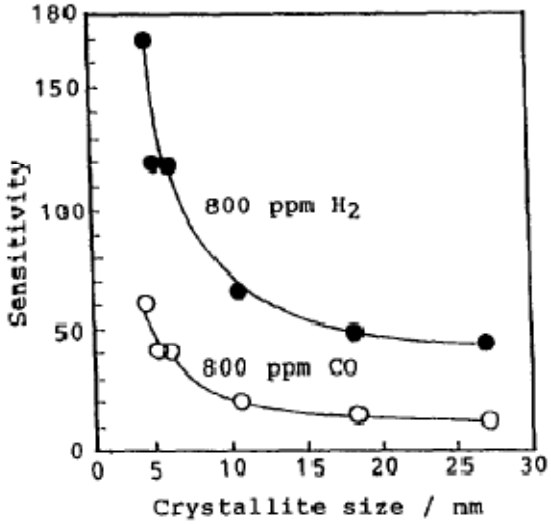

Figure 1.8: Effect of grain size on sensitivity to 800 ppm H_2 and CO of pristine SnO_2 annealed at 400°C [adopted from 42].

The Sensitivity hardly changes when crystallite size >20 nm. The sensitivity gradually increases with decrease in grain size <20 nm. When grain size is <10 nm, the change

in sensitivity is very large. Some literature suggests that in the case of SnO_2, 6 nm is a critical crystallite size (D_c) and the corresponding thickness of space charge layer (L_s) is twice this value [48-49].

Case I: For $D>>2L_s$:

In this case, electrical conductivity of the sensor depends on the grain boundary (GB) barriers which affect intergrain charge transport. In the case of larger grains, the electrical resistance of the sensor depends on Schottky barriers and rapidly changes with them (Fig. 1.9a). Here, the surface reaction with analyte utilizes a very small portion of the grains i.e. very little volume of the grains is utilized.

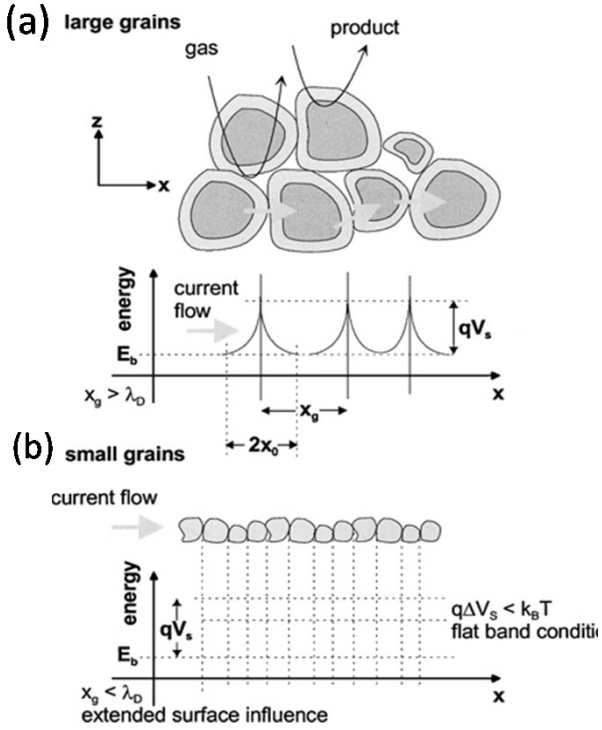

Figure 1.9: Schematic diagram of porous sensing layers of different grain sizes (a-larger grain and b-smaller grain) with energy bands. (λ_D is the Debye length, and X_g is the grain size)[Reprinted with permission[36]].

Case II: For $D\geq 2L_s$

Here, the grain size is somewhat larger or comparable with the width of the surface depletion layer and the core region being unaffected becomes smaller. The neck-like conduction channel is formed between the grains [Fig. 1.10a]. The conductivity of a sensor is controlled by both the grain boundary barrier and the cross sectional area of

the channels formed between the grains. In this case, these two factors lead to increase in sensitivity with decrease in grain size.

Case III: For $D<2L_s$

In this case, the grains are completely depleted of the charge carriers and the conductivity of the sensor abruptly decreases. The conduction channels between grains disappear (Fig. 1.10 b). The energy band in this case is almost flat and grain boundary barrier is very negligible. Hence the inter-grain charge transfer is not affected by the grain boundary. In this range, gas sensing mechanism of the grains is not yet clear.

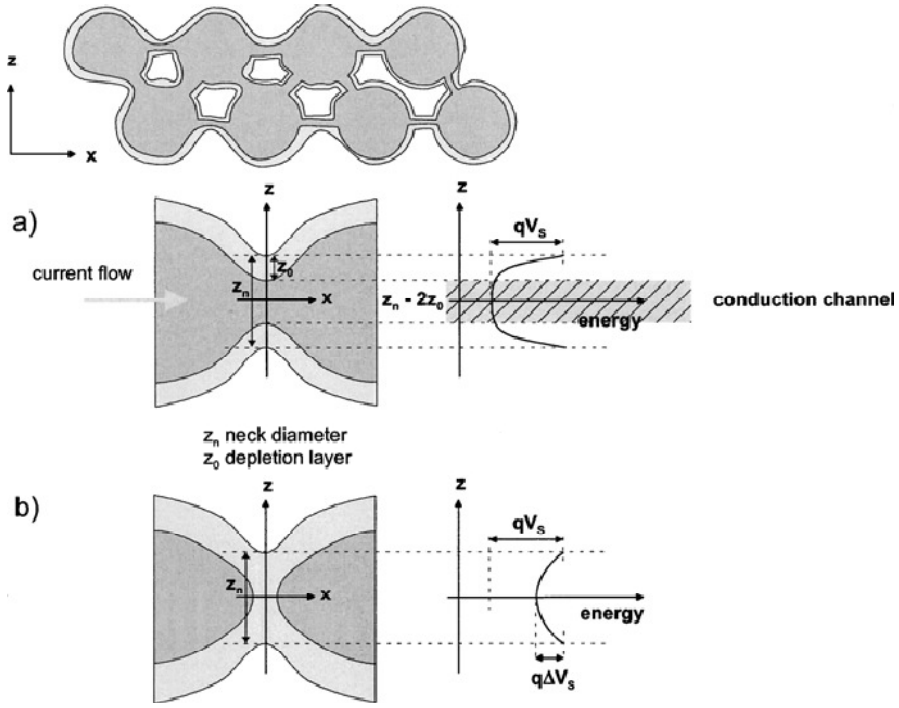

Figure 1.10: Schematic diagrams of a porous sensing layer with geometry and band energy of the neck between grains: a) partially depleted necks, b) completely depleted neck contact. (Z_n is the diameter of the neck; Z_0 is the depletion layer thickness) [Reprinted with permission [36]].

1.6.3.2. Effect of geometry

The analyte molecule reaction with the surface of sensor involves many factors. For illustration, consider a sensor with some thickness reacting with analyte molecules.

The entire sensing material does not participate in the reaction; however reactions occur upto certain depth from the surface of sensor. The kinetics of reactions is not same throughout the depth from surface of the sensor. This is observed due to competition between the reaction and diffusion processes. If reactions occurring at outer sites are faster as compared to diffusion of analyte molecules to inner sites then most of the inner surface remains unused. Thus it is necessary to consider the geometry of the crystallite and the distance between the outer sites and the inner sites.

G. Sakai et al. have used Knudsen diffusion approach to investigate how analyte molecules travel inside the film [50].

$$\frac{\partial C_A}{\partial t} = D_k \frac{\partial^2 C_A}{\partial x^2} - kC_A \tag{1.10}$$

Where, D_k is Knudsen diffusion coefficient, t is time, C_A is target gas concentration, x is (depth) distance from surface of sensing layer and k is the rate constant. The steady state concentrations ($\partial C_A/\partial t=0$), boundary conditions at the surface ($C_A=C_A$, at X=0), and $\partial C/\partial t=0$ bottom (X=L) are applied to equation 1.10. The following equation is obtained.

$$C_A = C_{As} \frac{Cosh\,(L-x)\sqrt{k/D_k}}{Cosh\,(L\sqrt{k/D_k})} \tag{1.11}$$

By using this equation, the concentration of analyte C_A against depth x for different values of $\sqrt{k/D_k}$ is plotted (Fig. 1.11) at a fixed temperature for a film thickness (L)=300 nm, $C_{A,s}$ being the normalized concentration at surface. For, high value of $\sqrt{k/D_k}$, the concentration of analyte drops very quickly and only shallow region gets occupied. As the value of $\sqrt{k/D_k}$ increases to 10^{-2} further concentration drops below 0.2 at the bottom. When value of $\sqrt{k/D_k}$ is low ~10^{-3}, very little drop in the concentration is observed and practically it is not considered to be a variation.

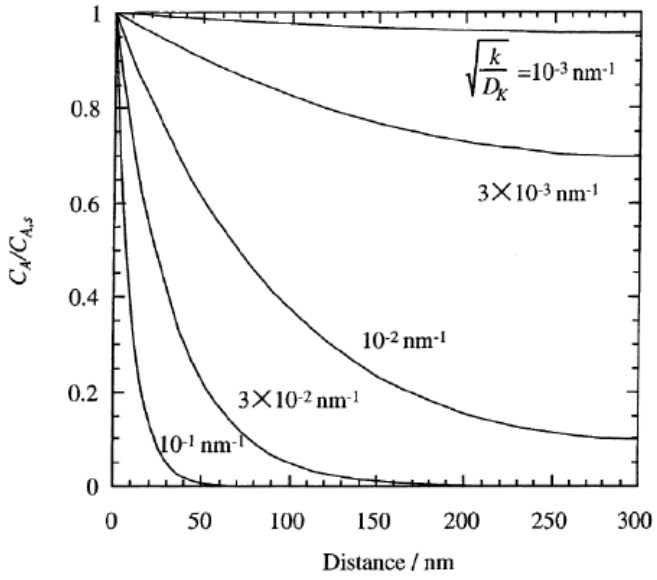

Figure 1.11: Simulated plot of gas concentration inside film of thickness 300 nm for different values of $\sqrt{k/D_k}$ at fixed temperature [Reprinted with permission[50]].

Porous film of SnO_2 could be used to confirm the theoretical study of Sakai et al. [50], although thin films of SnO_2 fabricated by using so-gel technique followed by hydrothermal treatment have exhibited significant behaviour and can also be useful to explain the behaviour in case of thick films. Gas sensor consists of small particles and larger pores so that analyte molecules can easily diffuse through and each particle should experience the same condition.

1.6.3.3. Crystallographic plane effects

The effect of crystallography on gas sensing properties is complicated and needs to consider size, microstructure and crystal shape. The external shape of crystallite and size is consistent with the growth of grains. The sensing properties are dependent on external planes of the nanocrystals. Crystallographic planes of each crystal determine its surface states density, adsorption and desorption energy etc. The size and shape of the crystals affect adsorption and adsorption process during gas/surface interaction. The effects of crystallographic planes on gas sensing properties are predominantly observed when the crystallite size is D>> 2L. The external crystallographic planes depend on the size of grain. The spray pyrolysed SnO_2 films on Si substrates have different crystallographic planes depending on the direction of growth. Four different crystallographic planes of SnO_2 are shown in Figure 1.12. According to PBS theory,

the reactivity of K faces (111 plane) is more as compared to the F-faces (110, 101 planes). This is due to the fact that the 110 and 101 planes have strong bonds. Different crystallographic planes have different distances of 'Sn' atoms and the order is as follows: d(110)<d(100)<d(101)<d(001). [51] Hence energy is required for chemisorption of oxygen and dissociation rate is different for different planes. This signifies that the gas sensing properties can be enhanced by controlling crystallographic planes.

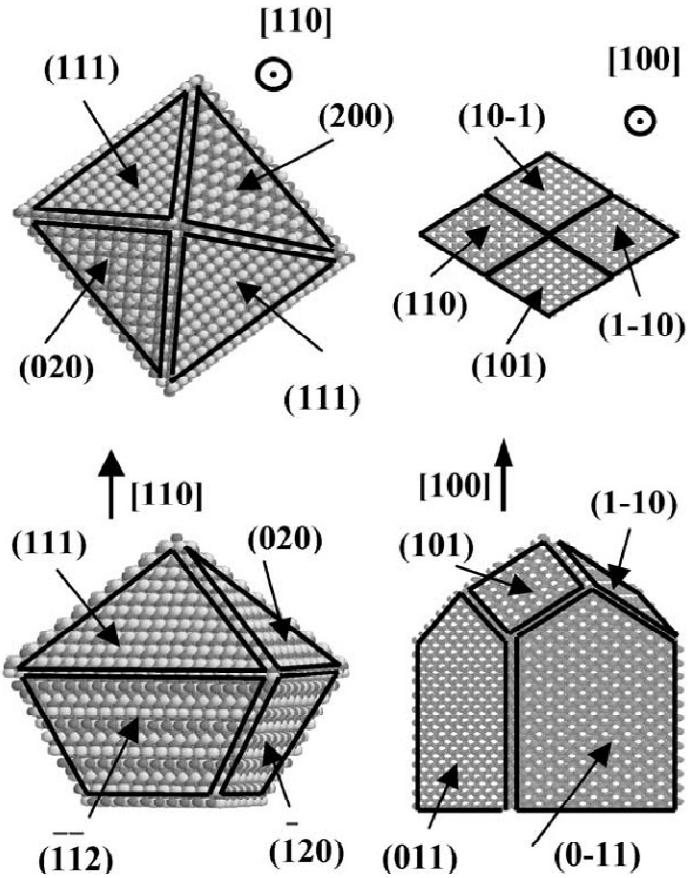

Figure 1.12: Structures obtained as result of simulation of thin films of SnO_2 of thickness a) d~40-80 nm, and (b) d~300 nm, deposited by spray pyrolysis at different temperatures between 400°C and 500°C [Reprinted with permission[52].

1.6.3. 4. Effect of dopants

The effect of noble metals like Pt, Pd and Ag on gas sensing properties of semiconductor gas sensors have been initially explored by Shaver and Loh[53]. This work suggested that doping addition of noble metals can be used to overcome certain limitations of the pristine sensor materials. Doping adds catalytically active sites to the surface of the sensor materials. Doping enhances performance of the sensor by

favouring selective interaction of target gas molecule with the sensor element, thereby increasing the sensitivity, response and recovery time. In addition, surface doping may improve thermal stability of the nanostructure and durability of the sensor. Two different mechanisms namely the electronic and chemical sensitization are usually applied to describe the effect of surface additives[35, 54-55]. The main objective of the use of dopant is to promote catalytic surface reaction of target molecules. The target molecules are preferentially adsorbed on to the surface of noble metals and forms activated fragments which spill over the surface of semiconductor. These fragments further react with the negatively charged oxygen and the coverage of ionosorbed oxygen is reduced, which results in a decrease in the resistance of the sensor. However noble metal cluster remains unaffected[56].

The catalytic properties of dopants do not necessarily coincide with the gas sensing performance. [28] The dopants should present an optimum environment between the surface of the cluster and the semiconductor oxide base for electrons and ions exchange. This suggests that high catalytic activity of dopant is important but not an adequate requisite to achieve high performance[57-59].

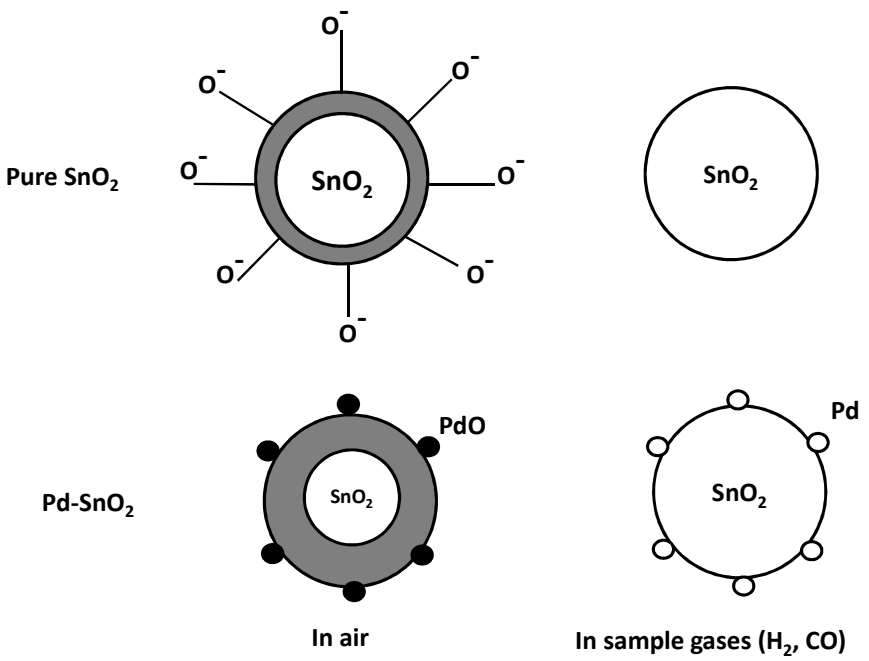

Figure 1.13: Gas sensing response of SnO_2 particles in pristine or in Pd or PdO-loaded SnO_2 element [Adopted from[60]].

The dopants in oxidized state extract electrons of the host semiconductor and act as electron acceptors. This leads to the formation of electron depletion layer near the surrounding of the interface. In the presence of reducing gas, additives react with the reducing gas and release back accepted electron to the host semiconductor. The significance of electronic sensitization can never be too strong in semiconductor metal oxides[60]. Figure [1.13] shows interaction of SnO_2 particles with test gas molecules. In the case of pristine SnO_2, oxygen get adsorbed on the surface and an electrons-deficient space charge layer is formed. In the presence of a test gas, relaxation of space charge layer occurs when oxygen molecules are consumed with the test gas. In the case of additives like Pd/Pt, a space charge layer is formed due to the interaction of Pd with SnO_2 in the presence of air due to the fact that depletion of electrons is stronger as compared to only adsorbed oxygen. When a reducing gas converts PdO to Pd, the space charge layer disappears. Hence, gas sensitivity of PdO-SnO_2 is superior to pristine SnO_2.

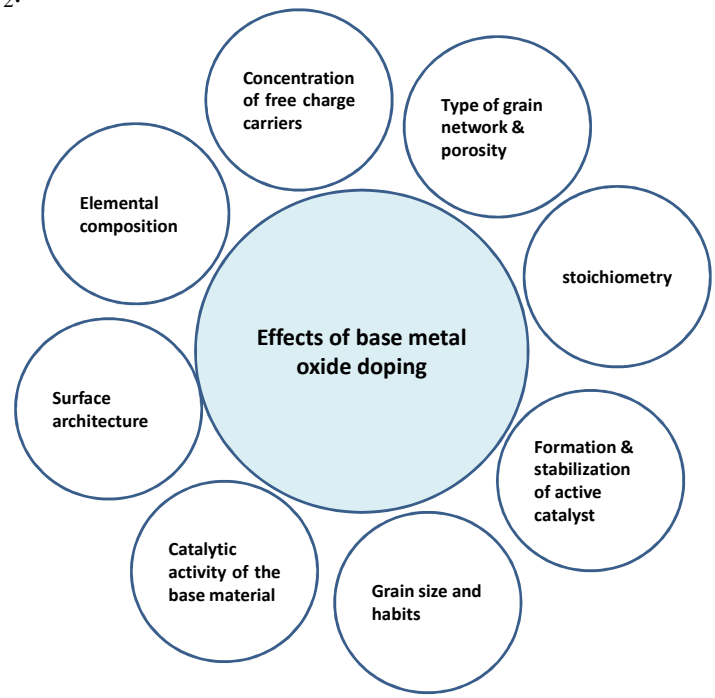

Figure 1.14: The parameters of metal oxides can be changed by doping metal oxide [adopted from[28].

In addition to nobel metals, many different metal/metal oxides are commonly used as additives/dopants in order to improve sensitivity and selectivity. For example, In the CuO-SnO_2 system, in the presence of H_2S, CuO converts into CuS, thereby changing

the chemical potential of the system that affects the charge state at interface of semiconductor/dopant and thus exhibits high sensitivity for H_2S [61-62].

It is necessary to anneal the sample at a desired temperature 300°-600°C in order to form metallic clusters, leading to enhancement of homogeneity in distribution which stabilizes gas sensing performance of the sensor [28, 63]. In reality, the effect on gas sensing performance due to doping is very complex as it affects properties of the host material. There are many parameters which are affected by doping foreign element into the host semiconductor oxide is shown in Fig. 1.14.

1.6.3.5 Effect of film architecture

The interaction of analyte with the surface of semiconductor metal oxides can be understood by ionosorption or oxygen vacancy theory. The interaction of analyte with film morphology plays an important role[36]. The gas sensing film can be subdivided into dense (compact) and porous films. In dense films, interaction of analyte molecules occurs only at the geometric surface and cannot penetrate into gas sensing film [Fig. 1.15]. However, in the case of porous films, gas molecules can penetrate deep and react with grain, sintered neck, and the interface between the electrode and the substrate[36]. There are several synthetic methods such as spray pyrolysis which can be used to produce porous nanocrystalline films with grains and their crystal properties are not uniform throughout the film[28].

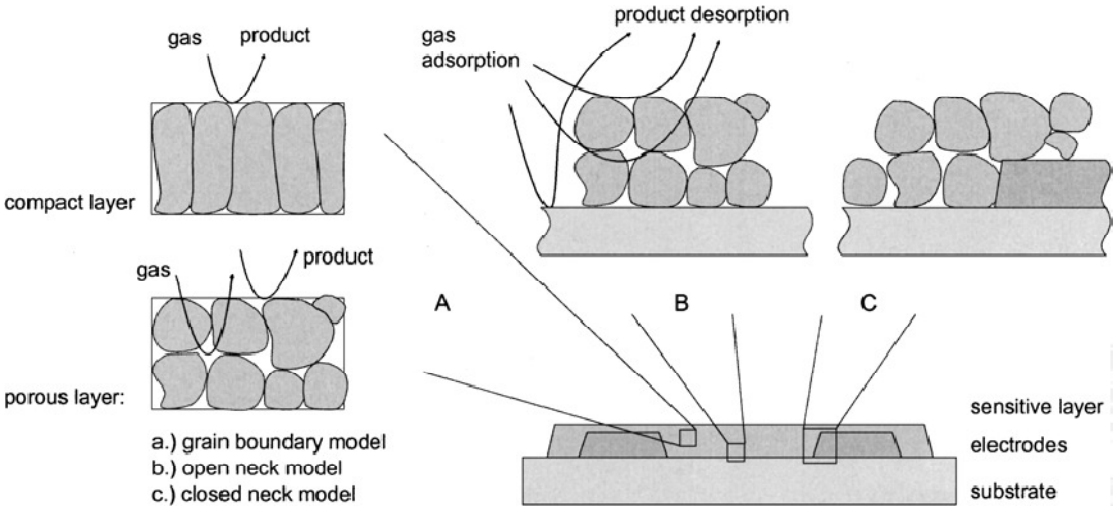

Figure 1.15: Schematic representation of compact and porous layered films and accessible surface for analyte molecules [Reprinted with permission[36]].

Film thickness: The gas sensing response decreases with increase in the film thickness as the fraction of the sensing element involved in sensing decreases. However, the effect of film thickness on gas sensing response is insignificant as increase in the reactive sites does not necessarily give a linear increase in the response as the gas concentration in the film changes with porosity of the film, catalytic activity, composition of analyte, temperature[64].

1.7 Gas Sensing performance characteristics

The gas sensor performance is judged by several parameters such as sensitivity, selectivity, response time, energy consumption, reversibility, adsorption capacity, fabrication cost etc.

1.7.1 Sensitivity

It is the ability to detect minimum concentration or volume of an analyte gas. When chemiresistive sensor is exposed to analyte gas, the resistance of the sensor experiences change. The interaction of analyte gas with the sensor surface leads to change in the electronic state of sensor which is explained earlier in the receptor and transducer section. There are two types of semiconductor metal oxides, namely the n-type and p-type semiconductor oxides. In the n-type semiconductor oxide, electrons are the main charge carriers. In the presence of air, oxygen molecules adsorb on the surface of sensor by extracting electrons and forming the depletion layer, thus the concentration of electron charge carriers is reduced. When n-type sensor is exposed to a test gas (reducing gas like CO), it removes adsorbed oxygen and forms CO_2, releasing electron back to the sensor. Hence concentration of electrons in the sensor increases and the resistance of the sensor decreases. In p-type semiconductor oxides, holes are the majority charge carriers. In this case, adsorption of oxygen leads to removal of electrons, leaving behind holes which are main charge carriers. This leads to a decrease in the resistance of the sensor. When oxygen is removed in the presence of a reducing analyte, electrons are released back resulting in a decrease in the density of holes concentration in the sensor. This leads in increase in the resistance of sensor. In the presence of an oxidizing gas, opposite reactions take place and thus an opposite trend in resistance is observed [Table 1.3].

Table 1.3: Chemiresistive behaviour of semiconductors oxide based gas sensors in reducing and an oxidizing atmosphere.

	n-type	p-type
Reducing Gas	Resistance decreases	Resistance Increases
Oxidizing gas	Resistance Increases	Resistance decreases

The gas sensor response is defined as ratio of resistance in air to the resistance in the presence of an analyte gas. The gas response "S" is expressed as

$$S = \frac{R_{air}}{R_{gas}} \quad \text{for n-type semiconductor} \tag{1.12}$$

$$S = \frac{R_{gas}}{R_{air}} \quad \text{for p-type semiconductor} \tag{1.13}$$

In some literature it may also be defined as

$$S = \frac{R_{air} - R_{gas}}{R_{air}} \tag{1.14}$$

The sensitivity is defined as a ratio of gas response (S) to the concentration of analyte gas and is expressed as follow:

$$Sensitivity = \frac{Gas response\ (S)}{Concentration of analyte} \tag{1.15}$$

1.7.2. Selectivity

The semiconductor gas sensor shows maximum sensitivity for a particular analyte gas. It should preferably exhibit selectively high sensitivity for one analyte in the presence of other interfering gases at a given operating condition.

Selectivity is expressed as,

$$Selectivity = \frac{Sensitivity of sensor for interferring gas}{Sensitivity of sensor for desired analyte gas} \tag{1.16}$$

Selectivity in semiconductor oxides can be tuned or optimized by different methods. These are classified into four groups as stated below. [60]

1. Use of chromatographic column/filters to differentiate gases based on molecular size/other physical properties.
2. Use of promoters, catalyst or specific surface additives
3. The fabrication of sensor
4. Analysis of sensor parameters such as transient response with change in the analyte concentration and the operating temperature of the sensor.

Mizsei noted that the physical and chemical properties of semiconductors depend significantly on temperature and thus affect gas sensing response of the sensor[65]. The factors such as rate of adsorption-desorption, decomposition of analyte, the Debye length, and concentration of charge carriers depend on temperature of the semiconductor. This suggests that the relationship between the change in resistance of sensor in the presence of analyte gas and the temperature of sensor is really very complex. In addition to this, exothermic chemical reaction of analyte with sensor contributes to uncontrolled rise in temperature of sensor[66]. Figaro gas sensor manufacturer specifies that sensor properties can be influenced by use of flow system for gas detection that causes decrease in temperature of the sensor. Apart from this the temperature modulation of sensor has certain advantages such as: a) cyclic temperature variation can offer a specific response for each gas, b) surface of the sensor can be cleaned up by periodically shifting the sensor to higher temperature, and c) the thermal cycling can improve selectivity for each gas due to changes in grain and grain boundary properties, thereby during cycling at certain temperature a specific gas exhibits a maximum response[67]. The main problem is the nonlinear gas response of the sensor which is needed to be overcome. However, to address this problem use of neural networks and soft-modelling techniques is made to recognize the gas sensing pattern[54].

As stated earlier, gas filter on the surface of a sensor can be used to improve the selectivity of the sensor. The sensitivity and selectivity towards hydrogen is enhanced by coating SnO_2 film using CVD of silicones on the surface of gas sensor[68-70]. Dutta et al. have enhanced the selectivity of TiO_2 for hydrocarbon over CO by using a filter of Pt in microporus zeolite[71].

The acid-base properties of metal oxide can be optimized or tuned by using dopants/additives. Hence, acid-base properties of sensor can be tuned depending on

acidic or basic properties of analyte to be detected. For example, ethanol sensing enhances in basic oxides while in acidic oxide it reduces. The catalytic oxidation of ethanol takes place via different routes by acidic or basic oxides[60].

1.7.3. Response and recovery time

It is the time taken by sensor to reach 90% of its final saturated value when sensor is exposed to an analyte gas. Recovery time is the time required for sensor to reach 10% of its original value when sensor was exposed to air atmosphere. Ideally, sensor should exhibit rapid response and recovery time.

1.7.4. Stability

The gas sensor should give stable and reproducible result over the period of time which fulfils the required guidelines setup by the gas sensing market. The gas sensor should not show any drift with time. There are certain factors which affect gas sensor stability. Design error, structural changes, phase shifts, poisoning due to chemical reactions, and variation of the surrounding environment. The following precaution should be taken to solve the above problems, namely, the use of elements with chemical and thermal stability, optimization of particle size and composition, surface pre-treatment using specialized technique(s).

1.8 Literature review of semiconductor metal oxides gas sensors

The gas sensing properties of solid state gas sensors can be optimized by structural engineering of metal oxides. It has been observed that many sensing properties such as sensitivity, selectivity, stability can be improved by optimization of bulk as well as surface structure of metal oxides. The technological potential of structural engineering for optimization of sensing performance has not been sufficiently studied. The structural engineering not only includes size but also crystallite shape, crystallographic orientation of crystallite planes, microscopic structure of gas sensing materials etc[52, 72-76].

1.8.1 Binary, ternary, doped metal oxides systems

Numerous metal oxides have been used as conductometric gas sensor elements for the detection of different reducing and oxidizing gases. The metal oxides such as NiO,

CuO, Cr_2O_3, Co_3O_4, CeO_2, GeO_2, MoO_3, Mn_2O_3, TiO_2, WO_3, ZnO, SnO_2, Fe_2O_3, In_2O_3, V_2O_3, Nd_2O_3, La_2O_3, SrO, Nb_2O_5, Ta_2O_5[27] etc. have been investigated for change in conductivity in the presence of an analyte. However, for gas sensing application, the selection of specific metal oxides is critical as these oxides provide a wide range of electro-physical properties. The electronic properties of metal oxides vary between metals to semiconductors (wide and small band gap) to insulators. Electronic structures are divided into two categories[31]:

1. Transition-metal oxides (TMOs, e.g. NiO, Fe_2O_3, Cr_2O_3)
2. Non-transition metal oxides: These can be subdivided into a) pre-transitions-metal oxides (e.g. Al_2O_3), b) post-transitions-oxides (e.g. SnO_2, ZnO etc.).

Pre-transition metal oxides cannot be easily oxidized or reduced as they exhibit a large band gap. It is impossible to optimize their properties by creating defects or using dopants or additives. Post-transition metal oxides provide stable oxidation states with s and p valance orbital symmetry. They exhibit optimum band gap which can be optimized by doping and/or creating defects etc. Transition-metal oxides exhibit different and complex bonding properties due to ‘d’ orbitals with variable oxidation states because of the small difference in energy between d^n configurations. Hence they are more sensitive towards ambient atmosphere. Certain transition-metal oxides provide preferred stable oxidation state which is useful for gas sensor design. It is easier to create defects in TMOs as compared to non-transition metal oxides. Therefore, non-optimality and structural instability parameters determine suitability of some oxides over the others. Binary transition-metal oxides with d^0 configurations (TiO_2, WO_3, V_2O_5, etc.) and post-transition metal oxides (like ZnO, SnO_2) with d^{10} electronic configuration have been extensively explored for gas sensing application.

Literature survey shows that simple metal oxides do not fulfil all gas sensing performance parameters to fabricate a perfect gas sensor. It is impossible to realize all gas sensor features in a single material. Therefore, it is necessary to modify the binary metal oxides by doping, using multi-element systems like ternary metal oxides, hetero-junctions etc.[77-79]. The gas sensing properties of binary metal oxides such as TiO_2, SnO_2, ZnO, WO_3, Fe_2O_3 can be improved by doping foreign elements or making their hetero-junctions. These approaches provide different physic-chemical properties to sensing elements which affect gas sensing properties. Gleiter reported

for the first time that incorporation of additional phase in nanocrystalline metal oxides leads to advancement in materials for sensor applications[80-81]. The catalytically active elements (like noble metals and transition metals) or inert impurities may be used for these purposes. An additive can significantly alter catalytic properties of the host oxide, forms active phases, stabilizes certain valance state, and increases the electron exchange rate properties. The parameters of host elements altered by additives are concentration of charge carriers, phase composition, sizes of crystallites, inter-crystallite barriers, surface potential, electronic and physic-chemical properties (surface state energetics, adsorption and desorption energy, sticking coefficients) and so on (see Fig. 1.10)[35, 52, 54, 57, 82-84]. It is known that even small amount of additives can change growth pattern of the host oxide. The crystallite size of SnO_2 decreased from 220 nm to 30 nm by 0.1% of Nb for the same reaction condition[81]. Similarly, crystallite size reductions were also observed for Ce, Y, and La doped SnO_2[85]. In chromium doped SnO_2, Cr^{3+} accelerates the [111] growth of SnO_2 and suppresses that along the [110] direction[86]. It is difficult discuss role of dopant in every systems however we have enlisted few cases of interest in the following table 1.4.

Table 1.4: Gas sensors investigated using various binary, ternary and doped metal oxides

Binary Metal Oxides			
Metal Oxide	**Morphology**	**Analyte gas**	**Ref.**
CdO	nanowires	NO_x	[87]
Co_3O_4	nanorods	acetone	[88]
Cu_2O,CuO	nanospheres	Ethanol, gas oil, H_2S	[89]
Fe_2O_3	nanotubes	Ethanol, H_2	[90]
Ga2O3	nanowires	Ozone	[91]
In2O3	hollow microsphere	Ethanol, Formaldehyde	[92]
MoO_3	nanoparticles	H_2S	[93]
Nb_2O_5	nanoporous film	H_2	[94]
NiO	microspheres	Butanol	[95]
SnO_2	nanowires	NO_2	[96]
TiO_2	nanotubes	O_2	[97]
WO_3	hollow sphere	acetone, CS_2, H_2S, alcohol	[98]
V_2O_5	nanobelts	ethanol	[99]
ZnO	nanopillars	H_2, ethanol	[100]

Ternary Metal oxides			
Metal Oxide	**Morphology**	**Analyte gas**	**Ref.**
$SrTiO_3$	nanoparticles	O_2	[101]
$ZnSnO_3$	nanocages	H_2S	[102]
$LaFeO_3$	honeycomb	ethanol	[103]
$NiMn_2O_4$	nanoparticles	Humidity	[104]
$BiFeO_3$	nanoparticles	ethanol, acetone	[105]
$ZnFe_2O_4$	-	ethanol	[106]
$NiFe_2O_4$	nanoparticles	LPG	[107]
$ZnTiO_3$	nanoparticles	LPG	[108]
$CoTiO_3$	nanoparticles	ethanol	[109]
Addition of dopant in metal oxides			
Base oxide	**Dopant**	**Analyte gas**	**Ref.**
SnO_2	Ag	propane	[110]
SnO_2	Fe	CO, ethanol	[111]
SnO_2	In	CO, H_2, methanol	[112]
SnO_2	CuO	H_2S	[62]
ZnO	Sn	NO_2	[113]
ZnO	Ru	NH_3	[114]
ZnO	Cu	CO	[115]
WO_3	Pt, Au	H_2S	[116]
WO_3	Ni	NO_2	[117]
Fe_2O_3	Pt, Ag	H_2S	[118]
	Ag	H_2S	[119]
Fe_2O_3	Cd	LPG	[120]
NiO	Li	H_2	[121]
NiO	Fe	ethanol	[122]
NiO	Cr	xylene, toluene	[123]
$ZnFe_2O_4$	CdO	Ethanol	[124]

1.8.2 Hetero-junction metal oxides

Literatures show that many gas sensing properties of metal oxides can be optimized by forming composites or hetero-interfaces (hetero-junction). This presents an opportunity to access and explore interface behaviour of various oxides in different ambient. The physical interface of two different elements is known as a heterojunction and material is referred as a hetero-structure [125]. When intimate heterojunction is formed between two components, charge transfer take place at heterojunction and fermi levels try to equilibrate to same energy as result charge depletion layer is formed. This is an unique feature of hetero-junction which forms the basis for improved gas sensing performance. Hetero-structure can also carry

synergistic reactions. It means first gas molecules react with one component and byproduct of this reaction react with second component.

Many factors attributed for enhanced response of composites are band bending [126-127], manipulation of depletion layer[128-130], separation of charge carriers[131], interfacial potential barrier[132], reduction in activation energy [133], catalytic activity[134], synergistic reaction[135], grain size refinement[136], enhanced surface area[136], gas accessibility[137]. Therefore, it is essential to understand gas sensing mechanism of hetero-structure for further development of sensor.

1.8.2.1Gas sensing mechanism of hetero-junction

There are different kind of hetero-junction can be formed such as p-n, n-n, and p-p junction.

Interface Role: The interface plays an important role in gas sensing of hetero-structure of semiconductor metal oxides composite. p-n junction is very commonly used for gas sensing investigation. When two electronically favourable materials brought together; electron from higher energy level transfer across the interface to low unoccupied energy level till Fermi levels matched/equilibrated with each other. This process is similar to electron-hole transfer in p-n junction. This process is known as Fermi level-mediated electron transfer. Figure 1.16a shows schematic p-n junction. This creates depletion regions at the interface. The electron transfer for levelling Fermi energy leads to band bending and forms potential barrier at the interface. Therefore electrons need to have sufficient energy equal to potential barrier to cross the interface.

1.8.2.2 Gas sensor based on p–n nanojunctions

Consider p-n heterojunction of ZnO nanowires (n-type) decorated with Co_3O_4 nano-islands (p-type)[138]. In the case of pristine ZnO nanowires, the resistance is higher due to the formation of the depletion region by oxygen adsorption. This is due to the fact that the depletion region is extended in the conduction channel of ZnO nanowire. Apart from the depletion region, heterojunction further increases the resistance caused by charge transfer across the p-n junction which further reduces conduction surface area by extending into ZnO nanowires. In the presence of a reducing gas, decrease in

resistance value is high as compared to the initial value. This is possible only if Co_3O_4 is more sensitive than ZnO nanowires itself towards the test gas[139]. In the presence of oxidizing NO_2 gas the response is low as base resistance of the hetero-structure is itself high which limits further increase in its resistance value. Thus, in this hetero-junction system selectively a high response towards ethanol is observed as compared to the interfering NO_2 gas[138].

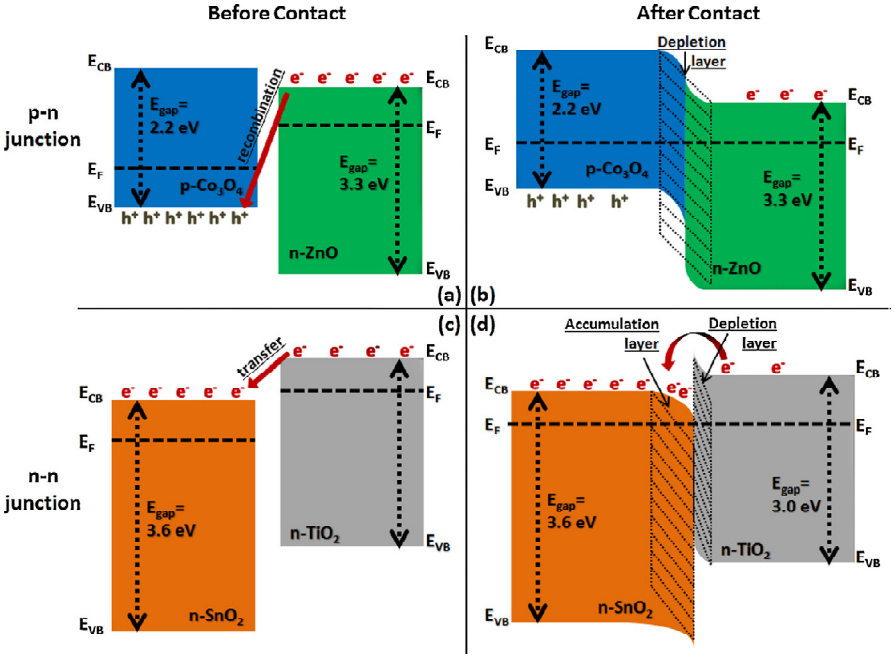

Figure 1.16: Schematics diagram of band bending at heterojunction interfaces with no adsorbed surface species. (a) energy alignment before contact between p-type Co_3O_4 and n-type ZnO. (b) Depletion layer formed at p–n junction due to recombination. (c) energy alignment before contact between n-type SnO_2 and n-typeTiO_2. (d) Loss of electrons creates depletion layer at n-TiO_2 surface and gain of electrons forms accumulation layer at SnO_2 surface, thus, enhances oxygen adsorption. A potential barrier was also formed at the interface. E_{CB}: conduction band edge energy, E_{VB}: valence band edge energy, E_{gap}: band gap energy, EF: Fermi energy ((c and d) [Reprinted with permission[125]].

1.8.2.3 Gas sensors based on n–n and p–p nanojunctions

Fermi level equilibration also leads to band bending in n-n and p-p hetero-junctions [140-141]. Zeng et al. reported enhanced adsorption of oxygen at SnO_2 sites due to

Table 1.5: Gas sensing performance of heterostructures of ZnO-based nanomaterials [Reprinted with permission [125].

Analyte gas	Composition	Meas. temp.	Response	Concen-tration	t_{res}	t_{rec}	Ref
Ethanol	ZnO@ZnS	210°C	23[a]	1000 ppm	15 s	15 s	[10]
Ethanol	ZnO@ZnS@Graphene	210°C	38[a]	1000 ppm	15 s	15 s	[10]
Ethanol	2:1 mol ZnO:SnO_2	300°C	18[a]	100 ppm	5 s	6 s	[74]
Acetone	ZnO@TiO_2	400◦C	22[i]	100 ppm	1 min	1 min CO,	[3]
H_2	TiO_2/NiO	200◦C	70[a]	10,000 ppm	NA	NA	[51]
H_2	ZnO@SnO_2	400°C	70[g]	500 ppm	NA	NA	[95]
H_2S	ZnO@3 wt% CuO	100◦C	39[a]*,	100 ppm	120 s	>150 s	[12]
NO_2	5% Eu_2O_3-ZnO	300 ◦C	16[b]	3 ppm	3 min	3 min	[43]
NH_3	2 mol% -Fe_2O_3-ZnO	RT	10,000[l]	0.4 ppm	20 s	20 s	[96]
NH_3	ZnO@Cr_2O_3	RT	13.7[j]	300 ppm	25 s	75 s	[97]
LPG	ZnO@0.47 wt% Cr2O3	350◦C	46[j]	100 ppm	18 s	42 s	[7]
H_2	20 wt% SnO_2–TiO_2	400◦C	9.9[c,*]	20 ppm	12–14 s	4.5–5 min	[30]
Ethanol	20 wt% SnO_2–TiO_2	553◦K	51[a,*]	200 ppm	10–15 s	14–20 s	[98]
O_2	90% CeO_2–TiO_2	420◦C	9.5[b]	103 ppm	50 s	80 s	[36]
Ethanol	In_2O_3@ZnO	350◦C	265i	400 ppm	NA	NA	[99]
O_3	(γ-Fe_2O_3–In_2O_3(9:1))/ In_2O_3	135◦C	8670[k]	100 ppb	NA	NA	[100]
Ethanol	γ-Fe_2O_3/In_2O_3	300◦C	68[j,*]	100 ppm	50–60 s	50–60 s	[49]
Ethanol	α-Fe_2O_3@SnO_2	350◦C	4.6[a]	10 ppm	NA	NA	[82]
Ethanol	Fe_2O_3@ZnO	220◦C	22.1[a]	500 ppm,	20 s	20 s	[88]
Ethanol	α-oO_3@SnO_2	300 ◦C	67.76[a]	500 ppm	<1 min*	<30 s*	[56]
Ethanol	1.4 wt% TiO_2-MoO_3	400◦C	250[j]	100 ppm	NA	NA	[44]
CO	20 wt% WO_3-MoO_3	200◦C	390[j]	15 ppm	2 min	2 min	[44]
O_3	MoO_3–TiO_2	300◦C	1.7	100 ppb	20 s	2 min	[39]
Ethanol	ZnO–Co_3O_4	170◦C	46[b]	100 ppm	NA	NA	[13]
Ethanol	CeO_2–CdO–Al_2O_3	190◦C	890[a]	1000 ppm	32 s	297 s	[101]
Ethanol	CdO-Al_2O_3	250◦C	6.4[a]	1000 ppm	NA	NA	[101]

Note: [a]S = Ra/Rg; [b]S = Rg/Ra; [c]S = ΔR/Rg; [d]S = ΔR/Ra; [e]S = (ΔR/Rg)×100; [f]S = (ΔR/Ra)×100; [g]S = (ΔI/Ia)×100; [h]S = Vg/Va; [i]S = Gg/Ga; [j]S = G/Ga; [k]S = ΔG/Gg; [l]S=

Ig/Ia. *Denotes a value not explicitly stated in the study, but approximated from a graphical plot.

increased electron density at the SnO_2 site by transfer of electron from TiO_2 in TiO_2-SnO_2 n-n hetero-junction[fig.1.16 (c,d)]. In p-n junction the interface has less number electrons as a result recombination of electron-hole. However in the case of n-n heterojunction, accumulation layer is formed at the interface due to transfer of electrons into the SnO_2 conduction band. This accumulation layer is further depleted by the adsorption of oxygen on the surface of SnO_2 which increases the potential barrier at the heterojunction that improves gas sensing performance. Hence, this study suggests that modulation of the potential barrier height at the interface of n-n heterojunction by oxygen adsorption plays important role in enhancing the gas sensing performance.

At present, it is impossible to address all hetero-junctions properties by a single theory considering structural diversity and availability of different materials systems. However, one must take into account fundamental properties such as the band structure, surface chemistry, catalytic behaviour, gas reactions under study, and the microstructure, in order to design the best possible combination of system properties for improving the gas sensing performance. Table 1.5 enlists briefly the results of gas sensing studies on some hetero-structures [Reprinted with permission[125].

1.9 Semiconductor metal oxides for Humidity Sensor

Humidity sensors are extremely necessary in various industrial processing, automobile industry, medical field, agricultural sector, domestic applications and environmental control. In industrial sector, humidity sensors are used to monitor humidity in chemical reactions, gas purification, ovens, desiccation of films, textile and paper manufacture and food processing. In medical sector, humidity sensors are necessary in incubators, sterilizers, respiratory equipments, pharmaceutical and biological products. In agricultural field, humidity sensors are useful in monitoring soil moisture, air- condition of green-houses, protection of plantation from dew, storage etc. In domestic applications such as intelligent control of microwave cooking, laundry control, air conditioning of living environment etc need humidity sensors.

Numerous humidity sensors based on polymers, inorganic and organic materials have been investigated. However, here we limit our discussion to metal oxide based humidity sensors. There are many binary and ternary metal oxides and their composites have been used for humidity sensing applications.

1.9.1 Humidity Sensing Mechanism

Metal oxides are also very useful for humidity sensing. The humidity sensing mechanism discussed here was reported ~200 years ago[142]. This mechanism of protonic conductivity was discovered during study of TiO_2 and Fe_2O_3[143-144], which is based on the conduction of proton inside layer of water adsorbed on sensing material[Fig. 1.17]. In the first step, a water molecule is chemisorbed on an active site and forms an adsorption complex as shown in Figs. 1.18 (a,b). It is then transferred to surface hydroxyl groups [fig. 1.18 c]. Incoming water molecule is adsorbed on neighbouring two hydroxyl groups through hydrogen bonding [Fig. 1.18 d]. This top water molecule cannot move freely on the surface due to restriction of hydrogen bonding formed. In this layer, no hydrogen bond is formed between the water molecules and this layer is known as the first physically adsorbed water layer. This layer is immobile and proton conduction does not occur at this stage.

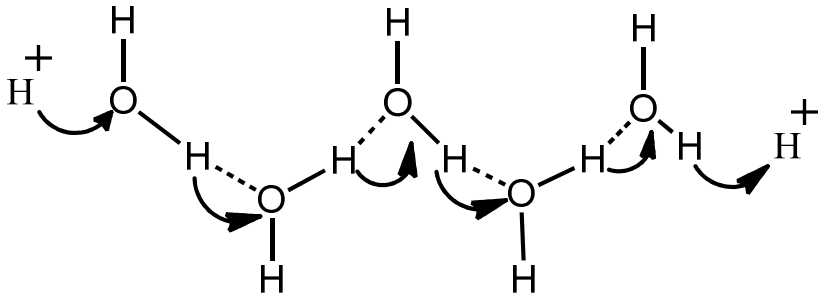

Figure 1.17: Brief illustration of Grotthuss mechanism of proton conductivity in water[142].

Further increase in water molecules leads to the formation of another layer on the physically-adsorbed water layer [Fig. 1.19]. This second physically-adsorbed layer is less organized as compared to the first physically adsorbed layer. This may be due formation of single hydrogen bond locally. If few more water layers are formed/condensed, protons move freely within the condensed water by Grotthuss

mechanism[142] and ordering of initial the surface gradually disappears. In other words, water molecules freely move like bulk liquid water from second physically-adsorbed water layer onwards. At this stage, Grotthus mechanism is dominant and sensing occurs purely via water-phase protonic conduction. This mechanism suggests that sensors based on protonic conduction happen to be less sensitive to low humidity condition as continuous water layer cannot be formed on the surface of sensor.

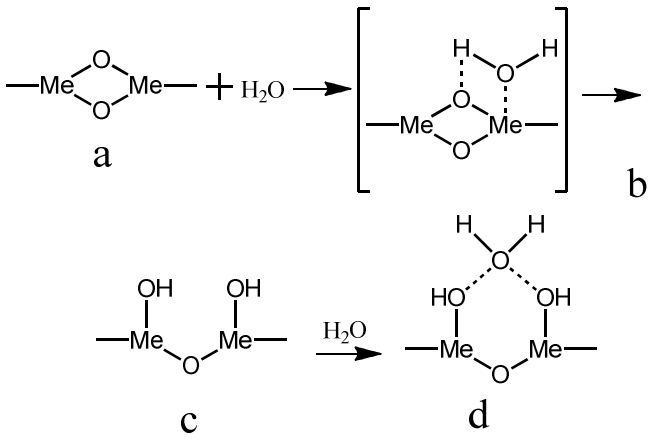

Figure 1.18: Four stages of water adsorption onto the surface of metal oxide[143].

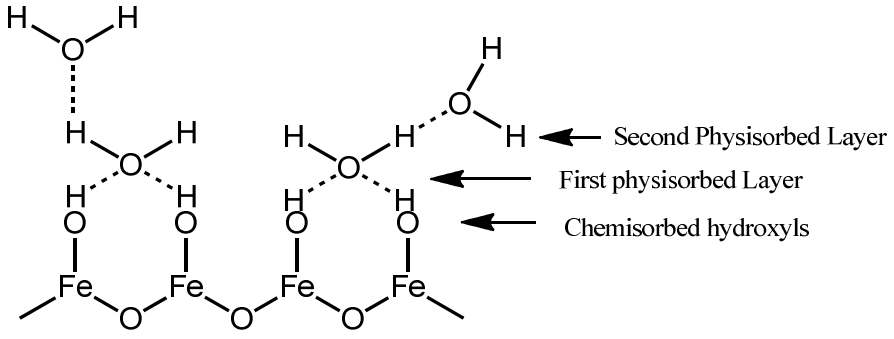

Figure 1.19: Multi-layer structure of condensed water[144].

The chemisorbed and the physically-adsorbed water layers are immobile and cannot contribute to the protonic conductivity. However, these layers can contribute to electron tunnelling among the donor water sites[145-146] and electrons transport is facilitated by tunnelling effect as well as surface ions energy which help in electron hopping along the surface. At low humidity, this mechanism is useful as the protonic conductivity is not effective.

Table 1.6: (a) Humidity sensors based on various materials synthesized by different synthesis procedures and b) operating principle involved[Adopted from[150]].

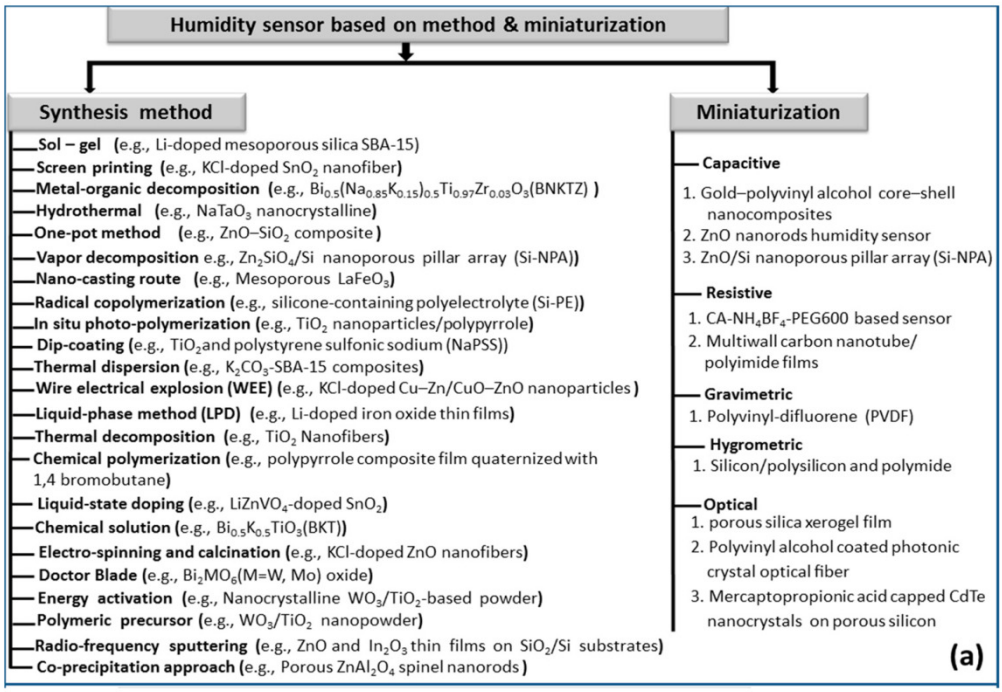

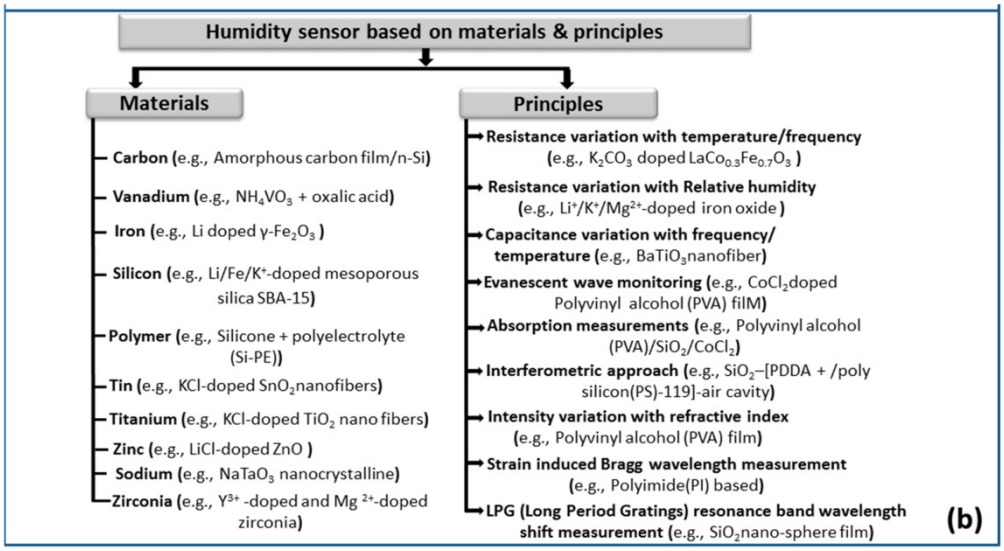

1.9. 2 Literature survey of humidity sensor of metal oxides

Metal oxides based humidity sensors exhibit superior advantages over polymers sensors such mechanical strength, resistance to chemical attack, physical and thermal stability[147]. Semiconductor oxides based humidity sensors have been widely used in industries and research laboratories. The unique microstructures and morphologies

such as grains, grain boundaries, porosities, high surface areas etc. enhance their applicability for humidity sensor[148-149]. There are many parameters such as sensitivity, rapid response and recovery, hysteresis, and stability which need to be optimized. Therefore, researchers have chosen to optimize the humidity sensing properties of materials by various methods such as doping, using composites, optimizing microstructure, miniaturization techniques for deposition, and sensing as well as the operating principle involved[147, 149-150].

1.10 Outline of the thesis

The organization of the thesis is as follows:

In second chapter, the synthesis and experimental techniques used in this study are briefly presented and discussed.

The third chapter comprises of two sections, namely a) the case of In-doped ZnO and b) the case of Al-doped ZnO films. The structural, morphological and gas sensing properties of these films are studied.

In the fourth chapter, light assisted gas sensing properties of ZnO/CdS heterojunction are explored.

The fifth chapter presents our work on the synthesis and gas sensing study of ternary FeV_3O_8 nanosheets.

In the sixth chapter, gas sensing properties of $NiCo_2O_4$ nanograss are analysed and discussed.

The seventh chapter presents a detailed humidity sensing study of Zn_2SnO_4 nanoparticles.

Finally, in the eighth chapter the summary of the thesis and scope for future work are discussed.

1.11. References

[1] B. Perret, Peter Gründler, Chemical sensors: An introduction for scientists and engineers, Analy and Bioanaly Chem, 392(2008) 21-2.

[2] A. Hulanicki, S. Glab, F. Ingman, Chemical Sensors Definitions and Classification, Pure Appl Chem, 63(1991) 1247-50.

[3] O.S. Wolfbeis, Chemical Sensors - Survey and Trends, Fresen J Anal Chem, 337(1990) 522-7.

[4] W. Göpel and K. Schierbaum, Chemical and biological sensors part I, Sensors , 2 (1991) 2.

[5] J. R. Stetter, W.R. Penrose, Understanding Chemical Sensors and Chemical Sensor Arrays (Electronic Noses): Past, Present, and Future, Sensors Update, 10(2002) 189.

[6] G.S. Korotchenkov, Chemical Sensors: Comprehensive Sensors Technologies. Solid-state Devices: Momentum Press; 2011.

[7] N. Yamazoe, Toward innovations of gas sensor technology, Sensors Actuat B-Chem, 108(2005) 2-14.

[8] H. Meixner, J. Gerblinger, U. Lampe, M. Fleischer, Thin Film Gas Sensors Based on Semiconducting Metal-Oxides, Sensor Actuat B-Chem, 23(1995) 119-25.

[9] T. Takeuchi, Oxygen Sensors, Sensor Actuator, 14(1988) 109-24.

[10] P.T. Moseley, B. Tofield, Solid-state gas sensors: A. Hilger; 1987.

[11] A. Mandelis, C. Christofides, Physics, chemistry and technology of solid state gas sensor devices: John Wiley & Sons; 1993.

[12] P. Moseley, Solid state gas sensors, Measurement Science and technology, 8(1997) 223-37.

[13] J.-E. Haugen, K. Kvaal, Electronic nose and artificial neural network, Meat Science, 49(1998) S273-S86.

[14] Y.P. Yakovlev, A.N. Baranov, A.N. Imenkov, M.P. Mikhailova, Optoelectronic LED-photodiode pairs for moisture and gas sensors in the spectral range 1.8-4.8 um, ECO4 (The Hague'91), International Society for Optics and Photonics, (1991) 170-7.

[15] P. Werle, F. Slemr, K. Maurer, R. Kormann, R. Mücke, B. Jänker, Near-and mid-infrared laser-optical sensors for gas analysis, Optics and lasers in engineering, 37(2002) 101-14.

[16] I. Eisele, T. Doll, M. Burgmair, Low power gas detection with FET sensors, Sensors and Actuators B: Chemical, 78(2001) 19-25.

[17] Y. Sadaoka, Organic semiconductor gas sensors, Gas Sensors, Springer, (1992) 187-218.

[18] W. Göpel, Ultimate limits in the miniaturization of chemical sensors, Sensors and Actuators A: Physical, 56(1996) 83-102.

[19] G. Monkman, Monomolecular Langmuir-Blodgett films-tomorrow's sensors?, Sensor Review, 20(2000) 127-31.

[20] L. Talazac, J. Brunet, V. Battut, J. Blanc, A. Pauly, J. Germain, et al., Air quality evaluation by monolithic InP-based resistive sensors, Sensors and Actuators B: Chemical, 76(2001) 258-64.

[21] B. Adhikari, S. Majumdar, Polymers in sensor applications, Progress in polymer science, 29(2004) 699-766.

[22] T. Doll, J. Lechner, I. Eisele, K.-D. Schierbaum, W. Göpel, Ozone detection in the ppb range with work function sensors operating at room temperature, Sensors and Actuators B: Chemical, 34(1996) 506-10.

[23] D. Walton, Electrically conducting polymers, Electronic Materials, Springer, (1991) 449-70.

[24] G. Harsányi, Polymer films in sensor applications: a review of present uses and future possibilities, Sensor Review, 20(2000) 98-105.

[25] G. Sberveglieri, Gas sensors: principles, operation and developments: Springer Science & Business Media; 2012.

[26] U. Lampe, M. Fleischer, N. Reitmeier, H. Meixner, J. McMonagle, A. Marsh, New Materials for Metal Oxide Sensors, Sensors Update, 2(1996) 1-36.

[27] E. Kanazawa, G. Sakai, K. Shimanoe, Y. Kanmura, Y. Teraoka, N. Miura, et al., Metal oxide semiconductor N_2O sensor for medical use, Sensors and Actuators B: Chemical, 77(2001) 72-7.

[28] G. Korotcenkov, Gas response control through structural and chemical modification of metal oxide films: state of the art and approaches, Sensors and Actuators B: Chemical, 107(2005) 209-32.

[29] Z. Chen, C. Lu, Humidity sensors: a review of materials and mechanisms, Sensor Lett, 3(2005) 274-95.

[30] G. Eranna, B. Joshi, D. Runthala, R. Gupta, Oxide materials for development of integrated gas sensors a comprehensive review, Critical Reviews in Solid State and Materials Sciences, 29(2004) 111-88.

[31] G. Korotcenkov, Metal oxides for solid-state gas sensors: What determines our choice?, Materials Science and Engineering: B, 139(2007) 1-23.

[32] W.H. Brattain, J. Bardeen, Surface properties of germanium, Bell System Technical Journal, 32(1953) 1-41.

[33] T. Seiyama, A. Kato, K. Fujiishi, M. Nagatani, A New Detector for Gaseous Components Using Semiconductive Thin Films, Anal Chem, 34(1962) 1502-3.

[34] N. Taguchi, A metal oxide gas sensor, Japanese Patent, 4(1962) 5-38200.

[35] S.R. Morrison, Selectivity in semiconductor gas sensors, Sensor Actuator, 12(1987) 425-40.

[36] N. Barsan, U. Weimar, Conduction model of metal oxide gas sensors, J Electroceram, 7(2001) 143-67.

[37] H.-J. Kim, J.-H. Lee, Highly sensitive and selective gas sensors using p-type oxide semiconductors: Overview, Sensors and Actuators B: Chemical, 192(2014) 607-27.

[38] S. Choopun, E. Wongrat, N. Hongsith, Metal-oxide nanowires for gas sensors: INTECH Open Access Publisher; 2012.

[39] H. Ogawa, M. Nishikawa, A. Abe, Hall measurement studies and an electrical conduction model of tin oxide ultrafine particle films, J Appl Phys, 53(1982) 4448-55.

[40] A. Tricoli, M. Righettoni, A. Teleki, Semiconductor gas sensors: dry synthesis and application, Angewandte Chemie International Edition, 49(2010) 7632-59.

[41] A. Gurlo, R. Riedel, In situ and operando spectroscopy for assessing mechanisms of gas sensing, Angewandte Chemie International Edition, 46(2007) 3826-48.

[42] J.N. Zemel, Theoretical description of gas-film interaction on SnO_x, Thin Solid Films, 163(1988) 189-202.

[43] N. Yamazoe, N. Miura, Some basic aspects of semiconductor gas sensors, Chemical sensor technology, 4(1992) 19-42.

[44] J. Szuber, The effect of oxygen adsorption on the electronic properties of the polar GaAs (111) surface after thermal cleaning in ultrahigh vacuum, Thin Solid Films, 170(1989) 219-26.

[45] J. Mizsei, V. Lantto, Simultaneous response of work function and resistivity of some SnO_2-based samples to H_2 and H_2S, Sensors and Actuators B: Chemical, 4(1991) 163-8.

[46] N. Yamazoe, G. Sakai, K. Shimanoe, Oxide semiconductor gas sensors, Catal Surv Asia, 7(2003) 63-75.

[47] V. Bochenkov, G. Sergeev, Preparation and chemiresistive properties of nanostructured materials, Advances in colloid and interface science, 116(2005) 245-54.

[48] C. Xu, J. Tamaki, N. Miura, N. Yamazoe, Correlation between gas sensitivity and crystallite size in porous SnO2-based sensors, Chem Lett, (1990) 441-4.

[49] C. Xu, J. Tamaki, N. Miura, N. Yamazoe, Grain size effects on gas sensitivity of porous SnO_2-based elements, Sensors and Actuators B: Chemical, 3(1991) 147-55.

[50] G. Sakai, N. Matsunaga, K. Shimanoe, N. Yamazoe, Theory of gas-diffusion controlled sensitivity for thin film semiconductor gas sensor, Sensors and Actuators B: Chemical, 80(2001) 125-31.

[51] M. Batzill, U. Diebold, The surface and materials science of tin oxide, Prog Surf Sci, 79(2005) 47-154.

[52] G. Korotcenkov, A. Cornet, E. Rossinyol, J. Arbiol, V. Brinzari, Y. Blinov, Faceting characterization of tin dioxide nanocrystals deposited by spray pyrolysis from stannic chloride water solution, Thin Solid Films, 471(2005) 310-9.

[53] P. Shaver, Activated tungsten oxide gas detectors, Applied Physics Letters, 11(1967) 255-7.

[54] W. Göpel, K. D. Schierbaum, SnO_2 sensors: current status and future prospects, Sensors and Actuators B: Chemical, 26(1995) 1-12.

[55] N. Yamazoe, Y. Kurokawa, T. Seiyama, Effects of additives on semiconductor gas sensors, Sensor Actuator, 4(1983) 283-9.

[56] G. Munuera, A. Gonzalez-Elipe, A. Munoz, A. Fernandez, J. Soria, J. Conesa, et al., Mechanism of hydrogen gas-sensing at low temperatures using Rh/TiO_2 Systems, Sensor Actuator, 18(1989) 337-48.

[57] T. Skala, K. Veltruska, M. Moroseac, I. Matolí, G. Korotchenkov, V. Matolí, Study of Pd–In interaction during Pd deposition on pyrolytically prepared In_2O_3, Appl Surf Sci, 205(2003) 196-205.

[58] V. Nehasil, P. Janeček, G. Korotchenkov, V.r. Matolín, Investigation of behaviour of Rh deposited onto polycrystalline SnO_2 by means of TPD, AES and EELS, Surf Sci, 532(2003) 415-9.

[59] N. Tsud, V. Johanek, I. Stara, K. Veltruska, V. Matolın, XPS, ISS and TPD study of Pd–Sn interactions on Pd–SnO_x systems, Thin Solid Films, 391(2001) 204-8.

[60] N. Yamazoe, N. Miura, Some Basic Aspects of Semiconductor Gas Sensors in Chemical Sensor Technology, vol 4Kodansha and Elsevier, Tokyo and Amsterdam, (1992) 19.

[61] T. Maekawa, J. Tamaki, N. Miura, N. Yamazoe, Sensing behavior of CuO-loaded SnO_2 element for H_2S detection, Chem Lett, (1991) 575-8.

[62] A. Chowdhuri, P. Sharma, V. Gupta, K. Sreenivas, K. Rao, H_2S gas sensing mechanism of SnO_2 films with ultrathin CuO dotted islands, J Appl Phys, 92(2002) 2172-80.

[63] A. Cabot, J. Arbiol, J.R. Morante, U. Weimar, N. Barsan, W. Göpel, Analysis of the noble metal catalytic additives introduced by impregnation of as obtained SnO_2 sol–gel nanocrystals for gas sensors, Sensors and Actuators B: Chemical, 70(2000) 87-100.

[64] X. Du, S. George, Thickness dependence of sensor response for CO gas sensing by tin oxide films grown using atomic layer deposition, Sensors and Actuators B: Chemical, 135(2008) 152-60.

[65] J. Mizsei, How can sensitive and selective semiconductor gas sensors be made?, Sensors and Actuators B: Chemical, 23(1995) 173-6.

[66] W. Sears, K. Colbow, F. Consadori, General characteristics of thermally cycled tin oxide gas sensors, Semiconductor Science and Technology, 4(1989) 351.

[67] W. Sears, K. Colbow, F. Consadori, Algorithms to improve the selectivity of thermally-cycled tin oxide gas sensors, Sensor Actuator, 19(1989) 333-49.

[68] K. Wada, M. Egashira, Hydrogen sensing properties of SnO_2 subjected to surface chemical modification with ethoxysilanes, Sensors and Actuators B: Chemical, 62(2000) 211-9.

[69] T. Hyodo, Y. Baba, K. Wada, Y. Shimizu, M. Egashira, Hydrogen sensing properties of SnO_2 varistors loaded with SiO_2 by surface chemical modification with diethoxydimethylsilane, Sensors and Actuators B: Chemical, 64(2000) 175-81.

[70] G. Tournier, C. Pijolat, Selective filter for SnO_2-based gas sensor: application to hydrogen trace detection, Sensors and Actuators B: Chemical, 106(2005) 553-62.

[71] J. Trimboli, P.K. Dutta, Oxidation chemistry and electrical activity of Pt on titania: development of a novel zeolite-filter hydrocarbon sensor, Sensors and Actuators B: Chemical, 102(2004) 132-41.

[72] V. Brinzari, G. Korotcenkov, V. Golovanov, J. Schwank, V. Lantto, S. Saukko, Morphological rank of nano-scale tin dioxide films deposited by spray pyrolysis from $SnCl_4 \cdot 5H_2O$ water solution, Thin Solid Films, 408(2002) 51-8.

[73] V. Golovanov, G. Korotcenkov, V. Brinzari, A. Cornet, J. Morante, J. Arbiol, et al., CO water interaction with SnO_2 gas sensors: role of orientation effects, Proceeding of the 16th International Conference on Transducers, Eurosensors-XVI (2002) 926-9.

[74] R.I. Masel, Principles of adsorption and reaction on solid surfaces: John Wiley & Sons; 1996.

[75] R.M. Lambert, G. Pacchioni, Chemisorption and Reactivity on Supported Clusters and Thin Films:: Towards an Understanding of Microscopic Processes in Catalysis: Springer Science & Business Media; 2013.

[76] P. Cox, The surface science of metal oxides: Cambridge university press; 1996.

[77] H. Meixner, U. Lampe, Metal oxide sensors, Sensors and Actuators B: Chemical, 33(1996) 198-202.

[78]V. Golovanov, V. Smyntyna, V. Brinzar, G. Korotcenkov, Cd_xS- and Sn_XWO_Y-based gas sensor: The role of chemical composition in CO sensing, (2001)6-11.

[79] S. Basu, A. Dutta, Modified heterojunction based on zinc oxide thin film for hydrogen gas-sensor application, Sensors and Actuators B: Chemical, 22(1994) 83-7.

[80] H. Gleiter, Nanostructured materials: basic concepts and microstructure, Acta materialia, 48(2000) 1-29.

[81] H. Gleiter, Materials with ultrafine microstructures: retrospectives and perspectives, Nanostructured materials, 1(1992) 1-19.

[82] I. Sunagawa, J. van Suchtelen, Morphology of crystals: Springer Science & Business Media; 1995.

[83] F. Kawamura, I. Yasui, M. Kamei, I. Sunagawa, Habit modifications of SnO_2 crystals in SnO_2–Cu_2O flux system in the presence of trivalent impurity cations, J Am Ceram Soc, 84(2001) 1341-6.

[84] G. Korotcenkov, A. Cerneavschi, V. Brinzari, A. Vasiliev, M. Ivanov, A. Cornet, et al., In_2O_3 films deposited by spray pyrolysis as a material for ozone gas sensors, Sensors and Actuators B: Chemical, 99(2004) 297-303.

[85] N. Carreño, A. Maciel, E. Leite, P.N. Lisboa-Filho, E. Longo, A. Valentini, et al., The influence of cation segregation on the methanol decomposition on nanostructured SnO_2, Sensors and Actuators B: Chemical, 86(2002) 185-92.

[86] F. Kawamura, T. Takahashi, I. Yasui, I. Sunagawa, Impurity effect on (111) and (110) directions of growing SnO_2 single crystals in SnO_2–Cu_2O flux system, Journal of crystal growth, 233(2001) 259-68.

[87] Z. Guo, M. Li, J. Liu, Highly porous CdO nanowires: preparation based on hydroxy-and carbonate-containing cadmium compound precursor nanowires, gas sensing and optical properties, Nanotechnology, 19(2008) 245611.

[88] H. Nguyen, S.A. El-Safty, Meso-and macroporous Co_3O_4 nanorods for effective VOC gas sensors, The Journal of Physical Chemistry C, 115(2011) 8466-74.

[89] J. Zhang, J. Liu, Q. Peng, X. Wang, Y. Li, Nearly monodisperse Cu_2O and CuO nanospheres: preparation and applications for sensitive gas sensors, Chem Mater, 18(2006) 867-71.

[90] J. Chen, L. Xu, W. Li, X.-l. Gou, α-Fe_2O_3 nanotubes in gas sensor and lithium-ion battery applications, Adv Mater, 17(2005) 582-6.

[91] S. Arnold, S. Prokes, F. Perkins, M. Zaghloul, Design and performance of a simple, room-temperature Ga_2O_3 nanowire gas sensor, Applied Physics Letters, 95(2009) 103102.

[92] B. Li, Y. Xie, M. Jing, G. Rong, Y. Tang, G. Zhang, In_2O_3 hollow microspheres: synthesis from designed $In(OH)_3$ precursors and applications in gas sensors and photocatalysis, Langmuir, 22(2006) 9380-5.

[93] W.-S. Kim, H.-C. Kim, S.-H. Hong, Gas sensing properties of MoO_3 nanoparticles synthesized by solvothermal method, J Nanopart Res, 12(2010) 1889-96.

[94] R.A. Rani, A.S. Zoolfakar, J.Z. Ou, M.R. Field, M. Austin, K. Kalantar-zadeh, Nanoporous Nb_2O_5 hydrogen gas sensor, Sensors and Actuators B: Chemical, 176(2013) 149-56.

[95] G. Zhu, C. Xi, H. Xu, D. Zheng, Y. Liu, X. Xu, et al., Hierarchical NiO hollow microspheres assembled from nanosheet-stacked nanoparticles and their application in a gas sensor, Rsc Adv, 2(2012) 4236-41.

[96] Y.-J. Choi, I.-S. Hwang, J.-G. Park, K.J. Choi, J.-H. Park, J.-H. Lee, Novel fabrication of an SnO_2 nanowire gas sensor with high sensitivity, Nanotechnology, 19(2008) 095508.

[97] H.F. Lu, F. Li, G. Liu, Z.-G. Chen, D.-W. Wang, H.-T. Fang, et al., Amorphous TiO_2 nanotube arrays for low-temperature oxygen sensors, Nanotechnology, 19(2008) 405504.

[98] X.-L. Li, T.-J. Lou, X.-M. Sun, Y.-D. Li, Highly sensitive WO_3 hollow-sphere gas sensors, Inorg Chem, 43(2004) 5442-9.

[99] J.-f. Liu, X. Wang, Q. Peng, Y. Li, Vanadium pentoxide nanobelts: highly selective and stable ethanol sensor materials, Adv Mater, 17(2005) 764-7.

[100] L.-J. Bie, X.-N. Yan, J. Yin, Y.-Q. Duan, Z.-H. Yuan, Nanopillar ZnO gas sensor for hydrogen and ethanol, Sensors and Actuators B: Chemical, 126(2007) 604-8.

[101] Y. Hu, O. Tan, J. Pan, H. Huang, W. Cao, The effects of annealing temperature on the sensing properties of low temperature nano-sized $SrTiO_3$ oxygen gas sensor, Sensors and Actuators B: Chemical, 108(2005) 244-9.

[102] Y. Zeng, K. Zhang, X. Wang, Y. Sui, B. Zou, W. Zheng, et al., Rapid and selective H_2S detection of hierarchical $ZnSnO_3$ nanocages, Sensors and Actuators B: Chemical, 159(2011) 245-50.

[103] Z. Dai, C.-S. Lee, B.-Y. Kim, C.-H. Kwak, J.-W. Yoon, H.-M. Jeong, et al., Honeycomb-like periodic porous $LaFeO_3$ thin film chemiresistors with enhanced gas-sensing performances, ACS Applied Materials & Interfaces, 6(2014) 16217-26.

[104] Y. Gawli, S. Badadhe, A. Basu, D. Guin, M.V. Shelke, S. Ogale, Evaluation of n-type ternary metal oxide $NiMn_2O_4$ nanomaterial for humidity sensing, Sensors and Actuators B: Chemical, 191(2014) 837-43.

[105] X.L. Yu, Y. Wang, Y.M. Hu, C.B. Cao, H.L.W. Chan, Gas-Sensing Properties of Perovskite $BiFeO_3$ Nanoparticles, J Am Ceram Soc, 92(2009) 3105-7.

[106] C. Xiangfeng, L. Xingqin, M. Guangyao, Preparation and gas sensitivity properties of $ZnFe_2O_4$ semiconductors, Sensors and Actuators B: Chemical, 55(1999) 19-22.

[107] S.L. Darshane, S. Suryavanshi, I. Mulla, Nanostructured nickel ferrite: a liquid petroleum gas sensor, Ceramics International, 35(2009) 1793-7.

[108] B. Yadav, A. Yadav, S. Singh, K. Singh, Nanocrystalline zinc titanate synthesized via physicochemical route and its application as liquefied petroleum gas sensor, Sensors and Actuators B: Chemical, 177(2013) 605-11.

[109] X. Chu, X. Liu, G. Wang, G. Meng, Preparation and gas-sensing properties of nano-$CoTiO_3$, Mater Res Bull, 34(1999) 1789-95.

[110] G. Carbajal-Franco, A. Tiburcio-Silver, J. Domínguez, A. Sánchez-Juárez, Thin film tin oxide-based propane gas sensors, Thin Solid Films, 373(2000) 141-4.

[111] E. Comini, A. Vomiero, G. Faglia, G. Della Mea, G. Sberveglieri, Influence of iron addition on ethanol and CO sensing properties of tin oxide prepared with the RGTO technique, Sensors and Actuators B: Chemical, 115(2006) 561-6.

[112] A. Salehi, M. Gholizade, Gas-sensing properties of indium-doped SnO_2 thin films with variations in indium concentration, Sensors and Actuators B: Chemical, 89(2003) 173-9.

[113] S.T. Shishiyanu, T.S. Shishiyanu, O.I. Lupan, Sensing characteristics of tin-doped ZnO thin films as NO_2 gas sensor, Sensors and Actuators B: Chemical, 107(2005) 379-86.

[114] M. Wagh, G. Jain, D. Patil, S. Patil, L. Patil, Modified zinc oxide thick film resistors as NH_3 gas sensor, Sensors and Actuators B: Chemical, 115(2006) 128-33.

[115] H. Gong, J. Hu, J. Wang, C. Ong, F. Zhu, Nano-crystalline Cu-doped ZnO thin film gas sensor for CO, Sensors and Actuators B: Chemical, 115(2006) 247-51.

[116] W.-H. Tao, C.-H. Tsai, H_2S sensing properties of noble metal doped WO_3 thin film sensor fabricated by micromachining, Sensors and Actuators B: Chemical, 81(2002) 237-47.

[117] W. Noh, Y. Shin, J. Kim, W. Lee, K. Hong, S.A. Akbar, et al., Effects of NiO addition in WO_3-based gas sensors prepared by thick film process, Solid State Ionics, 152(2002) 827-32.

[118] Y. Wang, S. Wang, Y. Zhao, B. Zhu, F. Kong, D. Wang, et al., H_2S sensing characteristics of Pt-doped α-Fe_2O_3 thick film sensors, Sensors and Actuators B: Chemical, 125(2007) 79-84.

[119] Y. Wang, Y. Wang, J. Cao, F. Kong, H. Xia, J. Zhang, et al., Low-temperature H_2S sensors based on Ag-doped α-Fe_2O_3 nanoparticles, Sensors and Actuators B: Chemical, 131(2008) 183-9.

[120] Z. Jing, Y. Wang, S. Wu, Preparation and gas sensing properties of pure and doped γ-Fe_2O_3 by an anhydrous solvent method, Sensors and Actuators B: Chemical, 113(2006) 177-81.

[121] M. Matsumiya, F. Qiu, W. Shin, N. Izu, N. Murayama, S. Kanzaki, Thin-film Li-doped NiO for thermoelectric hydrogen gas sensor, Thin Solid Films, 419(2002) 213-7.

[122] H.-J. Kim, K.-I. Choi, K.-M. Kim, C.W. Na, J.-H. Lee, Highly sensitive C_2H_5OH sensors using Fe-doped NiO hollow spheres, Sensors and Actuators B: Chemical, 171(2012) 1029-37.

[123] H.-J. Kim, J.-W. Yoon, K.-I. Choi, H.W. Jang, A. Umar, J.-H. Lee, Ultraselective and sensitive detection of xylene and toluene for monitoring indoor air pollution using Cr-doped NiO hierarchical nanostructures, Nanoscale, 5(2013) 7066-73.

[124] C. Xiangfeng, L. Xingqin, M. Guangyao, Effects of CdO dopant on the gas sensitivity properties of $ZnFe_2O_4$ semiconductors, Sensors and Actuators B: Chemical, 65(2000) 64-7.

[125] D.R. Miller, S.A. Akbar, P.A. Morris, Nanoscale metal oxide-based heterojunctions for gas sensing: a review, Sensors and Actuators B: Chemical, 204(2014) 250-72.

[126] A. Kusior, M. Radecka, M. Rekas, M. Lubecka, K. Zakrzewska, A. Reszka, et al., Sensitization of gas sensing properties in TiO_2/SnO_2 nanocomposites, Procedia Engineering, 47(2012) 1073-6.

[127] A. Chen, S. Bai, B. Shi, Z. Liu, D. Li, C.C. Liu, Methane gas-sensing and catalytic oxidation activity of SnO_2–In_2O_3 nanocomposites incorporating TiO_2, Sensors and Actuators B: Chemical, 135(2008) 7-12.

[128] S.-W. Choi, J.Y. Park, S.S. Kim, Synthesis of SnO_2–ZnO core–shell nanofibers via a novel two-step process and their gas sensing properties, Nanotechnology, 20(2009) 465603.

[129] L. Wang, Y. Kang, Y. Wang, B. Zhu, S. Zhang, W. Huang, et al., CuO nanoparticle decorated ZnO nanorod sensor for low-temperature H_2S detection, Materials Science and Engineering: C, 32(2012) 2079-85.

[130] Y. Liu, G. Zhu, J. Chen, H. Xu, X. Shen, A. Yuan, Co_3O_4/ZnO nanocomposites for gas-sensing applications, Appl Surf Sci, 265(2013) 379-84.

[131] X. Yu, G. Zhang, H. Cao, X. An, Y. Wang, Z. Shu, et al., ZnO@ZnS hollow dumbbells–graphene composites as high-performance photocatalysts and alcohol sensors, New J Chem, 36(2012) 2593-8.

[132] W. Wang, Z. Li, W. Zheng, H. Huang, C. Wang, J. Sun, Cr_2O_3-sensitized ZnO electrospun nanofibers based ethanol detectors, Sensors and Actuators B: Chemical, 143(2010) 754-8.

[133] H. Gu, Z. Wang, Y. Hu, Hydrogen gas sensors based on semiconductor oxide nanostructures, Sensors-Basel, 12(2012) 5517-50.

[134] M. Rumyantseva, V. Kovalenko, A. Gaskov, E. Makshina, V. Yuschenko, I. Ivanova, et al., Nanocomposites SnO_2/Fe_2O_3: sensor and catalytic properties, Sensors and Actuators B: Chemical, 118(2006) 208-14.

[135] B. de Lacy Costello, R.J. Ewen, N.M. Ratcliffe, P. Sivanand, Thick film organic vapour sensors based on binary mixtures of metal oxides, Sensors and Actuators B: Chemical, 92(2003) 159-66.

[136] A. Chen, X. Huang, Z. Tong, S. Bai, R. Luo, C.C. Liu, Preparation, characterization and gas-sensing properties of SnO_2–In_2O_3 nanocomposite oxides, Sensors and Actuators B: Chemical, 115(2006) 316-21.

[137] Z. Yi, Y.-f. BING, L. Chang, W.-t. ZHENG, G.-t. ZOU, Self-assembly of hierarchical $ZnSnO_3$-SnO_2 nanoflakes and their gas sensing properties, Transactions of Nonferrous Metals Society of China, 22(2012) 2451-8.

[138] C.W. Na, H.-S. Woo, I.-D. Kim, J.-H. Lee, Selective detection of NO_2 and C_2H_5OH using a Co_3O_4-decorated ZnO nanowire network sensor, Chem Commun, 47(2011) 5148-50.

[139] N. Bahlawane, E.F. Rivera, K. Kohse-Höinghaus, A. Brechling, U. Kleineberg, Characterization and tests of planar Co_3O_4 model catalysts prepared by chemical vapor deposition, Applied Catalysis B: Environmental, 53(2004) 245-55.

[140] S. Sen, P. Kanitkar, A. Sharma, K. Muthe, A. Rath, S. Deshpande, et al., Growth of $SnO_2/W_{18}O_{49}$ nanowire hierarchical heterostructure and their application as chemical sensor, Sensors and Actuators B: Chemical, 147(2010) 453-60.

[141] W. Zeng, T. Liu, Z. Wang, Sensitivity improvement of TiO_2-doped SnO_2 to volatile organic compounds, Physica E: Low-dimensional Systems and Nanostructures, 43(2010) 633-8.

[142] C. de Grotthuss, Theory of decomposition of liquids by electrical currents, Ann Chim(Paris), 58(1806) 54-74.

[143] T. Morimoto, M. Nagao, F. Tokuda, Relation between the amounts of chemisorbed and physisorbed water on metal oxides, The Journal of Physical Chemistry, 73(1969) 243-8.

[144] E. McCafferty, A. Zettlemoyer, Adsorption of water vapour on α-Fe_2O_3, Discussions of the Faraday Society, 52(1971) 239-54.

[145] V. Khanna, R. Nahar, Carrier-transfer mechanisms and Al_2O_3 sensors for low and high humidities, Journal of Physics D: Applied physics, 19(1986) 141.

[146] Y.C. Yeh, T.Y. Tseng, D.A. Chang, Electrical properties of porous titania ceramic humidity sensors, J Am Ceram Soc, 72(1989) 1472-5.

[147] E. Traversa, Ceramic sensors for humidity detection: the state-of-the-art and future developments, Sensors and Actuators B: Chemical, 23(1995) 135-56.

[148] Y. Shimizu, H. Arai, T. Seiyama, Theoretical studies on the impedance-humidity characteristics of ceramic humidity sensors, Sensor Actuator, 7(1985) 11-22.

[149] J.-M. Tulliani, C. Baroni, L. Zavattaro, C. Grignani, Strontium-Doped Hematite as a Possible Humidity Sensing Material for Soil Water Content Determination, Sensors-Basel, 13(2013) 12070-92.

[150] A. Tripathy, S. Pramanik, J. Cho, J. Santhosh, N.A. Abu Osman, Role of Morphological Structure, Doping, and Coating of Different Materials in the Sensing Characteristics of Humidity Sensors, Sensors-Basel, 14(2014) 16343-422.

Chapter 2

Experimental Methods and Characterization Techniques

This chapter briefly discusses different synthesis method used for synthesis of different metal oxides. The different techniques employed for characterization of metal oxides are discussed. Finally gas sensing set-up and measurement methods are also discussed.

In the last few decades, researchers have invented various synthesis and characterization techniques for materials with at least one dimension in the nanoscale such as nanoparticles, nanotubes, nanolayers, and nanocomposites[1]. However, it's an ongoing quest and challenge to design and synthesize/or fabricate nanomaterials with optimized properties for the desired application. This chapter gives a brief discussion of synthesis and characterization techniques used for my research.

2I: Experimental Methods

2.1. Spray pyrolysis technique

Coating technologies have many advantages such as processing flexibility, cost effectiveness and speed, and hence have received tremendous attention in the last few decades[2]. Both physical and chemical methods can be employed for film deposition. Chemical deposition is divided into gas or liquid phase deposition. Gas phase deposition comprises methods such as chemical vapour deposition, pulsed laser deposition, atomic layer epitaxy (ALE) etc. Liquid phase deposition can be done by sol-gel, dip coating, spin coating, evaporation, anodic oxidation and spray pyrolysis. The basic principle of spray pyrolysis technique is deposition of desired compound by pyrolytic decomposition of precursor solution. As droplet reached hot substrate, it decomposes pyrolytically forming single crystallite or cluster of crystallite. Such crystallites subsequently combine together to form coherent film. However, volatile solvents and by-product go off as thermal decomposition energy supplied by the substrate. In 1966, Chamberlin and Skarman[3] introduced spray pyrolysis technique for deposition of thin films of CdS for solar cell application. Ever since then numerous materials such SnO_2, In_2O_3, ZnO, PbO, ZrO_2 etc have been deposited using spray pyrolysis method[4-8]. The important features of spray pyrolysis comparable to other methods are cost effective, easy to perform, easy to coat complex geometric substrates, operation at moderate temperature (100-500^{o}C), high reproducibility and potential for mass production. Spray pyrolysis is less expensive which generates great industrial interest for commercial applications. Commercially spray pyrolysis is employed for fabrication of transparent layer on the glass substrate[9], SnO_2 for gas sensor[4],YSZ layer for solar cell[10], anodes for Li-ion batteries[11], devices for optoelectronic applications[12] etc. In spray pyrolysis following steps are involved,

atomization of the precursor solution, aerosol transport of the droplet, and evaporation of droplet, spreading on the substrate, drying and precursor salt decomposition to initiate film growth. There are many factors which affect quality of film deposited by spray pyrolysis such as the rate of deposition, aerosol droplet size, substrate temperature, distance between atomizer and substrate, the concentration of precursor solution, time of deposition, time lapse between each spray etc[13].

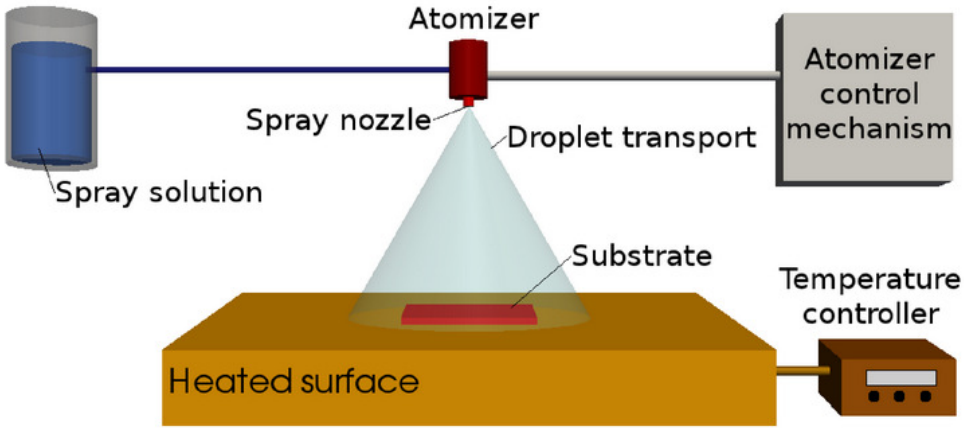

Figure 2.1: Schematic of spray pyrolysis technique[Reprinted with permission[13]].

It is also easy to form layered film or compositional gradient films only by changing/ varying the spraying solution. Spray pyrolysis provides an easy method for doping any element by simply adding the dopant into the spraying solution. The porosity, thickness and particle size can be optimized by using surfactants, monitoring precursor concentration, dopants etc.

In the present thesis work, spray pyrolysis technique has been used for deposition of good quality ZnO, indium-doped ZnO and aluminium-doped ZnO films. All the parameters such as the concentration of precursor, the rate of deposition, substrate temperature, distance between the atomizer and substrate are kept constant and only the dopant concentration is varied in the spraying solution.

2.2. Hydrothermal Synthesis

Hydrothermal synthesis is a common, invaluable technique for fabrication and processing of advanced materials. It can be defined as “any heterogeneous reaction under high pressure and temperature dissolves and recrystallize materials in aqueous

solvent or mineralizes which are insoluble at normal conditions". Karl Emilvon Schafhäutl in 1845, first grew quartz crystal in pressure cooker using hydrothermal techniques[14]. Its unique operational principle allows greater processing control therefore it has been used to synthesize advanced nanomaterials for many applications such as ceramics, catalysis, optoelectronics, electronics, biophotonics, biomedical, etc. It is very useful in the synthesis of mono-dispersed and uniform nanoparticles as well as the synthesis of complex materials such as nano-hybrid materials and nanocomposites. Hydrothermal embodies various processes such as hydrothermal synthesis, decomposition, transformation, treatment, extraction, sintering, structural stabilization, fabrication, recycling, microwave supported reactions, electrochemical reactions, dehydration, sonochemical, mechanochemical, phase equilibria, hydrothermal electrochemical processes, hot pressing, leaching, metal reduction, corrosion, crystal growth for synthesis of fine to ultra fine crystals, bulk single crystals and so on.

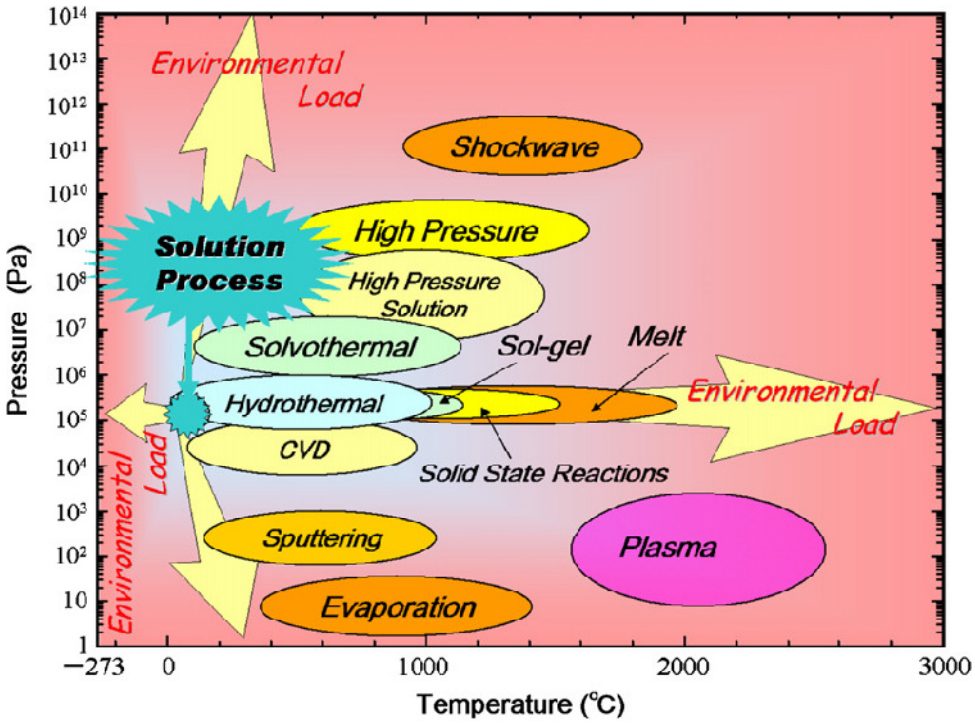

Figure 2.2 Pressure temperature map of materials processing techniques[14].

Hydrothermal processing has certain advantages and provides homogeneity, high quality, crystal symmetry, unique metastable compounds, low sintering temperature, single step reactions, fast reactions, lowest residence time, crystal growth with

polymorphic modification, low to ultra-low crystals solubility, various chemical compositions, sub-micro-to nanoparticles with narrow distribution of particle size etc. Figure 2.2 illustrates the pressure-temperature plot of different materials processing methods[15-16]. This process provides an atmosphere for controlled diffusion of nutrients in a solvent in the closed condition and can be used to tune physicochemical properties of nanomaterials depending on their applicability. It also offers certain advantages like recycling, disintegration, transformation of various toxic and organic wastes, improved nucleation control, shape control, use of larger reactors for reaction, better dispersion, higher reaction rates, lower operating temperature, energy efficient, environmental friendly etc.

Hydrothermal synthesis is typically performed in stainless steel pressure vessels known 'autoclaves' or 'bombs' with or without teflon liners. The reaction is carried out in aqueous solution under controlled temperature and/or pressure (Fig. 2.3). The temperature is generally kept above boiling point of water to reach the vapour saturation pressure. The internal pressure of the autoclave is determined by temperature and quantity of solution used. In the present thesis, hydrothermal process is used for synthesis of FeV_3O_8, $NiCo_2O_4$, and Zn_2SnO_4. The detailed procedure is mentioned in the respective chapter.

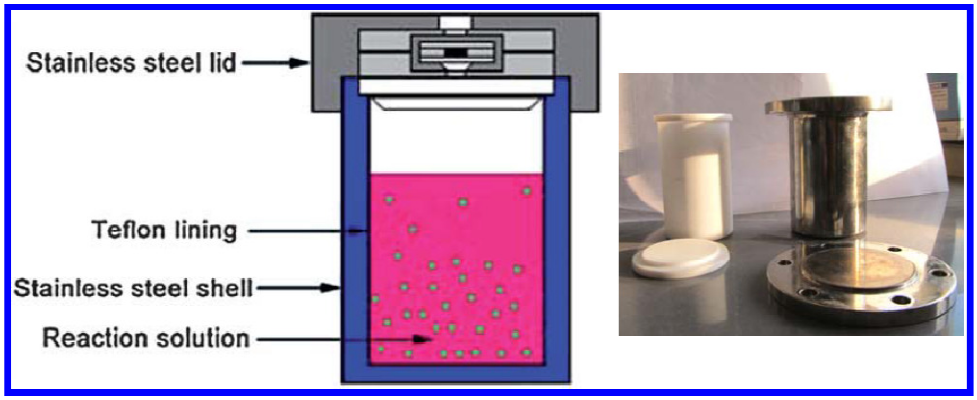

Figure 2.3: A schematic of a teflon-lined, stainless steel autoclave[17]. The inset: picture of stainless steel autoclave and teflon pot normally used for hydrothermal synthesis in the laboratory.

2.3. Successive Ionic Layer Adsorption and Reaction (SILAR) method

Though Ristov et. al.[18] first introduced the SILAR technique the actual term SILAR was coined by Nicolau et. al. in 1985[19]. SILAR technique is simple, easy and inexpensive. The raw materials used in coatings are cheap. The coating on different substrates having various dimensions can be deposited. The SILAR can be performed manually or by using specialized computer controlled machines. This technique is commonly used for deposition of thin films especially metal chalcogenides such ZnS, CdS, CdSe, $CuInS_2$ etc. Unlike pulsed laser deposition (PLD) and chemical vapor deposition (CVD), the most advantageous feature of SILAR is that it doesn't need specialized targets, substrates or high vacuum assembly. Doping can be easily done using this method. The SILAR can be done at room temperature however if required, temperature of reaction bath can be increased.

There are four steps involved in SILAR method is shown Fig. 2.4 and 2.5.

1) Initially, substrate is dipped for specific duration in cationic bath where cations are adsorbed on the substrate from precursor solution.
2) In a second step, substrate is rinsed in a solvent bath to remove unwanted/unadhered precursor.
3) In third step, substrate is dipped for desired time in anionic bath where anions react with cations to form compound.
4) In the last step, substrate is again dipped in solvent to remove unreacted species. One SILAR cycle is completed with this final step. Depending upon requirement multi cycles of SILAR can be performed.

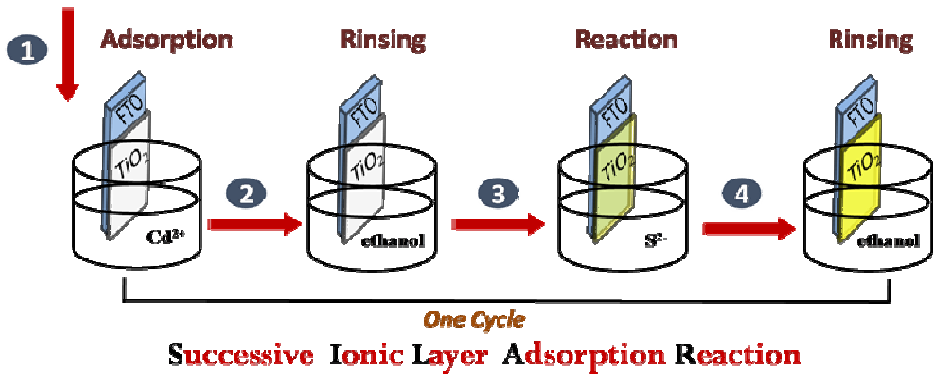

Figure 2.4: Schematic diagram illustrating steps involved in SILAR[20].

In the initial step, nucleation process begins and the concept of solubility product comes into play. Ions in the solution or on the substrate join to form nuclei when ionic

products exceeds solubility product. These nuclei are attached onto the surface of the substrate by means of weak vander Waal's forces, chemical forces and other unbalanced residual charges. This adsorption process is accompanied by sequential reactions to form the final product. Oriented nanostructures could be formed as a result of sequential growth of nuclei. Chalcogenides obtained by SILAR technique are amorphous in nature and need inert atmosphere post-heating to obtain crystallinity. In the thesis work SILAR method is used to form a few nanometer layer of CdS on ZnO nanorods

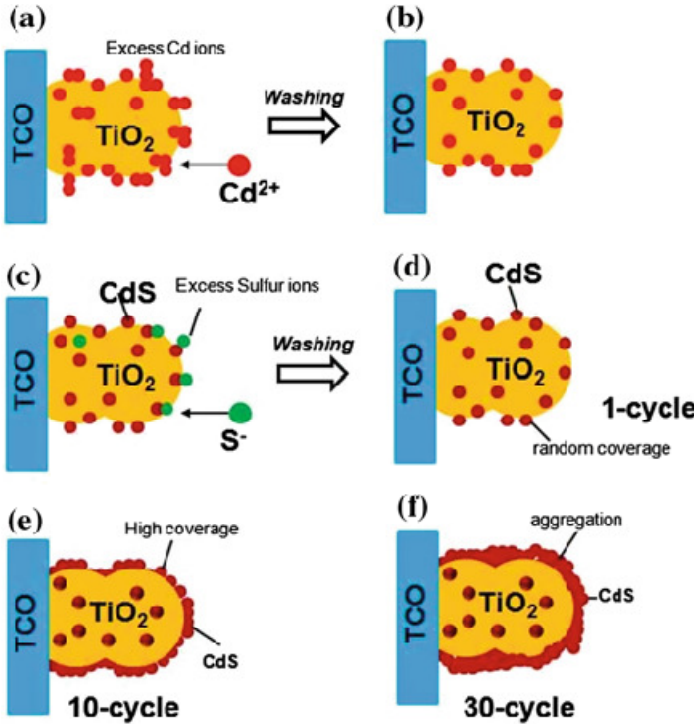

Figure 2.5: Schematic illustration of SILAR process with CdS as an example [21] (a) cationic adsorption, (c) CdS formation, (b, d) washing with solvent, and (e, f) 10 cycles and 30-cycles of SILAR, respectively.

2II: Characterization techniques

2.4 X-ray Diffraction (XRD)

The X-ray diffraction technique is a very powerful analytical tool commonly used for phase identification of crystalline compounds. The XRD technique was invented by English physicist William Lawrence Bragg and his son William Henry Bragg in 1913[22-23]. This is fast and non-destructive technique useful in phase identification,

crystallite size, strain and anisotropic growth of nanomaterials. Powder and film samples can be used for analysis. Basically, a monochromatic beam of X-rays of wavelength comparable to atomic spacings, falls on the sample and is diffracted in a specular fashion to undergo constructive interference. X-rays are diffracted at a specific angle (θ) by lattice planes and give constructive interference for a set of hkl planes whose path difference is an integral multiple of the incident light wavelength. The condition necessary for constructive interference is mathematically expressed by Bragg's law

$$2d \sin\theta = n\lambda \tag{2.1}$$

Where, d is interplanar distance, θ is the angle of scattering, n is order of diffraction and λ is the wavelength of incident angle.

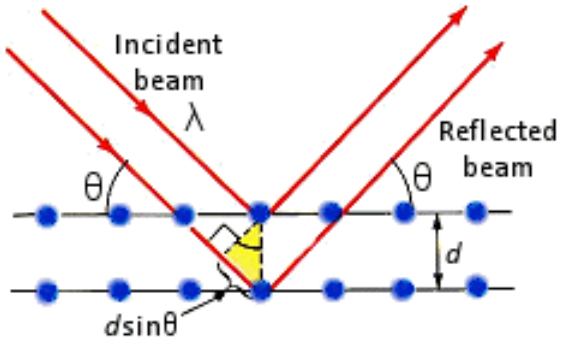

Figure 2.6: Schematic diagram of X-ray diffraction set up[Adopted from [24]]. (http://www.chemistryviews.org/details/ezine/2064331/100th_Anniversary_of_the_Discovery_of_X-ray_Diffraction.html)

In case of nanomaterials, as the size of the nanoparticles decreases the broadening in XRD peak increases. This may be due to stress induced in the sample. Generally, crystallite size (D) is calculated by the Scherrer formula which is expressed as:

$$D = \frac{0.9\,\lambda}{\beta \cos\theta} \tag{2.2}$$

Where, β is Full width half maxima (FWHM) of XRD peak at angel θ. λ is the incident wavelength X-ray beam.

2.5 Scanning Electron Microscopy (SEM):

An electron beam generated by electron gun at the top of the microscope is directed through different lenses towards the sample in presence of an electromagnetic field. The schematic diagram of scanning electron microscope is shown in Fig 2.7. In order to efficiently pass electron beam towards the sample, top columnar part is kept under high vacuum as a result of which the mean free path of electrons increases. A thermionic or field emitter electronic gun is usually used to generate electron beam. For soft specimens like biological and polymer based samples, a thermionic gun is normally preferred. However, field emission gun is quite reliable in the context of brightness of electrons and spot size.

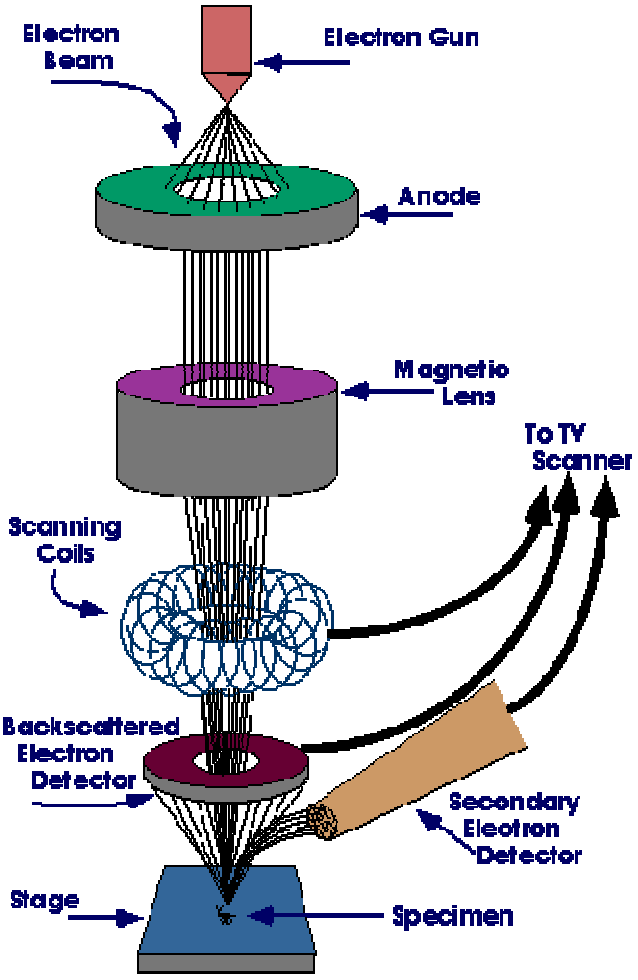

Figure 2.7: Schematic diagram of Scanning Electron Microscopy[Adopted from [25]] (Source: https://www.purdue.edu/ehps/rem/rs/sem.htm)

Thermionic tungsten filaments are widely used in SEM, whereas lanthanum hexaboride (LaB6) field emitter filaments are used in FESEM. In SEM, 3 KV

potential is applied to accelerate electrons however FESEM requires an applied potential of 30 KV. When the electron beam falls on the sample, it interacts with the sample surface and produces elastic and inelastic events. In inelastic scattering, the electrons that interact with the nucleus of an atom and deflect back are known as back scattered electrons (BSE). Electrons interact with atoms of the sample and transfer their energy in an inelastic event. This gives rise to auger electrons and secondary electrons (SE) and generate characteristic X-rays. Backscattered electron and secondary electron signals are processed to produce topographical images of a sample. These secondary and backscattered electrons play an important role for acquiring topographical images of the sample. The elemental identification is done by analyzing the characteristic X-rays produced. The X-rays are generated when high energy orbital electrons transfer to low energy orbitals after the electrons in the lower orbitals are removed by an incident beam of electrons. X-rays are then detected and provide characteristic information of elements present in the sample.

2.6 Transmission Electron Microscopy (TEM):

The schematic diagram of a transmission electron microscope is shown in Fig. 2.8.

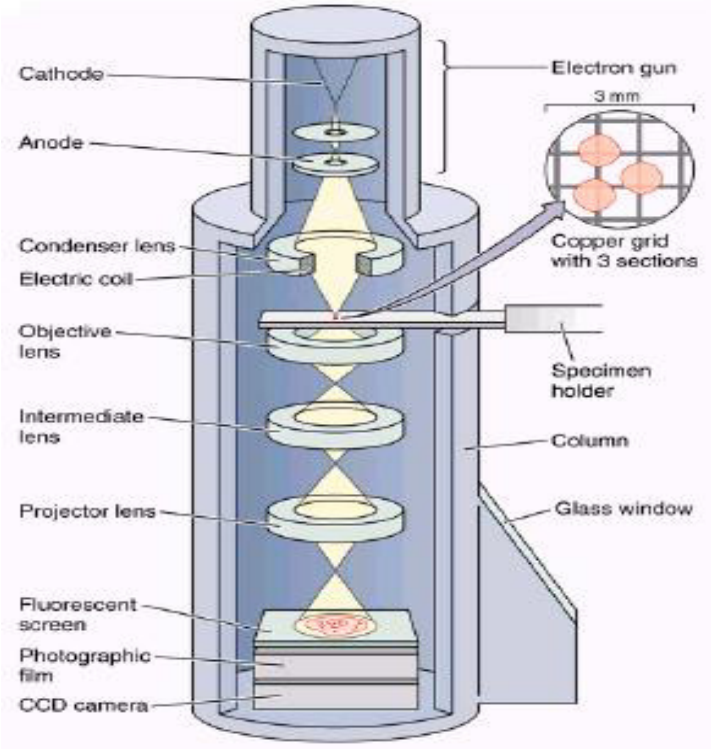

Figure 2.8: Schematic diagram of Transmission Electron Microscopy [Adopted from [26]] Source: http://www.ufrgs.br/imunovet/molecular_immunology/microscopy.html

The components of SEM and TEM are almost similar however difference is in applied accelerating voltage and working principle. The accelerating voltage of ~300 kV is used in TEM. In TEM, LaB_6 is used as field emitter. The atomic resolution is possible in TEM as high voltage (hundreds of kV) reduces de Broglies wavelength of an electron to a fraction of nanometer. TEM is an extremely powerful technique as it gives insight into many properties of sample like size, shape, crystal structure, lattice planes, localized defect, elemental analysis, and selected area electron diffraction (SAED). The transmitted electrons from the gun are focused through different lenses such as objective, intermediate and projector lens onto fluorescent screen [see Fig. 2.8] and thus image is produced. The projector lens decides whether it is low resolution TEM or high resolution TEM. Projector lens acquires only centrally transmitted beam of electrons in low resolution TEM however in HRTEM all transmitted beam are acquired. Therefore, HRTEM give high quality images. Elemental analysis of a sample can also be performed by EDAX.

2.7 Atomic force microscopy (AFM)

In 1986, Binnig and Quate invented atomic force microscope[27]. AFM gives atomic resolution of sample by analyzing the contour of a sample. Typical AFM schematic diagram is shown in Fig. 2.9.

Working principle: When a sharp tip (generally ~100-200 nm and 20-40 nm in radius of curvature) brought close to the sample then the force acting between sample surface and tip causes deflection in the spring. This deflection is then monitored optically. The image is obtained by quantifying forces between sample surface and cantilever tip (probe) [28]. Generally, AFM is used analyze the surface structure of thin films. AFM can be applied to almost all surface and measurements can be performed by sensing electrostatic, van der Waals, capillary, magnetic, and salvation forces. AFM is used to obtain particle size of nanoparticles, surface topography and 3D surface imaging of the thin films. AFM tapping mode gives information like grain size and its distribution and surface roughness etc.

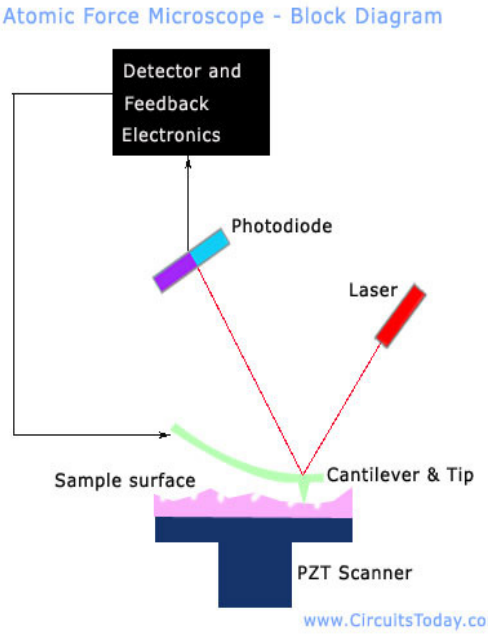

Figure 2.9: Schematic diagram of atomic force microscope[Adopted from [29]]

(http://www.circuitstoday.com/nanotechnology-tools-and-instruments)

2.8 Ultraviolet - Visible Spectroscopy:

UV spectroscopy is a very important non-destructive characterization technique used to study optical properties of semiconductors. The optical properties of samples can be studied by measuring transmittance/ reflectance/ absorption in UV visible region. The molecular interaction with electromagnetic radiation in this region deals with the electronic transition in the molecules which in turn relates to color of the sample.

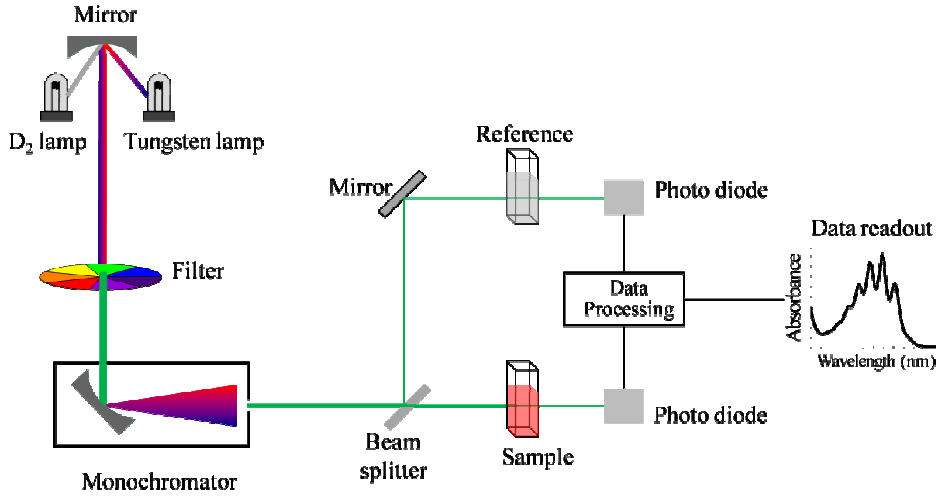

Figure 2.10: Schematic diagram of UV-Vis Spectrometer [Adopted from[30]]

(https://en.wikipedia.org/wiki/Ultraviolet%E2%80%93visible_spectroscopy)

An absorption spectrum of semiconductor nanomaterial is obtained when wavelength of incident light is greater than its band gap. UV visible spectrophotometer (Fig. 2.10) is used to acquire UV spectrum samples.

***Instrumentation*:** For UV visible measurement dual light source is used namely halogen or tungsten lamp (visible source) and Deuterium lamp (UV source) (see Fig. 2.10). These sources provide light of wavelength between (200 nm and 900 nm). The light of specific wavelength from monochromator is splitted into two by a beam splitter then one beam is directed through sample and other is through reference. Signals obtained from the sample and reference with respective detectors are further analyzed and processed and finally output signal is displayed on the monitor.

***Principle and Application*:** As discussed earlier, UV-VIS spectrometer can be operated in three different modes such as absorbance, reflectance and transmittance. The samples dispersed/dissolved in solvent or liquid samples can be measured in the absorbance mode. According to Lambert Beer's Law, absorbance is governed by the following expression:

$$I/I_0 = \exp(-kcl) \text{ or } I/I_0 = 10^{-\varepsilon cl} \quad (2.3)$$

Where, κ = constant (particular spectroscopic transition under consideration). ε = molar absorption coefficient, T = transmittance = I / I_0, ratio of intensity of incident radiation (I_0) to transmitted radiation (I). By inverting above equation and then taking logarithms, we get

$$\log\left(I_0/I\right) = \varepsilon cl = A \quad (2.4)$$

Where A = absorbance / optical density. Hence, absorbance of the sample is directly proportional its concentration. For powder samples or films, diffused reflectance mode of a spectrometer is used to analyze optical properties of samples. Band gap of a semiconductor can be calculated by using Tauc's plot. Tauc's plot is obtained from DRS spectrum by using the following expression:

$$[F(R)h\nu]^{1/n} \propto h\nu - E_g) \quad (2.5)$$

Where, $F(R) = \frac{(1-R)^2}{2R}$, n= ½ for direct band gap semiconductor and n=2 for indirect semiconductors. The band gap by extrapolating straight line to the tangent to plot obtained by plotting $[F(R)h\nu]^{1/n}$ vs hν[31].

2.9 Raman Spectroscopy:

Raman spectroscopy is a unique and non-destructive method of identification of samples. Raman spectroscopy deals with molecular rotation, vibration and other low frequency modes present. Like IR spectroscopy, Raman spectroscopic analysis also provides a molecular finger print hence very essential for identification of the molecule. It provides information of symmetry of molecule and vibrational frequency of chemical bond. It is also useful in material science for analysis of nanomaterials. Raman analysis of samples generates information like symmetry, orientation of crystallite, defects, stress induced in the system. The main advantage of this technique is that no sample preparation is required and very less amount of sample is needed because of the small dimension (1-100 µm dia.) of laser focus spot.

***Principle and instrumentation*:** In this technique, monochromatic light from a laser in the UV-VIS-IR range is focused on the sample which undergoes elastic (Rayleigh) or inelastic (Raman) scattering. Lasers such as Ar (632 nm), HeNe (514 nm), and diode (445-465 nm) are used in this technique. The laser beam is focused through a microscope on to the sample to a tiny spot. The electron cloud of a molecule is perturbed due to interaction with the electric component of the beam and excites it into a low or high rovibronic state which is also known as virtual state. There is an exchange of energy between a molecule and photon in inelastic scattering and scattered beam has either low or high value than the initial state.

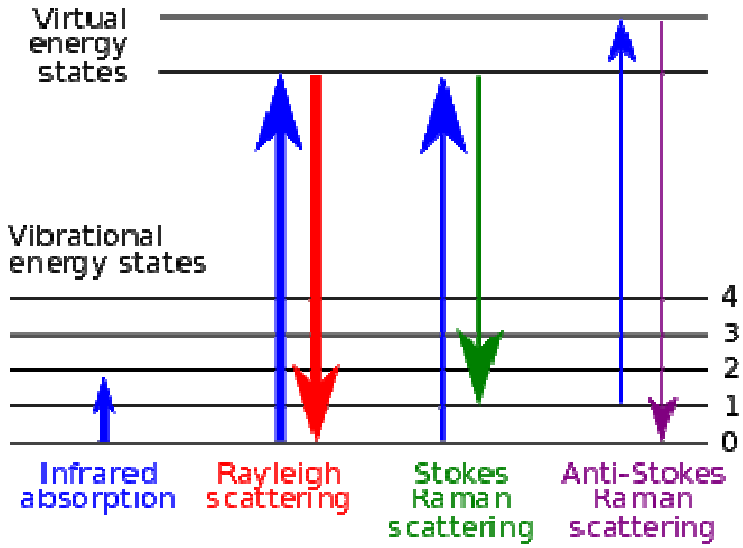

Figure 2.11: Energy level diagram for raman scattering[Adopted from[32]].

(https://en.wikipedia.org/wiki/Raman_spectroscopy)

The frequency difference between incident and scattered ray is known as *Raman shift.* If energy is gained by the system it is called as anti-stokes whereas if the system loses energy it is called as *stokes* [see Fig. 2.11]**.** Raman spectrum is plotted as the number of photons detected versus Raman shift. Only Raman scattering is passed through a lens and monochromator to the charge coupled detector (CCD) whereas the elastic scattering (Rayleigh scattering) is absorbed. Figure 2.12 shows schematic diagram of a Raman spectrometer.

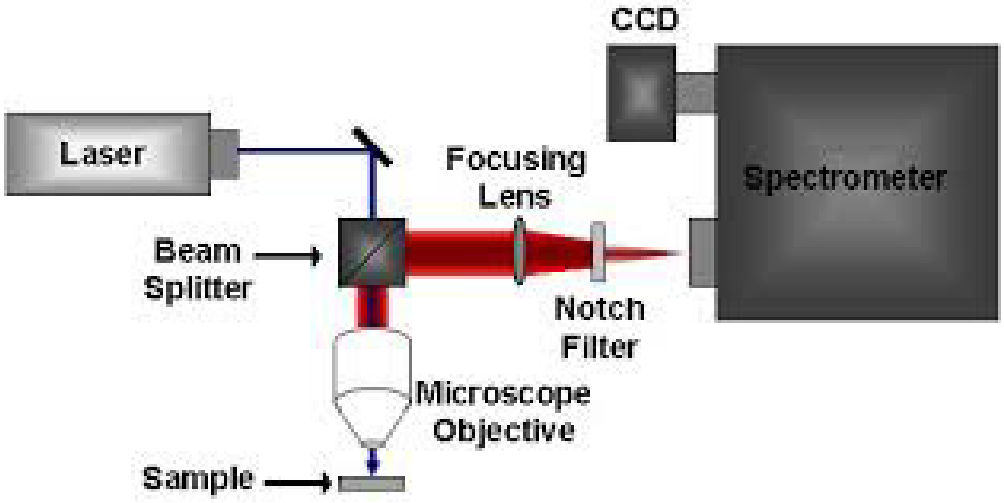

Figure 2.12: Schematic diagram of a Raman spectrometer[Adopted from [33]].

2.10 X-ray Photoelectron Spectroscopy (XPS):

X-ray Photoelectron Spectroscopy (XPS) is also known as *Electron Spectroscopy for Chemical Analysis* (ESCA). It is surface sensitive technique and provides surface finger print of sample. It is a quantitative technique hence used for investigation of surface composition, contamination and uniformity in the sample. XPS is especially popular for investigation of element's electronic and chemical state in the compound. It is regularly used for examination of almost all types of materials such as ceramics, organic inorganic compound, polymers, alloys, paper, glasses etc.

***Principle*:** The principle of this technique is based on the *photoelectric effect*. Every atom has unique characteristic properties like core binding energy of the electron. If photon energy supplied to the sample is greater than the binding energy of core

electron then core electron is ejected with greater energy than the binding energy known as photoelectron. The kinetic energy (K.E.) of photoelectron can be obtained by Einstein's equation is given below

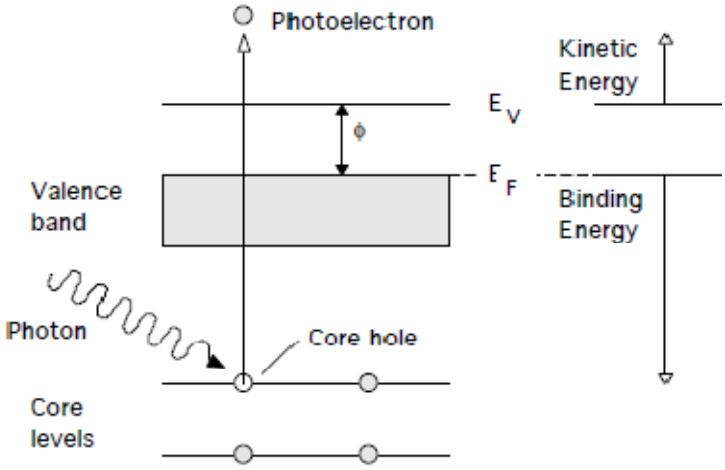

Figure 2.13: Schematic diagram of principle of X-ray photoelectron spectroscopy

$$h\nu = E_{K.E} + E_{B.E} + \varphi \tag{2.6}$$

$$E_{B.E} = h\nu - E_{K.E} - \varphi \tag{2.7}$$

Where, hν is X-ray photon energy, $E_{K.E.}$ is kinetic energy of the emitted electron measured by analyzer, ϕ is work function induced by the analyzer (4-5eV).

***Instrumentation*:** The schematic of XPS instrument is shown in figure 2.14. XPS is very special technique comprising electron energy analyzer, high vacuum assembly and fixed X-ray source. X-ray sources such as Al K_α (1486.6 eV) or Mg K_α (1253.6 eV) is used to obtain energy beam of ~10-15 KV. Sample surface is cleaned by irradiating Argon ions on sample which remove single layer of atoms and expose fresh surface of sample. The electrons are maintained in small orbit as opposite charges attract or repel them. Photoelectrons with certain energy are passed through oppositely charge plates maintained at high potential as too fast or slow electrons will crash with plates. Hence, spectrum arises as a result of a set of electrons with a known voltage.

***Interpretation of the spectrum*:** As discussed earlier, binding energy is a characteristic property of an element. The peak position of binding energy in the

spectrum is useful to identify which element is present in the sample and also which energy level photoelectrons are emitted. Hence, oxidation state of an atom can be determined. The chemical shift in binding energy is observed as a result of electronegativity effect or chemical bonding. Chemical shift is nothing but the chemical and physical environment associated with the element.

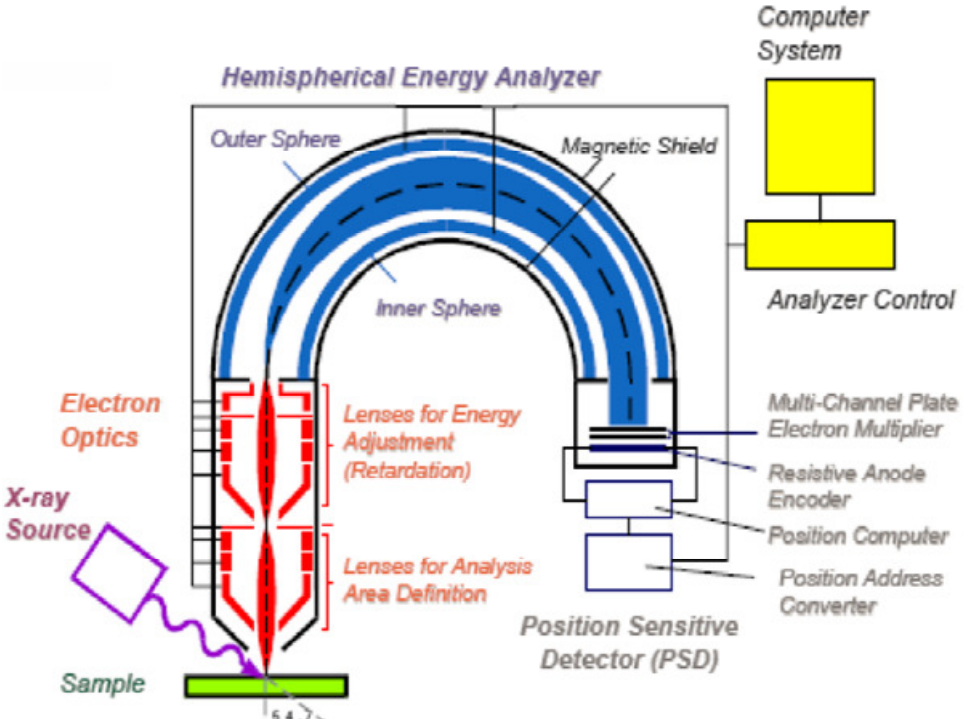

Figure 2.14: Instrumentation of XPS[Adopted from [34]].
(http://www2.cemr.wvu.edu/~wu/mae649/xps.pdf)

It is possible to analyze a doublet peak usually observed in the XPS spectrum due to spin orbital coupling of a certain element. Final state effect is observed due to weakening of screening of electrons that gives rise to *shake –up and shake off satellite* peaks. Quantitative elemental analysis of elements present in the sample can be obtained by calculating the area under the peaks. Investigation of chemical state and physical changes can be determined by Full width at half maxima (FWHM) peak. The broadening of FWHM of the peak is attributed to charging effect.

2.11 Gas sensing measurement Technique

The gas sensing properties of the sensor can be measured static or flow through measurement systems.

2.11.1. Static measurement system:

The schematic shown in Fig. 2.15 is used to measure static gas sensing study of sensor. The sensor under study is kept in an enclosed glass chamber of fixed volume having heating arrangement as shown in Fig. 2.15. The sensor is mounted on alumina plate having electrode arrangement and kept at the centre of the tube. The desired temperature is obtained by using thermocouple (k-type) kept near the sensor. The PID controller is used to control precisely temperature of sensor. The desired concentration of analyte is obtained by introducing known concentration of analyte using microsyringe into glass chamber. The outlet is used to pump out gas inside the chamber. The desired concentrations of analyte gases diluted in N_2 of purity (99.9%) were purchase from local vendor. The dry air is used as carrier gas for recovery process. The change in resistance /conductance of the sensor is measured by Keithley meter (Keithley 2612A). The recovery is obtained by exposing sensor to dry air.

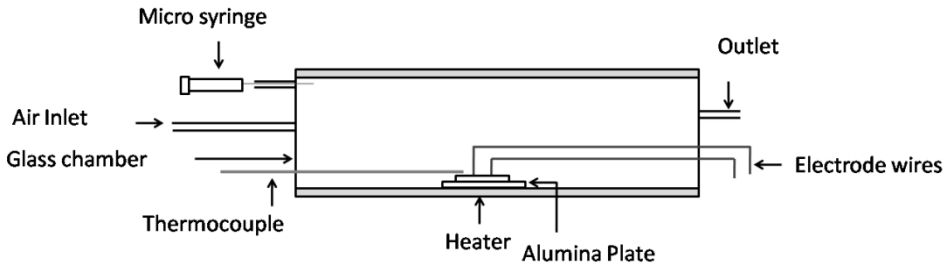

Figure 2.15: Static gas sensing measurement set up

2.11.2. Flow through measurement system:

In this system, the same gas sensor set up is used to study gas sensing properties. However, analyte of desired concentration is introduced by using Alicat mass flow controllers (USA make). Fig. 2.16 show typical flow through gas sensing measurement system.

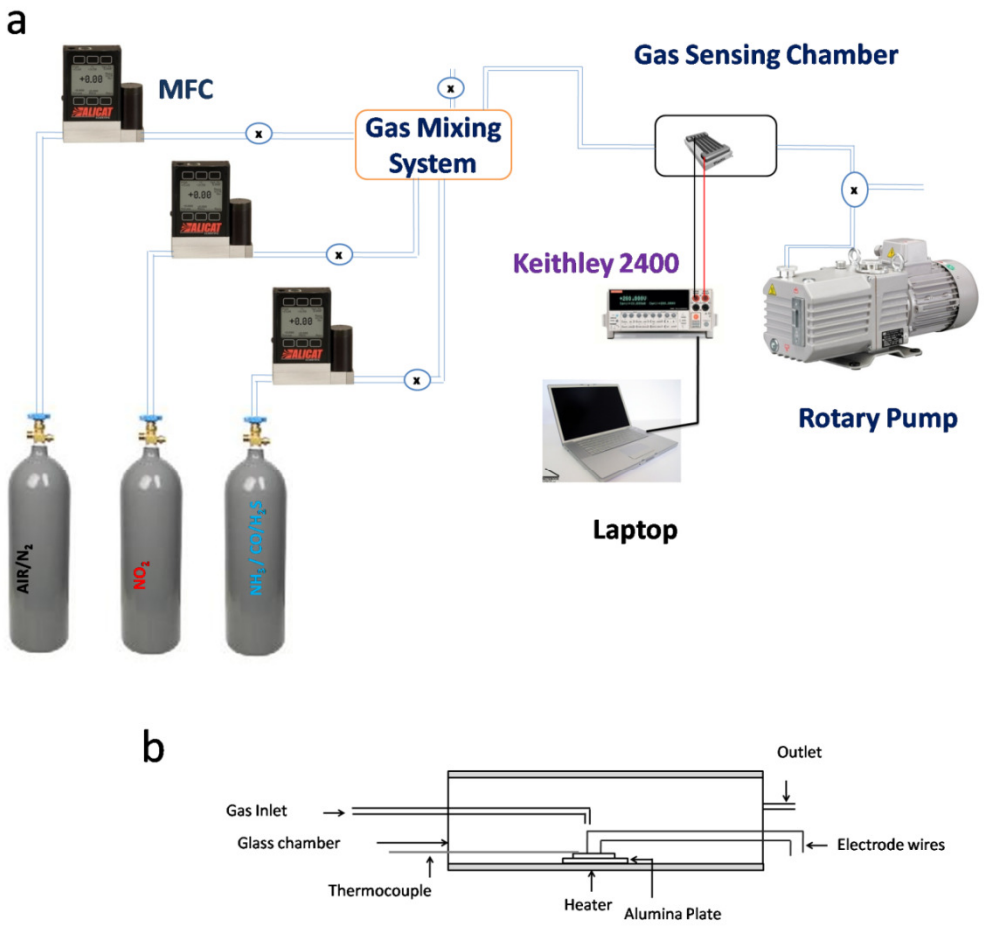

Figure 2.16: (a) Flow through gas sensing testing set up (b) enlarged view of gas sensing chamber.

2.12 References

[1] C.C. Koch, Ductility in nanostructured and ultra fine-grained materials: Recent evidence for optimism, Journal of Metastable and Nanocrystalline Materials, Trans Tech Publ 18 (2002), 9-20.

[2] A. Nakaruk, C. Sorrell, Conceptual model for spray pyrolysis mechanism: fabrication and annealing of titania thin films, J Coat Technol Res, 7(2010) 665-76.

[3] R. Chamberlin, J. Skarman, Chemical spray deposition process for inorganic films, J Electrochem Soc, 113(1966) 86-9.

[4] G. Korotcenkov, V. Brinzari, J. Schwank, M. DiBattista, A. Vasiliev, Peculiarities of SnO_2 thin film deposition by spray pyrolysis for gas sensor application, Sensors and Actuators B: Chemical, 77(2001) 244-52.

[5] G. Korotcenkov, A. Cerneavschi, V. Brinzari, A. Vasiliev, M. Ivanov, A. Cornet, J Moranteb, A. Cabotb, J. Arbiolb, In_2O_3 films deposited by spray pyrolysis as a material for ozone gas sensors, Sensors and Actuators B: Chemical, 99(2004) 297-303.

[6] E. Andrade, M. Miki-Yoshida, Growth, structure and optical characterization of high quality ZnO thin films obtained by spray pyrolysis, Thin Solid Films, 350(1999) 192-202.

[7] H. Koo, S. Hong, S. Ju, I. Seo, Y. Kang, $PbO–B_2O_3–SiO_2$ glass powders with spherical shape prepared by spray pyrolysis, J Non-Cryst Solids, 352(2006) 3270-4.

[8] G.L. Messing, S.C. Zhang, G.V. Jayanthi, Ceramic powder synthesis by spray pyrolysis, J Am Ceram Soc, 76(1993) 2707-26.

[9] S. Major, A. Banerjee, K. Chopra, Highly transparent and conducting indium-doped zinc oxide films by spray pyrolysis, Thin Solid Films, 108(1983) 333-40.

[10] D. Perednis, L. Gauckler, Solid oxide fuel cells with electrolytes prepared via spray pyrolysis, Solid State Ionics, 166(2004) 229-39.

[11] S.H. Ng, J. Wang, D. Wexler, S.Y. Chew, H.K. Liu, Amorphous carbon-coated silicon nanocomposites: a low-temperature synthesis via spray pyrolysis and their application as high-capacity anodes for lithium-ion batteries, The Journal of Physical Chemistry C, 111(2007) 11131-8.

[12] G. Blandenet, M. Court, Y. Lagarde, Thin layers deposited by the pyrosol process, Thin Solid Films, 77(1981) 81-90.

[13] L. Filipovic, S. Selberherr, G.C. Mutinati, E. Brunet, S. Steinhauer, A. Köck, et al., Methods of simulating thin film deposition using spray pyrolysis techniques, Microelectron Eng, 117(2014) 57-66..

14] K. Byrappa, M. Yoshimura, Handbook of hydrothermal technology: William Andrew; 2012.

[15] M. Yoshimura, W.L. Suchanek, K. Byrappa, Soft solution processing: A strategy for one-step processing of advanced inorganic materials, Mrs Bull, 25(2000) 17-25.

[16] K. Byrappa, T. Adschiri, Hydrothermal technology for nanotechnology, Progress in Crystal Growth and Characterization of Materials, 53(2007) 117-66.

[17] F. Xu, L. Sun, Solution-derived ZnO nanostructures for photoanodes of dye-sensitized solar cells, Energ Environ Sci, 4(2011) 818-41.

[18] M. Ristov, G. Sinadinovski, I. Grozdanov, M. Mitreski, Chemical deposition of tin (II) sulphide thin films, Thin Solid Films, 173(1989) 53-8.

[19] Y. Nicolau, Solution deposition of thin solid compound films by a successive ionic-layer adsorption and reaction process, Applications of Surface Science, 22(1985) 1061-74.

[20]R. Bhosale, Engineered Metal Oxide and Chalcogenide Nanomaterials for Sensitized Solar Cells and Solar Photoelectrochemical Water splitting, AcSIR thesis, 2015,

[21] P. Sudhagar, E.J. Juárez-Pérez, Y.S. Kang, I. Mora-Seró, Quantum Dot-Sensitized Solar Cells, Low-cost Nanomaterials, Springer, (2014) 89-136.

[22] B.E. Warren, X-ray Diffraction: Courier Corporation; 1969.

[23] C. Hammond, The basics of crystallography and diffraction: Oxford University Press Oxford; 2009.

[24]http://www.chemistryviews.org/details/ezine/2064331/100th_Anniversary_of_the_Discovery_of_X- ray_Diffraction.html

[25] https://www.purdue.edu/ehps/rem/rs/sem.htm

[26]Source: http://www.ufrgs.br/imunovet/molecular_immunology/microscopy.html

[27] G. Binnig, C.F. Quate, C. Gerber, Atomic force microscope, Phys Rev Lett, 56(1986) 930.

[28] S. Chatterjee, S.S. Gadad, T.K. Kundu, Atomic force microscopy, Resonance, 15(2010) 622-42.

[29]http://www.circuitstoday.com/nanotechnology-tools-and-instruments

[30]https://en.wikipedia.org/wiki/Ultraviolet%E2%80%93visible_spectroscopy

[31] O. Game, U. Singh, A.A. Gupta, A. Suryawanshi, A. Banpurkar, S. Ogale, Concurrent synthetic control of dopant (nitrogen) and defect complexes to realize broadband (UV–650 nm) absorption in ZnO nanorods for superior photo-electrochemical performance, J Mater Chem, 22(2012) 17302-10.

[32] https://en.wikipedia.org/wiki/Raman_spectroscopy

[33]http://cnx.org/contents/ba27839d-5042-4a40-afcf-0e6e39fb454@19.1:47/Surface-Enhanced-Raman-Spectro

[34]http://www2.cemr.wvu.edu/~wu/mae649/xps.pdf

Chapter 3

I: H_2S gas sensitive indium-doped ZnO thin films: Preparation and characterization

High quality indium-doped ZnO (IZO) thin films (~100 nm) have been deposited onto the glass substrates by using a conventional spray pyrolysis technique. Precursors such as zinc acetate, indium chloride with Brij-35 (polyoxyethylene lauryl ether) as a non-ionic surfactant were used. The morphology, crystal structure, elemental analysis and the gas response properties were investigated by using SEM, TEM, XRD, AFM and XPS techniques. The films show hexagonal wurtzite structure which reveal variations in (100), (002) and (101) intensities with indium doping. The crystallite size calculated by Scherrer formula was in the range of 30–50 nm. The SEM and AFM analysis show 50–70 nm sized grains, while the TEM confirms formation of grains in the range of ~10-50 nm sized particles. Their response towards various gases was measured at different operating temperatures and different levels of In-dopants. The 3 at% In-doped ZnO showed response as high as 13,000 for 1000 ppm H_2S at 250°C. It exhibited fast response (~2 s) and recovery time (~4 min). The gas response strongly depends on the morphology and indium concentration. The high gas response of IZO is explained on the basis of thickness dependent trap state density.

The content of this chapter has been published in "Sensors and Actuators B 143 (2009) 164–170,** Reproduced by permission of Elsevier*

http://www.sciencedirect.com/science/article/pii/S0925400509006868

3I.1 Introduction

It is highly important to detect and monitor various harmful and toxic gases/vapours such as H_2S, CO, SO_x, NO_x, alcohol and hydrocarbons for human and environmental safety. An enormous research has been going on to trace these harmful emissions. Semiconductors metal oxides such as ZnO, In_2O_3, and SnO_2 [1–5] etc. are highly useful in this context. Gas sensing properties of these oxides are based on the change in their electrical conductivity on exposure to the analyte gases. An optimum dopant modulated electronic properties increase the impact of oxygen partial pressure on the resistivity of semiconductor oxides. ZnO has been doped with various dopants such as Ga, Sn, Fe, Al, Cu, Ru, In, etc. for enhancing its applicability in piezoelectric devices, gas sensors, and the opto-electrical devices [6–9]. Hydrogen sulfide is a toxic and foul-smelling gas often produced in sewage, natural gas manufacturing, gasoline coal, coal oil, and natural gases. Hydrogen sulfide is highly toxic and leads to neurobehavioral toxicity and may even cause death on exposure to concentration >250 ppm [10]. Therefore, it is essential to develop H_2S gas sensors with high sensitivity, selectivity, fast response and recovery time. Such sensors, based on different oxides such as ZnO, CeO_2, SnO_2, αFe_2O_3, In_2O_3, WO_3, ZrO_2, have been reported[11–14]. However, most H_2S gas sensors are reported to operate well at high operating temperatures and room temperature response is realized only in a few cases [14,15]. Zinc oxide is a wide band gap (~3.4 eV) n-type semiconductor metal oxide having wurtzite structure and possesses potential applicability in the field of gas sensor[16-18]. The main advantage of ZnO is its high electron mobility and tunability into different morphologies. It is widely used in a transparent electrode for solar cells, acoustic wave devices and photovoltaic devices[19-23]. Doped and undoped ZnO films have been deposited by different techniques such as spray pyrolysis, plasma enhanced chemical vapour deposition, vacuum arc deposition, sputtering, sol–gel process, pulsed laser deposition, spin coating and dip coating [17,21,24-30]. Among these, spray pyrolysis technique is a simple and inexpensive technique having advantages such as high growth rate, mass production capability, reproducibility, and ease of doping various materials[31]. Generally, to obtain low resistive films, group III elements such as In, Al, Ga are mostly used as dopants which substitute Zn atom thereby releases free electrons and increase the carrier concentration[9,32]. Search through literature suggests a scope to study the detailed properties of these materials

for their applicability part such as gas response[9,33–36]. More significantly, the effect of precursors, deposition temperature, thickness, dopants and their concentrations needs further study. In the present work, we have studied gas sensing properties of ZnO and IZO thin films prepared by spray pyrolysis on the glass substrate.

3I.2. Experimental

3I.2.1. Synthesis

The chemicals such as zinc acetate dihydrate, indium (III) chloride (99.9% Merck), Brij-35 (polyoxyethylene lauryl ether), ethanol (A.R.) were used without further purification. In a typical synthesis ZnO films are deposited as follows; zinc acetate dihydrate was dissolved in the mixture of ethanol (10 ml) and distilled water (5 ml). This solution was then added drop-wise to the 1% solution of Brij-35 in ethanol to obtain 0.1 M zinc acetate solution. Such solution was used for the spray pyrolysis onto the cleaned glass substrate maintained at 475°C. Prior to use, the glass substrates were cleaned by soap solution, boiled in hydrochloric acid for 30 min, and finally ultrasonically washed in the distilled water for 15 min. Similarly, IZO thin films deposition was carried out by using atomic ratio of [In/Zn] = 1, 3, 5 at% (the percentage refers to those in the spray solution). The as deposited films were subjected to post deposition annealing at 475°C for 5 h in air to obtain highly uniform crystalline films. Simultaneously 10 substrates (2.5 cm × 2.5 cm) in a batch were deposited by spray pyrolysis technique.

3I.2.2. Morphological and structural analysis

The crystalline structure of the thin films was confirmed by using XRD (‘X’ PertPro) operating at a voltage of 30 kV diffractometer with Cu Kα (λ = 0.154056 nm) radiation in the range of 25°–75°. The average crystallite sizes (D) of ZnO and IZO films were calculated by using the Scherrer formula (see Eq.2.2). The study of surface morphology was performed using field emission scanning electron microscopic (FESEM) images captured by a Nova NanoSEM 450 model. The transmission electron microscopy (TEM) and high-resolution transmission electron microscopy (HRTEM) were obtained on a Tecnai F30 FEG machine operated at 300 kV. The atomic force microscopic (AFM) images of the undoped and 3 at% In-doped ZnO thin

films were captured by using a NanoScope IV Multimode scanning probe microscope of VEECO Inc. unit. The thickness of the deposited films was measured with AMBIOS MAKE XP-1 Surface Profiler, Make, USA, Version 5.5.5 between the ranges 10 Å–100 μm. The elemental analysis was carried out by the X-ray photoelectron spectroscopy (XPS); VG Micro Tech ESCA 3000 instrument at a pressure of $>1\times10^{-9}$ Torr (pass energy of 50 eV, electron take off angle 60°, and overall resolution 1 eV).

3I.2.3. Gas response measurements

The ZnO and IZO thin films deposited by the spray pyrolysis were randomly selected for finding their gas responses. Their response was found by connecting through the gold electrodes. A stabilized constant DC voltage was applied through Aplab 7212 (India) DC power supply and the current was measured by the Keithely485 autoranging picoammeter. The gas response of the ZnO and IZO films were tested at different operating temperatures in the dynamic mode described earlier [37]. Air with controlled rate was used as a carrier gas; the known amount of different test gases was introduced to achieve the desired part per million (ppm) level of concentration. The gas response of the sensor element (S) was calculated as the ratio of resistance of film in the air (R_a) to the resistance in the test gas (R_g).

$$S = \frac{R_a}{R_g} \qquad \text{(3I.1)}$$

3I.3. Results and discussion

3I.3.1. Structural properties

Fig. 3I.1 shows XRD patterns of undoped and indium-doped zinc oxide thin films deposited at 475°C on the glass substrate. Undoped zinc oxide film shows a prominent peak at (002) plane along with weak intensity peaks corresponding to (100) and (101) indicating (002) as the preferential orientation plane. On doping with 1 at% indium (1% IZO), intensities of all the peaks gets reduced indicating their lower crystallinity as compared with the undoped zinc oxide film, while 3% and 5% IZO

films show enhancement in intensities of all the peaks thus indicating their higher crystallinity. It is observed that all the compositions exhibit (002) as a preferred orientation plane with 5% IZO film exhibiting highest crystallinity. We also observed that the intensity of (101) peak increases on 5 at% indium doping. The change in orientation from (002) to (101) with increase in indium concentration has earlier been reported [25,38], however, we observed this phenomenon only in 5% IZO.

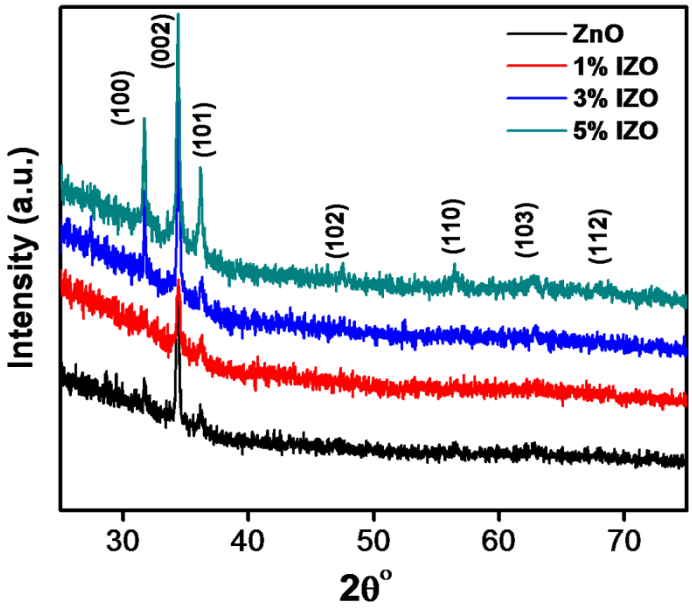

Figure 3I.1: XRD patterns of undoped and indium-doped zinc oxide thin film deposited at 475°C.

We report intensity ratios of (100)/(002) and (101)/(002) in the Table 3I.1 to understand the effect of indium doping in the growth of crystallinity.

Table 3I.1: Ratio of intensities for different planes of undoped and IZO films.

Composition	100/002	101/002	Crystallite size (nm)
ZnO	0.23	0.19	32
1% IZO	0.30	0.36	36
3% IZO	0.40	0.12	48
5% IZO	0.48	0.38	39

It shows that in undoped ZnO (100)/(002) ratio is 0.23 which is lowest indicating highest orientation of c-axis in undoped ZnO while IZO films show increase in this ratio with increase in indium concentration, suggesting (100) orientation with indium doping. However, on comparison with (101)/(002) intensity ratios, it is observed that 3% IZO has highest orientation of (002) as compared with (101) plane.

3I.3.2. Morphological properties

Fig. 3I.2 shows FESEM images of ZnO and IZO films deposited onto the glass at 475°C. The undoped ZnO film shows uniform grains and grain size observed to be reduced in1% IZO film. Interestingly, the grains grow distinctly (size 50–70 nm) as the percentage of indium increased from 1 to 3 at%. On further doping (5% In) the grain size have increased with grains having irregular size and shape. Although the X-ray diffraction patterns indicate that with increase in indium concentration from 3 to 5%; the crystallite size decreases from 48 to 39 nm, increase in the grain size observed in the FESEM images may be attributed to the agglomeration of the smaller particles which could not be resolved due to the limitations of SEM instrument.

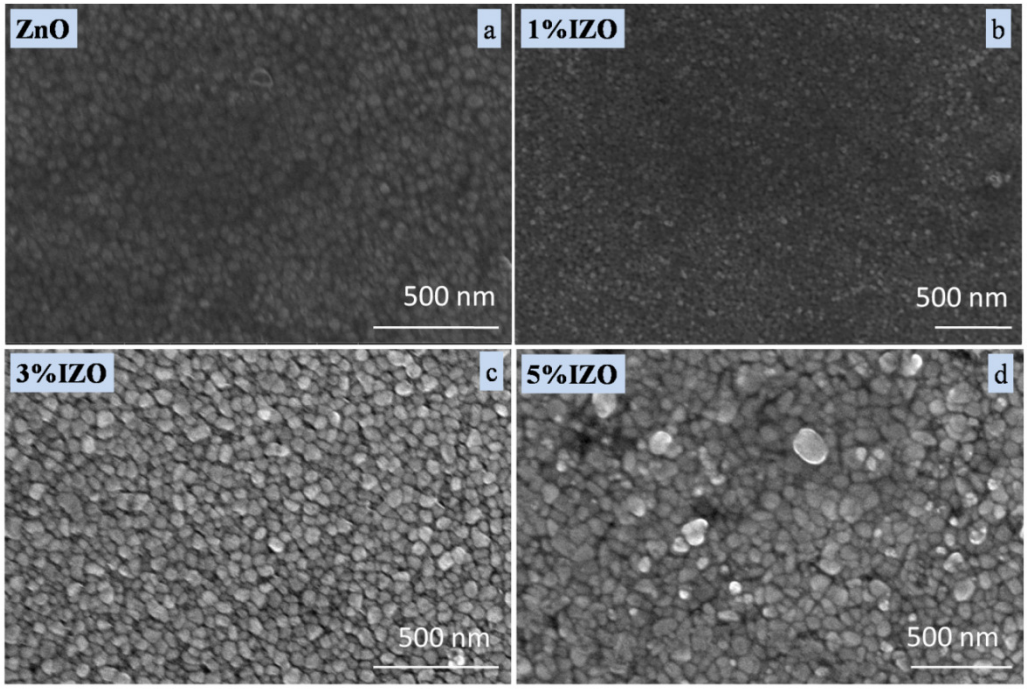

Figure 3I.2:SEM micrographs of undoped and indium-doped zinc oxide films deposited at 475 ◦C (a) undoped ZnO, (b) 1% IZO, (c) 3% IZO and (d) 5% IZO.

The TEM analysis of 3% IZO film (Fig. 3I.3a) clearly shows particles of ~10-50 nm size. Their uniform distribution indicates that by spray pyrolysis it is possible to deposit IZO film with nanosized particles. Moreover, our results regarding grain size

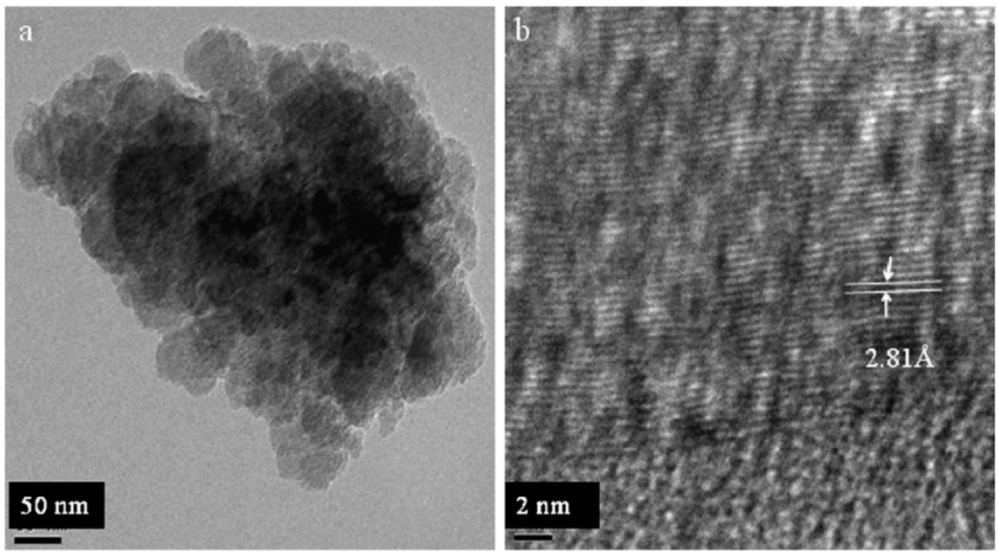

Figure 3I.3: (a) Low-magnification TEM image and (b) High-magnification TEM image of 3% IZO.

match well with the value reported in transmission electron microscopy results on indium-doped ZnO thin films deposited by spray pyrolysis[25]. More significantly, the thin films we report herewith have thickness of only ~100 nm and hence uniformity and their nanosize play a crucial role. The HRTEM image of 3% IZO film (Fig. 3I.3b) reveals fringes of (100) planes with the lattice spacing of 0.281 nm between two adjacent planes indicating (100) as a growth direction. AFM imaging of the undoped and 3% IZO film surface deposited on silicon substrate at 475°C temperature are shown in Fig. 3I.4. AFM characterization (Fig. 3I.4 (a, b)) of these films reveal a granular, polycrystalline morphology with good uniformity in grain size (~60 nm) in 3% IZO then undoped ZnO. The only difference seen is the sharper growth of ZnO towards z-axis as compared with blunt heads as seen in the 3% IZO films. The change in the morphology can be attributed to the microstructural changes that are directly attributed to the presence of the indium. The AFM image shows grain size nearly similar to that obtained by SEM. The marginal change in the morphology can be attributed to change in substrate from glass to silicon.

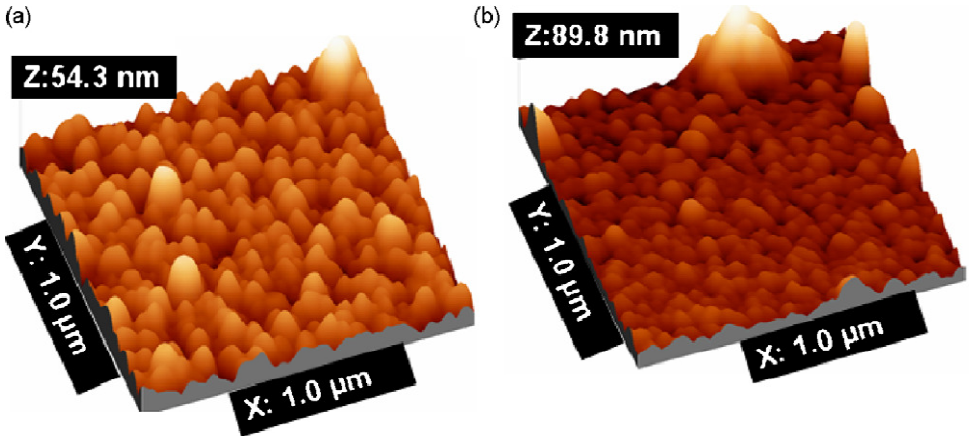

Figure 3I.4: Atomic force microscopic images of undoped ZnO (a) and 3% IZO (b) films deposited at 475°C.

3I.3.3. X-ray photoelectron spectroscopic studies

Further evidence of quality and composition of films was investigated by the X-ray photoelectron spectroscopic studies. The binding energy obtained in the XPS analysis

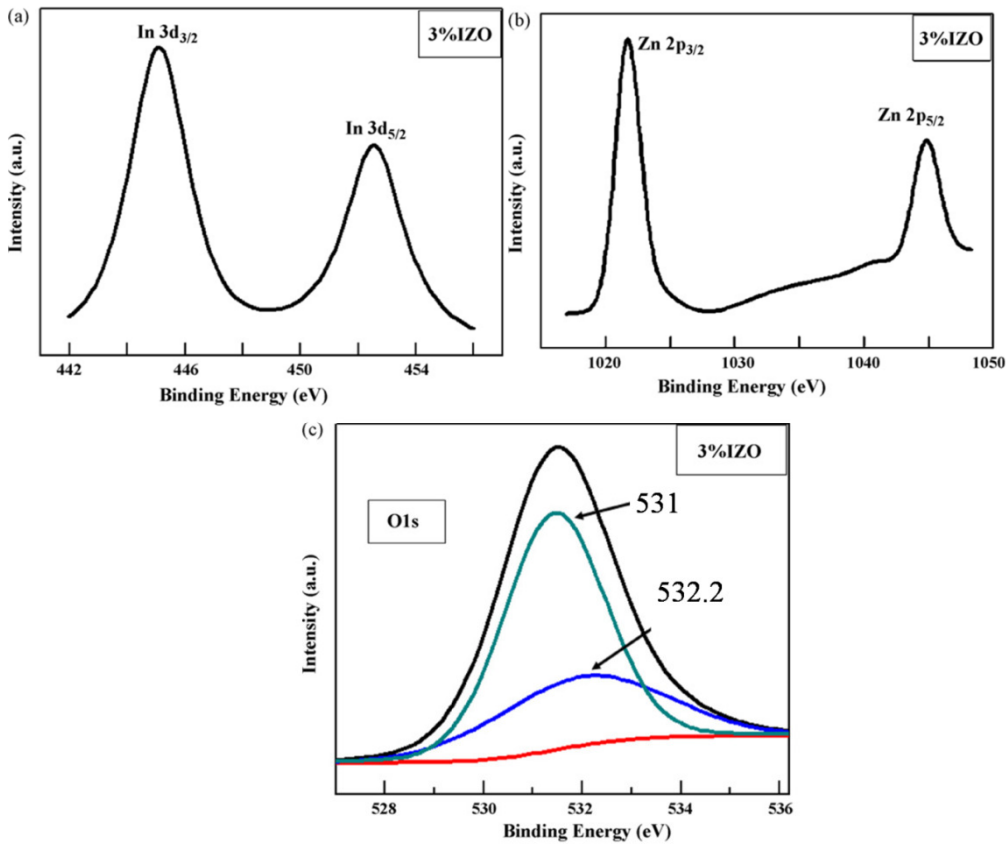

Figure 3I.5: XPS analysis of the 3% IZO thin film of In region (a), Zn region (b) and O region (c).

was corrected for the specimen charging by referring the C 1s to 284.6 eV. Fig. 3I.5 shows X-ray photoelectron spectra of In, Zn, and O region of 3% IZO film deposited on the glass substrate at 475°C. Fig. 3I.5(a) shows peaks at 445.1 and 452.3 eV corresponding to In $3d_{3/2}$ and In $3d_{5/2}$, respectively, confirming the presence of indium in the doped ZnO film. Fig. 3I.5(b) shows strong peaks at 1021.74 and 1044.77 eV which are typical peaks corresponding to Zn $2p_{3/2}$ and Zn $2p_{1/2}$ [29]. Fig. 3I.5(c) shows O1s signal illustrating major peak maxima at binding energy 531.53 eV which can be deconvoluted in to two peaks at binding energies of 531.47 and 532.24 eV. The major peak at 531.47 eV corresponds to the O^{-2} in the ZnO, whereas the weaker peak at 532.24 eV is due to the chemisorbed oxygen caused by surface hydroxyl group corresponding to O–H bonds [41]. The spectrum does not show any peak corresponding to the other element or impurity.

3I.3.4. Gas response properties

It is known that the gas response gets significantly influenced by the surface morphology, crystallinity, amount of additives and operating temperature of semiconducting oxides. The undoped and IZO thin films were examined for finding their response towards various reducing and oxidizing gases. All the films have been tested for gases, such as H_2S, NH_3, CO, H_2, NO_x, liquid petroleum gas (LPG) and ethanol vapors for their 1000 ppm concentrations, at operating temperatures ranging from 50 to 350°C. It is observed that ZnO as well as all the IZO films show poor response ($S < 30$) towards these test gases; interestingly, only 3% IZO exhibits exceptionally high response towards H_2S gas at 250°C. Fig. 3I.6(a) shows histogram of 3% IZO indicating its selectivity towards 1000 ppm of various test gases at 250°C. It clearly shows that except hydrogen sulfide gas, it displays negligible response towards ethanol vapors ($S = 30$), LPG ($S = 15.8$), carbon monoxide (1.5), hydrogen (11) and no response towards ammonia and nitric oxide gas. Such a unique and exceptionally high response of $S = 13{,}000$ indicates amazing selectivity towards hydrogen sulfide of this film at low operating temperature of 250°C. In order to determine the optimum operating temperature and the amount of indium, the responses of all the compositions were tested for 1000 ppm of H_2S gas at the operating temperatures from 50 to 350°C.

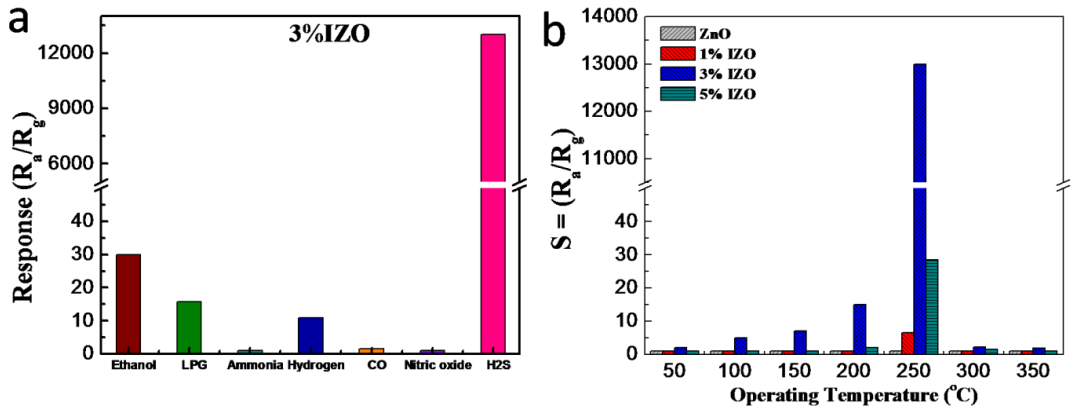

Figure 3I.6: (a) Histogram indicating selectivity of 3% IZO thin film for 1000 ppm of various gases at 250°C, (b) Variations in the response towards 1000 ppm of H_2S gas with operating temperatures for undoped ZnO and 1, 3, 5 at% of indium in ZnO.

The histogram (Fig. 3I.6b) reveals that the response not only changes with the concentration of indium but also the operating temperature. It is observed that 3% IZO show enhancement in response with operating temperatures and attains a maximum response at 250°C. Interestingly, its response towards H_2S decreases markedly with further increase in temperature. Undoped ZnO film does not show any response towards hydrogen sulfide gas while 1% IZO and 5% IZO do show low response of S = 6.5 and 28.4, respectively. As remarkably high response has been exhibited by 3% IZO; the detailed studies of the same was carried out by varying concentration of the H_2S gas.

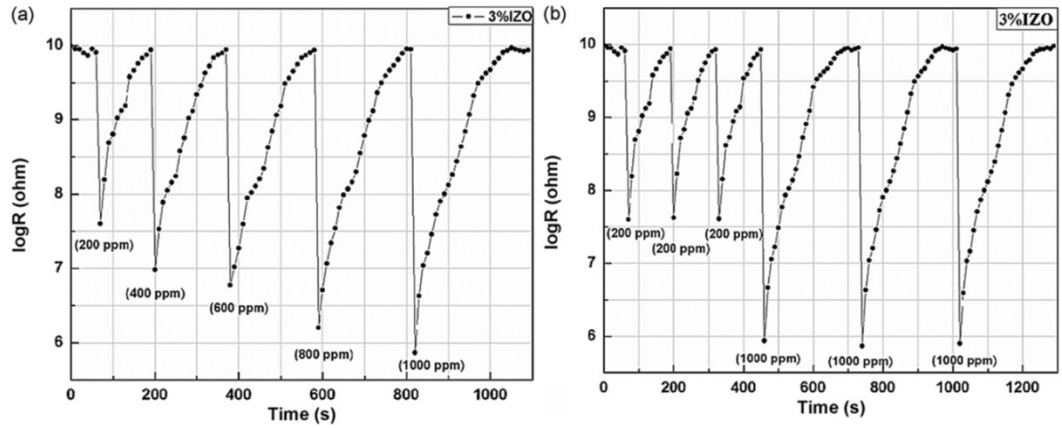

Figure 3I.7: (a) Variations in response with concentration of H_2S gas at 250°C. (b) Cyclic stability of 3% IZO at 250°C for 200 and 1000 ppm of H_2S gas concentration.

Fig. 3I.7(a) shows response and recovery behavior of 3% IZO film for 200–1000 ppm of H_2S concentration at 250°C. In the present study we report 100% response and 100% recovery time. It is interesting to find 100% recovery after every cycle, showing its potential as an ideal H_2S gas sensor. As obvious, the response increases with the increase in the H_2S concentration. The other advantage exhibited is the fast response (~2 s) and recovery time (~4 min) indicating again its high prospective as a sensor for the commercial application. Fig. 3I.7(b) indicates the cyclic stability of the sensor.

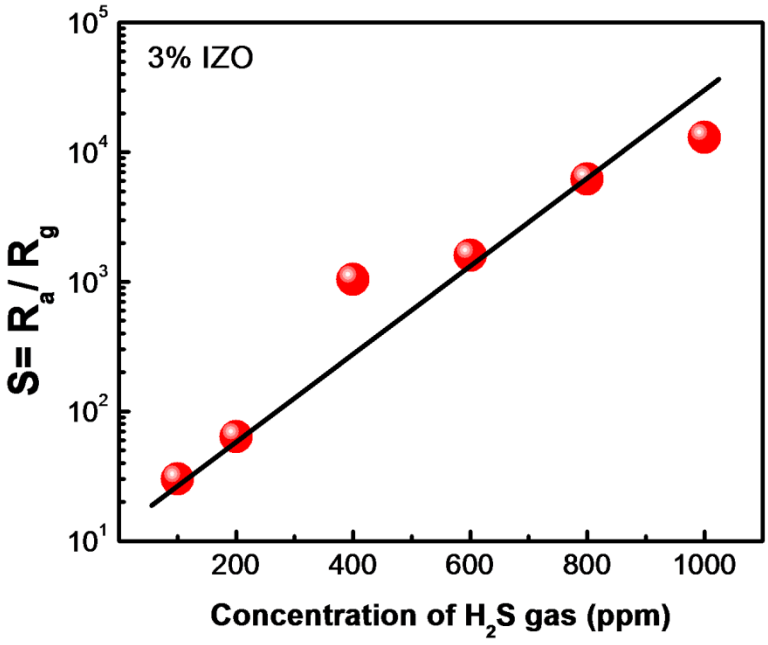

Figure 3I.8: Response (S) with gas concentration of 3% IZO at 250°C.

Figure 3I.8 shows variations in response of 3% IZO film with concentration of H_2S at 250°C, indicating logarithmic increase with the concentration of H_2S. It is well known that the gas sensing mechanism in the oxide based materials is surface controlled, wherein; the grain size, surface states and oxygen adsorption play a significant role. The larger surface area usually offers more adsorption–desorption sites and thus the enhanced sensitivity [42,43]. The atmospheric oxygen gets adsorbed on the surface, and depending upon the temperature of operation; different oxygen species are formed on the surface. The gas response by metal oxide semiconductor, in general, can be described as

$$O_{2(gas)} + 2e \rightarrow 2O_{ads}^{-} \qquad (3I.2)$$

$$R + O_{ad}^{-} \rightarrow RO + e \quad (3I.3)$$

Initially, (Eq. (3I.2)) the atmospheric oxygen acquires electron from the conduction band of ZnO and forms O_{ads}^{-} species on the surface thus decreasing the conductance of the ZnO. In the presently used IZO, the doping of In^{3+} increases the conductivity of ZnO due to enhancement in the electron density. Thus, in IZO films, the In^{3+}facilitates formation of more number of O_{ads}^{-} species. Further, the high surfaces to volume ratio of nanosized (~10 nm) particles offer larger number of sites for the adsorption of the oxygen species. It is known that the gas response depends directly on the number of O_{ads}^{-} species. The reducing gas (R), reacts with O_{ads}^{-} and forms RO (Eq. (3I.3)) with releases of electron back to the conduction band. In the process the conductance again increases. Therefore, gas response in general, depends on the reaction (Eq. (3I.3)) that is, availability of R and O_{ads}^{-} species. The rejuvenation of the conductance takes place on removal of R and the presence of ambient oxygen(Eq. (3I.2)).

More specifically, in the presence of H_2S gas, the reaction (Eq.(3I.4)) takes place thereby forms H_2O and SO_2 gas by releasing electrons back to the conduction band, thus increasing the conductance of the sensor. Again on removal of H_2S, the reaction (Eq. (3.2)) takes place leading to a decrease in the conductance.

$$H_2S_{ads} + 3O_{ads}^{-} \longrightarrow H_2O + SO_2 + 3e \quad (3I.4)$$

It has been known that at higher temperatures and in the air the increase in resistivity is due to the chemisorption of oxygen at the grain boundaries, which in turn leads to the formation of extrinsic trap states localized at the grain boundaries. Major et al.[44] have reported a correlation of crystal orientation, grain boundaries and film thickness on the density of trap states formed due to chemisorbed oxygen in the IZO films deposited by the spray pyrolysis. Such states trap free electrons from the bulk of the grain to create a potential barrier by causing depletion in the region adjacent to the grain boundaries. Such potential barriers also decrease the mobility of the carrier.

It is known that the thickness causes immense influence on the resistivity of the film. For the thickness greater than 100 nm a gradual decrease in the resistivity (ρ) has been earlier reported in IZO thin films [44], which were found to reach to its saturation at ~

1000 nm thickness. More importantly, they observed a sharp increase in the resistance in films having thickness less than 100 nm. Such increase in the resistivity (ρ) was attributed to the decrease in the carrier concentration (N) and mobility (μ) caused due to the increased trap state density. The thickness dependent trap state density was attributed to the increase in resistivity of the film with a decrease in the thickness caused by enhanced localized trap states of the grain boundaries. Such a change can be expected due to the thickness dependent crystal orientation. In the present work, we report thin films deposited using a non-ionic polyoxyethylene lauryl ether (Brij-35) as a surfactant which promotes dehydroxylation and crystallize the sample above 400°C. The surfactant facilitates formation of high surface area thin films with the crystallite size considerably smaller than that of the films reported by the conventional precursors. In our studies on undoped ZnO and 1, 3, 5% IZO, we observe film thickness of about 100 nm having crystallite size between 30 and 50 nm and particle size of ~10 nm with different orientations. More precisely, the 3% IZO films show highest crystallite, with maximum uniformity in grain size and exhibits highest response (S = 13,000) towards H_2S gas. It is interesting to find that owing to the extremely degenerate nature, the 3% IZO is not affected by exposure to high temperature and therefore exhibit better thermal stability which is ideal for a good sensor. The orientation ratio of (101)/(002) is lowest in 3% IZO as compared with undoped and 1, 5% IZO. In contradiction to earlier reports [25,38], showing change in orientation from (002) to (101) with increase in indium concentration. However, all such findings are related to films having thickness higher than 500 nm. This clearly indicates that the growth direction, thickness along with the concentration of indium plays an important role in deciding the H_2S gas response. The highest response at 250°C, is found to decrease with the increase in the operating temperature up to 350°C. The increase in resistance at lower temperature is attributed to the chemisorbed oxygen on the surface causing decrease in the carrier concentration, while at higher temperatures the decrease in the resistance is due to the increase in the carrier concentration as result of activation of deep donors occur due to native defects such as interstitial zinc and oxygen vacancies. Hence, at the higher operating temperatures the apparent ratio of change in resistance with and without presence of reducing gas is lower than that observed in the lower temperature. According to Hard soft acid base (HSAB) concept, In^{3+} may be acts as an active site for adsorption for

sulfur compare to Zn^{2+} and lowering activation energy of its adsorption leads to selectively high response for In-doped ZnO film.

3I.4. Conclusions

It can be concluded that the use of non-ionic surfactant (Brij-35) helps to obtain 100 nm thick films of undoped and indium-doped zinc oxide by a simple spray pyrolysis technique at 475 °C. The films are comprised of uniformly distributed nanosized particles. The XRD, SEM, XPS, AFM, TEM and film thickness studies reveal features of the nanosized materials, facilitating the excellent gas response towards hydrogen sulfide gas. The 3% IZO film exhibits maximum response towards H_2S gas. More significantly, it shows 4 order change in response (S = 13000) to 1000 ppm concentration of H_2S with fast response (~2 s) and recovery time (~4 min). The increase in surface area due to use of the surfactant and the presence of 3 at% indium in zinc oxide induces such high response towards the hydrogen sulfide gas at 250°C. The high selectivity towards H_2S is due to optimized amount of indium and film morphology; however, it needs more detailed investigations for understanding such a selective response. It can be concluded that nanosized indium-doped zinc oxide thin film could be a good candidate material for H_2S gas sensing device.

3I.5 References

[1] G. Sberveglieri, Recent developments in semiconducting thin-film gas sensors, Sens. Actuators B 23 (1995) 103–109.

[2] N. Yamazoe, New approaches for improving semiconductor gas sensors, Sens. Actuators B 5 (1991) 7–19.

[3] A.P. Chatterjee, P. Mitra, A.K. Mukhopadhyay, Chemically deposited zinc oxide thin film gas sensor, J. Mater. Sci. 34 (1999) 4225–4231.

[4] J. Xu, X. Wang, J. Shen, Hydrothermal synthesis of In_2O_3 for detecting H_2S in air, Sens. Actuators B 115 (2006) 642–646.

[5] D. Vuong, G. Sakai, K. Shimanoe, N. Yamazoe, Hydrogen sulfide gas sensing properties of thin films derived from SnO_2 sols different in grain size, Sens. Actuators B 105 (2005) 437–442.

[6] D.F. Paraguay, M. Miki-Yoshida, J. Morales, J. Solis, L.W. Estrada, Influence of Al, In, Cu, Fe and Sn dopants on the response of thin film ZnO gas sensor to ethanol vapor, Thin Solid Films 373 (2000) 137–140.

[7] M. Aslam, V.A. Chaudhary, I.S. Mulla, S.R. Sainkar, A.B. Mandale, A.A. Belhekar, K. Vijayamohanan, A highly selective ammonia gas sensor using surface ruthenated zinc oxide, Sens. Actuators A 75 (1999) 162–167.

[8] S.C. Navale, V. Ravi, I.S. Mulla, S.W. Gosavi, S.K. Kulkarni, Low temperature synthesis and NO_x sensing properties of nanostructured Al-doped ZnO, Sens. Actuators B 126 (2007) 382–386.

[9] M. Olvera, H. Gomez, A. Maldonado, Doping, vacuum annealing, and thickness effect on the physical properties of zinc oxide films deposited by spray pyrolysis, Sol. Energy Mater. Sol. Cells 91 (2007) 1449–1453.

[10] A.B. Bodade, A.M. Bende, G.N. Chaudhary, Synthesis and characterization of CdO-doped nanocrystalline ZnO:TiO2-based H_2S gas sensor, Vacuum 82 (2008) 588–593.

[11] C. Rout, M. Hegde, C.N.R. Rao, H_2S sensors based on tungsten oxide nanostructures, Sens. Actuators B 128 (2008) 488–493.

[12] Y. Wang, Y. Wang, J. Cao, F. Kong, H. Xia, J. Zhang, B. Zhu, S. Wang, S. Wu, Low-temperatureH_2S sensors based on Ag-doped-Fe2O3 nanoparticles, Sens. Actuators B 131 (2008) 183–189.

[13] C.M. Ghimbeu, M. Lumbreras, M. Siadat, R.C. van Landschoot, J. Schoonman, Electrostatic sprayed SnO_2 and Cu-doped SnO_2 films for H_2S detection, Sens. Actuators B 133 (2008) 694–698.

[14] Z. Zeng, K. Wang, Z. Zhang, J. Chen, W. Zhou, The detection of H_2S at room temperature by using individual indium oxide nanowire transistors, Nanotechnology 20 (2009) 045503 (4 pp.).

[15] R.S. Niranjan, V.A. Chaudhary, I.S. Mulla, K. Vijayamohanan, A novel hydrogen sulfide room temperature sensor based on copper nanocluster functionalized tin oxide thin films, Sens. Actuators B 85 (2000) 26–32.

[16] D.P. Norton, Y.W. Heo, M.P. Ivill, K. Ip, S.J. Pearton, M.F. Chisholm, T. Steiner, ZnO: growth, doping and processing, Mater. Today (2004) 34–40.

[17] P.P. Sahay, S. Tewari, Sprayed ZnO thin films for ethanol sensors, J. Mater. Sci. 40 (2005) 4791–4793.

[18] N. Koshizaki, T. Oyama, Sensing characteristics of ZnO-based NO_x sensor, Sens. Actuators B 66 (2000) 119–121.

[19] T. Mizuta, T. Ishibashi, T. Minemoto, H. Takakura, Y. Hamakawa, Chemical deposition of zinc oxide thin films on silicon substrate, Thin Solid Films 515 (2006) 2458–2463.

[20] W.J. Jeong, S.K. Kim, G.C. Park, Preparation and characteristic of ZnO thin film with high and low resistivity for an application of solar cell, Thin Solid Films 506/507 (2006) 180–183.

[21] B. Rech, T. Repmann, S. Wieder, M. Ruske, U. Stephan, A new concept for mass production of large area thin-film silicon solar cells on glass, Thin Solid Films 502 (2006) 300–305.

[22] H.P. Loebl, C. Metzmacher, R.F. Milsom, P. Lok, F. Van Straten, A. Tuinhout, RFbulk acoustic wave resonators and filters, J. Electroceram. 12 (2004) 109–118.

[23] P. Nunes, E. Fortunato, P. Tonello, F. Braz Fernandes, P. Vilarinho, R. Martins, Effect of different dopant elements on the properties of ZnO thin films, Vacuum 64 (2002) 281–285.

[24] M.N. Islam, M.O. Hakim, H. Rahman, The effects of deposition variables on spray-deposited ZnO thin film prepared from Zn $(C_2H_3O_2)_2$, J. Mater. Sci. 22 (1987) 1379–1384.

[25] S. Major, A. Banerjee, K.L. Chopra, Highly transparent and conducting indiumdopedzinc oxide films by spray pyrolysis, Thin Solid Films 108 (1983) 333–340.

[26] N.S. Ramgir, Y.K. Hwang, S.H. Jhung, H. Kim, J. Hwang, I.S. Mulla, J. Chang, CO sensor derived from mesostructured Au-doped SnO2 thin film, Appl. Surf. Sci. 252 (2006) 4298–4305.

[27] M.A. Martinez, J. Herrero, M.T. Gutierrez, Properties of RF sputtered zinc oxide based thin films made from different targets, Sol. Energy Mater. Sol. Cells 31(1994) 489–498.

[28] H. Takikawa, K. Kimura, R. Miyano, T. Sakakibara, ZnO film formation using a steered and shielded reactive vacuum arc deposition, Thin Solid Films 377/378 (2000) 74–80.

[29] K.R. Murali, Properties of sol–gel dip-coated zinc oxide thin films, J. Phys. Chem. Solids 68 (2007) 2293–2296.

[30] N. Kumar, R. Kaur, R.M. Mehra, Photoluminescence studies in sol–gel derived ZnO films, J. Lumin. 126 (2007) 784–788.

[31] M. Suchea, S. Christoulakis, K. Moschovis, N. Katsarakis, G. Kiriakidis, ZnO transparent thin films for gas sensor applications, Thin Solid Films 515 (2006) 551–554.

[32] S. Major, A. Banerjee, K.L. Chopra, Optical and electronic properties of zinc oxide films; prepared by spray pyrolysis, Thin Solid Films 125 (1985) 179–185.

[33] P. Nunes, E. Fortunato, P. Vilarinho, R. Martins, Effect of different dopants on the properties of ZnO thin films, Int. J. Inorg. Mater. 3 (2001) 1211–1213.

[34] P. Barquinha, A. Pimentel, A. Marques, L. Pereira, R. Martins, E. Fortunato, Effect of UV and visible light radiation on the electrical performances of transparent TFTs based on amorphous indium zinc oxide, J. Non-Cryst. Solids 352 (2006) 1756–1760.

[35] C. Lee, K. Lim, J. Song, Highly textured ZnO thin films doped with indium prepared by the pyrosol method, Sol. Energy Mater. Sol. Cells 43 (1996) 37–45. [36] M. Olvera, A. Maldonado, R. Asomoza, M. Konagai, M. Asomoza, Growth of textured ZnO:In thin films by chemical spray deposition, Thin Solid Films 229 (1993) 196–200.

[37] M.V. Vaishampayan, R.G. Deshmukh, I.S. Mulla, Influence of Pd doping on morphology and LPG response of SnO_2, Sens. Actuators B 131 (2008) 665–672.

[38] S.S. Shinde, P.S. Shinde, C.H. Bhosale, K.Y. Rajpure, Optoelectronic properties of sprayed transparent and conducting indium doped zinc oxide thin films, J. Phys. D: Appl. Phys. 41 (2008) 105109 (6).

[39] S. Ilican, Y. Caglar, M. Caglar, B. Demirci, Polycrystalline indium-doped ZnO thin films: preparation and characterization, J. Optoelectron. Adv. Mater. 10 (2008) 2592–2598.

[40] Z. Li, Y. Xiong, Y. Xie, Selected-control synthesis of ZnO nanowires and nanorods via a PEG-assisted route, Inorg. Chem. 42 (2003) 8105–8109.

[41] M. Futsuhara, K. Yoshioka, O. Takai, Structural, electrical and optical properties of zinc nitride thin films prepared by reactive rf magnetron sputtering, Thin Solid Films 322 (1998) 274–281.

[42] A. Rothschild, Y. Komem, The effect of grain size on the sensitivity of nanocrystalline metal-oxide gas sensors, J. Appl. Phys. 95 (2004) 6374–6380.

[43] M.E. Franke, T.J. Koplin, U. Simon, Metal and metal oxide nanoparticles in chemiresistors: does the nanoscale matter? Small 2 (2006) 36–50.

[44] S. Major, A. Banerjee, K.L. Chopra, Thickness-dependent properties of indium doped ZnO films, Thin Solid Films 143 (1986) 19–30.

Chapter 3

II: Effect of aluminium doping on structural and gas sensing properties of zinc oxide thin films deposited by spray pyrolysis

A facile spray pyrolysis route is used to deposit aluminium doped ZnO (AZO) thin films on to the glass substrates. It is observed that on aluminium doping the particle size of ZnO reduces significantly; moreover, uniformity of particle also gets enhanced. Their XRD study reveals that intensity ratio of crystal planes depend on the aluminium doping concentration. The gas response studies of; ~800 nm thick Al-doped ZnO films at different operating temperatures show that 5 at% Al-doped ZnO thin film exhibits highest response towards H_2S gas at 200°C. The results suggest that the gas response strongly depends on the particle size and aluminium doping in the ZnO.

The content of this chapter has been published in "Sensors and Actuators B 156 (2011) 943– 948",** Reproduced by permission of Elsevier*

http://www.sciencedirect.com/science/article/pii/S0925400511002061

3II.1. Introduction

In gas sensor technology the base material used, the type and amount of additive and microstructure of material play a significant role in deciding sensor performance [1–3]. Extensive research has been going in order to detect and monitor harmful gases and more importantly understanding the sensor properties. The nanosized gas sensor with compatible size and ease of operation is requisite. The gas sensor is a surface phenomenon, in which interaction of analyte gas molecules with chemisorbed oxygen leads to change in electronic properties. The reasoning behind selectivity towards specific gas and the magnitude of response depends upon various factors such as additives/dopants, grain size, surface states and amount of adsorbed oxygen, their activation energy and extent of lattice distortion [1–3]. The enhancement in gas response with decrease in particle size is well studied [4–6]. The effect of dopant on grain size and gas sensor behavior has been extensively studied[7,8]. It is known that when the particle size is comparable to surface depletion layer, the energy band bending no longer depends on the surface but extends into the bulk of the grains and gas sensor response is dramatically enhances.

The zinc oxide is a multifunctional semiconductor oxide and has respectable value in gas sensor technology. The physical and chemical properties of zinc oxide can be easily tailored by using suitable impurity material. We have recently reported In-doped ZnO (IZO) films for H_2S sensor [9]. It has been observed that 3 at% In doped ZnO film shows maximum response towards H_2S at 250°C. In the present work, expensive In(III) is replaced by inexpensive Al(III) to find the effect on gas response behavior. We used similar spray pyrolysis approach for the deposition of undoped and Al-doped(AZO) ZnO thin films. The systematic doping of 1, 3 and 5 at% of aluminium indicates that 5 at% doping (AZO5) demonstrate high response towards H_2S gas at 200°C. Interestingly, in comparison with indium, the doping of Al reduces operating temperature by 50°C, i.e., from 250 to 200°C.

As per literature survey no one has tested response of Al-doped ZnO towards H_2S gas. The report, in general, is on response towards trimethyl amine, dimethyl amine, H_2, acetone, ethanol and CO etc., Nanto et al. [10] have reported 1–5 wt% aluminium doped ZnO thin films (300 nm) deposited by the magnetron sputtering. The 5 wt%

Al-doped ZnO film was found to be more sensitive towards trimethylamine gas (S =~55 at 450°C). Sahay et al. [11] have studied the LPG sensing properties of spray pyrolysed aluminium doped zinc oxide thin films (250–350 nm) and reported response of ~89% at 325°C for 1 vol% of LPG for 0.5 at% Al-doped ZnO film. Chang et al. investigated gas response of AZO films (65–390 nm) deposited by the rf magnetron sputtering and observed that gas response enhances with the decrease in thickness and the 65 nm thick film shows a maximum response of 61.6% at operating temperature of 400°C [12]. The thick films (25–35 μm) of ZnO with 1–9 wt% of Al was deposited using screen printing by Patil et al. [13]. They reported 1 wt% Al-doped ZnO film showing highest response towards ethanol (S=73, 300°C). In general, the literature shows Al-doped ZnO films sensitive towards various gases except H_2S. Such a variation in selectivity may be attributed to the method of deposition, morphology, particle size and the defects formed in the Al:ZnO. In this work, we report the correlation between structure, morphology, aluminium doping concentration and gas response in the ZnO thin films spray pyrolysed using non-ionic surfactant.

3II.2. Experimental

3II.2.1 Synthesis

The undoped and aluminium doped ZnO thin films were deposited by spray pyrolysing the precursors on to the glass substrate at 450°C. The as-deposited films were annealed at the deposition temperature for 5 h. The glass substrates were cleaned before use as explained elsewhere [9]. The precursor solution was prepared as follows; zinc nitrate was dissolved in the mixture of ethanol:distilled water (2:1). This solution was added dropwise to 1% solution of Brij-35 [polyoxyethylene (23) lauryl ether($C_{12}H_{25}$-CH_2-CH_2-O]$_{22}$-CH_2-OH)] in ethanol to obtain 0.48 M solution. The resultant solution was spray pyrolysed on to the hot glass substrate (2.5 cm × 2.5 cm). Similarly, aluminium doped ZnO thin films were deposited by varying atomic ratio of aluminium to zinc in the range of 1-5 at%.

3II.2.2 Morphological and structural analysis

The undoped and Al-doped ZnO thin films were characterized by using X-ray diffraction (XRD), scanning electron microscopy (SEM), high-resolution transmission

electron microscopy (HRTEM) and X-ray photoelectron spectroscopy (XPS). The XRD of thin films were recorded by an 'X' PertPro operating at a voltage of 40 kV diffractometer using Cu-Kα (λ= 0.154056 nm) radiation in the (2θ) range between 20° and 80°. The Scherrer formula was used to calculate average crystallite sizes (D) of doped and undoped ZnO thin films (see equation 2.2). The SEM analysis was carried out by a Lieca Stereoscan 440 model and the TEM and HRTEM studies were done by a Tecnai F30 FEG machine operated at 300 kV. The XPS analysis was performed by using a VG Micro Tech ESCA 3000 instrument at a pressure of $>1\times10^{-9}$ Torr (pass energy of 50 eV, electron take off angle 60° and overall resolution 1 eV). The thicknesses of the films were measured using an AMBIOS MAKE XP-1 Surface Profiler, Make – USA, Version– 5.5.5 between 10 Å and 100 μm.

3II.2.3 Gas response measurements

The gas response studies of ZnO and AZO thin films at different operating temperatures and gas concentrations were performed in the gas sensing assembly described elsewhere [9]. The gas response(S) of the sensor element is defined as the ratio of resistance of film in the air (R_a) to its resistance in the test gas (R_g) (see equation 3I.1).

3II.3. Results and discussion

3II.3.1. Structural properties

Fig. 3II.1 depicts the X-ray diffraction patterns of undoped and 1, 3, 5 at% Al-doped ZnO thin films. All the XRD peaks corresponding to the hexagonal wurtzite structure of ZnO are indexed according to the JCPDS 36-1451. We do not observe any impurity phase of aluminium oxide or zinc aluminate in the XRD patterns. It is found that all the samples exhibit significant orientation along (100), (002) and (101) planes. Minor peaks corresponding to (102), (110), (103), and (112) have also been observed in these films. We observed effect of Al-doping on the relative intensities corresponding to (100), (002) and (101) planes. The XRD profile of undoped ZnO exhibits a strong preferential orientation along c-axis (002), while on doping with aluminium this orientation decreases and that of (100) and (101) get enhanced. Interestingly, we observed schematic reduction in peak intensity of (002) in earlier reported indium doped ZnO films [9].

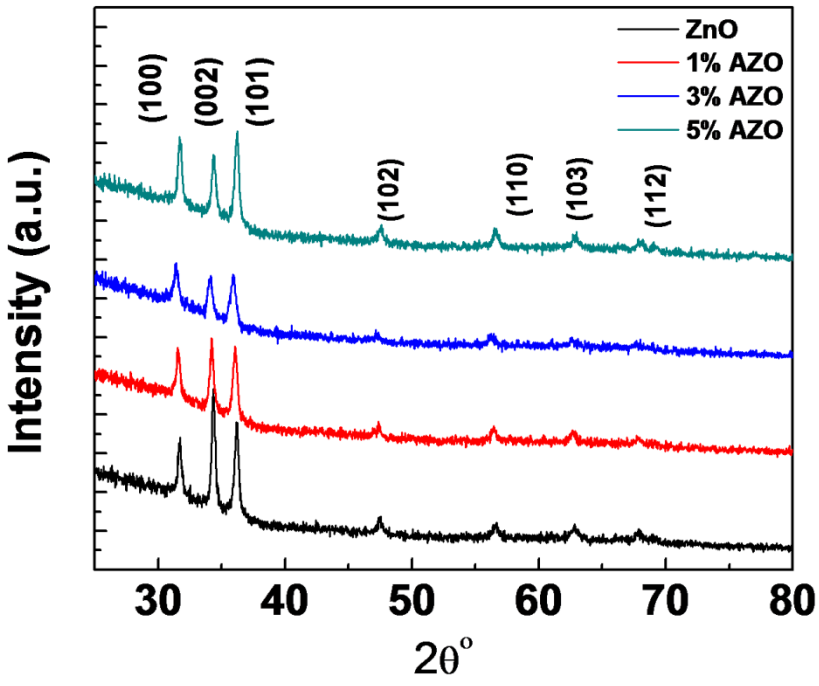

Figure 3II.1: The X-ray diffraction patterns of undoped and Al-doped ZnO thin film deposited at 450°C.

However, we cannot compare the ratio of intensities of AZO and IZO as the film thickness of the two are 800 and 100 nm, respectively. The average crystallite size using (002) orientation of the undoped ZnO is 34 nm and that of 1, 3 and 5 at% Al-doped ZnO are 36, 40 and 28 nm, respectively. It clearly indicates the effect of optimum concentration of aluminium (5 at%) in the significant reduction of crystallite size. It is observed that for undoped ZnO the 'a' axis is 3.253Å which goes on decreasing with aluminium doping, more significantly, for 5AZO it reduces to 3.249 Å while the c-axis remains nearly unchanged on Al-doping. This can be attributed to lower ionic size of Al (53.5 pm) than that of Zn (74 pm).

3II.3.2. Morphological properties

The scanning electron micrographs (Fig.3II.2) of pure ZnO exhibits grains with size variation between 50 and 250 nm; indicating agglomeration of some of the grains. On doping of aluminium the agglomeration reduces and thus gives slightly better uniformity.

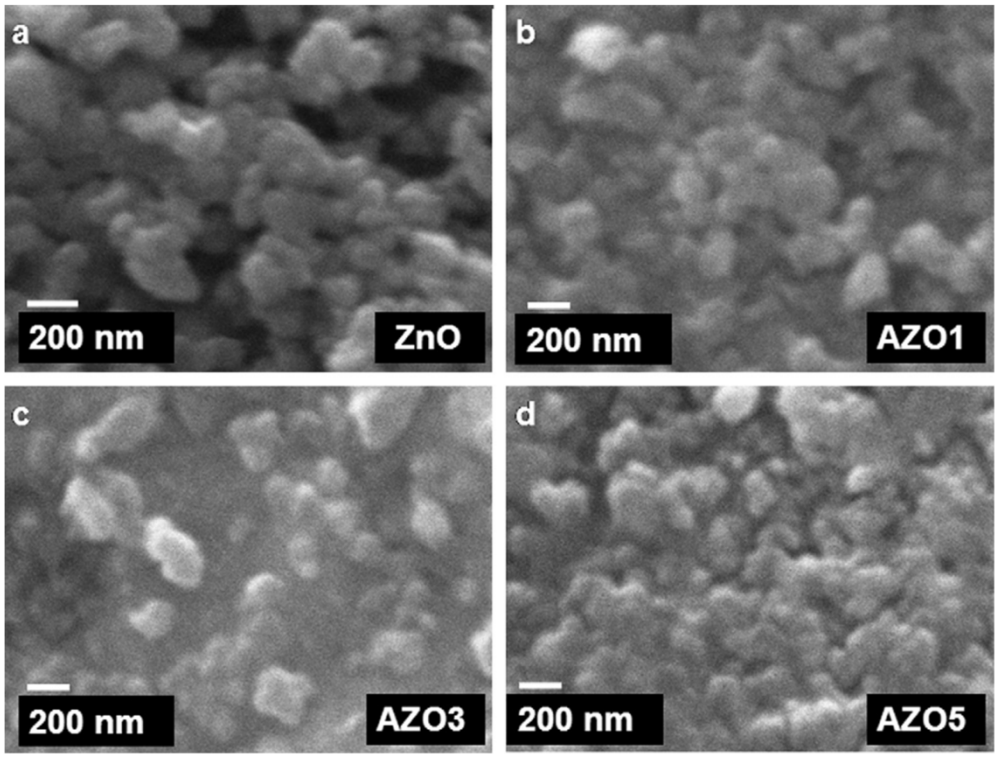

Figure 3II.2: SEM images of undoped and Al-doped zinc oxide films deposited at 450°C (a) undoped ZnO, (b) AZO1 (c) AZO3 and (d) AZO5.

The TEM analysis of undoped ZnO (Fig. 3II.3(a)) shows particles varying in size from 10 to 50 nm. The effect of 1 at% Al-doping is seen in Fig. 3II.3(b), it shows a decrease in the particles size with size variation between 10 and 35 nm. On further doping of 3 at% Al the particles size reduces to ~5 nm (Fig. 3II.3(c)), and remains nearly constant in 5 at% Al. However, the 5 at% Al shows better uniformity in particle size (Fig. 3II.3(d)). The HRTEM image of AZO5 (Fig. 3II.3(e)) reveals fringes of (100) indicating it to be a growth direction.

3II.3.3 X-ray photoelectron spectroscopic studies

The X-ray photoelectron spectroscopic studies of AZO5 film are carried out to determine the presence of aluminium. The peak at 74.1 eV corresponding to Al $2p_{3/2}$ (Fig. 3II.4(a)) confirms the presence of Al^{3+}. Unlike In-doped ZnO [9], we observe asymmetric peak in the oxygen binding energy spectrum which can be attributed to the higher thickness of the present film. The asymmetric profile (Fig. 3II.4 (b)) of O 1s is resolved into three components by a Gaussian fit.

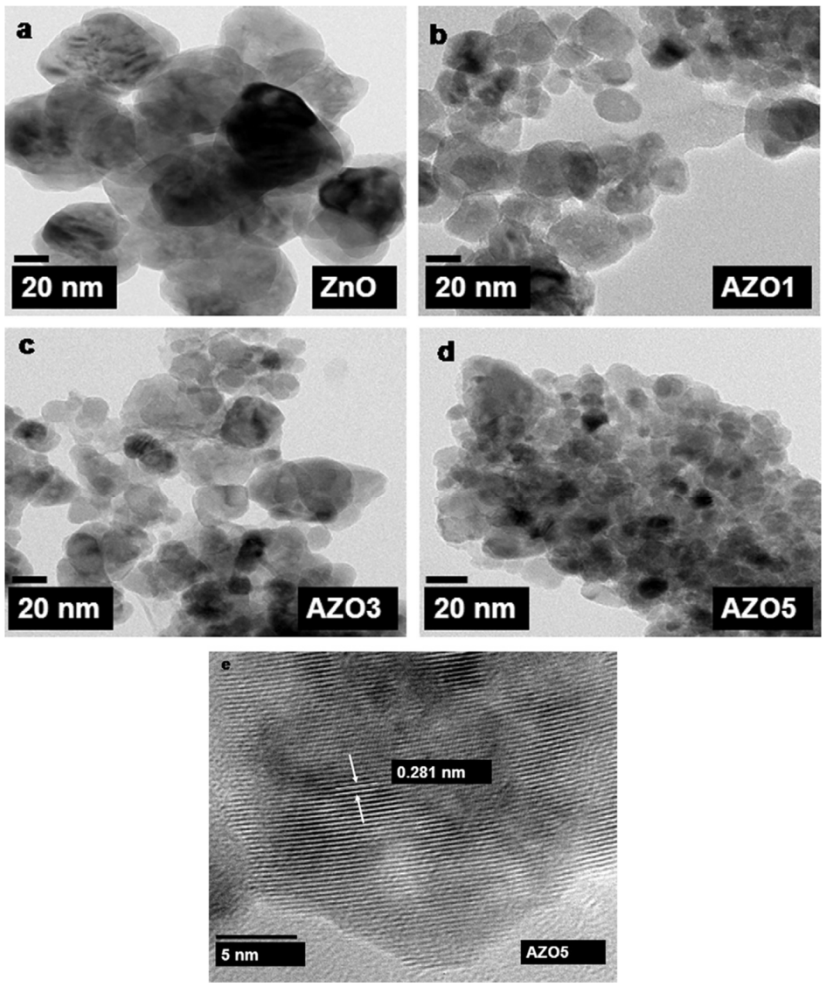

Figure 3II.3: Low-magnification TEM image of (a) undoped ZnO, (b) AZO1, (c) AZO3, (d) AZO5 and (e) high-resolution TEM image of AZO5.

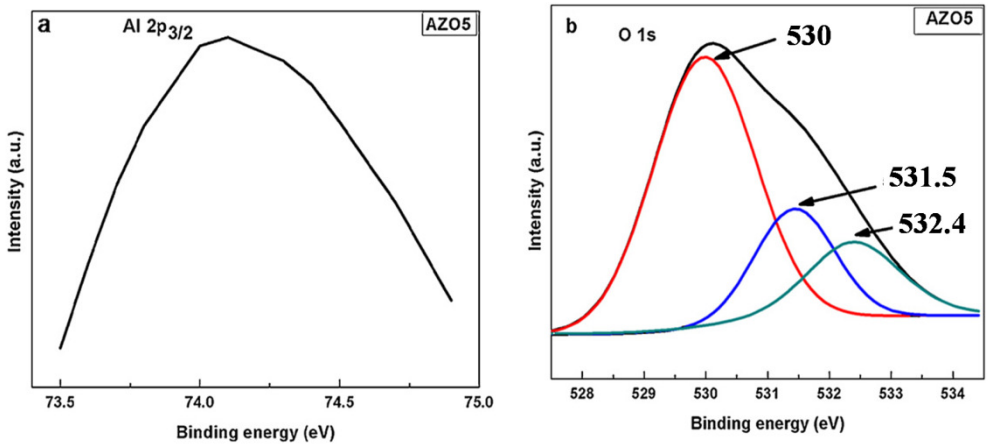

Figure 3II.4: XPS analyses of (a) aluminium region and (b) oxygen region of 5 at% Al-doped ZnO thin film.

The component at the low binding energy (529.96 eV) can be attributed to O^{2-} ions of wurtzite structure in the hexagonal Zn^{2+} ion array. The higher binding energy peak at

532.4 eV is usually ascribed to chemisorbed or dissociated oxygen or OH^- species of the ZnO surface. The intermediate binding energy can be attributed to the oxygen associated with Al^{3+} and oxygen deficient regions within the ZnO matrix [14,15]. The spectrum does not show any peak corresponding to the other element or impurity.

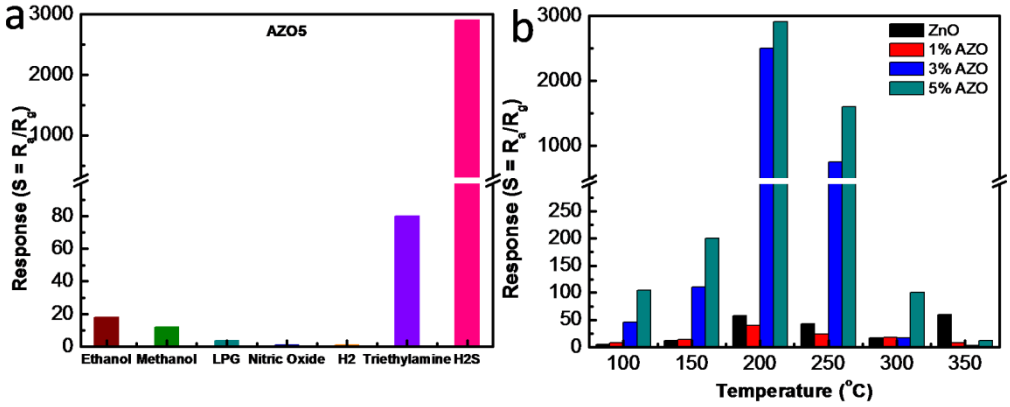

Figure 3II.5: (a) Histogram of 5 at% Al-doped ZnO thin film for 1000 ppm of different gases at 200°C. (b)The response towards 1000 ppm of H_2S gas with operating temperatures for pure and Al-doped ZnO.

3II.3.4. Gas response properties

The thin film oxide semiconductor gas sensors are well explored. The gas response depends on factors, such as morphology, dopants and their concentrations, thickness of film and operating temperatures. We tested response for pure and Al doped ZnO towards various reducing and oxidizing gases, such as H_2S, H_2, NO_x, triethylamine, liquid petroleum gas, and methanol, ethanol vapors. The pure and Al-doped thin films have been tested for 1000 ppm concentrations of all the above mentioned gases individually at temperatures between 100 and 350°C. We do not observe any significant response for the above gases by undoped or 1 at% Al-doped ZnO films. However, for higher Al concentrations remarkable response towards H_2S gas is observed at 200°C operating temperature. It is found that in comparison to AZO1 and AZO3, the AZO5 (5 at% Al) shows the highest response towards H_2S gas and hence we carried out the detailed gas response studies of this composition. The selectivity of AZO5 thin film towards 1000 ppm of various test gases at 200°C is shown in Fig. 3II.5(b). The significantly high response (S = 2900) reveals its remarkable selectivity towards hydrogen sulfide gas at low operating temperature of 200°C. In comparison, itshows marginal response towards triethylamine (S = 80) and other test gases. The

histogram (Fig. 3II(b)) clearly displays the dependence of response on aluminium content and operating temperature. It is observed that undoped ZnO and AZO films show their highest response at 200°C. It is interesting to note that even at low operating temperature of 100°C the AZO5 film shows as high as 100 (S) response towards H_2S. The response and recovery time of AZO5 film for 200–1000 ppm of H_2S at 200°C is shown in Fig. 3II.6(a). It is observed that AZO5 film attains nearly 100% recovery after every cycle, more precisely; nearly 95% recovery is achieved within 5 min. The other advantage exhibited is the fast response (~10 s) indicating its potential as a sensor material for the commercial application. Fig.3II.6(b) fairly linear increase in gas response with increase in H_2S gas concentration. In our earlier report on In-doped ZnO, we observed response towards H_2S gas at 250°C which indicates that the operating temperature significantly lowers due to Al-doping. However, due to the difference in film thickness of the two systems, one cannot really compare the gas response behavior. It confirms from TEM images that the particle size decreases with increase in doping content. Thus surface to volume ratio increases, which provides more adsorption site for oxygen molecule and as a result gas response increases in the doped film. It can be seen that gas response reduces with increase in the grain size. The influence of grain size on gas response is extensively discussed on the basis of grain boundary and neck model by several researchers [4,5]. The working principle of metal–oxide gas sensors is based on a shift of the state of equilibrium of the surface oxygen reaction in the presence of the test gas (receptor function).

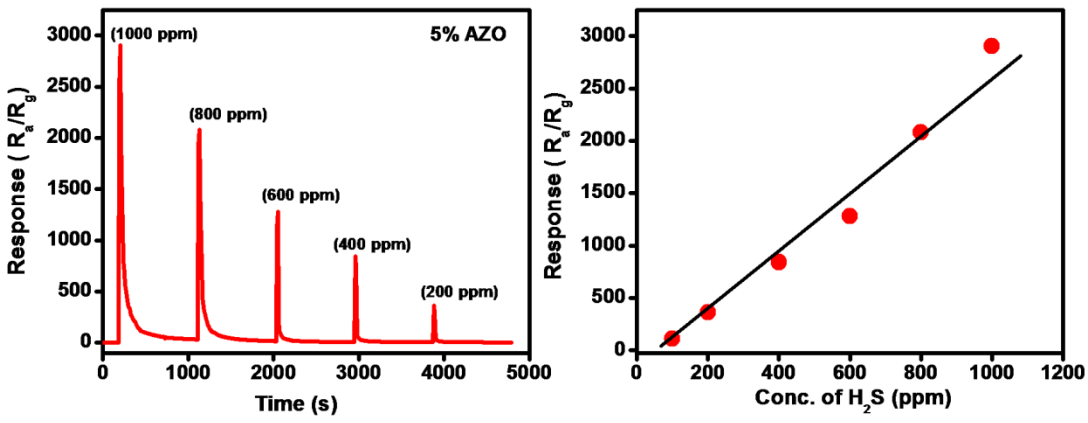

Figure 3II.6. The response and recovery of 5 at% Al-doped ZnO upon exposure to different concentration of H_2S gas at 200°C. (b) Response with increase in H_2S gas concentration.

The resulting change in chemisorbed oxygen is measured as a change in the conductivity of sensor material, i.e., transform of chemical signal to an electrical signal (transducer function). The receptor function is provided by charge transfer interactions between the sensor and ambient gas molecules. These interactions largely involve chemisorption of oxygen adions and removal of O^-_{ad} ions by interaction with reducing gases such CO, H_2S, hydrocarbons etc. Here, it can be explained by equations (see equation 3I.2 and 3I.4).

The gas response of the sensor depends on the surface reaction between the metal oxide and the gas molecules in the ambient; therefore microstructure of material plays a critical role in determining sensor response. The dependence of sensitivity on grain size (D) is explained by Xu et al. [4]. They reported enhanced gas response with a decrease in the grain size and observed that for grain size ≤10 nm the increase in the sensitivity occurs by several orders of magnitude. They proposed semi-quantitative model to explain effect of grain size (D) and gas response (S). Further, they proposed the dependence of grain size (D) and width of the depletion layer (L) produced around the surface of crystallites due to chemisorbed adions (mostly oxygen adions $O^-_{(ad))}$ to explain grain size dependant gas response. For larger grains (D>2L) the gas response depends on grain boundaries. When grain size (D) is comparable to the depletion layer (L), the gas response is neck controlled since in that case neck dominates the electrical resistance of the element. Finally, when D is less than 2L, the depletion region extends throughout the whole grain and the crystallites are almost fully depleted of mobile charge carriers, in this case the electric resistance of grains dominates the whole resistance of the chain, therefore the gas response is controlled by grains themselves (grain control). They have also reported the alteration of depletion region (L) due to impurity. To examine the effect of grain size on the sensitivity of nanocrystalline metal–oxide gas sensors Rothschild et al. gave numerical simulation [6]. They calculated the effective carrier concentration (n_{eff}) as a function of the surface state density (N_t) for nanosized SnO_2 crystallites with different grain size between 5 and 80 nm. Normally the trapped charge density (N_t-) at the surface of the sensor largely depends on the density of chemisorbed oxygen adions $(N_t-)\approx[O^-_{(ad)}]$ where, the square brackets designate density per unit surface area and therefore it is sensitive to the ambient gas composition due to interactions with gas molecules. Effective carrier concentration (n_{eff}) is affected by trapped state density

(N_t−). At a particular surface state density ($N_{t,crit}$), the effective carrier concentration decreases by several orders and potential steeply increases. Rothschild et al. further reported that the value of $N_{t,crit}$ decreases with a decrease in the grain size. Thus it can be concluded that for smaller grains, such huge change in effective carrier concentration takes place at the lower surface state density. From the above discussion, it is clear that the gas response of sensor increases with decrease in grain size. The gas response also depends on critical surface state density as at this point the effective carrier concentration decreases and surface potential increases. This supports our observations of enhancement in the gas response by the lowering of grain size from ~50 nm to ~10 nm. In the present work, we used a similar technique for the deposition of Al^{+3} as applied earlier by us for the deposition of In^{+3} doped ZnO film. Moreover, we used same non-ionic surfactant viz. polyoxyethylene(23) lauryl ether (Brij-35) and observed the response towards H_2S in both the cases. The surfactant forms a protective layer around the Zn^{2+} ions and controls the decomposition process. Thus it prevents the aggregation of particles and favors the formation of nanoparticles at the higher deposition temperature. We annealed the sample for longer duration to completely remove the Brij-35 and favor oxidation. This suggests that the non-ionic surfactant plays a vital role in deciding the specific morphology which further leads to their precise response towards H_2S.

3II.4. Conclusions

The uniform thin films of undoped and Al-doped ZnO having ~800 nm thickness are deposited by a simple spray pyrolysis technique using surfactant. It is observed that the particle size decreases on doping of aluminium (from ~45 nm to ~5 nm) and consequently provides a larger surface to volume ratio. More specifically, the 5 at% Al-doped film shows uniform particle size of ~5 nm and exhibits selectively high response (S=2900 for 1000 ppm) towards hydrogen sulfide gas. It shows fast response (~10 s) and recovery time (5 min, >95%) for H_2S at 200°C. Thus, it can be assumed that the nanosized Al-doped ZnO thin films deposited using surfactant have a potential to become a good H_2S gas sensing material.

3II.5. References

[1] G. Korotcenkov, Metal oxide for solid-state gas sensors: what determines our choice? Mater. Sci. Eng. B 139 (2007) 1–23.

[2] N. Yamazoe, G. Sakai, K. Shimanoe, Oxide semiconductor gas sensors, Catal. Surv. Asia 7 (2003) 63‑64.

[3] C. Wang, L. Yin, L. Zhang, D. Xiang, R. Gao, Metal oxide gas sensors: sensitivity and influencing factors, Sensors 10 (2010) 2088‑2106.

[4] C. Xu, J. Tamaki, N. Miura, N. Yamazoe, Grain size effects on gas sensitivity of porous SnO_2-based elements, Sens. Actuators B 3 (1991) 147‑155.

[5] Z.A. Ansari, S.G. Ansari, T. Ko, J.H. Oh, Effect of MoO3 doping and grain size on SnO_2-enhancement of sensitivity and selectivity for CO and H_2 gas sensing, Sens. Actuators B 87 (2002) 105‑114.

[6] A. Rothschild, Y. Komem, The effect of grain size on the sensitivity of nanocrystalline metal‑oxide gas sensors, J. Appl. Phys. 95 (2004) 6374‑6380.

[7] T. Sun, S. Donthu, M. Sprung, K. D’ Aquila, Z. Jiang, A. Srivastava, J. Wang, V.P. Dravid, Effect of Pd doping on the microstructure and gas-sensing performance of nanoporous SnO_x thin films, Acta Mater. 57 (2009) 1095‑1104.

[8] G. Zhang, M. Liu, Effect of particle size and dopant on properties of SnO_2‑based gas sensors, Sens. Actuators B 69 (2000) 144‑152.

[9] S.S. Badadhe, I.S. Mulla, H_2S sensitive indium-doped ZnO thin films: preparation and characterization, Sens. Actuators B 143 (2009) 164‑170.

[10] H. Nanto, H. Sokooshi, T. Usuda, Smell sensor using aluminium-doped zinc oxide thin film prepared by sputtering technique, Sens. Actuators B 10 (1993)79‑83.

[11] P.P. Sahay, R.K. Nath, Al-doped zinc oxide thin films for liquid petroleum gas (LPG) sensors, Sens. Actuators B 133 (2008) 222‑227.

[12] J.F. Chang, H.H. Kuo, I.C. Leu, M.H. Hon, The effects of thickness and operation temperature on ZnO:Al thin film CO gas sensor, Sens. Actuators B 84 (2002) 258‑264.

[13] D.R. Patil, L.A. Patil, D.P. Amalnerkar, Ethanol gas sensing properties of Al_2O_3-doped ZnO thick film resistors, Bull. Mater. Sci. 30 (2007) 553‑559.

[14] P.T. Hsieh, Y.C. Chen, K.S. Kao, C.M. Wang, Luminescence mechanism of ZnO thin film investigated by XPS measurement, Appl. Phys. A: Mater. Sci. Process.90 (2008) 317‑321.

[15] L.J. Li, H. Deng, L.P. Dai, J.J. Chen, Q.L. Yuan, Y. Li, Properties of Al heavy doped ZnO thin films by RF magnetron sputtering, Mater. Res. Bull. 43 (2008)1456‑1462.

Chapter 4

Visible light assisted room temperature gas sensing property of ZnO NR/CdS heterojunction

We report on the visible light assisted room temperature NO_2 and H_2S gas sensing properties of ZnO nanorods (NRs)/CdS heterojunction system. Vertically aligned zinc oxide (ZnO) nanorods are prepared using a simple hydrothermal process at low temperature (95°C), and cadmium sulfide (CdS) is grown thereupon by the successive ionic layer adsorption and reaction (SILAR) method. It is shown that in the presence of visible light the ZnO NR/CdS heterojunction system shows a highly enhanced response to NO_2 and H_2S as compared to the ZnO NR case.

Submitted to Sensors and actuators B: chem. 2015

4.1 Introduction

As a consequence of the rapid all-round development and related industrial growth, tons of hazardous and eco-antagonist gases are being constantly released into the atmosphere around the world. Safeguard of environment and living creatures is thus a serious problem of this century. To protect and preserve our environment, it is essential to monitors harmful gases such as NH_3, CO, NOx, H_2S, SO_2, etc. Hence, developing robust sensors with high efficiency for such gases is an unending quest. Understanding the mechanism behind a specific sensing performance is equally important to be able to tune them for optimal performance. Semiconducting gas sensors based on change in carrier concentration are being constantly investigated due to their small dimensions, compatibility with microelectronic processing, simplicity of operation, low cost, and the ease of commercialization [1-3].

Semiconducting metal oxide gas sensors based on ZnO, SnO_2, Fe_2O_3, WO_3, NiO have been widely investigated[4-8]. Among these ZnO has attracted tremendous attention due to its mixed covalent/ionic character in the chemical bonding, earth abundant nature, and technologically tuneable properties[9-10]. This is exemplified by versatility of ZnO in many useful applications such as solar cells[11], light emitting diodes[12], field effect transistor[13], water splitting[14], batteries[15], supercapacitor[16], photocatalyst[17], piezoelectric devices[18], and sensors[4]. It is a wide direct band gap oxide semiconductor (band gap, 3.4 eV). The most important property of the ZnO is its capability to form different interesting morphologies with specific crystalline facets and high surface area[19-20]. Hence, opto-electronic properties of ZnO can be tuned using varying sizes and shapes of the corresponding nanomaterials[21]. Zinc oxides properties can also be optimized using different dopants[22-24].

Gas sensors based on ZnO have been explored in various sizes and shapes such as nanowires[25], nanorods[26], nanobelts[27], hierarchical morphology[28] etc. In gas sensor technology, the gas sensor must show high sensitivity, selectivity, rapid response and recovery time, and low operating temperature. It is generally difficult realize all these properties in a single material. Therefore, specific morphologies, doped systems, composites, hybrid materials are useful in this context[28-32]. However, most of these ZnO based gas sensors operate at higher operating

temperature (>200°C). As higher operating temperature may cause issues related to safety, power consumption and stability of the sensor, room temperature gas sensors are a prerequisite in several applications. There are a few reports on UV enhanced gas sensors which operate at room temperature[33-36]. However, availability of UV source and related cost are the concern in the corresponding application. It is necessary therefore to develop room temperature visible light enhanced gas sensor, which was the object of the present work.

In present case we have studied ZnO NRs/CdS system which has favourable band alignment for electron transport. There are a few very interesting reports based on ZnO/CdS systems based gas sensors. Zhaia et al. have reported formaldehyde sensor based on CdS nanoparticles distributed on ZnO microcrystals using sonochemical method[37]. Zhai et al. have also reported formaldehyde sensor based on CdS nanowires/ZnO nanoparticles via hydrothermal method[38]. In both the cases, pristine CdS did not exhibit response towards formaldehyde. It suggests that heterojunction plays a clear role in gas sensing. Yang et al. have fabricated CdS nanowire/ZnO (core/shell) by hydrothermal synthesis for NO_2 sensing[39]. However the main disadvantage of this system is its base current which is of the order of a few nanoamperes making its practical application rather difficult.

In these reports the sensing elements are also needed to be drop-casted on the electrodes weakening the electric transport. Moreover, the adhesion of sensing materials with electrodes cannot be enhanced by post annealing due to presence of CdS. Therefore, in present case we have directly grown sensing materials onto the electrodes. The ZnO NR/CdS heterojunction is formed by two step process, namely fabrication of ZnO nanorods by simple hydrothermal method followed by a SILAR technique for deposition of few nanometer thick CdS layer on the ZnO nanorods. In this study a uniform coverage of CdS on ZnO surface is formed. Here, we demonstrate visible light assisted NO_2 and H_2S gas sensing properties of the ZnO NR/CdS heterojunction at room temperature. The significance of ZnO NR/CdS heterojunction on gas sensing performance is discussed.

4.2. Experimental

4.2.1 Synthesis of ZnO nanorods

ZnO nanorods were grown on the glass and patterned FTO coated glass substrates by chemical route as reported earlier[40]. Prior to ZnO nanorods growth, platinum electrodes with a spacing of ~120 μm were deposited by pulsed laser deposition technique on the glass substrates. Initially, seeding was done which acts as nucleating sites for growth of ZnO nanorods. A 22.8 mM zinc acetate solution was prepared in ethanol. This solution was used to prepare the seed layer. Zinc acetate solution was drop casted on clean substrates and heated for 5 min at 350°C to decompose zinc acetate and form zinc oxide. This process was repeated twice and subsequently the substrates were annealed at 450°C for 30 min to obtain uniform ZnO seed layer with good adhesion of nuclei on the substrates.

The ZnO nanorods were prepared by using these ZnO seeded substrates. Zinc nitrate hexahydrate (Merck, 25 mM) and Hexamethylenetetramine (HMTA) (Sigma Aldrich, 25 mM) solutions were prepared individually in deionized (DI) water. Polyethylenimine (PEI) (Sigma Aldrich, M_w: 1800, 5 mM) was added with continuous stirring to the HMTA solution. The resulting solution was then mixed with the Zinc nitrate solution. The ZnO seeded substrates were dipped in a closed glass container containing the above growth solution with the seeded side facing the bottom of the container. This glass container was heated at 95°C with constant magnetic stirring for 3h. After the completion of reaction, the ZnO NRs substrates were thoroughly rinsed with DI water several times and lastly with ethanol, and then dried at 60°C. The obtained ZnO nanorods films were annealed at 450°C for 2h to remove the residual polymer and achieve good adhesion.

4.2.2 Synthesis of ZnO nanorods/CdS heterojunction

Cadmium sulfide was grown on ZnO nanorods using a simple SILAR technique. In a typical synthesis, individual solutions of 0.05 M cadmium nitrate $Cd(NO_3)_2$ and 0.05 M sodium sulfide (Na_2S) were prepared in ethanol. The ZnO nanorods films were successively immersed in solutions of $Cd(NO_3)_2$ and Na_2S for 1 min each. However, the films were thoroughly rinsed with ethanol while switching between these

precursors solution. Five such SILAR cycles were carried out on the ZnO nanorod films. These films were dried at room temperature. The schematic of ZnO NR/CdS heterojunction synthesis procedure is shown in fig. 4.1(a).

4.2.3 Characterization

For the determination crystallinity and phase formation X-Ray diffraction (XRD) data were recorded on a Philips X'Pert PRO using operating at a voltage of 40 kV diffractometer using Cu-K_α (λ = 0.154056 nm) radiation in the (2θ) range between 20° and 80°. Morphological analysis was carried out by scanning electron microscopy (SEM) technique. SEM images of ZnO, ZnO NR/CdS films were acquired using E-SEM Quanta 200 3D. Transmission electron micrographs and high-resolution transmission electron micrographs of samples were captured using HR-TEM, FEI Tecnai 300. UV–Visible diffused reflectance spectra were recorded using a Jasco V-570 spectrophotometer. The dark and blue light assisted NO_2 and H_2S gas sensing response of ZnO NR and ZnO NR/CdS thin films at room temperatures were examined. The blue LED of ~0.50 mW power (at distance 3 cm from device) was used for gas sensing study. The desired concentrations of test gases were achieved using mass flow controllers (Alicate Scientific make). The gas response (S) of the sensor element is defined as follows:

$$S = (I_a - I_g)/I_a \quad \text{Oxidizing gas (4.1)}$$

$$S = (I_g - I_a)/I_a \quad \text{Reducing gas (4.2)}$$

Here (I_a) is the current through the film in air ambient and (I_g) the current in the specific gas ambient.

4.3. Results and Discussion

4.3.1 Structural and morphological study

The schematic of synthetic protocol of ZnO NR/CdS heterojunction is shown in fig. 4.1(a). Fig. 4.1(b) shows X-ray diffraction (XRD) patterns of ZnO NRs and ZnO NRs/CdS films grown on FTO.

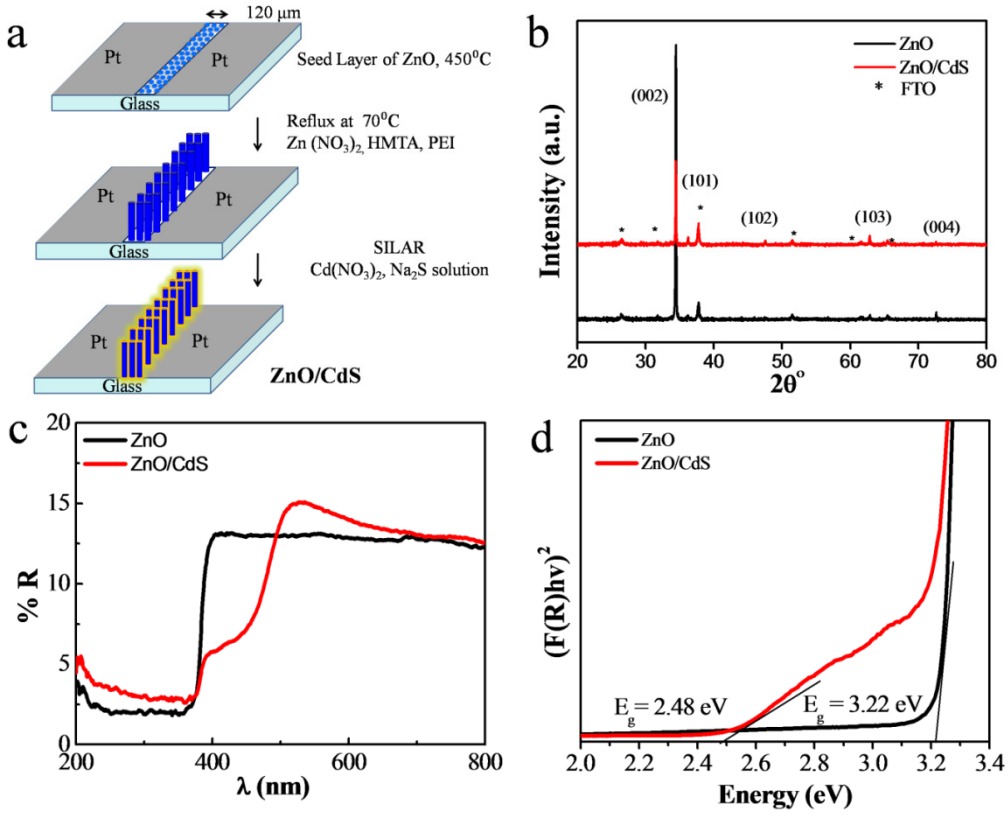

Figure 4.1: a) Schematic of ZnO NR/CdS heterojunction synthesis protocol, b) X-ray diffraction pattern, c) diffused reflectance spectra and d) Tauc's plots of ZnO NRs and ZnO NR/CdS films.

Both X-ray patterns match well with PCPDF file (80-0075) corresponding to ZnO and CdS contribution is not discernible it being a nanoscale film. The XRD patterns exhibit c-axis growth (0001) plane as the preferential growth axis implying oriented growth of this wurtzite phase. The optical properties of ZnO NRs and ZnO NR/CdS films were analysed by diffused reflectance spectra [Fig. 4.1(c, d)]. The confirmation of CdS formation on the ZnO nanorods is clear from the comparison of the UV Visible analysis of ZnO NRs and ZnO NR/Cds films. ZnO NRs do not exhibit visible absorption, as expected; however the ZnO NR/CdS heterojunction case shows decrease in the diffused reflectance between 380 nm and 520 nm. The band gap of ZnO (~3.22 eV) was calculated using Kubelka–Munk function. In the case of ZnO/CdS heterojunction the observed gap (~2.48 eV) is clearly dominated by CdS and is in the visible region. Fig. 4.2 (a, b) show FESEM images of ZnO NRs and ZnO NR/CdS films. The ZnO nanorods [Fig. 4.2(a)] were obtained using seed-induced growth indicating formation of highly dense fairly oriented nanorods. The diameter of

ZnO nanorods is seen to be between 30-80 nm. The cross-section shapes of these nanorods are perfectly hexagonal, as expected. The SEM image for the ZnO NR/CdS heterojunction case shown in Fig 4.2(b) brings out that the ZnO nanorods are properly and uniformly covered by CdS nanomaterial. The transmission electron microscopy (TEM) and high-resolution TEM (HRTEM) images for the samples are shown in Fig. 4.2 (c and d). Figure 4.2(c) shows low magnification TEM image of ZnO hexagonal nanorods. A gradual decrease in the diameter of ZnO nanorod from base to tip is observed. Fig. 4.2(d) shows low magnification TEM image of ZnO NR/CdS heterojunction. It can be seen that ZnO nanorod is being covered by CdS nanoparticulate layer with a thickness ~5-10 nm. These CdS nanoparticles are seen to form a thin shell around the ZnO nanorods. The high-resolution TEM image (fig. 4.2e) is a magnified view of CdS nanoparticles coated on ZnO nanorod. The lattice spacing of 0.35 nm corresponds to (100) planes of CdS [PCPDF 80-0006]. The clear lattice fringes indicate good crystalline nature of the CdS nanoparticles.

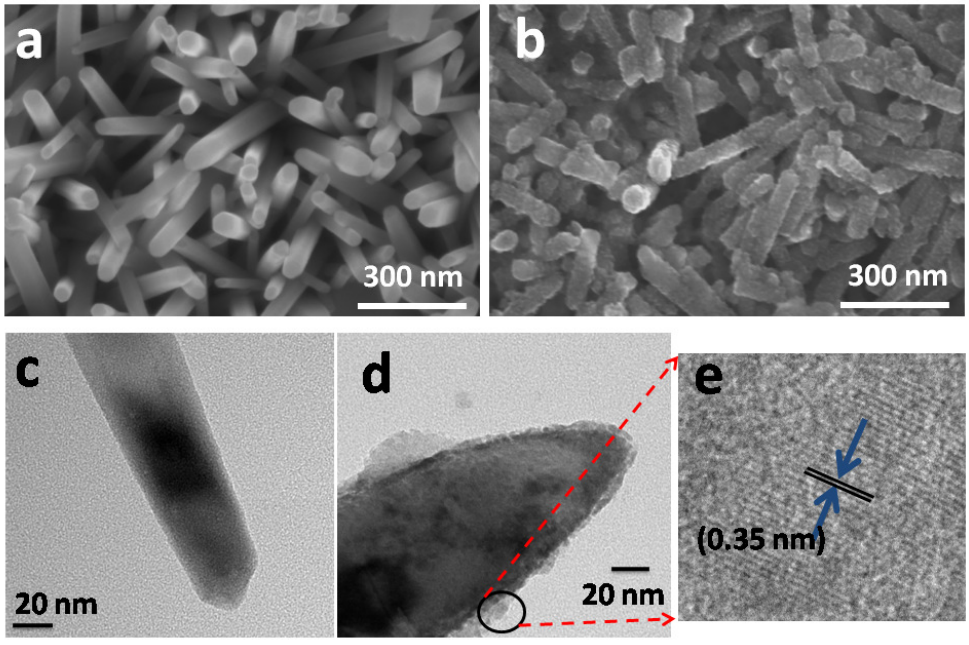

Figure 4.2: FESEM images of (a) ZnO NRs and (b) ZnO NR/CdS heterojunction; (c, d) show low magnification TEM images of ZnO NR and ZnO NR/CdS; (e) shows high resolution TEM image of CdS nanoparticle.

4.3.2 Gas sensing study

The dynamic technique was used to evaluate gas sensing performance of ZnO NRs and ZnO NR/CdS films for the detection of H_2S and NO_2. The films were tested in dark and under blue LED illumination. First the ZnO NRs were tested for 500 ppm of NO_2 gas in dark and in presence of light [Fig. 4.3]. In the dark, ZnO nanorods film show a moderate response (S=17%) to NO_2 with no recovery.

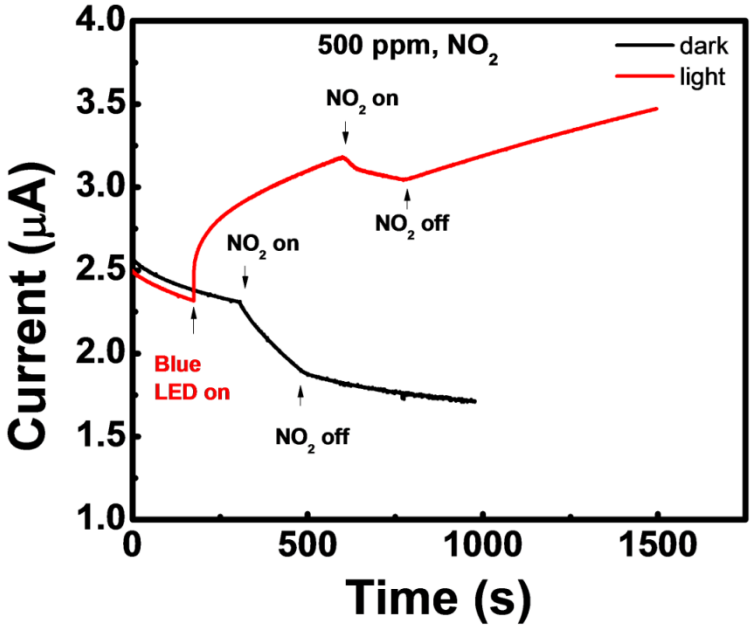

Figure 4.3: NO_2 gas response of ZnO nanorods in dark and under blue LED illumination.

However, in the presence of blue LED (0.5 mW intensity, at distance 3 cm from device), ZnO nanorods exhibit lower response (S=5%) as compared to NO_2 response in dark. The ZnO NR/CdS heterojunction on the other hand exhibits a significant response with recovery for NO_2 as compared to the ZnO nanorods. Fig. 4.4 (a, b) show transient gas response of ZnO NRs and ZnO NR/CdS samples in the presence of blue LED with increasing NO_2 concentration between 100 ppm and 500 ppm. ZnO NRs do not show any response for NO_2 concentration below 300 ppm. They show a slight response above 300 ppm and the recovery is also sluggish (Fig.4.4a). This suggests that ZnO NRs are not sensitive towards NO_2 as there is only few charge carriers are generated in the ZnO NRs in presence of blue LED. The ZnO NRs/CdS heterojunction sample shows an optimum response (3.5%) with almost full recovery at a low concentration of 100 ppm. The gas response did not saturate till 500 ppm and

was found to increase with NO_2 concentration in the range between 100 and 500 ppm (fig. 4.4 b).

The H_2S gas sensing study of the ZnO NR/CdS heterojunction sample was performed at room temperature in dark and in the presence of blue LED. The device exhibits no response in dark towards 500 ppm H_2S [Fig. 4.4(c)]. Interestingly, in the presence of blue LED, ZnO NR/CdS heterojunction sample displays a significant response to H_2S [fig. 4.4 (d)]. In this case, the recovery is attained by switching off the blue LED. The recovery process is slow because in presence of light, H_2S molecules remain adsorbed on the surface due to strong interaction between photo-generated holes/Cd^{2+} ions and S^{2-} of H_2S. The ZnO/CdS heterojunction shows a systematic increase in response with increase in the H_2S concentration. Blue LED illumination was kept on after recovery (last dotted region Fig. 4.4 (d)) to confirm that enhanced current is only because of H_2S sensing. It depicts a sudden rise followed by fall in photocurrent, revealing that the increase in current is mainly due to remaining adsorbed H_2S molecules.

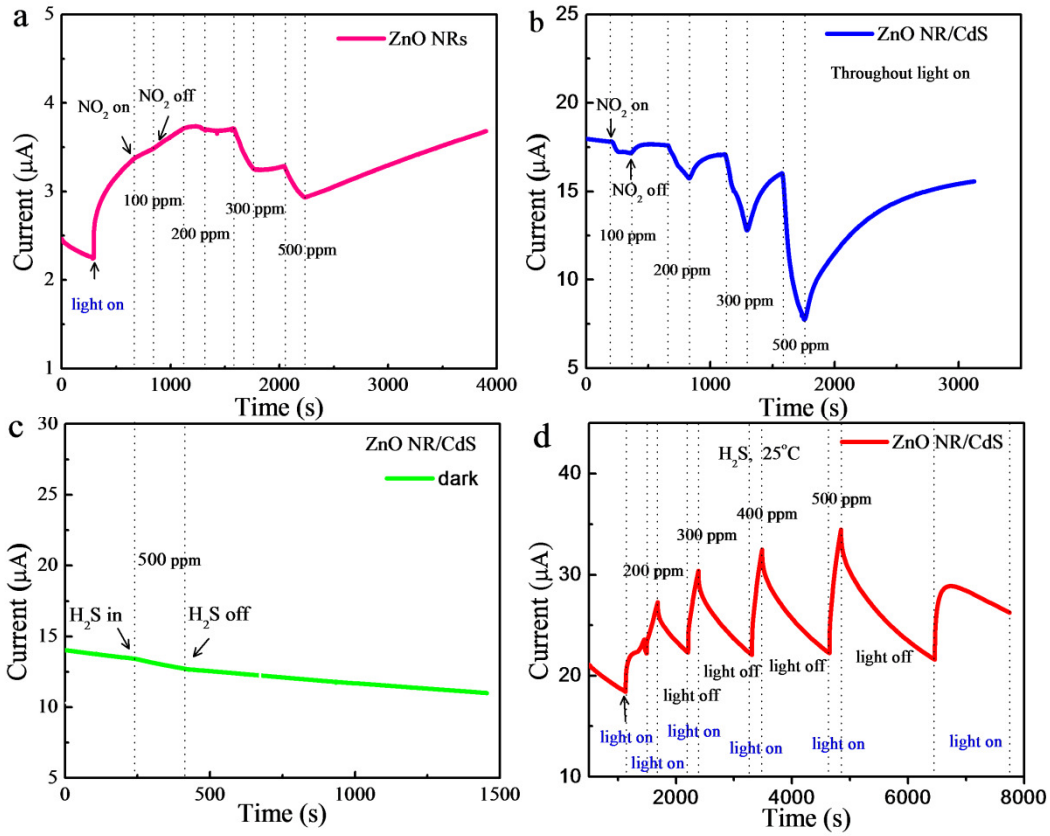

Figure 4.4: (a, b) Response and recovery for the ZnO NRs and ZnO NR/CdS samples, respectively, as a function of NO_2 concentration under blue LED illumination; (c, d) H_2S gas response of the ZnO NR/CdS heterojunction in dark and under blue LED illumination, respectively.

This confirms that light plays a key role in H_2S sensing by the ZnO NR/CdS heterojunction sample.

In semiconductor based gas sensors, many factors affect gas sensor performance such as morphology, surface area, catalytic active sites, defect levels, porosity, dopant, analyte gas[41]. In semiconductors, analyte gas molecules react with surface adsorbed oxygen (O_2^-, O^-, and O^{2-}) species leading to a change in the carrier concentration of the sensor element. The gas sensing mechanism in present case can be described on the basis of modulation of energy barrier between the heterojunction partners (Fig. 4.5)[34, 36].

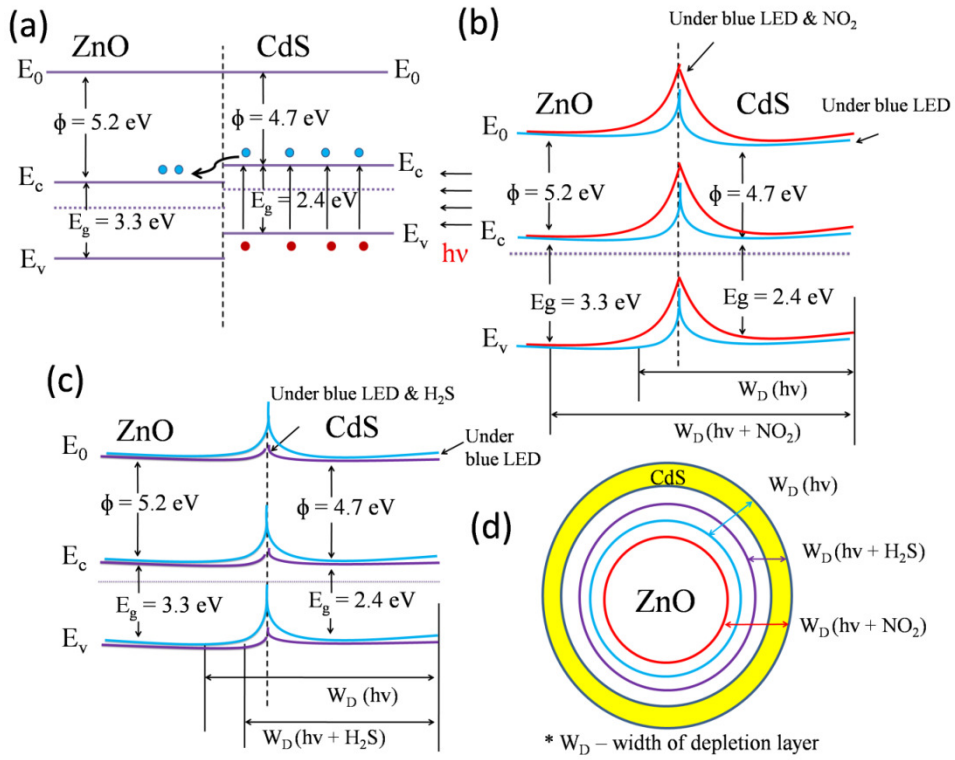

Figure 4.5: Schematic diagrams showing a mechanism proposed for the enhanced response of the ZnO NR/CdS sample towards NO_2 and H_2S gases under blue LED illumination: (a) Energy band diagram for the ZnO NR/CdS system; Energy band modulation in the presence of test gases [(b) NO_2 (c) H_2S] under blue LED illumination; (d) Pictorial illustration of the variation of the width of depletion layer (W_D) in test gases under light illumination.

In the present case, ZnO nanorods are covered with a few nanometres of CdS layers by using a simple SILAR method. The work functions of CdS and ZnO are 4.7 eV and 5.2-5.3 eV, respectively. The alignment of valance and conduction bands is

favourable [Fig. 4.5]. As both CdS and ZnO are n-type semiconductors, they form an-n type heterojunction. In semiconductors, surface states and defects in the crystal create trap energy levels at the surface and in the interface region which result in band bending and Fermi level pinning. Such states trap free charge carriers at the surface and interface region and create a potential barrier[42-44]. The thickness of the CdS shell on ZnO NRs core surface is ~5-10 nm [fig. 4.2 (d)]. The thickness of CdS is very less compare to surface depletion layer which is order of debye length ~100 nm [45]. In case of ZnO, surface depletion layer which corresponds to debye length is ~ 30 nm[46,47,48]. Thus, the depletion region of CdS extends or overlaps over to the ZnO NRs surface. Apart from the surface depletion region, energy barrier exists at the interface of heterojunction due to trapping of electrons in these trap states. Hence, electron transport is mainly governed by the modulation of the energy barrier formed at the heterojunction. In semiconductors, conductivity (σ) is expressed by using following equation[49]

$$\sigma = \sigma_o(\exp(\phi_{eff}/kT) \quad (4.3)$$

Where, ϕ_{eff} is energy barrier at the heterojunction, K is Boltzman constant, T is absolute temperature and σ_o is absolute conductivity. The modulation of ϕ_{eff} in the presence of test gas decides the electron transport properties of the sensor element. In the presence of NO_2 gas, the energy barrier height (ϕ_{eff}) increases leading to a decrease in the current through the sensor[fig. 4.5(b)]. However in the presence of electron donating groups like H_2S, ϕ_{eff} reduces further hence the current through the sensor element increases [fig. 4.5(c)]. In the dark, the modulation of ϕ_{eff} and surface depletion region are very small, therefore a negligible response is seen for both the ZnO NRs/CdS heterojunction and the ZnO nanorods. Park et al have explained gas sensing by modulation of energy barrier at heterojunction[50,51]. In the presence of air, O_2 molecules adsorbed on the surface and take electrons from conduction band, forming ionic species such as O^-, O^{2-} and O_2^-[52,53].

Adsorption of oxygen species on the surface creates a depletion layer in the surface region of the ZnO NR/CdS due to the consumption of electrons in the surface region. When blue LED is illuminated on the ZnO NR/CdS heterojunction, electron-hole pairs are generated in the CdS shell. Some of the photo-generated electrons and holes

combine with each other, however the remaining photo-generated holes react with the negatively charged adsorbed oxygen ions on the surface. This can be expressed as follows[54]

$$h^+ (h\nu) + O_2^- (ads) \rightarrow O_2 (g) \quad (4.4)$$

$$h^+ (h\nu) + O^- (ads) \rightarrow ½\, O_2 (h\nu) \quad (4.5)$$

or

$$2h^+ (h\nu) + O^{2-} (ads) \rightarrow ½\, O_2 (h\nu) \quad (4.6)$$

As a result of blue LED illumination the surface depletion layer in the CdS shell of ZnO NR/CdS herterojunction reduces according to equation (4.4,4.5,4.6). When the sensor is exposed to NO_2 gas, NO_2 molecules adsorb on the CdS surface, and the remaining photo-generated electrons react with NO_2 molecules. NO_2 being an strong oxidizing gas, it acts as an electron acceptor, as shown in the following reaction[49]

$$NO_2 (g) + e^- (h\nu) \rightarrow 2\, NO (h\nu) + O^{2-} (h\nu) \quad (4.7)$$

Equation (4.7) broadens the surface depletion layer in the CdS resulting in an increase in the resistance of the sensor in the presence of NO_2. In the presence of light, more number of photo-generated charge carriers are available to react with NO_2, hence the response of a sensor towards NO_2 increases in the presence of light. Thus the surface depletion layer of CdS overlaps with the interface depletion layer and also WD (hv+ NO2) > WD (hv) > CdS layer width; where, WD is width of the interface depletion layer. Therefore, electron transport is modulated by the variation in the depletion layer of the ZnO NR/CdS heterojunction system. This suggests that the electron transport is facilitated or restricted by ZnO NR/CdS heterojunction thereby rendering sensing properties to the device. Hence, in the presence of light, large number of electron charge carriers are available to react with NO_2, therefore the change in the resistance of the sensor is more. This means that the energy barrier at the interface (ϕ_{eff}) is modulated more in the presence of light.

In the presence of the reducing H_2S gas, the ZnO NR/CdS heterojunction system does not exhibit response in the dark. However, it exhibits significant response in the

presence of blue LED illumination. It suggests that in the dark the interaction between the sensor element and H_2S gas is very feeble and change in ϕ_{eff} is negligible. However, in the presence of blue LED illumination, photo-generated holes could facilitate the interaction between H_2S and adsorbed oxygen species and/or holes and H_2S molecules. These interactions lead to injection of electrons into the conduction band of CdS and reduction in the surface depletion layer, thereby decreasing the height of the electron energy barrier at the interface of the ZnO NR/CdS heterojunction. Thus, depletion layer thickness reduces in presence of H_2S molecules as shown in Fig (4.5d). Therefore, conductance of the device increases with increase in the H_2S concentration. In the presence of blue LED illumination, improved response for NO_2 and H_2S is due to the interaction with the photo-generated charge carriers leading to modulation of the energy barrier at the ZnO NR/CdS interface. Thus, proper combinations of heterojunction can facilitate detection of toxic gases even at room temperature.

4.4. Conclusions

Visible light assisted gas sensing properties of the ZnO NR/CdS heterounction are investigated for NO_2 and H_2S. ZnO nanorods (~30-70 nm diameters) coated by 5-10 nm thick CdS layer by SILAR technique show significantly enhanced NO_2 and H_2S gas sensing in the presence of visible light as compared to ZnO. In the case of NO_2 the recovery (after turning off the gas input) is observed even in the presence of illumination, but in the case of H_2S the recovery is observed only by switching off blue LED illumination. The ZnO/CdS heterojunction exhibits recovery time of ~20-25 min for 500 ppm of NO_2 and H_2S.

4.5. References

[1] G. Korotcenkov, Metal oxides for solid-state gas sensors: What determines our choice?, Mat Sci Eng B-Solid, 139(2007) 1-23.

[2] N. Barsan, D. Koziej, U. Weimar, Metal oxide-based gas sensor research: How to?, Sensor Actuat B-Chem, 121(2007) 18-35.

[3] K.J. Choi, H.W. Jang, One-Dimensional Oxide Nanostructures as Gas-Sensing Materials: Review and Issues, Sensors-Basel, 10(2010) 4083-99.

[4] Z.H. Jing, J.H. Zhan, Fabrication and Gas-Sensing Properties of Porous ZnO Nanoplates, Adv Mater, 20(2008) 4547-51.

[5] S.H. Jeong, S. Kim, J. Cha, M.S. Son, S.H. Park, H.Y. Kim, et al., Hydrogen Sensing under Ambient Conditions Using SnO_2 Nanowires: Synergetic Effect of Pd/Sn Codeposition, Nano Lett, 13(2013) 5938-43.

[6] M. D'Arienzo, L. Armelao, C.M. Mari, S. Polizzi, R. Ruffo, R. Scotti, et al., Macroporous WO_3 Thin Films Active in NH_3 Sensing: Role of the Hosted Cr Isolated Centers and Pt Nanoclusters, J Am Chem Soc, 133(2011) 5296-304.

[7] L. Xu, R.F. Zheng, S.H. Liu, J. Song, J.S. Chen, B. Dong, et al., NiO@ZnO Heterostructured Nanotubes: Coelectrospinning Fabrication, Characterization, and Highly Enhanced Gas Sensing Properties, Inorg Chem, 51(2012) 7733-40.

[8] Y. Wang, J.L. Cao, S.R. Wang, X.Z. Guo, J. Zhang, H.J. Xia, et al., Facile Synthesis of Porous alpha-Fe_2O_3 Nanorods and Their Application in Ethanol Sensors, J Phys Chem C, 112(2008) 17804-8.

[9] U. Ozgur, Y.I. Alivov, C. Liu, A. Teke, M.A. Reshchikov, S. Dogan, et al., A comprehensive review of ZnO materials and devices, J Appl Phys, 98(2005).

[10] U. Ozgur, D. Hofstetter, H. Morkoc, ZnO Devices and Applications: A Review of Current Status and Future Prospects, P Ieee, 98(2010) 1255-68.

[11] Y.H. Sung, W.P. Liao, D.W. Chen, C.T. Wu, G.J. Chang, J.J. Wu, Room-Temperature Tailoring of Vertical ZnO Nanoarchitecture Morphology for Efficient Hybrid Polymer Solar Cells, Adv Funct Mater, 22(2012) 3808-14.

[12] X.W. Sun, J.Z. Huang, J.X. Wang, Z. Xu, A ZnO nanorod inorganic/organic heterostructure light-emitting diode emitting at 342 nm, Nano Lett, 8(2008) 1219-23.

[13] D.I. Suh, S.Y. Lee, J.H. Hyung, T.R. Kim, S.K. Lee, Multiple ZnO nanowires field-effect transistors, J Phys Chem C, 112(2008) 1276-81.

[14] M. Zhong, Y.B. Li, I. Yamada, J.J. Delaunay, ZnO-$ZnGa_2O_4$ core-shell nanowire array for stable photoelectrochemical water splitting, Nanoscale, 4(2012) 1509-14.

[15] H.M. Xiong, Z.D. Wang, D.P. Xie, L. Cheng, Y.Y. Xia, Stable polymer electrolytes based on polyether-grafted ZnO nanoparticles for all-solid-state lithium batteries, J Mater Chem, 16(2006) 1345-9.

[16] S.J. Shi, X.P. Zhuang, B.W. Cheng, X.Q. Wang, Solution blowing of ZnO nanoflake-encapsulated carbon nanofibers as electrodes for supercapacitors, J Mater Chem A, 1(2013) 13779-88.

[17] J. Mani, H. Sakeek, S. Habouti, M. Dietze, M. Es-Souni, Macro-meso-porous TiO_2, ZnO and ZnO-TiO_2-composite thick films. Properties and application to photocatalysis, Catal Sci Technol, 2(2012) 379-85.

[18] X.D. Wang, J. Zhou, J.H. Song, J. Liu, N.S. Xu, Z.L. Wang, Piezoelectric field effect transistor and nanoforce sensor based on a single ZnO nanowire, Nano Lett, 6(2006) 2768-72.

[19] Y.H. Tong, Y.C. Liu, L. Dong, D.X. Zhao, J.Y. Zhang, Y.M. Lu, et al., Growth of ZnO nanostructures with different morphologies by using hydrothermal technique, J Phys Chem B, 110(2006) 20263-7.

[20] L. Xu, Y.L. Hu, C. Pelligra, C.H. Chen, L. Jin, H. Huang, et al., ZnO with Different Morphologies Synthesized by Solvothermal Methods for Enhanced Photocatalytic Activity, Chem Mater, 21(2009) 2875-85.

[21] M. Raula, M.H. Rashid, T.K. Paira, E. Dinda, T.K. Mandal, Ascorbate-Assisted Growth of Hierarchical ZnO Nanostructures: Sphere, Spindle, and Flower and Their Catalytic Properties, Langmuir, 26(2010) 8769-82.

[22] X.Q. Yan, Y.S. Gu, X.M. Zhang, Y.H. Huang, J.J. Qi, Y. Zhang, et al., Doping Effect on High-Pressure Structural Stability of ZnO Nanowires, J Phys Chem C, 113(2009) 1164-7.

[23] Z.G. Yu, H. Gong, P. Wu, Dopant sources choice for formation of p-type ZnO Phosphorus compound sources, Chem Mater, 17(2005) 852-5.

[24] N.C.S. Selvam, J.J. Vijaya, L.J. Kennedy, Effects of Morphology and Zr Doping on Structural, Optical, and Photocatalytic Properties of ZnO Nanostructures, Ind Eng Chem Res, 51(2012) 16333-45.

[25] N.S. Ramgir, M. Ghosh, P. Veerender, N. Datta, M. Kaur, D.K. Aswal, et al., Growth and gas sensing characteristics of p- and n-type ZnO nanostructures, Sensor Actuat B-Chem, 156(2011) 875-80.

[26] C.S. Rout, S.H. Krishna, S.R.C. Vivekchand, A. Govindaraj, C.N.R. Rao, Hydrogen and ethanol sensors based on ZnO nanorods, nanowires and nanotubes, Chem Phys Lett, 418(2006) 586-90.

[27] X.G. Wen, Y.P. Fang, Q. Pang, C.L. Yang, J.N. Wang, W.K. Ge, et al., ZnO nanobelt arrays grown directly from and on zinc substrates: Synthesis, characterization, and applications, J Phys Chem B, 109(2005) 15303-8.

[28] Y. Zhang, J.Q. Xu, Q. Xiang, H. Li, Q.Y. Pan, P.C. Xu, Brush-Like Hierarchical ZnO Nanostructures: Synthesis, Photoluminescence and Gas Sensor Properties, J Phys Chem C, 113(2009) 3430-5.

[29] S.S. Badadhe, I.S. Mulla, Effect of aluminium doping on structural and gas sensing properties of zinc oxide thin films deposited by spray pyrolysis, Sensor Actuat B-Chem, 156(2011) 943-8.

[30] W.Q. Li, S.Y. Ma, Y.F. Li, G.J. Yang, Y.Z. Mao, J. Luo, et al., Enhanced ethanol sensing performance of hollow ZnO-SnO_2 core-shell nanofibers, Sensor Actuat B-Chem, 211(2015) 392-402.

[31] X. Liu, J.B. Sun, X.T. Zhang, Novel 3D graphene aerogel-ZnO composites as efficient detection for NO_2 at room temperature, Sensor Actuat B-Chem, 211(2015) 220-6.

[32] R.J. Oweis, B.A. Albiss, M.I. Al-Widyan, M.A. Al-Akhras, Hybrid Zinc Oxide Nanorods/Carbon Nanotubes Composite for Nitrogen Dioxide Gas Sensing, J Electron Mater, 43(2014) 3222-8.

[33] S.W. Fan, A.K. Srivastava, V.P. Dravid, UV-activated room-temperature gas sensing mechanism of polycrystalline ZnO, Applied Physics Letters, 95(2009).

[34] T. Wagner, C.D. Kohl, C. Malagu, N. Donato, M. Latino, G. Neri, et al., UV light-enhanced NO_2 sensing by mesoporous In2O3: Interpretation of results by a new sensing model, Sensor Actuat B-Chem, 187(2013) 488-94.

[35] S. Park, S. An, Y. Mun, C. Lee, UV-activated gas sensing properties of ZnS nanorods functionalized with Pd, Current Applied Physics, 14(2014) S57-S62.

[36] S. Park, S. An, Y. Mun, C. Lee, UV-Enhanced NO2 Gas Sensing Properties of SnO_2-Core/ZnO-Shell Nanowires at Room Temperature, ACS Applied Materials & Interfaces, 5(2013) 4285-92.

[37] J.L. Zhai, L.L. Wang, D.J. Wang, H.Y. Li, Y. Zhang, D.Q. He, et al., Enhancement of Gas Sensing Properties of CdS Nanowire/ZnO Nanosphere Composite Materials at Room Temperature by Visible-Light Activation, ACS Applied Materials & Interfaces, 3(2011) 2253-8.

[38] J.L. Zhai, D.J. Wang, L. Peng, Y.H. Lin, X.Y. Li, T.F. Xie, Visible-light-induced photoelectric gas sensing to formaldehyde based on CdS nanoparticles/ZnO heterostructures, Sensor Actuat B-Chem, 147(2010) 234-40.

[39] Z. Yang, L.J. Guo, B.Y. Zu, Y.A. Guo, T. Xu, X.C. Dou, CdS/ZnO Core/Shell Nanowire-Built Films for Enhanced Photodetecting and Optoelectronic Gas-Sensing Applications, Adv Opt Mater, 2(2014) 738-45.

[40] O. Game, U. Singh, A.A. Gupta, A. Suryawanshi, A. Banpurkar, S. Ogale, Concurrent synthetic control of dopant (nitrogen) and defect complexes to realize broadband (UV-650 nm) absorption in ZnO nanorods for superior photo-electrochemical performance, J Mater Chem, 22(2012) 17302-10.

[41] G. Korotcenkov, Gas response control through structural and chemical modification of metal oxide films: state of the art and approaches, Sensor Actuat B-Chem, 107(2005) 209-32.

[42] I. Shalish, H. Temkin, V. Narayanamurti, Size-dependent surface luminescence in ZnO nanowires, Phys Rev B, 69(2004).

[43] D. Wang, H.W. Seo, C.C. Tin, M.J. Bozack, J.R. Williams, M. Park, et al., Lasing in whispering gallery mode in ZnO nanonails, J Appl Phys, 99(2006).

[44] Z.M. Liao, H.Z. Zhang, Y.B. Zhou, J. Xu, J.M. Zhang, D.P. Yu, Surface effects on photoluminescence of single ZnO nanowires, Phys Lett A, 372(2008) 4505-9.

[45] D. Li, J. Zhang, Q. Xiong, Surface depletion induced quantum confinement in CdS nanobelts, Acs Nano, 6(2012) 5283-90.

[46] N. Barsan, U. Weimar, Conduction model of metal oxide gas sensors, J Electroceram, 7(2001) 143-67.

[47] R. Calarco, M. Marso, T. Richter, A.I. Aykanat, R. Meijers, A. vd Hart, et al., Size-dependent photoconductivity in MBE-grown GaN-nanowires, Nano Lett, 5(2005) 981-4.

[48] M. Purahmad, M.A. Stroscio, M. Dutta, A numerical analysis on the effect of piezoelectric charges on the surface depletion layer of ZnO nanowires, 15th International workshop on computational electronics (IWCE)2012.

[49] T. Weis, R. Lipperheide, U. Wille, S. Brehme, Barrier-controlled carrier transport in microcrystalline semiconducting materials: Description within a unified model, J Appl Phys, 92(2002) 1411-8.

[50]S. Park, S. An, Y. Mun, C. Lee, UV-enhanced NO2 gas sensing properties of SnO2-core/ZnO-shell nanowires at room temperature, ACS Applied Materials & Interfaces, 5(2013) 4285-92.

[51] S. Park, S. An, H. Ko, C. Jin, C. Lee, Enhanced Gas Sensing Properties of Bi2O3-Core/In2O3-Shell Nanorod Gas Sensors, B Korean Chem Soc, 33(2012) 3368-72.

[52] Z.-M. Liao, H.-Z. Zhang, Y.-B. Zhou, J. Xu, J.-M. Zhang, D.-P. Yu, Surface effects on photoluminescence of single ZnO nanowires, Phys Lett A, 372(2008) 4505-9.

[53] N. Yamazoe, G. Sakai, K. Shimanoe, Oxide semiconductor gas sensors, Catal Surv Asia, 7(2003) 63-75.

[54] S.-W. Fan, A.K. Srivastava, V.P. Dravid, UV-activated room-temperature gas sensing mechanism of polycrystalline ZnO, Applied Physics Letters, 95(2009) 142106.

Chapter 5

Facile synthesis and gas sensing properties of FeV_3O_8 nanosheets

Vertically aligned randomly oriented nanosheets of FeV_3O_8 on the fluorine doped tin oxide (FTO) are synthesized by simple hydrothermal technique. The dimensions of FeV_3O_8 nanosheets are ~0.5 and 3 µm. The potential use of FeV_3O_8 nanosheets in gas sensor application is discussed in this chapter. Systematic gas sensing study of FeV_3O_8 nanosheets was performed for NH_3, CO, H_2S and NO_2 at different operating temperatures between 50^0 and 350^0C. The FeV_3O_8 nanosheets exhibit good response and selectivity towards H_2S at low operating temperature of 200^0C.

5.1 Introduction

Exceptional industrial development in the last few decades has created major concern over constant release of harmful gases and their adverse impact on environmental and biological systems. Hence it is a primary objective to monitor and control such harmful gases. It is an endless quest to develop gas sensor with superior qualities to trace these harmful emissions. Toxic gas sensors based on semiconductor metal oxides have drawn tremendous attention due to good response, ease of fabrication, low cost, and high stability[1]. Binary metal oxides such as ZnO[2], SnO_2[3], Fe_2O_3[4] and WO_3[5] have been widely explored but have an issue related to selectivity and high operating temperature. Therefore, doped system[6], composites[7], core/shell[8], have been explored to improve sensitivity, selectivity and lower operating temperature of gas sensors. Recently, gas sensing properties of ternary metal oxides ($M_xM_yO_z$) such as Zn_2SnO_4[9], $ZnSnO_3$[10], $CdIn_2O_4$[11], $ZnCo_2O_4$[12] $LaFeO_3$[13] Bi_2WO_6[14], $Ag_2V_4O_{11}$[15]etc have attracted tremendous attention.

As transition metal oxides need low energy to fluctuate between the different oxidation states; provide an opportunity to detect harmful emission at relatively lower operating temperature. Hence, proper combination of ternary systems offer the possibility of selective tracing of desired test gas over other at relatively low operating temperature due to their electronic correlation and cooperative effects. Among various transition metal oxides; vanadium oxide is an important class of materials owing to their applicability in different fields such as catalysis[16], field emission[17] and batteries[18]etc. Hence many promising ternary metal oxides based on vanadium oxides such as $AgVO_3$[19-20], $Ag_2V_4O_{11}$[20], $LaVO_4$,[21], $BiVO_4$[22], $CeVO_4$[23], $PrVO_4$[24] $FeVO_4$[25], $GdVO_4$[26], $NdVO_4$[27], NaV_6O_{15}[28]etc have been synthesized and characterized so far. An iron vanadium oxide is an important ternary system due to their low band gap (~2 eV), variable oxidation states and can be synthesized into nanoparticles[29], nanorods[30]and nanosheets[31]. Hitherto, there is a single report on FeV_3O_8[32] ultrathin nanosheets and nanoparticles synthesis and their promising use for photocatalytic dye degradation. Herein, we have directly grown FeV_3O_8 nanosheets in an insulating gap of (~150 μm) on FTO substrates and

directly used it for gas sensing study. FeV_3O_8 nanosheets exhibit selectively high response for hydrogen sulfide gas at 200°C.

5.2 Experimental

5.2.1 Synthesis of FeV_3O_8 nanosheets

All the chemicals of analytical grade were used. In typical synthesis chemicals such as ammonium metavanadate (NH_4VO_3), Ferric nitrate $Fe(NO_3)_3$, nitric acid, and hydrochloric acid were used to obtain FeV_3O_8 nanosheets. In the round bottom flask, 0.234 g of NH_4VO_3 was added in de-ionized water (35 ml) and kept at 70°C with continuous stirring till solution become clear solution. An air condenser was fitted to the round bottom flask to prevent loss of solvent during the progress of the reaction. Ferric nitrate solution (0.808 g of $Fe(NO_3)_3$ in 35 ml of DI water) was added to the NH_4VO_3 reaction mixture dropwise. An instantly yellow particles suspension was formed. This suspension was further stirred for a few hours to ensure the completion of reaction. The pH of the solution observed to be 3. The reaction mixture is allowed to cool to room temperature then concentrated HCl was added dropwise to bring down the pH to 1. The particles in the suspension dissolved and a clear yellow solution was obtained. The above solution is then transferred to a 100 ml teflon lined autoclave. The FTO substrates were first cleaned and heated at 450°C to remove all impurities. FTO substrates were then fixed to a glass slide using teflon tape and dipped in autoclave containing above reaction mixture with FTO side facing to the bottom of the autoclave. The autoclave was then heated for 160°C for 3 h. FeV_3O_8 was then grown on FTO substrates during the hydrothermal process. The FTO substrates were removed and a deposition of a thin layer of brown FeV_3O_8 was observed on them. The films so obtained were then annealed at 450°C for 1 h with a heating rate of $5^0C\ min^{-1}$.

5.2.2 Characterization

The FeV_3O_8 nanosheets were characterized for crystal structure and phase formation by X-ray diffraction (XRD) analysis. The X-ray diffraction data were recorded on a Philips X'Pert PRO operating at a voltage of 40 kV diffractometer using Cu-Kα (λ = 0.154056 nm) radiation in the (2θ) range between 20^0 and 80^0. Morphological analysis was carried out by field emission scanning electron microscopic technique

(FESEM). FESEM images of FeV_3O_8 films were acquired from NOVA NANOSEM 450 of FEI. Transmission electron micrographs and high-resolution transmission electron micrographs of samples were captured using HR-TEM, FEI Tecnai 300. Optical band gap of FeV_3O_8 nanosheets was derived by diffused reflectance spectroscopy using Jasco V 570 spectrophotometer. Raman analysis of FeV_3O_8 nanosheets was carried out using a Horiba JobinYvon Lab RAM HR system.

5.2.3 Gas sensing measurements

For gas sensing study, FeV_3O_8 nanosheets were directly grown in an insulating gap (~150 μm) at center of FTO substrates. These FeV_3O_8nanosheetdevices were stabilized in air at 350^0C for 24 h before gas sensing experiments being performed. Gas sensing performance of FeV_3O_8 thin films were carried out at different operating temperatures. Mass flow controllers (MFCs) (Alicat Scientific, USA make) were used to obtain the desired concentration of test gases. Here, air is used as carrier gas. The electrical properties of the sensor were measured using a Keithley 2612A source meter. The gas response (S) is the ratio of sensor current in the air atmosphere (I_a) to its current in the test gas (I_g) for oxidizing gas and vice-versa for reducing gas(see equation 4.1, 4.2). Fig. 5.1 (a) shows the device architecture used for gas sensor.

5.3 Results and Discussion

5.3.1 Structural and morphological study:

The typical device architecture used for gas sensing of FeV_3O_8 nanosheets is shown in Fig. 5.1 (a). Figure 5.1(b) shows X-ray diffraction pattern of FeV_3O_8 nanosheets. All diffraction peaks can be indexed as end centred monoclinic FeV_3O_8 phase with lattice parameters a=12.13 Å, b=3.679 Å, c=6.547Å [JCPDS file No. 75-0811]. The XRD pattern indicates crystalline nature and phase purity of the FeV_3O_8 nanosheets. The optical properties of FeV_3O_8 nanosheets were analyzed by diffused reflectance of FeV_3O_8 nanosheets grown on FTO substrate [Fig. 5.1(c)]. Fig. 5.1(c) shows variation in % reflectance vs wavelength of FeV_3O_8 on FTO. FeV_3O_8 nanosheets exhibit a gradual drop in the reflectance in range 800-570 nm.

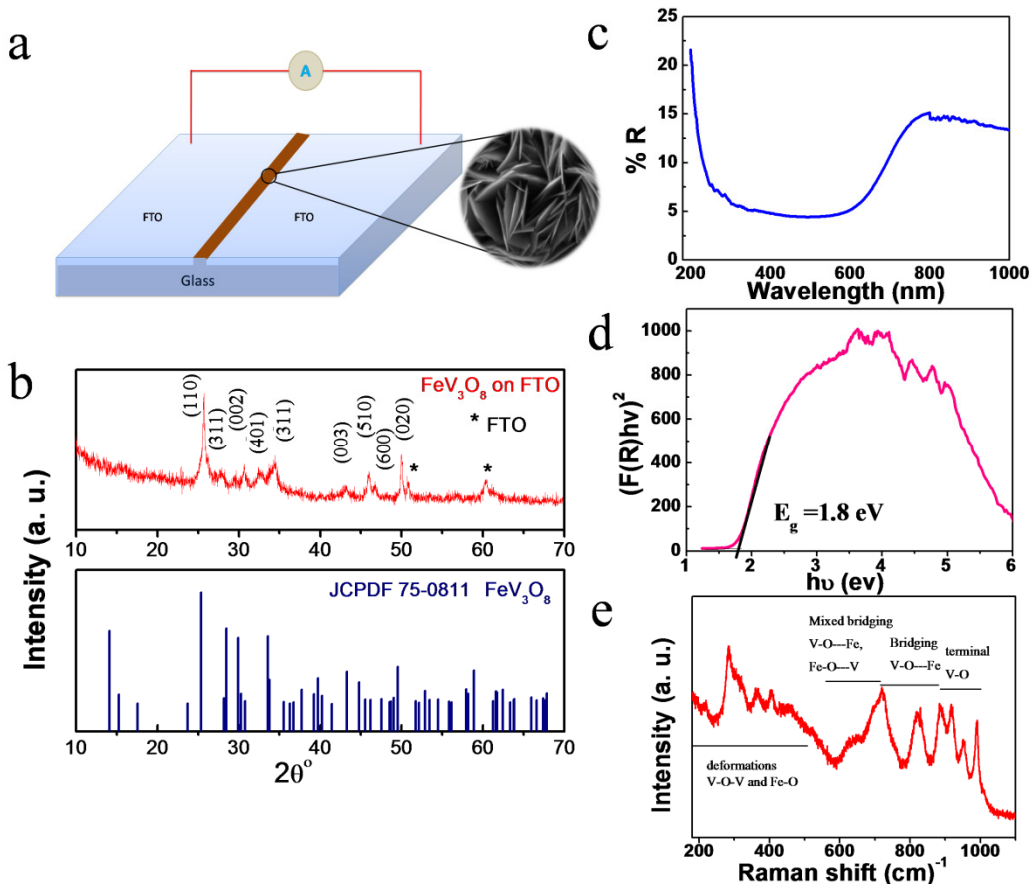

Figure 5.1: (a) Device architecture used for gas sensor,(b)X-ray diffraction pattern (c) diffused reflectance spectrum (d) Tauc's plot (e) Raman spectra of FeV_3O_8 nanosheets grown on FTO substrate.

The band gap for FeV_3O_8 nanosheets was obtained from Tauc's plot by extrapolating the tangent as shown in Fig. 5.1(c)]. FeV_3O_8 nanosheets exhibit band gap ~1.8 eV. FeV_3O_8 nanoplatelates (~10 nm in size) reported by Zhang et al. shows the band gap (2.23 eV) however such small variation of ~0.4 eV can be attributed to morphology and quantum size confinement effects. The Raman analysis of FeV_3O_8 nanosheets were used to examine of various stretching modes. Fig. 5.1(e) shows raman spectra of FeV_3O_8 nanosheet. Here different modes have been assigned based on previous study of iron vanadium oxide[33]. Raman bands are observed from four different groups like terminal V-O stretching which lies between 990-885 cm^{-1}, bridging V-O---Fe stretching which arises between 880-720 cm^{-1}, mixed bridging of V-O---Fe and V---O---Fe stretching which observed in the range 700-550 cm^{-1}, and deformations of V-O-V and Fe-O stretching can be seen between below 550 cm^{-1}.

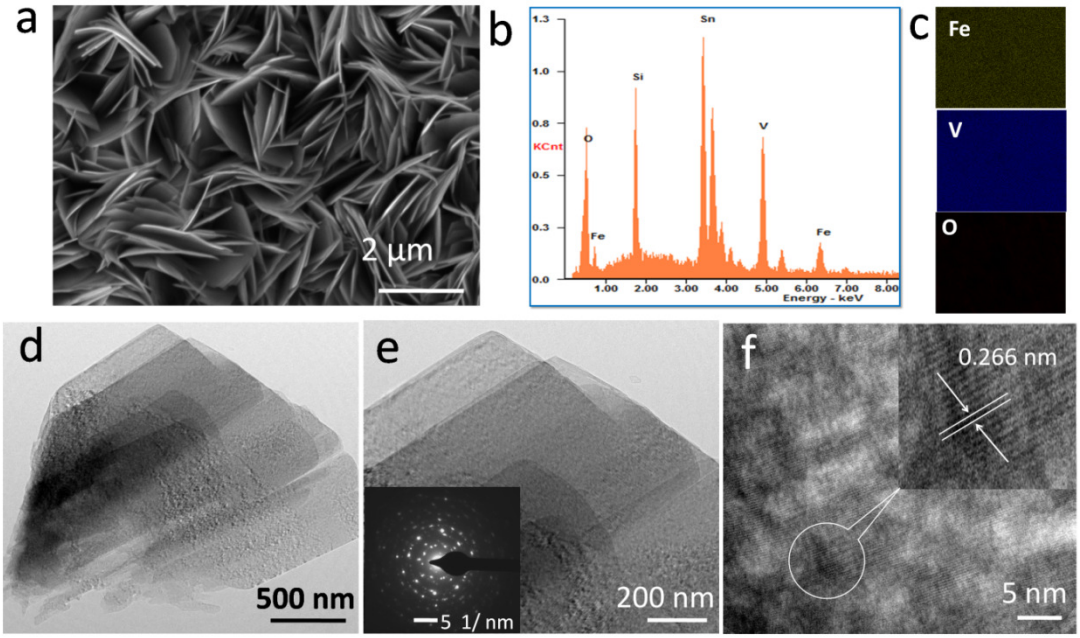

Figure 5.2: FESEM image (a), EDX micrograph (c) and elemental scanning of Fe, V, O and corresponding ratio of elements (d, e) TEM image of FeV_3O_8 nanosheet, inset SAED pattern (f) HR-TEM of FeV_3O_8 nanosheets grown on FTO substrate.

FESEM images of FeV_3O_8 nanosheets are shown in Fig. 5.2 (a). SEM images show that uniform randomly oriented vertically aligned nanosheets growth of FeV_3O_8 nanostructures on FTO using simple hydrothermal process. Growth of FeV_3O_8 nanosheets was found to be uniform throughout the substrate. The FeV_3O_8 nanosheets are smooth, uniform with length in the range of 0.5-3 µm. These nanosheets are closely spaced together forming compact irregular stack of nanosheets with nanometre to few micrometer sized spacing between adjacent nanosheets which help in easy access of nanosheets to analyte molecules. The FeV_3O_8 nanosheets were further analysed by EDX to determine elemental stoichiometry [Fig. 5.2(b)]. The ratio of Fe:V is found to be 1: 3.14 is very close to Fe and V ratio (1:3) of FeV_3O_8. The elemental scanning map of FeV_3O_8 nanosheets for Fe, V, and O is shown in Fig. 5.2(c). The uniform throughout distribution of elemental mapping scan of Fe, V and O supports formation FeV_3O_8. In order to get more insight of FeV_3O_8 nanosheets, the low and high resolution TEM analysis were performed. The dimensions of FeV_3O_8 nanosheets are in between ~0.5 µm and 1.5 µm[Fig. 5.2 (d)]. The magnified view of nanosheets reveals formation of thin uniform nanosheets[Fig. 5.2(e)]. The selected area electron diffraction (SAED) pattern of FeV_3O_8 nanosheets is shown in the inset

of Fig. 5.2(e). The diffused rings and the bright spots indicate the polycrystalline nature of FeV_3O_8 nanosheets. The high resolution (HR) TEM micrograph of FeV_3O_8 nanosheet exhibits lattice spacing of about 0.266 nm[Fig 5.2(f)], which corresponds to (310) plane of FeV_3O_8 which is good in agreement with JCPDS data.

5.3.2 Gas sensing study

Gas sensing behavior of FeV_3O_8 nanosheets directly grown on an insulating gap of 150 µm, attained on the FTO was studied. For gas sensing studies, gas cylinder of specific gases were purchased from a local vendor. To be specific, 1% test gas was diluted in 99% of N_2. The desired concentration of test gas is obtained by using mass flow controllers (MFC). The gas sensing behavior of FeV_3O_8 nanosheets was measured for different oxidizing and reducing gases such as NO_2, CO, NH_3 and H_2S.

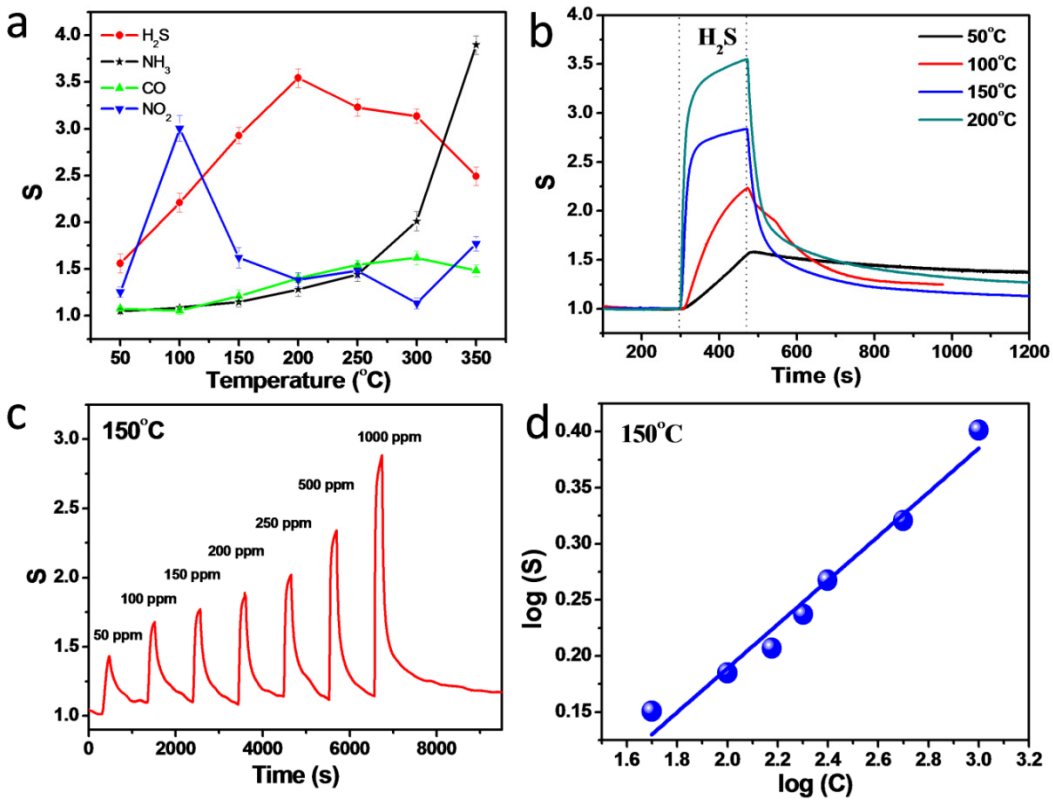

Figure 5.3: (a) Gas response study for H_2S, NH_3, CO and NO_2 at different operating temperatures between 50^0C and 350^0C (b) transient H_2S gas response for temperature between 50-200^0C, (c) H_2S gas response of FeV_3O_8 nanosheets with concentration between 50 ppm and 1000 ppm (d) corresponding log (S) vs log (C) plot at 150°C.

The sensitivity of a gas sensor is greatly depends on the operating temperature. Hence, the sensitivity of the FeV_3O_8 nanosheets was evaluated as a function of operating temperature. Fig. 5.3(a) shows gas response behavior of FeV_3O_8 nanosheets towards 1000 ppm these gases at different operating temperatures. FeV_3O_8 nanosheets show maximum response to NO_2 at 100°C and further drastically decreased with increase in temperature. However for H_2S, FeV_3O_8 nanosheets show increase in response with operating temperature upto 200°C and further gradually decreases with further increase in operating temperature. Specifically, FeV_3O_8 nanosheets exhibit maximum response to H_2S at 200°C. FeV_3O_8 nanosheets depict insignificant response over the entire range of temperature towards CO. For NH_3, FeV_3O_8 nanosheets exhibit negligible response till 300°C and further rise in response observed at 350°C. Such a temperature dependent sensitivity for different gases reveals that optimum activation energy is necessary for different reactions to take place effectively. FeV_3O_8 nanosheets exhibit good selectivity for H_2S over other test gases for operating temperature between 150°C-250°C (Fig. 5.3. (a)).

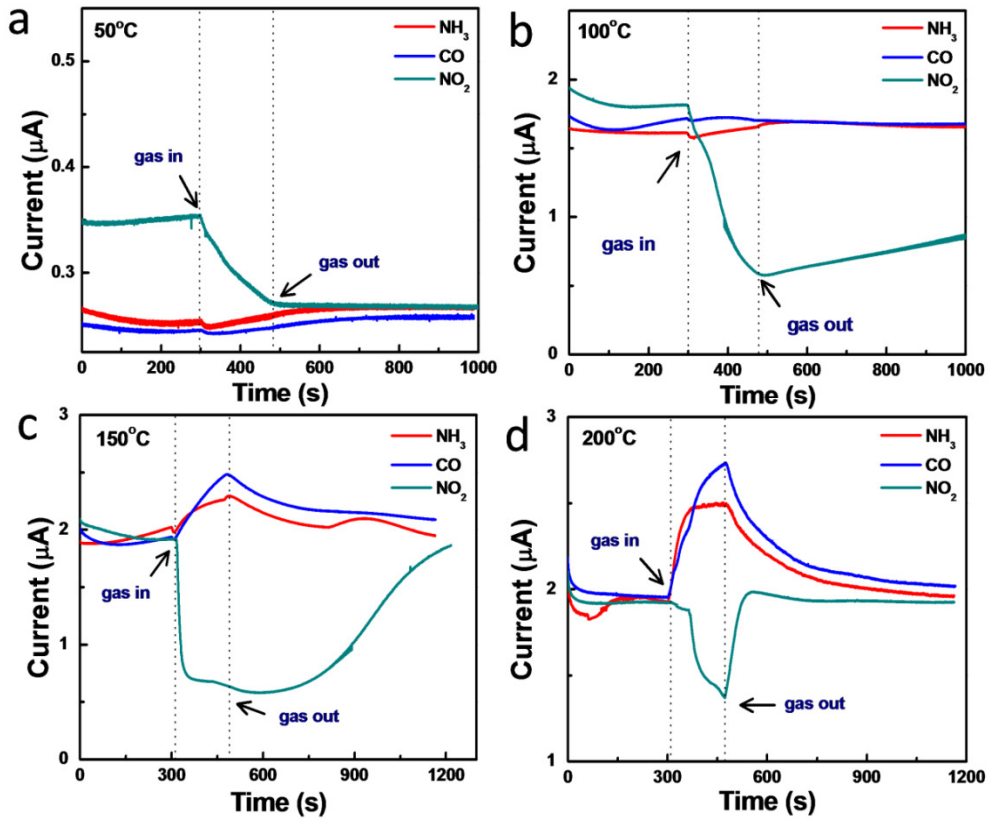

Figure 5.4: (a) Response and recovery behaviour of FeV_3O_8 nanosheets for NH_3, CO and NO_2 at different operating temperatures between 50°C and 350°C.

Fig. 5.4 shows transient gas response of FeV_3O_8 for NO_2, CO, NH_3. It shows negligible response towards NH_3 and CO below 250°C. At 100°C, the device shows the maximum response to NO_2, however recovery is incomplete. For temperature (>100°C), FeV_3O_8 nanosheets exhibit negligible response to NO_2. Fig. 5.3 (b) shows response and recovery behavior of FeV_3O_8 nanosheets for H_2S gases with increase in temperature till 200°C (For clarity, transient behavior for H_2S for temperature >200°C is not included here and is shown in Fig. 5.5. For hydrogen sulfide, device shows slow response and recovery below 100°C. For temperature (>100°C), FeV_3O_8 nanosheets response and recovery is improved for H_2S.

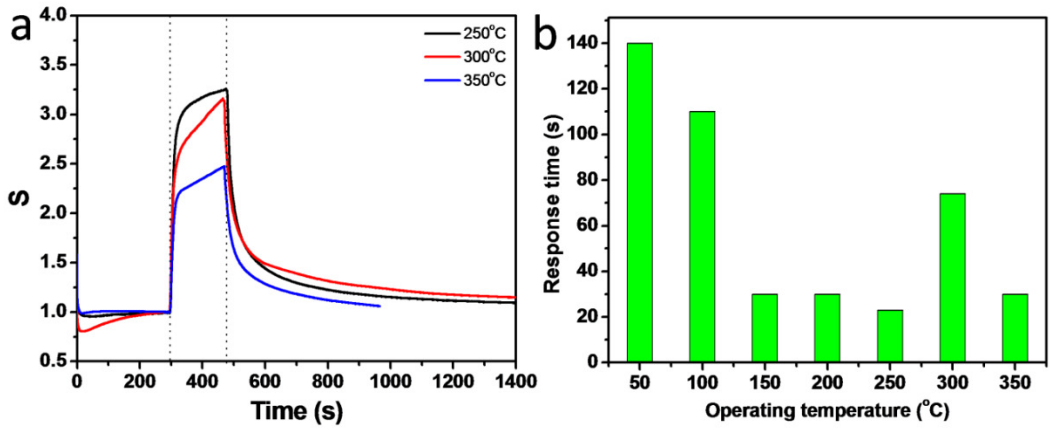

Figure 5.5: (a) H_2S response behavior of FeV_3O_8 at different operating temperatures between 250°C and 350°C, (b) H_2S gas response time of FeV_3O_8 nanosheets for operating temperature between 50 and 350°C.

Specifically, it exhibits response time (t) (Here, t is defined as when gas response reaches to 90% of final value) is of ~ 30 s for temperature between 150-250°C where optimum H_2S response is observed Fig. 5.5(b). Thus, FeV_3O_8 demonstrates maximum response and also a good response and recovery behavior for H_2S compared to other test gases. Moreover, it is observed that FeV_3O_8 nanosheets display better selectivity at comparatively lower temperature of 150°C. Further concentration dependent H_2S response was studied at this temperature [Fig. 5.3 (c)]. It can be seen that with increase in concentration of H_2S, FeV_3O_8 nanosheets exhibit increase in gas response. FeV_3O_8 nanosheets also exhibit almost complete recovery after every cycle.

The gas response (S) of FeV_3O_8 can be expressed empirically as $S = 1 + A_g P_g^{\beta}$ where, A_g is prefactor, $P_g$is partial pressure of analyte gas (i.e concentration of analyte gas(C)), which is directly proportional to the concentration of anlayte, and β is exponent of P_g. Generally, β has value either 0.5 or 1. The values can be derived from surface interaction of analyte gas and chemisorbed oxygen [34-35]. Hence response (S) should be linear with logarithmic concentration (C) of analyte gas. Fig.5.3 (d) represents log(S) vs log(C). The graph shows linear response with increase in concentration of H_2S. The value of β obtained from a linear fit to Fig. 5.3(d) is ~0.19. The disorder and insensitive region could give rise to deviation from ideal value[34]. Such a temperature dependent response can be governed by many factors such as adsorbed oxygen species, available active sites, energy of adsorption of analyte etc. Different oxygen species form on the surface semiconductor oxides with increase in temperature namely chemisorbed O_2^-, O^-, O^{2-} species. It suggests that with increase in temperature, surface becomes more oxidized. At lower temperature, (here 100^0C), NO_2 being an oxidizing gas favorably gets adsorbed on surface and extract an electron from conduction band and the current of the material decreases[Fig.5.4]. On further increase in temperature, FeV_3O_8 nanosheets get more oxidized and available active sites for adsorption of NO_2 reduce significantly. Hence above 100^0C, FeV_3O_8 nanosheets exhibit sudden fall in response for NO_2. However, in case of H_2S, being reducing gas its response is increased with temperature due to surface reactions with adsorbed oxygen ions lead to release back electrons in conduction band. Thus the overall current of sensor increases and can be seen from Fig. 5.3 (b). The detailed gas sensing mechanism in the case of H_2S can be explained by using Fig. 5.6. The H_2S gas sensing mechanism of n-type semiconductor metal oxides can be explained by charge modulation due to surface reaction occurring between test gas and adsorbed oxygen species. In presence of air, O_2 molecules get adsorbed on the surface of FeV_3O_8 nanosheets and thus generate chemisorbed O_2^-, O^- and/or O^{2-} species depending on operating temperature by capturing free electrons from the conduction band of FeV_3O_8. As a result the charge carrier concentration decreases and the depletion layer is formed on the surface of FeV_3O_8, which reduces the current of the material. When H_2S is introduced into the test chamber, H_2S molecules react with the chemisorbed oxygen (O^{2-} or O^-) species that are present on the surface of FeV_3O_8 to form SO_2 and H_2O (see equation-3I.4).

Thus, the trapped electrons are released back into the materials leads to an increase in electron concentration in the conduction band and hence there is an increase in overall conductivity of the material.

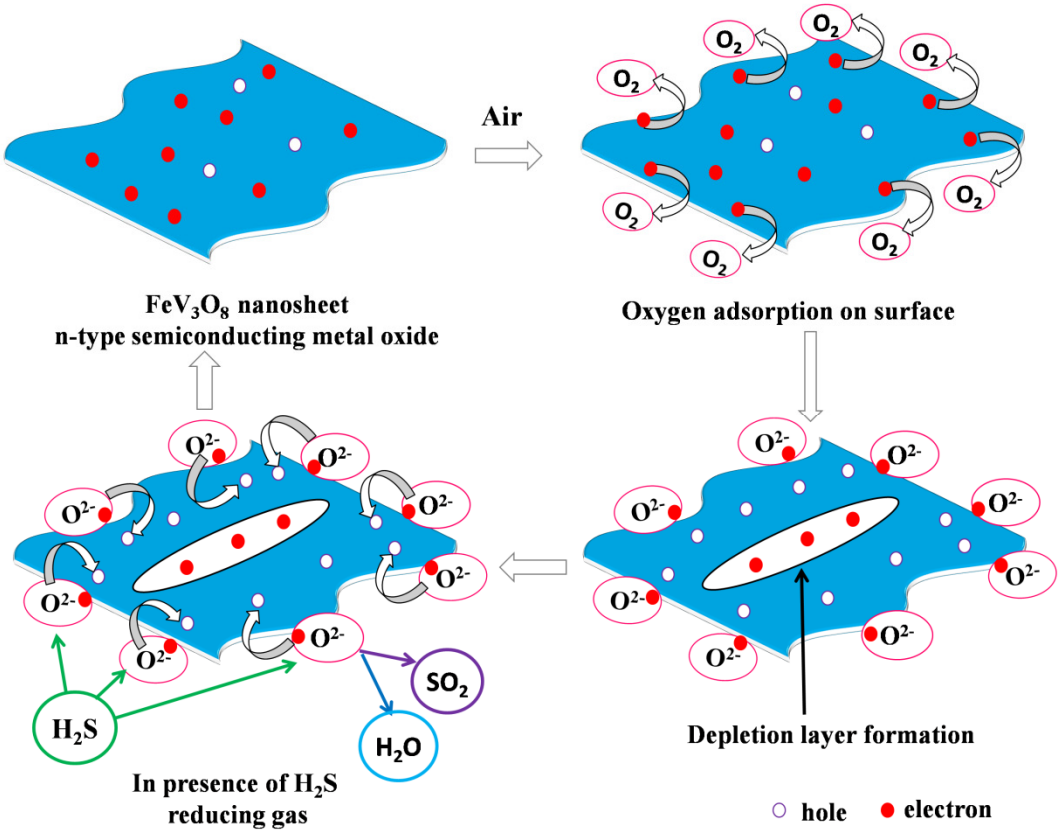

Figure 5.6: Pictorial representation of H_2S sensing mechanism of FeV_3O_8 nanosheets (n-type semiconductor metal oxide).

In the present case, FeV_3O_8 nanosheets exhibit better and selective response towards H_2S. In this ternary system, FeV_3O_8; Fe is in Fe^{3+} and two V are in V^{+4} and one in V^{5+}. This suggests that here Fe and V are in their highest oxidation states. Therefore both of these elements support adsorption of H_2S and favor subsequent reaction. The ionic radii of these elements are as follows: Fe in Fe^{3+} (64.5 pm), V in V^{+4} (58 pm) and in V^{5+} (54 pm), and S^{2-} (184 pm). However, on the basis of hard soft acid base (HSAB) concept, as ionic radii of vanadium are comparatively smaller than iron thus, H_2S molecules preferentially adsorb on iron over vanadium and may further facilitate the reaction. Many other factors like crystal defects, quantum confinement, could contribute in sensing performance. Hence only HSAB concept may not be the only

reason of better response of FeV_3O_8 nanosheets for H_2S but cooperative effect of both metals might be playing a crucial role.

5.4 Conclusions

In summary, we have developed one-step simple and efficient template free hydrothermal approach for the synthesis of uniform FeV_3O_8 nanosheets. Randomly oriented vertically aligned FeV_3O_8 nanosheets were directly grown on the FTO. The FeV_3O_8 nanosheets exhibit good selectivity, response and recovery toward H_2S at comparatively low temperature of 200^0C.

5.5 References

[1] G. Korotcenkov, Metal oxides for solid-state gas sensors: What determines our choice?, Mat Sci Eng B-Solid, 139(2007) 1-23.

[2] J. Kim, K. Yong, Mechanism Study of ZnO Nanorod-Bundle Sensors for H_2S Gas Sensing, J Phys Chem C, 115(2011) 7218-24.

[3] A.S. Ryzhikov, A.N. Shatokhin, F.N. Putilin, M.N. Rurayantseva, A.M. Gaskov, M. Labeau, Hydrogen sensitivity of SnO_2 thin films doped with Pt by laser ablation, Sensor Actuat B-Chem, 107(2005) 387-91.

[4] J.M. Ma, L. Mei, Y.J. Chen, Q.H. Li, T.H. Wang, Z. Xu, et al., alpha-Fe_2O_3 nanochains: ammonium acetate-based ionothermal synthesis and ultrasensitive sensors for low-ppm-level H_2S gas, Nanoscale, 5(2013) 895-8.

[5] J. Li, J.W. Zhu, X.H. Liu, Synthesis, characterization and enhanced gas sensing performance of WO_3 nanotube bundles, New J Chem, 37(2013) 4241-9.

[6] J. Wang, L.M. Wei, L.Y. Zhang, J. Zhang, H. Wei, C.H. Jiang, et al., Zinc-doped nickel oxide dendritic crystals with fast response and self-recovery for ammonia detection at room temperature, J Mater Chem, 22(2012) 20038-47.

[7] N.D. Hoa, S.A. El-Safty, Highly sensitive and selective volatile organic compound gas sensors based on mesoporous nanocomposite monoliths, Anal Methods-Uk, 3(2011) 1948-56.

[8] X.Y. Xue, L.L. Xing, Y.J. Chen, S.L. Shi, Y.G. Wang, T.H. Wang, Synthesis and H_2S sensing properties of CuO-SnO_2 core/shell PN-junction nanorods, J Phys Chem C, 112(2008) 12157-60.

[9] Z. Chen, M.H. Cao, C.W. Hu, Novel Zn_2SnO_4 Hierarchical Nanostructures and Their Gas Sensing Properties toward Ethanol, J Phys Chem C, 115(2011) 5522-9.

[10] Y. Zeng, T. Zhang, H.T. Fan, G.Y. Lu, M.H. Kang, Synthesis and gas-sensing properties of $ZnSnO_3$ cubic nanocages and nanoskeletons, Sensor Actuat B-Chem, 143(2009) 449-53.

[11] Y.L. Liu, W. Wang, T.Q. Lin, F.H. Liao, F.Q. Huang, J.H. Lin, Enhanced Cl_2 sensing performance by decorating discrete Au nanoparticles on octahedral $CdIn_2O_4$ crystals, Crystengcomm, 15(2013) 2929-33.

[12] X. Zhou, W. Feng, C. Wang, X.L. Hu, X.W. Li, P. Sun, et al., Porous $ZnO/ZnCo_2O_4$ hollow spheres: synthesis, characterization, and applications in gas sensing, J Mater Chem A, 2(2014) 17683-90.

[13] Y.M. Zhang, Q.J. Liu, J. Zhang, Q. Zhu, Z.Q. Zhu, A highly sensitive and selective formaldehyde gas sensor using a molecular imprinting technique based on $Ag\text{-}LaFeO_3$, J Mater Chem C, 2(2014) 10067-72.

[14] D.J. Wang, Y.Z. Zhen, G.L. Xue, F. Fu, X.M. Liu, D.S. Li, Synthesis of mesoporous Bi_2WO_6 architectures and their gas sensitivity to ethanol, J Mater Chem C, 1(2013) 4153-62.

[15] Y. Liang, L.F. Zhu, P. Liu, H.B. Li, J. Xiao, X.W. Ji, et al., $Ag_2V_4O_{11}$ nanostructures for highly ethanol sensitive performance, Crystengcomm, 15(2013) 6131-5.

[16] K. Syslova, P. Cicmanec, J. Tichy, Mixed vanadium-molybdenum oxides as catalysts for partial oxidation of crotonaldehyde, Oxid Commun, 30(2007) 842-8.

[17] J.S. Ke, S.F. Weng, M.C. Wu, C.S. Lee, Controlled synthesis of VO_2(R), VO_2(B), and V_2O_3 vanadium-oxide nanowires, J Nanopart Res, 15(2013).

[18] S. Tepavcevic, H. Xiong, V.R. Stamenkovic, X.B. Zuo, M. Balasubramanian, V.B. Prakapenka, et al., Nanostructured Bilayered Vanadium Oxide Electrodes for Rechargeable Sodium-Ion Batteries, Acs Nano, 6(2012) 530-8.

[19] L.Q. Mai, L. Xu, Q.A. Gao, C.H. Han, B. Hu, Y.Q. Pi, Single beta-$AgVO_3$ Nanowire H_2S Sensor, Nano Lett, 10(2010) 2604-8.

[20] S.Y. Zhang, W.Y. Li, C.S. Li, J. Chen, Synthesis, characterization, and electrochemical properties of $Ag_2V_4O_{11}$ and $AgVO_3$ 1-D nano/microstructures, J Phys Chem B, 110(2006) 24855-63.

[21] A.A. Ansari, M. Alam, J.P. Labis, S.A. Alrokayan, G. Shafi, T. N. Hasan, et al., Luminescent mesoporous $LaVO_4:Eu^{3+}$ core-shell nanoparticles: synthesis, characterization, biocompatibility and their cytotoxicity, J Mater Chem, 21(2011) 19310-6.

[22] T.W. Kim, K.S. Choi, Nanoporous $BiVO_4$ Photoanodes with Dual-Layer Oxygen Evolution Catalysts for Solar Water Splitting, Science, 343(2014) 990-4.

[23] Y.Q. Shen, Y.C. Huang, S.J. Zheng, X.F. Guo, Z.X. Chen, L.M. Peng, et al., Nanocrystals of $CeVO_4$ Doped by Metallic Heteroions, Inorg Chem, 50(2011) 6189-94.

[24] D. Errandonea, S.N. Achary, J. Pellicer-Porres, A.K. Tyagi, Pressure-Induced Transformations in $PrVO_4$ and $SmVO_4$ and Isolation of High-Pressure Metastable Phases, Inorg Chem, 52(2013) 5464-9.

[25] T. Lehnen, M. Valldor, D. Niznansky, S. Mathur, Hydrothermally grown porous $FeVO_4$ nanorods and their integration as active material in gas-sensing devices, J Mater Chem A, 2(2014) 1862-8.

[26] W.Y. Yin, L.J. Zhou, Z.J. Gu, G. Tian, S. Jin, L. Yan, et al., Lanthanide-doped $GdVO_4$ upconversion nanophosphors with tunable emissions and their applications for biomedical imaging, J Mater Chem, 22(2012) 6974-81.

[27] X.C. Wu, Y.R. Tao, L. Dong, J.J. Zhu, Z. Hu, Preparation of single-crystalline $NdVO_4$ nanorods, and their emissions in the ultraviolet and blue under ultraviolet excitation, J Phys Chem B, 109(2005) 11544-7.

[28] H.M. Liu, Y.G. Wang, L. Li, K.X. Wang, E. Hosono, H.S. Zhou, Facile synthesis of NaV_6O_{15} nanorods and its electrochemical behavior as cathode material in rechargeable lithium batteries, J Mater Chem, 19(2009) 7885-91.

[29] V.D. Nithya, R.K. Selvan, C. Sanjeeviraja, D.M. Radheep, S. Arumugam, Synthesis and characterization of $FeVO_4$ nanoparticles, Mater Res Bull, 46(2011) 1654-8.

[30] H. Ma, X.J. Yang, Z.L. Tao, J. Liang, J. Chen, Controllable synthesis and characterization of porous $FeVO_4$ nanorods and nanoparticles, Crystengcomm, 13(2011) 897-901.

[31] Y. Zhao, K. Yao, Q. Cai, Z.J. Shi, M.Q. Sheng, H.Y. Lin, et al., Hydrothermal route to metastable phase $FeVO_4$ ultrathin nanosheets with exposed {010} facets: synthesis, photocatalysis and gas-sensing, Crystengcomm, 16(2014) 270-6.

[32] L.F. Zhang, J. Zhou, C.Y. Zhang, pH-controlled growth of ultrathin iron vanadium oxide (FeV_3O_8) nanoplatelets with high visible-light photo-catalytic activity, J Mater Chem A, 2(2014) 14903-7.

[33] A.S. Vuk, B. Orel, G. Drazic, F. Decker, P. Colomban, UV-visible and IR spectroelectrochemical studies of $FeVO_4$ sol-gel films for electrochromic applications, J Sol-Gel Sci Techn, 23(2002) 165-81.

[34] I.D. Kim, A. Rothschild, T. Hyodo, H.L. Tuller, Microsphere templating as means of enhancing surface activity and gas sensitivity of $CaCu_3Ti_4O_{12}$ films, Nano Lett, 6(2006) 193-8.

[35] J.X. Wang, X.W. Sun, H. Huang, Y.C. Lee, O.K. Tan, M.B. Yu, et al., A two-step hydrothermally grown ZnO microtube array for CO gas sensing, Appl Phys a-Mater, 88(2007) 611-5.

Chapter 6

Synthesis, characterization and gas sensing behavior of nickel cobalt oxide (NCO) nanograss

We report gas sensing properties of $NiCo_2O_4$ (NCO) nanograss synthesized by a simple hydrothermal method. The X-ray diffraction pattern shows formation of single phase $NiCo_2O_4$. Scanning and Transmission electron microscopies reveal nanograss-like morphology and further confirm the formation of the pure phase $NiCo_2O_4$. Interestingly, each blade of the NCO nanograss is assembled in the form of ~10-15 nm sized nanoparticles rendering the desired mesoporosity. Gas sensing study on such NCO exhibits a very good response to NH_3 and CO gases.

6.1 Introduction

Semiconductor metal oxides based sensors based on resistivity change due to analyte have been investigated for quite some time due to high response, simplicity of fabrication, stability, ease of operation[1]. Gas sensors based on both n-type and p-type binary metal oxides have been explored intensely[1-4]. The gas response properties of these systems have been improved by doping, using additives in the form of catalytically active noble metals such as Pt, Pd, Au etc.[5-7]. Morphological effects on gas sensing performance have also been studied[8-10]. Specifically, gas sensors based on p-type metal oxide based binary systems such as NiO, Co_3O_4, etc. have been explored extensively[11-14]. Ternary oxide systems provide the additional advantages of the contributions of electronic structures of both the elements and enable further ability to tune their properties through stoichiometry control, doping etc.

$NiCo_2O_4$ (NCO) is one of the interesting p-type ternary metal oxides due high catalytic activities of both nickel and cobalt. NCO has spinel crystallographic structure[15]. Nickel occupies the octahedral sites whereas cobalt occupies both octahedral and octahedral sites [Fig.6.1]. In NCO, nickel provides stable oxidation states, however the oxidation states of cobalt can vary during the reaction. Another reason for use of NCO is its non-toxicity, low cost, abundance in nature, and most importantly the tendency to be easily engineered into one-dimensional systems[16-17]. NCO exhibits two orders of magnitude higher electronic conductivity as compared to pure NiO or Co_3O_4. $NiCo_2O_4$ is an electrochemically active material. It has been used for supercapacitor application [18]. It has also been widely studied for applications in Li-ion battery, photoelectrochemical cell, photodetector and electrocatalyst[15,19-21]. In nanomaterial form, the reactivity and electronic properties of oxides depend on the size and shape of the particles [22]. The micro-electronics industry has been emphasizing on reduction in size of the device elements like capacitors, resistors, and transistors[23-25]. Thus if sensors are also built on the nanoscale platforms they may have a good compatibility for integration with signal processing circuit architectures. Doping Co_3O_4 with Ni is shown to enhance the electrical conductivity considerably while maintaining the spinel structure. This doped

system exhibits p-type behaviour similar to the intrinsic spinel Co_3O_4[26]. However, gas sensing study of p-type ternary forms of such oxides is hitherto lacking.

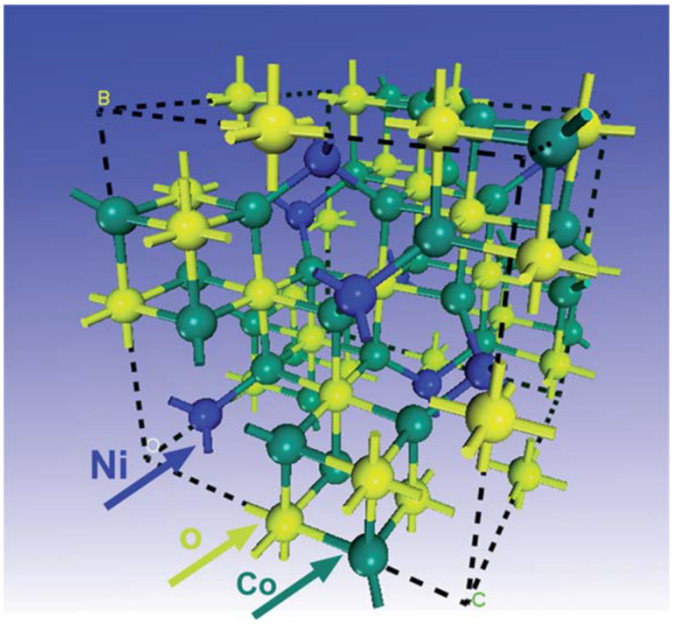

Figure 6.1: Crystal structure of NCO unit cell with the spinel structure. [reprinted with permission[15]]

6.2 Experimental

6.2.1 Synthesis and growth of $NiCo_2O_4$ nanograss on FTO

All the chemicals of analytical grade were used without further purification. In typical synthesis, 4 mmol cobalt nitrate hexahydrate [$Co(NO_3)_2.6H_2O$], 2 mmol nickel nitrate hexahydrate [$Ni(NO_3)_2.6H_2O$)], and 10 mmol of urea [$CO(NH_2)_2$] were mixed in 100 ml DI water and ultrasonicated till a homogeneous solution is obtained. This solution was then added into the teflon-lined stainless steel autoclave of 200 ml capacity. The normal glass substrates and commercially available FTO glass pieces of the desired size were washed by ultrasonication in DI water, then in ethanol for 15 min each and dried at room temperature. Few pieces of such glass and FTO glass with 150 µm insulating gap in the center were fixed on a glass slide using teflon tape and hung vertically into the above reaction solution such a that the parts of the substrates over which the deposition was desired were completely immersed into the solution. The autoclave was heated to 120°C for 20 h. It was allowed to cool to room temperature

and the substrates were removed from the solution. The substrates were washed with DI water and ethanol for a few times and then dried at room temperature. The samples were then annealed at 350°C for 2 h and further used for gas sensing study.

6.2.2 Characterization

X-Ray diffraction (XRD) analysis was carried out to determine formation crystal structure and phase purity of NCO. The XRD pattern in the range of 20°-80° (2θ)was measured on a Philips X'Pert PRO, using Cu-Kα (λ = 0.154056 nm) radiation. FESEM technique was used for morphological study. FESEM images were obtained from Nova NanoSEM. Transmission electron microscope (HR-TEM, FEI Tecnai 300) was used to acquire low magnification and high-resolution images of NCO. The gas sensing properties of NCO thin films were evaluated in the presence of different toxic gases at different operating temperatures. The gas sensing response (S) of a NCO sensor was obtained from the ratio of resistance of film in the air (R_a) to its resistance in the test gas (R_g) for oxidizing gas and vice-versa for the reducing gas (see equation 1.14).

6.3 Results and Discussion

6.3.1. Structural and morphological study

Figure 6.2 (a) shows X-ray diffraction pattern of NCO nanograss grown on a glass substrate. There are no other impurity peaks corresponding to NiO and Co_3O_4. All the X-ray peaks can be indexed with JCPDS data [20-0781] which confirms the formation of pure single phase $NiCo_2O_4$. Figure 6.2 (b) shows uniform dense growth of 1-D NCO nanograss on the FTO surface. The length of nanograss is ~ 1-3 μm and width of a typical nanoblade is ~200 nm. Each nanoblade is distinctly formed which suggests that the initial nuclei formed during the growth process facilitate further growth in an axial direction. There is a good adhesion with the substrates as well which can enable better electronic transport across the entire surface. Additionally, the magnified FESEM image of NCO nanograss exhibits a smooth surface [Inset of Fig.6.2 (b)]. For detailed understanding of the microstructures of the NCO nanograss, TEM and HR-TEM analyses were carried out.

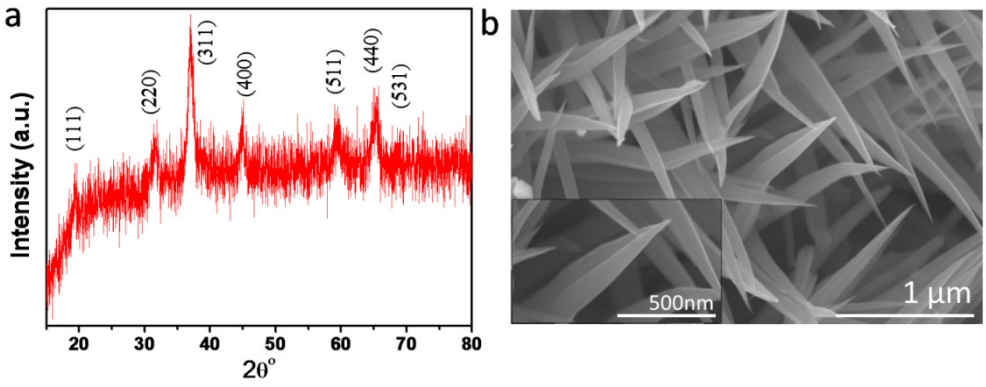

Figure 6.2: (a)X-ray diffraction pattern, and (b) FESM images (inset: magnified view) of $NiCo_2O_4$ nanograss sample.

Figure 6.3(a) shows a low magnification TEM image of the NCO nanoblade. The width of nanoblade decreases gradually from bottom to top, showing a tapered nature. The nanoblade seems to be broken at the tip as a result of sonication treatment used for the preparation of the TEM sample.

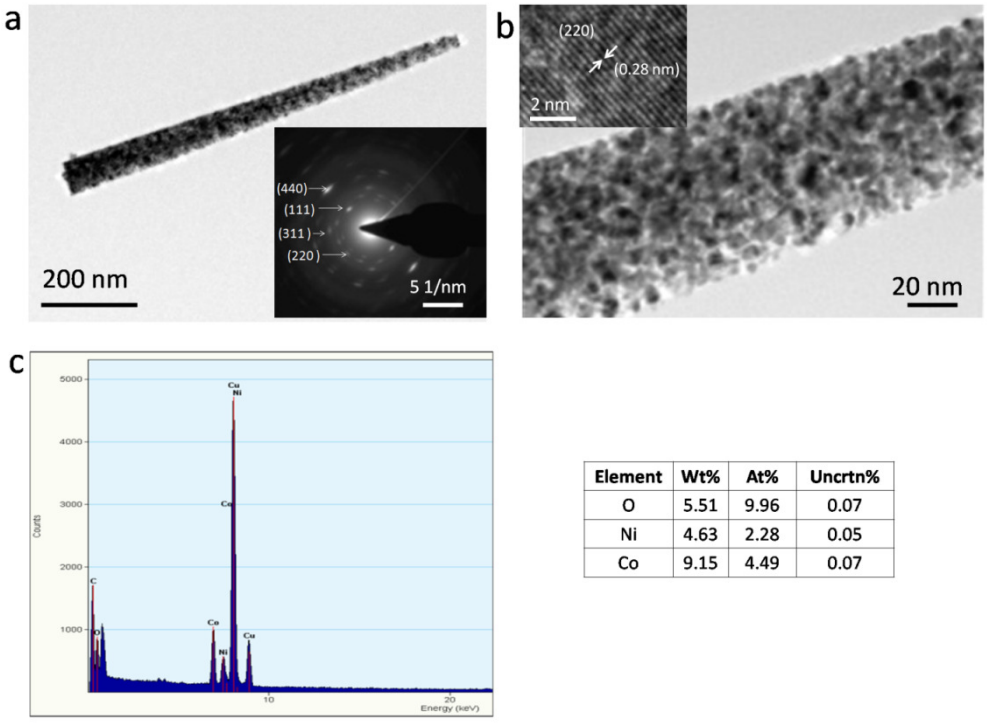

Element	Wt%	At%	Uncrtn%
O	5.51	9.96	0.07
Ni	4.63	2.28	0.05
Co	9.15	4.49	0.07

Figure 6.3:(a) low magnification TEM image (inset: SAED pattern), (b) magnified view of nanoblade and TEM images, and (c) EDAX analysis of the $NiCo_2O_4$ nanograss.

The porous polycrystalline nanoblades are seen to be formed by nanosized particles of ~10-15 nm in diameter with porosity in between the nanoparticles[Fig. 6.3(b)]. Thus, nanograss not only offers high surface area but also presents porosity which enhances accessibility to more active sites for the gas molecules. HR-TEM was used to determine lattice planes. All diffraction spot of SEAD pattern indexed with spinel NCO [inset of Fig.6.3(a)] The HR-TEM image of NCO nanoaprticle exhibits lattice spacing of ~ 0.28 nm which corresponds to (220) plane [inset of Fig 6.3(b)]. Energy Dispersive X-ray analysis (EDAX) was used to identify the elemental composition [Fig 6.3(c)]. The atomic percentage ratio of the elements Ni, Co and O is nearly found to be 1: 2: 4, respectively. It confirms the formation of stoichiometric $NiCo_2O_4$. Additional peaks corresponding to carbon and copper arise from carbon coated copper grid used for the TEM analysis.

6.3.2 Gas sensing study

Gas sensing behavior of NCO nanograss directly grown on an insulating gap of 150 µm attained on the FTO was studied in details. For gas sensing studies, gas cylinders of specific gases were purchased from a local vendor. To be specific, 1% test gas was diluted in 99% of N_2. The desired concentration for the measurement for a test gas was obtained by using mass flow controllers (MFC). Sensing behavior of the fabricated device was measured for different oxidizing and reducing gases, such as NO_2, CO, NH_3. The sensing measurements were performed by varying the concentration of the test gas at different operating temperatures. Among these gases, $NiCo_2O_4$ exhibited a good response to NH_3 and CO. $NiCo_2O_4$ nanograss showed no response towards NO_2. Therefore, detailed gas sensing behavior of $NiCo_2O_4$ nanograss was studied for NH_3 and CO gases.

Figure 6.4 illustrates the gas response for 1000 ppm NH_3 and CO gases at the operating temperatures between 150°C and 300°C. At lower operating temperature the device exhibits a negligible response. % S represents percentage gas response of the material and is calculated as,

$$\%S = \left(\frac{R_a}{R_g} - 1\right) * 100 \qquad (6.1)$$

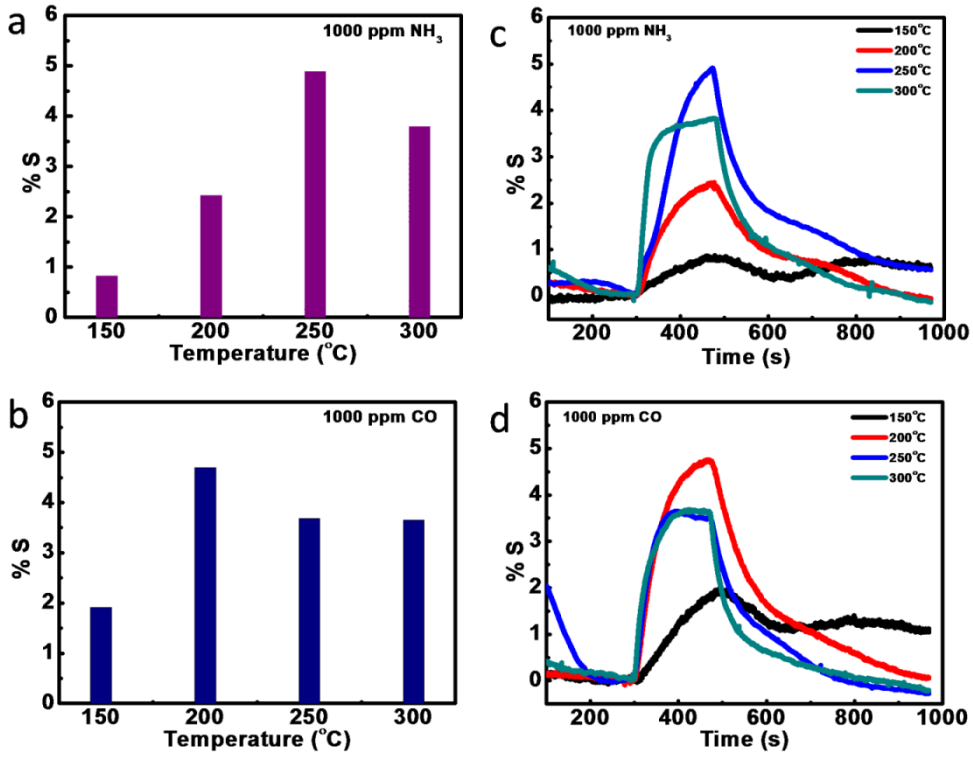

Figure 6.4: (a, b) % gas response (%S) with increase in an operating temperature for 1000 ppm of NH_3, CO, and (c, d)Gas sensing behavior of NCO at various operating temperatures for 1000 ppm NH_3 gas.

Figure 6.4 illustrates bar graphs of %S gas response to different operating temperatures. NCO shows maximum response for NH_3 at 250°C. However, the optimum operating temperature for CO is 200°C. It was found that the gas response increases with increase in the temperature but decreases at higher operating temperatures. At high operating temperatures, thermal energy increases which decreases the rate adsorption of gas molecules on the surface of sensor. It can be clearly seen from Fig. 6.4 (c, d) that the response and recovery of 1000 ppm of the test gas is faster at 300°C. Thus, response-recovery dynamics were studied for different concentrations of the test gases at 300°C, which is shown in Fig. 6.5. It can be seen from Figs. 6.5 (a,b) that with an increase in concentration of the test gas the response of the sensor increases, as expected.

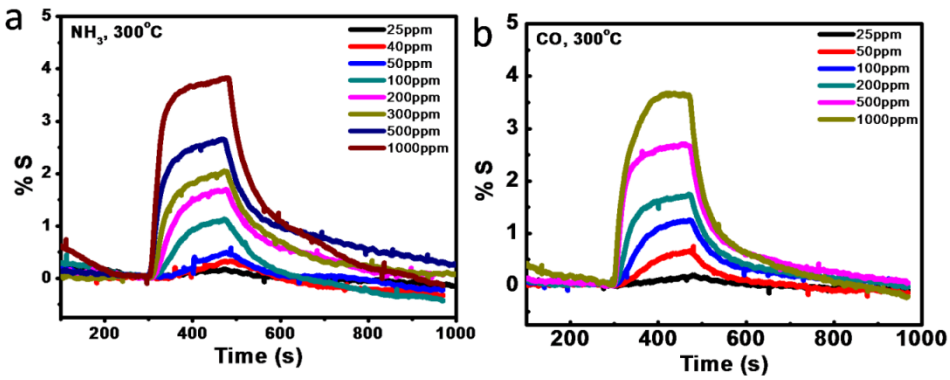

Figure 6.5: Gas sensing behavior of NCO for different concentrations of NH_3(a), and CO (b), gases.

The band diagram can be used to describe gas sensing mechanism of a semiconductor metal oxide[27-28]. The acceptor levels are present near the valance band (VB) in a p-type semiconductor. These levels accept electrons, leaving holes in the VB at room temperature and vacancies of metal ions acts acceptors [Figure 6.6 (a)]. In air atmosphere, oxygen trap electrons from the surface state of NCO and get adsorbed on its surface as shown in Fig. 6.6(b). This leads to band bending and rise in hole concentration and therefore a decrease in the resistance of NCO. In the presence of reducing gases (like NH_3, CO), the reaction between gas molecules and chemisorbed oxygen and/or adsoptrion of gas molecules results in the release of electrons into the NCO. Thus, electrons and holes recombine which results in the reduction of the hole accumulation layer accompanied by band bending relaxation (shown as $q\Delta V$) and increase in the resistance of the NCO [Fig. 6.6(c)]. When reducing gas molecules desorbed from the NCO surface(Fig. 7(b)), the holes concentration is again restored which results in a decrease in the resistance of NCO. However, in the presence of oxidizing gas like NO_2, gas molecules get adsorbed on the surface of metal oxide by withdrawing electrons and leaving behind holes. This leads to further increase in the holes concentration and thus reduction in the resistance of NCO, which is further restored by desorption of NO_2 from the surface in the recovery process by passing air.

In chemoresistive type metal oxide sensor, the sensitivity of the gas sensors is highly influenced by the concentration of analyte gas and temperature of the sensor. Thus, the temperature dependent gas response is controlled by the surface stoichiometry of metal oxide and the chemical interaction between the analyte and the surface.

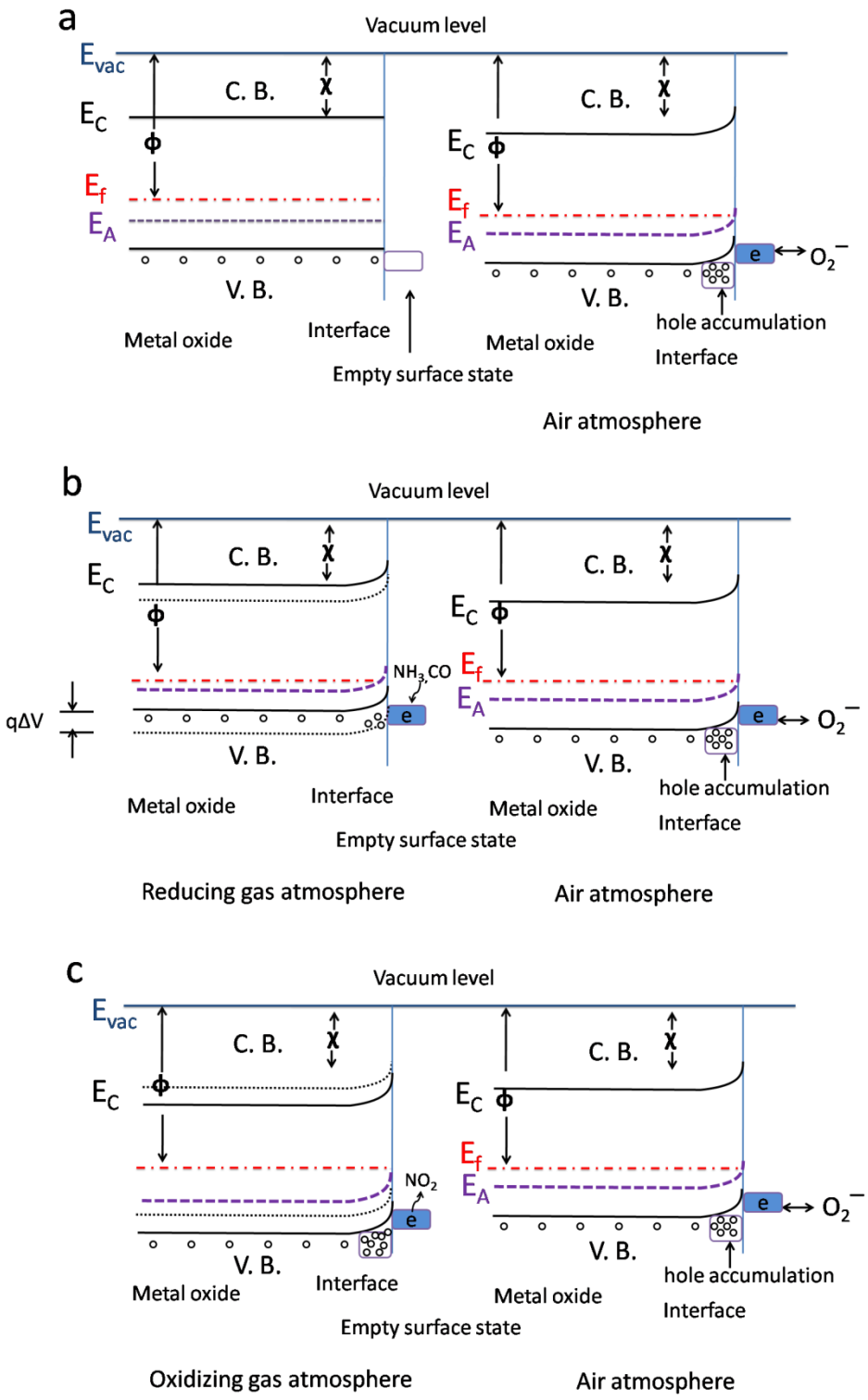

Figure 6.6: (a, b, c) Schematics of band diagram illustrating gas sensing mechanism in the presence of reducing and oxidizing gases.

The kinetics of surface chemisorption reactions depends on the adsorption–desorption(A/D) activation energies which are governed by the temperature of the sensor, thereby influencing the response and recovery times of the sensor. Thus, the

response and recovery times depend on A/D reactions of the analyte molecules. In the present case, NH_3 and CO gas molecules show complete recovery at 300°C temperature which suggests their easy desorption from the surface of NCO. This implies that the porous NCO nanograss material is a good candidate for the detection of NH_3 and CO. However, the gas response values are on the slower side which could be enhanced by the integration with other materials.

6.4 Conclusions

Single phase NCO nanograss was synthesized using hydrothermal technique. The nanograss is composed of tapered nanoblades that are ~1-3 μm in length with a mean width of ~200 nm. Each nanoblade is formed by nanoparticles of ~10-15 nm size (diameter) connected with each other rendering nanoporosity over the entire range. Such NCO material shows maximum response towards NH_3 and CO at 250°C and ~200°C, respectively.

6.5. References

[1] G. Korotcenkov, Metal oxides for solid-state gas sensors: What determines our choice?, Materials Science and Engineering: B, 139(2007) 1-23.

[2] C. Wang, L. Yin, L. Zhang, D. Xiang, R. Gao, Metal oxide gas sensors: sensitivity and influencing factors, Sensors-Basel, 10(2010) 2088-106.

[3] G. Eranna, B. Joshi, D. Runthala, R. Gupta, Oxide materials for development of integrated gas sensors—a comprehensive review, Critical Reviews in Solid State and Materials Sciences, 29(2004) 111-88.

[4] H.-J. Kim, J.-H. Lee, Highly sensitive and selective gas sensors using p-type oxide semiconductors: Overview, Sensors and Actuators B: Chemical, 192(2014) 607-27.

[5] M. Schweizer-Berberich, J. Zheng, U. Weimar, W. Göpel, N. Barsan, E. Pentia, et al., The effect of Pt and Pd surface doping on the response of nanocrystalline tin dioxide gas sensors to CO, Sensors and Actuators B: Chemical, 31(1996) 71-5.

[6] B. Bahrami, A. Khodadadi, M. Kazemeini, Y. Mortazavi, Enhanced CO sensitivity and selectivity of gold nanoparticles-doped SnO_2 sensor in presence of propane and methane, Sensors and Actuators B: Chemical, 133(2008) 352-6.

[7] N. Yamazoe, New approaches for improving semiconductor gas sensors, Sensors and Actuators B: Chemical, 5(1991) 7-19.

[8] J. Hsieh, C. Liu, Y. Ju, Response characteristics of lead phthalocyanine gas sensor: effects of film thickness and crystal morphology, Thin Solid Films, 322(1998) 98-103.

[9] G. Korotcenkov, The role of morphology and crystallographic structure of metal oxides in response of conductometric-type gas sensors, Materials Science and Engineering: R: Reports, 61(2008) 1-39.

[10] C. Wu, P. Yin, X. Zhu, C. OuYang, Y. Xie, Synthesis of hematite (α-Fe_2O_3) nanorods: diameter-size and shape effects on their applications in magnetism, lithium ion battery, and gas sensors, The Journal of Physical Chemistry B, 110(2006) 17806-12.

[11] J.A. Dirksen, K. Duval, T.A. Ring, NiO thin-film formaldehyde gas sensor, Sensors and Actuators B: Chemical, 80(2001) 106-15.

[12] G. Zhu, C. Xi, H. Xu, D. Zheng, Y. Liu, X. Xu, et al., Hierarchical NiO hollow microspheres assembled from nanosheet-stacked nanoparticles and their application in a gas sensor, Rsc Adv, 2(2012) 4236-41.

[13] H. Nguyen, S.A. El-Safty, Meso-and macroporous Co_3O_4 nanorods for effective VOC gas sensors, The Journal of Physical Chemistry C, 115(2011) 8466-74.

[14] A.-M. Cao, J.-S. Hu, H.-P. Liang, W.-G. Song, L.-J. Wan, X.-L. He, et al., Hierarchically structured cobalt oxide (Co_3O_4): the morphology control and its potential in sensors, The Journal of Physical Chemistry B, 110(2006) 15858-63.

[15] Q. Wang, B. Liu, X. Wang, S. Ran, L. Wang, D. Chen, et al., Morphology evolution of urchin-like $NiCo_2O_4$ nanostructures and their applications as psuedocapacitors and photoelectrochemical cells, J Mater Chem, 22(2012) 21647-53.

[16] J. Xiao, S. Yang, Sequential crystallization of sea urchin-like bimetallic (Ni, Co) carbonate hydroxide and its morphology conserved conversion to porous $NiCo_2O_4$spinel for pseudocapacitors, Rsc Adv, 1(2011) 588-95.

[17] H. Wang, Q. Gao, L. Jiang, Facile approach to prepare nickel cobaltite nanowire materials for supercapacitors, Small, 7(2011) 2454-9.

[18] J. Du, G. Zhou, H. Zhang, C. Cheng, J. Ma, W. Wei, et al., Ultrathin porous $NiCo_2O_4$ nanosheet arrays on flexible carbon fabric for high-performance supercapacitors, ACS Applied Materials & Interfaces, 5(2013) 7405-9.

[19] L. Hu, L. Wu, M. Liao, X. Fang, High-Performance $NiCo_2O_4$ Nanofilm Photodetectors Fabricated by an Interfacial Self-Assembly Strategy, Adv Mater, 23(2011) 1988-92.

[20] A.K. Mondal, D. Su, S. Chen, X. Xie, G. Wang, Highly porous $NiCo_2O_4$ nanoflakes and nanobelts as anode materials for lithium-ion batteries with excellent rate capability, ACS Applied Materials & Interfaces, 6(2014) 14827-35.

[21] H.S. Jadhav, R.S. Kalubarme, J.-W. Roh, K.-N. Jung, K.-H. Shin, C.-N. Park, et al., Facile and Cost Effective Synthesized Mesoporous Spinel $NiCo_2O_4$ as Catalyst for Non-Aqueous Lithium-Oxygen Batteries, J Electrochem Soc, 161(2014) A2188-A96.

[22] E. Roduner, Size matters: why nanomaterials are different, Chemical Society Reviews, 35(2006) 583-92.

[23] T. Someya, J. Small, P. Kim, C. Nuckolls, J.T. Yardley, Alcohol vapor sensors based on single-walled carbon nanotube field effect transistors, Nano Lett, 3(2003) 877-81.

[24] D.E. Williams, Semiconducting oxides as gas-sensitive resistors, Sensors and Actuators B: Chemical, 57(1999) 1-16.

[25] A. Samman, S. Gebremariam, L. Rimai, X. Zhang, J. Hangas, G. Auner, Silicon-carbide MOS capacitors with laser-ablated Pt gate as combustible gas sensors, Sensors and Actuators B: Chemical, 63(2000) 91-102.

[26] J. Tareen, A. Małecki, J. Doumerc, J. Launay, P. Dordor, M. Pouchard, et al., Growth and electrical properties of pure and Ni-doped Co_3O_4 single crystals, Mater Res Bull, 19(1984) 989-97.

[27] S. Pokhrel, C. Simion, V. Quemener, N. Barsan, U. Weimar, Investigations of conduction mechanism in Cr_2O_3 gas sensing thick films by ac impedance spectroscopy and work function changes measurements, Sensors and Actuators B: Chemical, 133(2008) 78-83.

[28] V.B. Kamble, A.M. Umarji, Gas sensing response analysis of p-type porous chromium oxide thin films, J Mater Chem C, 1(2013) 8167-76.

Chapter 7

Hydrothermal synthesis and remarkable humidity sensing properties of zinc stannate

We report humidity sensing property of hydrothermally synthesized single phase zinc stannate nanoparticles. X-ray diffraction analysis clearly shows formation of single phase Zn_2SnO_4 (ZTO). Transmission electron microscopy confirms formation of faceted nanoparticles in the range between 5 and 50 nm. Such ZTO film shows ~4 order of magnitude change in its response towards entire range of humidity with good linearity. The detailed complex ac impedance analysis of ZTO films is also carried out at 1 V with 50 mV amplitude of ac signal in the range of 10^{-2}-10^{6} Hz for relative humidity (RH) between 11% and 92%.

7.1. Introduction

Zinc stannate is technologically a very important material as its electronic properties can be tuned with doping, stoichiometry control and through size effects. It also has several positive attributes such as good optoelectronic properties, non-toxic nature, natural abundance of the corresponding elements etc. [1-2]. This material has shown promising applications in many fields such as solar energy, water splitting, Lithium ion battery etc. [3-5]. It possesses two important elements namely zinc and tin which are widely established in the field of materials science because of their earth abundance and the fascinating range of the properties of their various compounds. In particular, the oxides of these elements have been widely exploited in the field of sensors [6,7].

Zinc stannate has shown fairly high sensitivity to toxic and other industrially important gases such as CO, NO_2, H_2S, ethanol, etc. [8-11]. Humidity is an important factor which affects various industrial and domestic processes. Therefore, it is essential to detect and control environmental humidity. The search through literature reveals that zinc stannate shows very diminutive humidity sensing response. Stambolova et al. deposited zinc stannate films by spray pyrolysis at ~450°C and further annealed them at 1000°C for 8-10 h and tested them for humidity sensing. A very small response (R_a/R_g=10) was seen with linearity only over the range above 50% RH[12]. The composite thick film based on ZTO with $LiZnVO_4$ however showed an excellent humidity sensing property (more than 3 orders of magnitude change). Gang Fu et al. have explained this change due to humidity sensitive character of the $LiZnVO_4$ layer. They did not however explain the exact role of Zn_2SnO_4 in this study[13]. In another work $ZnSnO_3$ pallet was prepared by physical mixing of different weight ratios of zinc and tin and the same was annealed at 600°C[14]. This system once again showed very low humidity response and exhibited no change in resistance above 50% RH. Kovancheva et al. prepared pellets of ZTO and $Zn_{2-x}Mg_XSnO_4$ composite; in this case the humidity response was observed only above 50% RH[15]. The search through literature has shown low humidity response of ZTO films and pallets with nonlinear behavior vis a vis humidity. It is therefore interesting to study the effect of nanostructure and film fabrication on the humidity properties of material.

In the present study, single phase zinc stannate (Zn_2SnO_4) nanoparticles are successfully synthesized via hydrothermal method. Humidity sensing properties of nano-particulate porous ZTO films were performed at room temperature using an ac impedance analysis. Zinc stannate films synthesized by this method have shown good sensitivity over the full range of % RH.

7.2. Experimental

7.2.1 Synthesis of Zn_2SnO_4

Single phase zinc stannate was synthesized by simple hydrothermal method. Tin chloride (IV) hydrated, $SnCl_4.5H_2O$ (Lobachemie); Zinc chloride, $ZnCl_2$ (Merck) and sodium carbonate, Na_2CO_3 (Merck) were used without further purification. In a typical synthesis 0.701 g $SnCl_4$. $2H_2O$, 0.545 g $ZnCl_2$, 0.635 g Na_2CO_3were dissolved in the 200 ml DI water. The reaction mixture was then transferred in 250 ml capacity teflon vessel. It was placed in stainless steel jacket and kept at 180°C for 12 h. The obtained product was washed with DI water and dried in the vacuum at 80°C for 24 h. The effect of Na_2CO_3 mineral on the properties of ZTO has been studied by Annamalai et al.[2].

7.2.2 Fabrication of ZTO films

A homogeneous paste of ZTO was prepared using the following protocol. Initially, in a 100 mg of ZTO powder water (0.5 ml), a drop of triton and acetyl acetone were added and the mixture was ground for 10 min. The above mixture was then further ground in 1 ml of ethanol successively for two times with 20 min grinding after successive addition. The obtained homogeneous paste was then applied on the surface of Fluorine-doped tin oxide (2 cm^2) with an insulating gap of 150 μm in the centre that split the conducting layer in two parts. This film was allowed to dry at room ambient and was further heated at 450°C for 5 h. ZTO films thus formed were directly used for sensing studies.

7.2.3 Characterizations

XRD data of zinc stannate powder was acquired on a Philips X'Pert PRO using Cu-Kα radiation source. The measurement was carried for 2θ values between 20° and 80°. The film morphology was obtained from E-SEM Quanta 200 3D scanning

electron microscope. FEI Tecnai 300 transmission electron microscope was used to acquire low and high-resolution micrographs of samples. The band gap of ZTO was obtained from the diffused reflectance spectrum (DRS) measured on a Jasco V-570 spectrophotometer. The humidity sensing studies on the ZTO films were carried out by an Autolab PGSTAT30 (Eco-Chemie) at different frequencies. The complex impedance analysis was carried out between 10^{-2} - 10^{6} Hz with 50 mV amplitude at 1 V.

7.2.4 Humidity sensing measurements

Different % relative humidity ambient values were achieved by using air tight chambers of saturated salt solutions of different salts. The saturated salt solutions such as LiCl(11%), $MgCl_2.6H_2O$(33%), $Ca(NO_3)_2.4H_2O$(54%), NaCl(75%), KCl(84%), and KNO_3 (92%) were used in the present study[16]. The salt chambers were kept for 24 h at 25°C (±1°C) to achieve stable humidity. The humidity sensing study was performed at 25°C (±1°C) by switching the ZTO film rapidly between the different humidity chambers. A Keithley 6517A electrometer/high resistance meter was used to measure the change in the resistance of the ZTO film. The humidity response (S) of the ZTO film is defined as the ratio of resistance of film in the 11% RH ($RH_{11\%}$) to its resistance in the test humidity (t%)[16].

$$S = \frac{RH_{11\%}}{RH_{t\%}} \tag{7.1}$$

7.3. Results and Discussion

7.3.1 Structural and morphological study:

The XRD pattern of as synthesized ZTO powder is shown Fig. 7.1(a). This XRD is identical with the JCPDS file no. 74-2184 and does not exhibit any impurity peak corresponding to ZnO or SnO_2. Therefore, it clearly signifies formation of single phase zinc stannate. The SEM image of the ZTO film annealed at 450°C for 5 h is shown in Fig 7.1(b). The organic compounds used in doctor blading technique to form uniform paste were decomposed off during annealing treatment that developed microcracks in the film. It seems that aggregates of few hundred nanometer sizes were formed from integration of smaller nanoparticles. The annealing is essential as it creates good adhesion of sample with FTO and also to form electronic connection

between the nanoparticles. The SEM image exhibits high surface area with microporous nature of ZTO film. In humidity sensing application such microporosity is very essential. The morphology of hydrothermal synthesized powder was also analyzed using TEM micrographs. Figure 7.1(c) exhibits widely distributed nanoparticles of ~5-50 nm in diameters. The shapes of particles are however faceted but irregular. The lattice d spacing of a typical particle is observed to be (0.49 nm) which corresponds to the (111) lattice plane of ZTO [(inset of Fig. 7.1(c)]. The selected area diffraction pattern is shown in Fig. 7.1(d). The diffraction points match with the JCPDs data (74-2184) of zinc stannate. Hence, both XRD and TEM analysis reveal single phase ZTO formation.

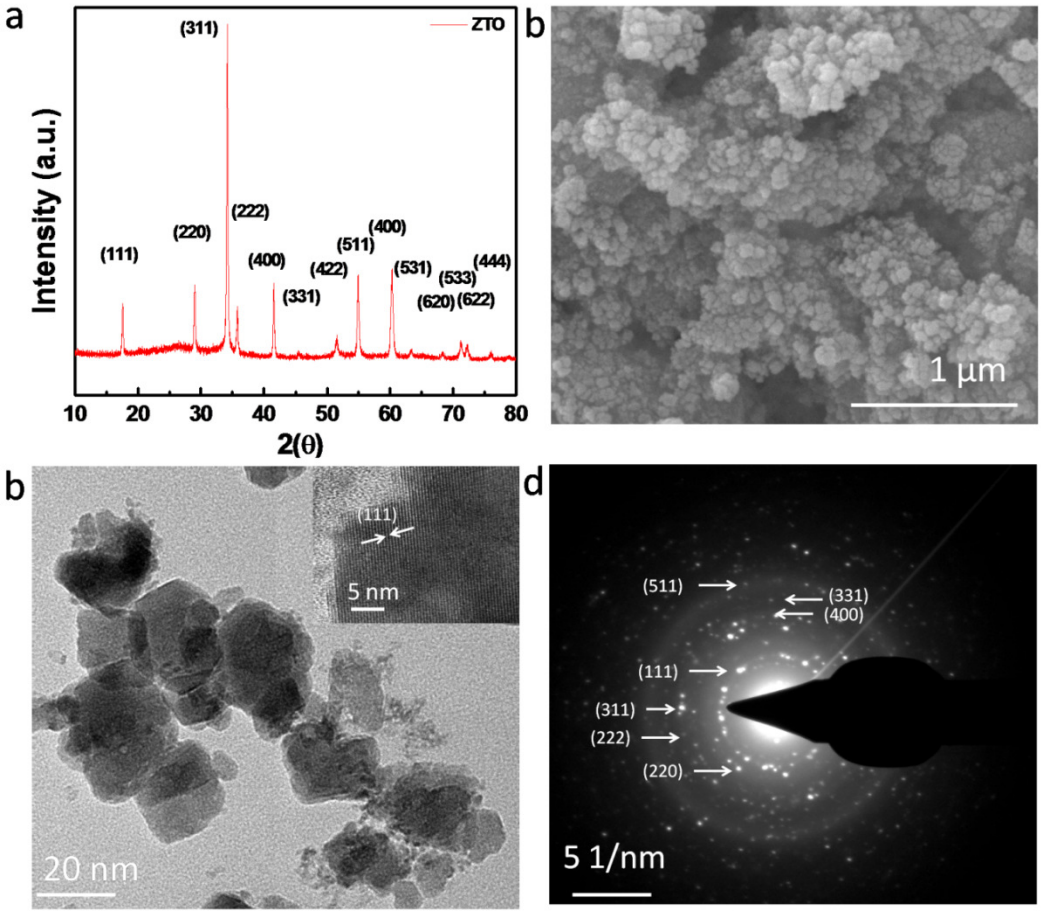

Figure 7.1: (a) X-ray pattern of as synthesized Zn_2SnO_4, (b) SEM image of ZTO film annealed at 450°C for 5h, (c) low magnification (inset: high resolution) TEM images of ZTO nanoparticles, (d) selected area electron diffraction (SAED) pattern of Zn_2SnO_4 nanoparticles.

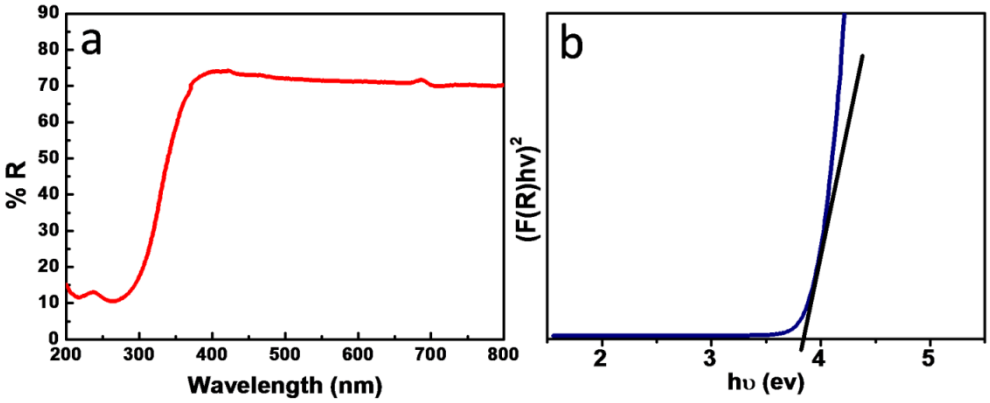

Figure 7.2. (a) Diffused reflectance spectrum, and d) Tauc's plots for the ZTO powder.

The optical properties of ZTO powder were analyzed by using UV-VIS diffuse reflectance spectroscopy (DRS). Fig. 7.2 (a) shows the diffused reflectance spectra of ZTO powder. The band gap of the materials can be derived from the Kubelka–Munk method (see equation 2.5). The band gap ZTO is found to be 3.84 eV[see ig. 7.2(b)]. The small increase in the band gap as compared to bulk can be attributed to the small nanosized particle of hydrothermally synthesized ZTO.

7.3.2 Humidity Sensing study:

The hydrothermally synthesized ZTO powder was used to form uniform porous films on FTO substrates by the doctor blading technique (as discussed earlier). The ZTO films were annealed in air in order to decompose the organic content and form electronic connections between nanoparticles. Air tight chambers of different saturated salt solutions were used to study the humidity sensing of ZTO film. The humidity measurements were carried out by rapidly switching films between different humidity environments. The impedance analysis of ZTO films were performed for RH between 11% and 92%. The impedance measurements were carried out for frequency range between of 10^{-2} to 10^{6} Hz with 50 mV ac potential at 1 V[Fig.7.3 (a)]. As operating frequency increases the impedance of ZTO film was seen to decrease [Fig. 7.3(a)]. For lower operating frequency (0.01-1 Hz), the change in impedance with frequency is somewhat linear. However, in the high frequency range (10^{2} to 10^{6}), the change in the impedance of the film is faster. Fig. 7.3(b) reveals the change of impedance with increase in humidity at different operating frequencies.

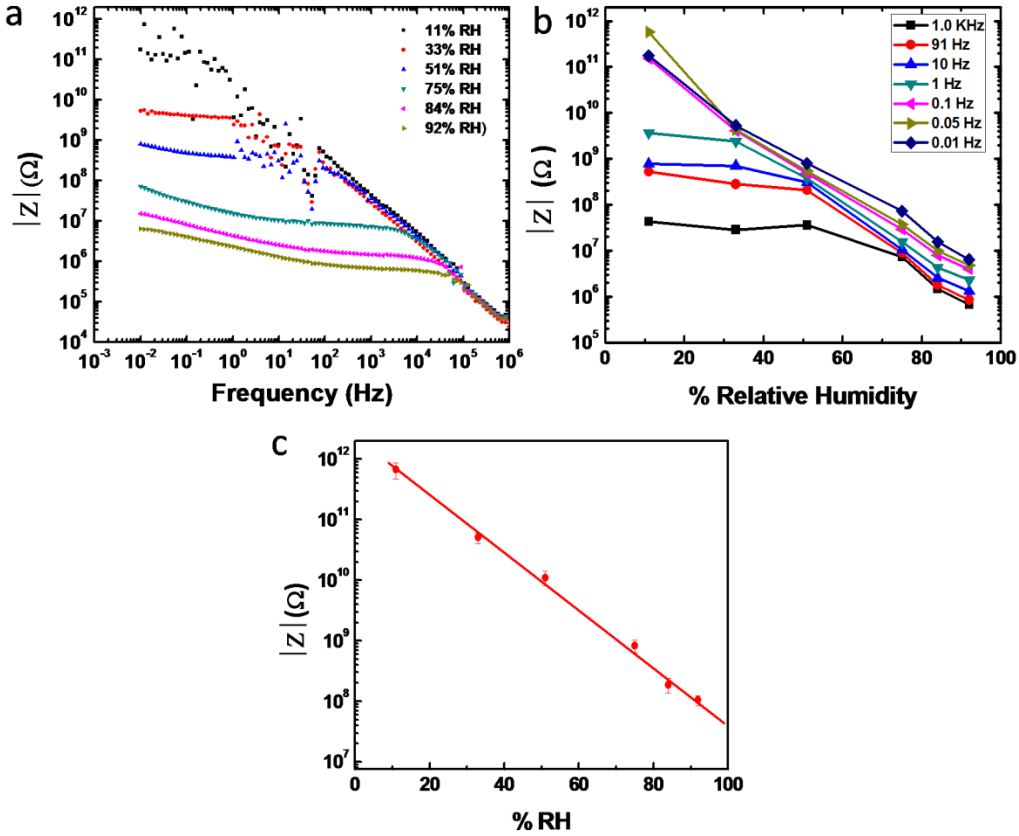

Figure 7.3: (a) Impedance change with increase in frequency at different humidity, (b) The variation of impedance with humidity for different operating frequency,(c) the change in impedance with humidity for 0.1 Hz operating frequency.

It suggests that over the lower frequency region, the change in impedance for the different humidity values is prominent. There is a rapid departure from linearity at higher operating frequency (>1 Hz). At lower frequencies, however, the films show better linearity in contrast to higher frequency range. The ZTO film exhibits a good linearity at 0.1 Hz as shown in Fig.7.3(c). For lower humidity range <54%, there are fluctuations of the impedance in the frequency range between 10 Hz and 100 Hz. The exact reason for this is not known at this stage, however, it might be due to the interaction between inline frequency and operating frequency which becomes pronounced at higher resistance.

Figure 7.4 (a,b) show the ac complex impedance analysis of the ZTO film. In an ac impedance plot, semicircle nature indicates that the resistor and the capacitor parts of an equivalent circuit are in parallel. The resistance value can be obtained from the diameter of the semicircle and capacitor value is calculated from the expression, $\omega \tau = \omega RC=1$, where, ω is peak angular frequency, τ is relaxation time or time constant of each parallel RC circuit[18]. The semicircle arc signifies diffusion and polarization of

charge carriers on the surface of sensor. The inclined line at lower frequency deals with electrolytic conduction and diffusion processes between the interface of the sensor and the electrode. The impedance arising in this region is known as the Warburg impedance.

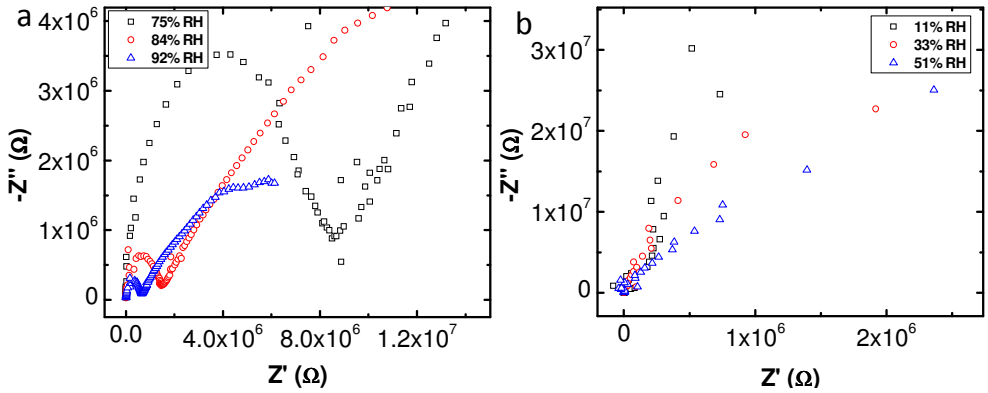

Figure 7.4: The complex impedance plots for ZTO film at different humidity values at 25°C.

The complex ac impedance of ZTO film shows a semicircle arc at higher frequency and is inclined line at lower frequency [Fig.7.4 (a)]. As RH increases the size of the semicircle reduces. For high RH, many water molecule layers are adsorbed on the surface of the sensor and the concentration of proton (H^+ ion) charge carriers increases, as the hydration of hydronium ion (H_3O^+) to H_2O and H^+ is energetically a favorable process[19]. In high humidity environment, charge carriers move freely within liquid water which results in a decrease in the grain surface resistance. However at low concentration of humidity (less than monolayer adsorption), water molecules are adsorbed on the active sites to form chemisorbed hydroxyl group. The proton is transferred to water molecule and forms H_3O^+ ion[20]. In such a condition, hydronium ion is bonded to two hydroxyl groups and the charge carrier is H_3O^+. Therefore, resistance is high at low humidity as a result of low concentration of charge carries.

As per dielectric theory, resistor indicates transport and capacitance signifies polarization of charged species. As humidity increases many charge carriers are available and hence polarization effect is enhanced therefore capacitance at grain boundary region and sensor-electrolyte interface increases. In an ac complex

impedance analysis, the completion of semicircle depends on value of resistor, capacitor and operating frequency[21-23]. At low humidity range (<54%), the semicircles are not evolved due to high resistance and low density of charge carriers available for conduction[(Fig. 7.4(b)]. Thus, at low frequency the capacitor part of the equivalent circuit is absent; hence we do not get the semicircle behavior.

The response and recovery behavior data for the ZTO films are shown in Fig. 7.5. In the present experimental condition it is difficult to get precise response time as we expose the sensor to laboratory ambient humidity (though very briefly) while switching between the different humidity chambers. Hence, the extracted values are only nominal estimations. Figure 7.5 show the transient response between $RH_{11\%}$to different test humidity values. The ZTO film shows a reasonably rapid response ~ 2-3 min to reach the ~85% response value. However, the recovery time is higher in all the cases. The slow recovery time may be due porous nature of the ZTO film[Fig. 1(b)] and also the strong interaction of water molecules with zinc stannate which could leads to their slow dissociation. [24].

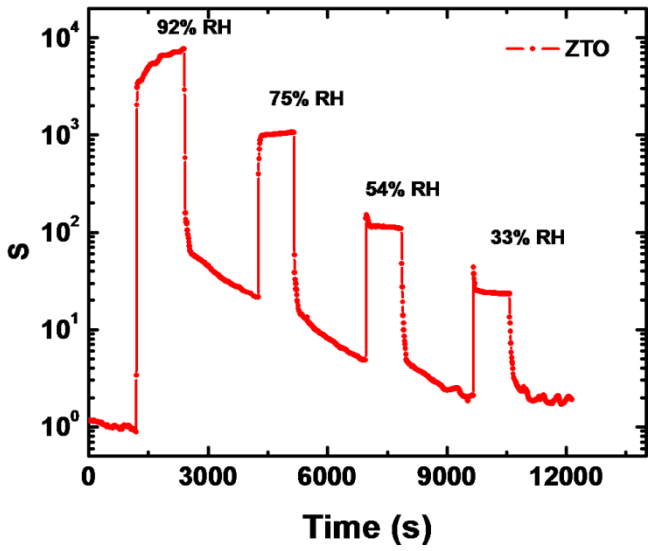

Figure 7.5: Response and recovery of the ZTO film in different humidity environments at 25°C

It is necessary to understand the possible contribution of each element Zn and Sn towards humidity by using hard soft acid base (HSAB) principles[25]. According to the principle hard species bind easily with hard species and the soft species with the

soft one. There is an electrostatic nature in hard–hard species while covalent nature in soft–soft species. In ZTO, Zn^{2+} is borderline acid however; Sn^{4+} ion is a hard acid. Water is acts a hard base. Hence, Sn^{4+} will easily facilitate adsorption of water. Hence, the humidity sensitivity of Sn^{4+} ions is more compared to Zn^{2+} ions. In the present study, the nanosize ZTO provide high surface area which presents more active sites for the adsorption of water. Thus, ZTO film shows high sensitivity and good linearity owing to porous nature of nanoparticulate film.

7.4 Conclusions

We report highly humidity sensitive ZTO nanoparticles synthesized by hydrothermal method. The corresponding film of ZTO exhibits ~ 4 order change in the impedance between 11% and 92% RH. It also displays good linearity over the whole range of operating humidity. Thus, ZTO films synthesized by this method hold good promise for humidity sensing with high response and good linearity.

7.5 References:

[1] S. Baruah, J. Dutta, Zinc stannate nanostructures: hydrothermal synthesis, Science and Technology of Advanced Materials, 12(2011) 013004.

[2] A. Annamalai, D. Carvalho, K. Wilson, M.-J. Lee, Properties of hydrothermally synthesized Zn_2SnO_4 nanoparticles using Na_2CO_3 as a novel mineralizer, Mater Charact, 61(2010) 873-81.

[3] B. Tan, E. Toman, Y. Li, Y. Wu, Zinc stannate (Zn_2SnO_4) dye-sensitized solar cells, J Am Chem Soc, 129(2007) 4162-3.

[4] M.A. Alpuche-Aviles, Y. Wu, Photoelectrochemical study of the band structure of Zn_2SnO_4 prepared by the hydrothermal method, J Am Chem Soc, 131(2009) 3216-24.

[5] A. Rong, X. Gao, G. Li, T. Yan, H. Zhu, J. Qu, et al., Hydrothermal synthesis of Zn_2SnO_4 as anode materials for Li-ion battery, The Journal of Physical Chemistry B, 110(2006) 14754-60.

[6] A. Wei, L. Pan, W. Huang, Recent progress in the ZnO nanostructure-based sensors, Materials Science and Engineering: B, 176(2011) 1409-21.

[7] M. Batzill, Surface science studies of gas sensing materials: SnO_2, Sensors-Basel, 6(2006) 1345-66.

[8] J. Yu, G. Choi, Current–voltage characteristics and selective CO detection of Zn_2SnO_4 and ZnO/ Zn_2SnO_4, SnO_2/Zn_2SnO_4 layered-type sensors, Sensors and Actuators B: Chemical, 72(2001) 141-8.

[9] Y. Yamada, Y. Seno, Y. Masuoka, K. Yamashita, Nitrogen oxides sensing characteristics of Zn_2SnO_4 thin film, Sensors and Actuators B: Chemical, 49(1998) 248-52.

[10] D. Chen, J. Xu, B. Liang, X. Wang, P.-C. Chen, C. Zhou, et al., Electric transport, reversible wettability and chemical sensing of single-crystalline zigzag Zn_2SnO_4 nanowires, J Mater Chem, 21(2011) 17236-41.

[11] G. Ma, R. Zou, L. Jiang, Z. Zhang, Y. Xue, L. Yu, et al., Phase-controlled synthesis and gas-sensing properties of zinc stannate ($ZnSnO_3$ and Zn_2SnO_4) faceted solid and hollow microcrystals, Crystengcomm, 14(2012) 2172-9.

[12] I. Stambolova, K. Konstantinov, D. Kovacheva, P. Peshev, T. Donchev, Spray pyrolysis preparation and humidity sensing characteristics of spinel zinc stannate thin films, J Solid State Chem, 128(1997) 305-9.

[13] G. Fu, H. Chen, Z. Chen, J. Zhang, H. Kohler, Humidity sensitive characteristics of Zn_2SnO_4–$LiZnVO_4$ thick films prepared by the sol–gel method, Sensors and Actuators B: Chemical, 81(2002) 308-12.

[14] S. Rama, Y. Avadhesh Kumar, G. Chandkiram, Synthesis and Humidity Sensing Investigations of Nanostructured $ZnSnO_3$, Journal of Sensor Technology, 2011(2011).

[15] D. Kovacheva, T. Bacalova, A. Batchvarov, K. Petrov, Structural and humidity sensing characteristics of Zn_2− XMg_XSnO_4 spinels, J Mater Sci Lett, 20(2001) 1597-9.

[16] Y. Gawli, S. Badadhe, A. Basu, D. Guin, M.V. Shelke, S. Ogale, Evaluation of n-type ternary metal oxide $NiMn_2O_4$ nanomaterial for humidity sensing, Sensors and Actuators B: Chemical, 191(2014) 837-43.

[17] O. Game, U. Singh, A.A. Gupta, A. Suryawanshi, A. Banpurkar, S. Ogale, Concurrent synthetic control of dopant (nitrogen) and defect complexes to realize broadband (UV–650 nm) absorption in ZnO nanorods for superior photo-electrochemical performance, J Mater Chem, 22(2012) 17302-10.

[18] J.T. Irvine, D.C. Sinclair, A.R. West, Electroceramics: characterization by impedance spectroscopy, Adv Mater, 2(1990) 132-8.

[19] C. de Grotthuss, Theory of decomposition of liquids by electrical currents, Ann Chim(Paris), 58(1806) 54-74.

[20] Y. Yeh, T. Tseng, Analysis of the dc and ac properties of K_2O-doped porous $Ba_{0.5}Sr_{0.5}TiO_3$ ceramic humidity sensor, J Mater Sci, 24(1989) 2739-45.

[21] D. Wang, C. Song, Z. Hu, X. Fu, Fabrication of hollow spheres and thin films of nickel hydroxide and nickel oxide with hierarchical structures, The Journal of Physical Chemistry B, 109(2005) 1125-9.

[22] K. Al Abdullah, A. Bui, A. Loubiere, Low frequency and low temperature behavior of ZnO-based varistor by ac impedance measurements, J Appl Phys, 69(1991) 4046-52.

[23] K.P. Biju, M.K. Jain, Sol–gel derived TiO_2:ZrO_2 multilayer thin films for humidity sensing application, Sensors and Actuators B: Chemical, 128(2008) 407-13.

[24] Z. Chen, C. Lu, Humidity sensors: a review of materials and mechanisms, Sensor Lett, 3(2005) 274-95.

[25] R.G. Pearson, Recent advances in the concept of hard and soft acids and bases, Journal of Chemical Education, 64(1987) 561.

List of Publications

1. Evaluation of n-type ternary metal oxide $NiMn_2O_4$ nanomaterial for humidity sensing Gawli, Y[#]., **Badadhe, S[#].**, Basu, A., D. Guin, Shelke, M.V., Ogale, S. Sensors and Actuators, B: Chemical 191 (2014) 837-843 ([#] = Equal contribution).
2. CdS nanowires: Ultra-long growth and enhanced field emission properties, Chavan, P.G., Kashid, R.V., **Badadhe, S. S**., More, M. A., Joag, D. S., Vacuum 101 (2014) 38-45
3. Effect of aluminium doping on structural and gas sensing properties of zinc oxide thin films deposited by spray pyrolysis, **Badadhe S. S**., Mulla I. S., Sensors and Actuators, B: Chemical 156 (2011) 943-948
4. Synthesis of single crystalline CdS nanocombs and their application in photo-sensitive field emission switches, Chavan, P.G., **Badadhe, S. S**., Mulla, I. S., More, M.A., Joag, D.S., Nanoscale 3 (3), (2011) 1078-1083
5. H_2S gas sensitive indium-doped ZnO thin films: Preparation and characterization, **Badadhe, S. S**., Mulla, I. S., Sensors and Actuators, B: Chemical 143 (2009) 164-170
6. Microwave-assisted synthesis and humidity sensing of nanostructured α-Fe_2O_3, Deshmukh, R.G., **Badadhe, S. S**., Mulla, I. S. , Materials Research Bulletin 44 (2009) 1179-1182
7. Facile synthesis and gas sensing properties of nanotriangular tin oxide, Deshmukh, R. G., **Badadhe, S. S**., Vaishampayan, M. V., Mulla, I. S., Materials Letters 62 (2008) 4328-4331
8. Synthesis, electron field emission, microstructure and optical investigation of iron vanadium oxide nanosheets, **Badadhe S. S.**, Suryawanshi S. R., Naphade R. A., Chaudhary M. V., More M. A., Shelke M. V.,and Ogale S. B. (Journal of Physics D: Applied Physics 2016 (Article Ref. JPhysD-107037.R1)

Manuscript submitted/preparation

1. Visible light assisted room temperature gas sensing property of ZnO NR/CdS heterojunction, **Badadhe S. S.**, Madhora J. A., Ogale S. B. and Shelke M. V. (submitted to Sensors and actuators B chem. 2015)

2. Facile synthesis and gas sensing properties of FeV_3O_8 nanosheets, **Badadhe S. S.**, Madhora J. A., Ogale S. B. and Shelke M. V. (Manuscript under preparation)
3. Synthesis, characterization and gas sensing behavior of nickel cobalt oxide (NCO) nanograss, **Badadhe S. S.**, Banerjee A., Madhora J. A., Ogale S. B. and Manjusha V. Shelke (Manuscript under preparation)

Conference proceedings

1. Hydrothermal synthesis and humidity sensing properties of Zn_2SnO_4, **Badadhe S. S.,** Shelke M. V., Ogale S. B., ICONSAT-2014
2. Extremely stable field emission and photo-sensitive field emission from single crystalline CdS nanowires, Chavan, P.G., More, M.A., Joag, D.S., **Badadhe, S.S**., Mulla, I. S. , 2011 Proceedings - IVNC (2011) 159-160
3. Field emission and photo-enhanced field emission investigations of CdS nanowires array, Chavan, P.G., **Badadhe, S. S.**, Mulla, I.S., More, M.A., Joag, D.S., 2011 IEEE International Vacuum Electronics Conference, IVEC-2011 (97-98)